JOHAN POHL

STRUCTURE AND PROPERTIES OF DEFECTS IN PHOTOVOLTAIC ABSORBER MATERIALS: ATOMIC SCALE COMPUTER SIMULATIONS OF Si AND $Cu(In,Ga)Se_2$

Zur Erlangung des akademischen Grades des Doktors der Ingenieurwissenschaften (Dr.-Ing.) genehmigte Dissertation vorgelegt von Dipl.-Phys. Johan Pohl
geboren in Friedberg

Fachgebiet Materialmodellierung
Fachbereich Material- und Geowissenschaften
Technische Universität Darmstadt

Hochschulkennziffer: D17

Referent: Prof. Dr. Karsten Albe,
Technische Universität Darmstadt

Korreferent: Prof. Dr. Hans-Werner Schock,
Helmholtz-Zentrum Berlin

Tag der Einreichung: 20. November 2012
Tag der Prüfung: 23. Januar 2013

Erscheinungsort: Darmstadt
Erscheinungsjahr: 2013

STRUCTURE AND PROPERTIES OF DEFECTS IN PHOTOVOLTAIC ABSORBER MATERIALS: ATOMIC SCALE COMPUTER SIMULATIONS OF Si AND $Cu(In,Ga)Se_2$

JOHAN POHL

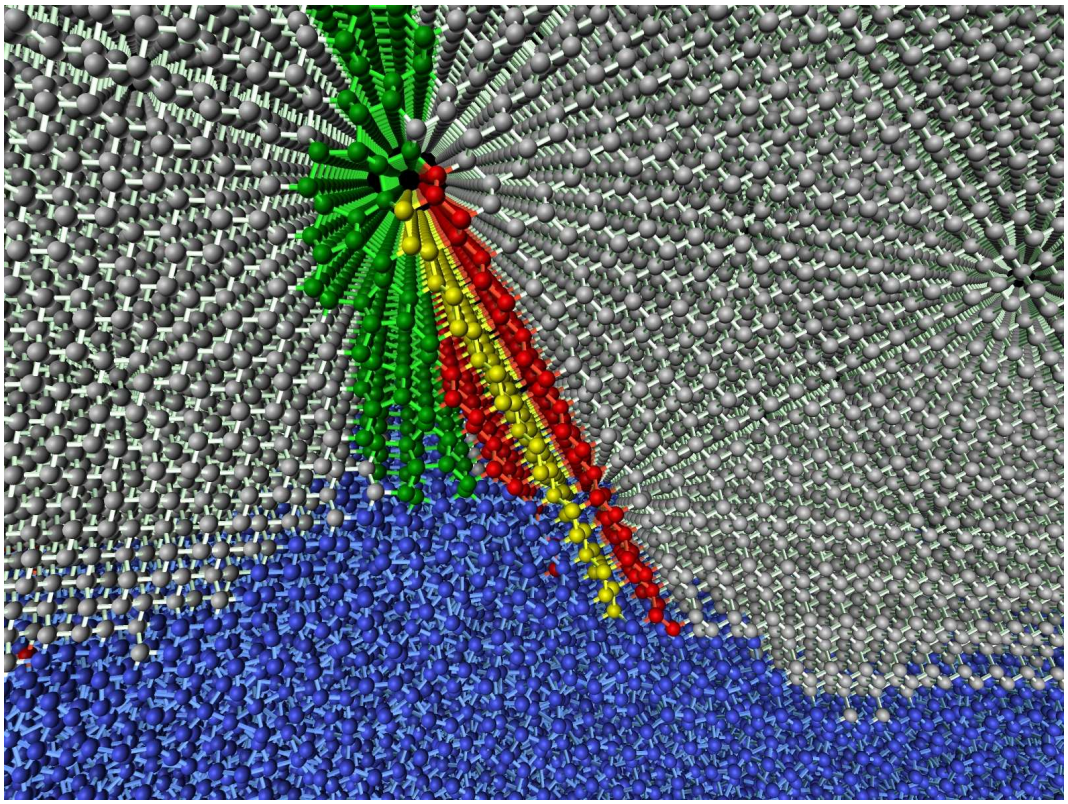

Dissertation

2013

On the cover: Twin boundaries originating at a grain boundary during silicon growth from the melt. Obtained from molecular dynamics simulations and visualized with OVITO. This image was awarded the second prize in the category *Digitally modified images* at the 17th American Conference for Crystal Growth and Epitaxy, Lake Geneva, USA.

CONTENTS

LIST OF ABBREVIATIONS

CB	conduction band
CBM	conduction band minimum
CI-NEB	climbing image nudged elastic band method
DFT	density functional theory
DLTS	deep-level transient spectroscopy
GGA	generalized gradient approximation
HSE06	Heyd-Scuseria-Ernzerhof screened-exchange hybrid functional (version of 2006)
LDA	local density approximation
LDA+U	local density approximation with +U Hubbard correction
NMR	Nuclear magnetic resonance
ODC	ordered defect compound
PAW	Projector augmented wave method
PBE-GGA	GGA parameterization of Perdew, Burke and Ernzerhof
PL	photoluminescence
VASP	Vienna ab-initio simulation package
VB	valence band
VBM	valence band maximum

Denomination of point defects

Cu_i	Interstitial defects: Copper interstitial
In_{Cu}	Antisite defects: Indium atom on a copper site
V_{Se}	Vacancies: Selenium vacancy

In_{DX}	Indium atom forming a DX-type defect
$In_{Cu} - 2V_{Cu}$	Defect complexes: In_{Cu} antisite defect paired with two copper vacancies
In_{Cu}^{+2}	Charge state denomination: In_{Cu} antisite defect in charge state +2

ABSTRACT

Solar cell technology is becoming a viable alternative to fossil fuels. The main challenge remains to deliver electricity at grid parity. To achieve this goal increasing the efficiency of solar cells remains the top priority. Most of the solar cells on the market are still based on silicon wafers. Cu(In,Ga)Se_2 thin-film technology, however, is becoming one of the main competitors with substantial advantage through reduced material and energy consumption in the production process. Knowledge-based improvement of the silicon as well as the Cu(In,Ga)Se_2 absorber material requires a better understanding of the material at the atomic scale. For this purpose, atomistic simulations are a useful approach to gain an understanding of properties and processes in the absorber material, which are hard or even impossible to access experimentally.

The scope of this thesis is to investigate the properties of intrinsic point defects in Cu(In,Ga)Se_2 and interface-related defect formation processes in silicon grown from the melt. For this purpose, various atomic-scale simulations methods are employed, ranging from ab-initio methods such as screened-exchange hybrid density functional theory to molecular dynamics simulation employing classical interatomic potentials and Lattice Monte Carlo techniques. This choice of methods allows to access the relevant system sizes and time scales relevant to the chosen problems. The detailed characterization of the intrinsic point defects in $CuInSe_2$ and $CuGaSe_2$ based on screened-exchange hybrid density functional theory yields a complete and consistent picture of the defect thermodynamics and the electronic properties of all relevant defects. Most importantly, copper self-diffusion is found to be mediated by both copper vacancy as well as by the interstitial and interstitialcy mechanisms. The interstitial mechanism has a particularly low migration barrier and is a likely source of fast electric field-enhanced diffusion as measured in some experiments. Cu_{In} and Cu_{Ga} antisites are found to act as a hole traps in both $CuInSe_2$ and $CuGaSe_2$ and are assigned to the N2 level, a prominent signal in admittance spectroscopy measurements in many samples. It is most likely also the source of a second deeper hole trap level which is consistent with measurements using photocapacitance spectroscopy. Ga_{Cu} antisites are found to exhibit a deep electron trap level in Cu(In,Ga)Se_2 only when the gallium content is sufficiently high, whereas In_{Cu} antisites are always shallow. The deep Ga_{Cu} trap level was confirmed by photoluminescence measurements in ternary $CuGaSe_2$ devices. The full picture of the intrinsic point defects including several proposed metastable defects is analyzed in detail and conclusions for device optimization are drawn. In addition, the results are put into perspective

to former results from local density theory in the literature and possible sources of deviations are discussed.

With respect to defect formation processes at the solid-liquid interface in silicon crystal growth, the formation mechanism of twin boundaries at the interface is revealed by molecular dynamics simulations. In contrast to former models, it is shown that twin boundaries can form at the triple line between two grains and the melt. In contrast, the spontaneous formation of twin boundaries at the interface is generally not possible in the absence of grain boundaries since this would inevitably lead to the formation of coherency and anti-coherency dislocations. The excess formation energy of these dislocations inhibits spontaneous twin boundary formation without grain boundaries. At elevated undercooling, however, faulted dislocation loops can be grown into the crystal at the interface. Molecular dynamics simulations show that subsequent shrinkage of these loops is responsible for an interface-related mechanism by which nanoscale vacancy clusters can be directly grown into the crystal. These clusters are large enough to be sustained at typical growth temperatures and may act as nucleation seeds for larger voids. Finally, a new lattice Hamiltonian model for the simulation of the solid-liquid growth interface is presented. This model extends the commonly used lattice models to include stacking faults and twin boundaries for the diamond cubic lattice. The model is applied to study the growth dynamics at the solid-liquid interface and accurately takes into account the formation energy of stacking faults. The simulations show that an undercooling of 50 K is sufficient for the spontaneous formation of faulted islands to occur at the interface.

MOTIVATION

The search for economic and sustainable access to energy generated by the sun remains one of the key challenges of the 21st century. Photovoltaics is the most direct way to convert photons from the sun into electricity. Much progress has been made in this area within the last decades, but the challenge remains to transfer efficient solar cells to mass production at a cost competitive to fossil fuels.

The maximum reachable theoretical efficiency is 30 % for a single-junction solar cell with an optimal band-gap of 1.1 eV as given by the Shockley-Queisser limit [1]. In practice, this efficiency limit is not attained due to imperfections and inefficient design of photovoltaic devices. Amongst other sources of efficiency losses, described in more detail in the following chapter, the inefficient design of devices with regard to the multiple valence and conduction band offsets involved in the band diagram and carrier recombination mostly due to defect states in the gap limit the efficiency of solar cells. For this reason, structural defects are a major concern for the performance of solar cells and should be avoided as far as possible. The present thesis will investigate many aspects of the defect physics by atomic-scale simulations in two of the most efficient single-junction absorber materials for solar cells known today: Silicon and Cu(In,Ga)Se_2.

Silicon is the prototypical solar cell absorber material and still largely dominates the solar module market. The highest purity single-crystal silicon solar cells hold the efficiency record for single-junction solar cells with 25.0 % efficiency reached in the laboratory (Figure 1) [2]. Even though silicon has been extensively studied since the advent of microelectronics in the 1950s, many questions concerning the formation processes and properties of defects remain. The formation mechanisms of twin boundaries, stacking faults and voids, as important examples of such defects in melt-grown silicon, are studied in Part IV of this thesis.

Cu(In,Ga)Se_2 shows properties very different from crystalline silicon, which help to attain high-efficiency polycrystalline thin-film solar cells [3]. First, it is a direct band gap semiconductor [4]. This is very favorable for thin-films since it goes in hand with an enhanced absorption coefficient in contrast to the indirect band-gap material silicon [5]. Second, it shows interesting properties concerning its defect physics. Unlike silicon, in which minor amounts of impurities can literally destroy the efficiency of a cell, Cu(In,Ga)Se_2 can tolerate deviations in stoichiometry up to several per cent [6]. Even grain boundaries in Cu(In,Ga)Se_2 seem not to decrease the performance of cells significantly and it has sometimes been put forward that they may even be beneficial [3]. In fact, the most efficient

thin-film solar cells today have reached laboratory efficiencies of up to 20.3 % (Figure 1) [7]. This is already comparable to the record reached by the highest efficiency multicrystalline silicon cells of 20.4 % [2]. The advantages of modern thin-film technology with film thicknesses of a few micrometers in comparison to standard wafer-based silicon technology are attractive: greatly reduced use of material and greatly reduced energy consumption in production while maintaining high single-junction efficiencies. This opens up huge potential for reduced production costs of solar cells, which is finally the only chance to establish photovoltaics as a sustainable and economic energy source. For this reason, $Cu(In,Ga)Se_2$ research projects remain a priority on the funding budgets of governmental funding agencies and innovative companies. As a result, the number of publications related to $Cu(In,Ga)Se_2$ has risen substantially during the past years, reaching more than 700 in 2011 (see Figure 2). In comparison to the semiconductor prototype silicon, however, our knowledge of $Cu(In,Ga)Se_2$ remains still limited. This should not come as a surprise considering the substantially increased complexity of a quaternary semiconductor compound. Even though numerous studies have focused on the point defect physics in the material, many issues are not sufficiently understood. The importance and impact of computational studies on point defects in $Cu(In,Ga)Se_2$ is well illustrated by the fact that the seminal paper *Defect physics of the $CuInSe_2$ chalcopyrite semiconductor* by Zhang *et al.* [8] is the second-most cited work out of the more than 6000 publications concerned with research on $Cu(In,Ga)Se_2$ as displayed in Figure 2 (with 506 citations reported on ISI Web of Knowledge as of November 2012). It is the purpose of the present thesis to advance our knowledge of the point defect physics in $Cu(In,Ga)Se_2$ by means of screened-exchange hybrid density functional theory in Part III. The identification of detrimental defects and understanding of their properties by simulations should help to avoid them in real world devices, which will hopefully lead to more efficient cells.

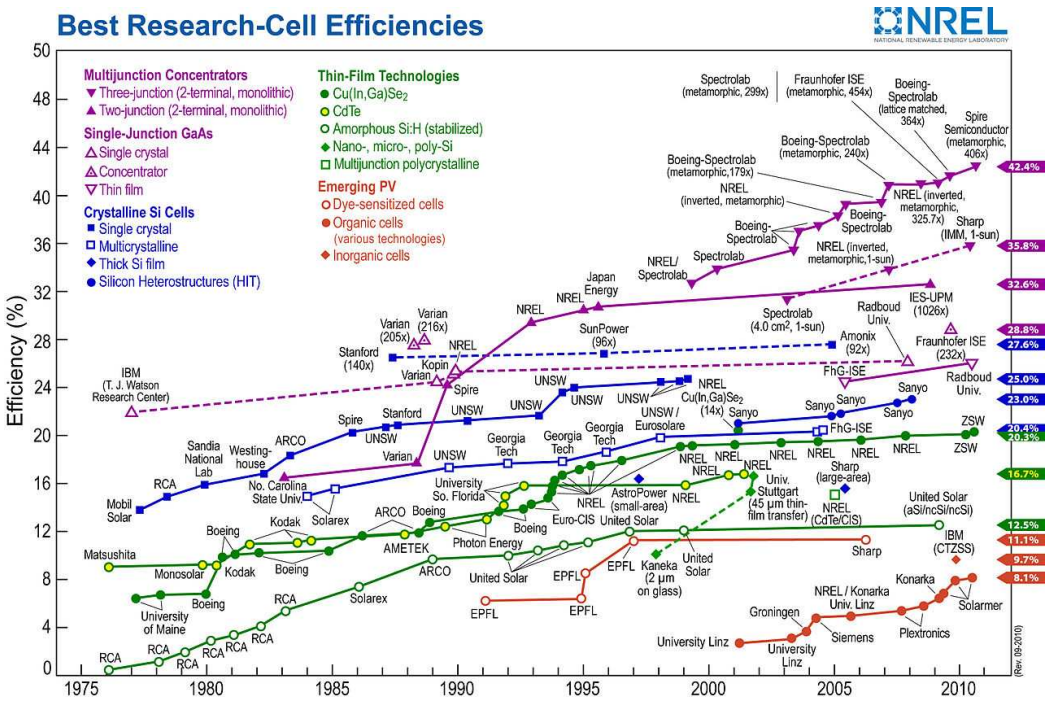

Figure 1: Best research cell efficiencies. Image and data compiled by Lawrence Kazmerski, National Renewable Energy Laboratory (NREL).

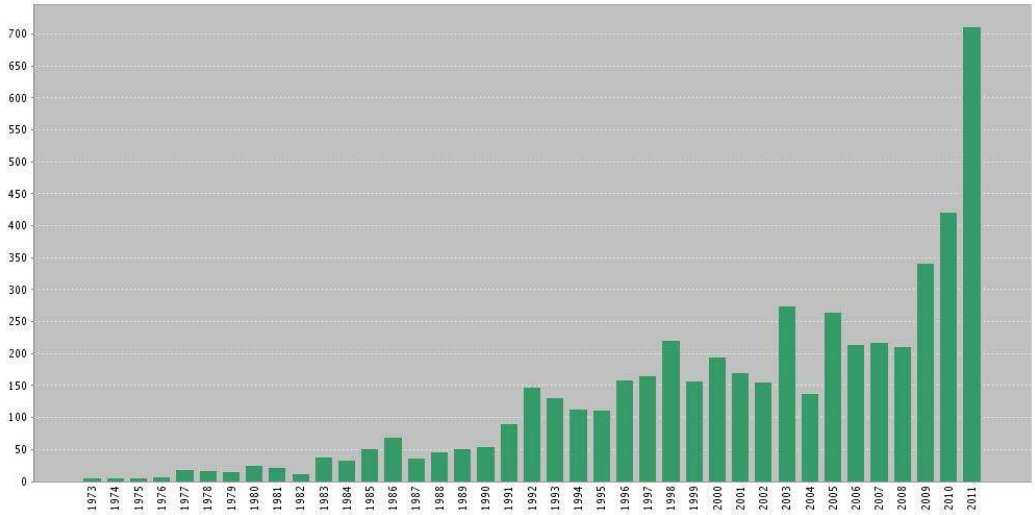

Figure 2: Number of published articles containing the words "CIGS", "CuInSe2", "CuGaSe2" or "CuInGaSe2" in the topic or title, Source: ISI Web of Knowledge, November 2012.

Part I

INTRODUCTION

The following part introduces the physics of solar cell devices as related to silicon and Cu(In,Ga)Se_2 in Chapter 1 and briefly reviews of the state knowledge about these materials as relevant to the topics of this thesis in Chapters 2 and 3.

1

SOLAR CELLS: PRINCIPLES AND CONCEPTS

1.1 INTRODUCTION

It is a challenging task to fully understand the physics which determines the efficiency of a solar cell. Many fields of physics, in particular solid state physics, but also fundamental concepts of statistical and quantum physics are needed to grasp the full picture. In this chapter a brief introduction into the physics of single-junction crystalline and thin-film solar cells is given based on the two examples relevant to the present thesis: Crystalline silicon solar cells and $Cu(In,Ga)Se_2$ thin-film cells.

For more in-depth treatments, excellent textbooks are available on the physical principles behind solar cells, e.g. by Würfel [9], approaching the subject from thermodynamics. Fonash's book, which makes extensive use of band diagrams, gives excellent descriptions of loss processes and discusses the semiconductor device governing equations [10]. Focusing on $Cu(In,Ga)Se_2$ thin-film solar cells, the recent book by Scheer and Schock provides an excellent review on the state-of-the art in the field [11], but it is also worth to mention a recent book about advanced characterization methods of these devices, which includes a treatment of modern simulation methods [12]. Finally, Greene [13] gives an excellent review of advanced third generation concepts for photovoltaics beyond single-junction solar cells.

1.2 BASIC CONCEPTS

A single junction solar cell is a p-n junction made up by a p- and an n-type semiconductor layer connected to an electric circuit via front and back contacts. In such a device impinging photons are absorbed and generate electron-hole pairs. These electrons and holes with opposite charges are separated in the space charge zone by the electric field. The separated charges can then be collected at the front and back contacts leading to an electric current. The process is visualized in form of a simple schematic band diagram of a p-n homojunction solar cell, such as a typical silicon cell, in Figure 3. Band diagrams are a useful and intuitive tool to think about photovoltaic devices and we will present more

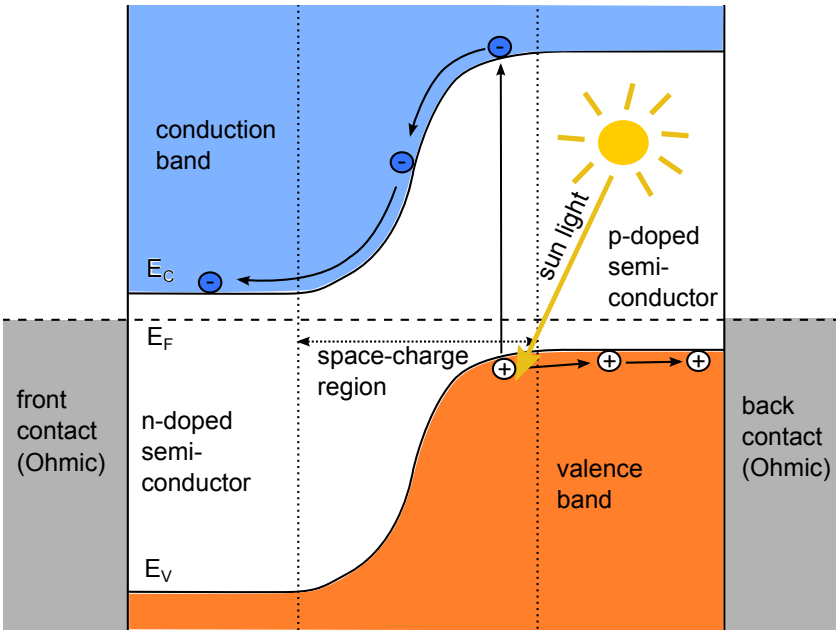

Figure 3: Typical schematic band diagram of a silicon solar cell.

detailed examples in the following. The figure shows the valence band, which is filled for a semiconductor and the conduction band, which is empty. A photon may be absorbed and creates an electron hole pair, when its energy exceeds the band gap energy. The excited electrons and holes are diffusing in their respective bands but are separated when they diffuse into the space charge region. In this region there exists a directed electric field and a gradient in the electrostatic potential. In case of the simple p-n junction in Figure 3, the negative electrostatic potential follows the form of the band edges. The electron may therefore gain electrostatic energy by moving down in its band, while the hole wins energy by moving upward. Electrons and holes are collected at the front and the back via metal contact and represent the generated electric current.

There are numerous ways to engineer a semiconductor p-n junction. One way is to in-diffuse impurities as is usually done for silicon by p-type doping e.g. with boron and n-type doping with phosphorus, which creates a homojunction. Another way is to deposit two layers of different materials on top of each other which are already n- and p-type conducting. This is called a heterojunction. Cu(In,Ga)Se_2 solar cells represent a heterojunction in a certain sense. For these cells there is an n-type buffer layer deposited on a p-type Cu(In,Ga)Se2 absorber layer. However, research has shown that the exact location of type inversion seems to be located within the absorber, approximately 50-80 nm away from the interface [14]. In this case we speak of a *buried junction*.

1.3 THE P-N HOMOJUNCTION

The Poisson equation

$$\frac{\partial^2 \phi}{\partial x^2} = \frac{n(x)}{\epsilon} \tag{1.1}$$

is at the heart of the description of semiconductor devices such as a p-n junction [15] and is therefore essential also to photovoltaics. It relates the the charge distribution $n(x)$ in the device to the electrostatic potential $\phi(x)$. ϵ is the dielectric constant. The total charge in the device

$$n(x) = q_A N_A(x) + q_D N_D(x) + n + p \tag{1.2}$$

is due to ionized donor and acceptor impurities with the concentration profiles N_A and N_D and the charges q_A and q_D, and due to free charge carriers, i.e. electrons and holes with the concentration profiles n and p. The concentrations of electrons and holes are related to the Fermi energy E_F by the expressions

$$n = N_C \exp\left(-\frac{E_C - E_F}{k_B T}\right) \tag{1.3}$$

and

$$p = N_V \exp\left(-\frac{E_F - E_V}{k_B T}\right), \tag{1.4}$$

where N_C and N_V are the effective density of states at the conduction and valence band edges, respectively, and E_C and E_V are the band edge energies.

Putting the above equations together and considering the relation between the Fermi energy, the band edges and the electrostatic potential one obtains

$$\frac{\partial^2 \phi}{\partial x^2} = \frac{1}{\epsilon}\left[q_A N_A(x) + q_D N_D(x) + n_i \exp\left(-\frac{\phi}{k_B T}\right) - n_i \exp\left(\frac{\phi}{k_B T}\right)\right], \tag{1.5}$$

which can be solved for any given impurity concentration level. In the current form the dopants have one fixed charge state q_A and q_B and n_i is the intrinsic carrier density. It is not a conceptual problem to write down the Poisson equation for any number of dopants and with charge states depending on the Fermi level. The dependency of charge states and defect formation energies on the Fermi level will be further discussed in Part II.

Solving the above equation yields useful information such as the charge distribution, the electric field and the potential distribution. Figure 4 shows the typical analytical textbook solution to the problem of an abrupt p-n junction. This solution makes use of the so-called *depletion approximation*, i.e. the approximation that the space-charge region is fully depleted of electrons and holes. Today's

numerical solvers can quickly solve Equation 1.5 for any dopant concentration profile without the use of such approximations.

The above example is for the equilibrium case, but can be generalized to the non-equilibrium steady-state description needed for example for the simulation of photovoltaic devices during operation by introducing the quasi Fermi levels E_{Fn} and E_{Fp} [10]. Away from thermal equilibrium the concentrations n and p are not directly related via a single Fermi level. There is one quasi-Fermi level for electrons E_{Fn} and one for holes E_{Fp} and they simply replace the equilibrium Fermi level in the expressions for concentrations above:

$$n = N_{\mathrm{C}} \exp\left(-\frac{E_{\mathrm{C}} - E_{\mathrm{Fn}}}{k_{\mathrm{B}}T}\right) \tag{1.6}$$

and

$$p = N_{\mathrm{V}} \exp\left(-\frac{E_{\mathrm{Fp}} - E_{\mathrm{V}}}{k_{\mathrm{B}}T}\right). \tag{1.7}$$

It is intuitive to understand that the concentration of electrons as well as holes can become large under illumination, when many electron hole pairs are generated.

For Cu(In,Ga)Se_2, additional complications may arise which render the above equations insufficient for device modeling. The doping distributions may not be constant in time when the solar cell is illuminated or a voltage bias is applied due to electromigration. This leads to a highly coupled problem in which basically all properties of the photovoltaic device are a function of time and illumination or bias. In this case, the above equations have to be coupled with a drift-diffusion model for ion migration for the mobile dopant species. In order to understand the full band diagram, which can give very useful information, such as the open circuit-voltage, short-circuit current, and from these the fill factor and efficiency of the device, all additional layers such as the buffer, back and front contact need to be included. Solving the Poisson equation is at the core of commonly used TCAD (technology computer-aided design) software used for process simulation and device modeling in microelectronics [16], but also increasingly so for research and design of solar cells. Well-known software packages for solar device simulation include the free packages SCAPS [17] and AMPS [18] as well as general-purpose commercial packages. In the following, we turn to the schematic band diagram of Cu(In,Ga)Se_2 solar cells.

1.4 A P-N HETEROJUNCTION: BAND DIAGRAM OF CU(IN,GA)SE_2 CELLS

The band diagram of a Cu(In,Ga)Se_2 cell is schematically shown in Figure 5. At the front of the cell ZnO is deposited as transparent conductive window layer.

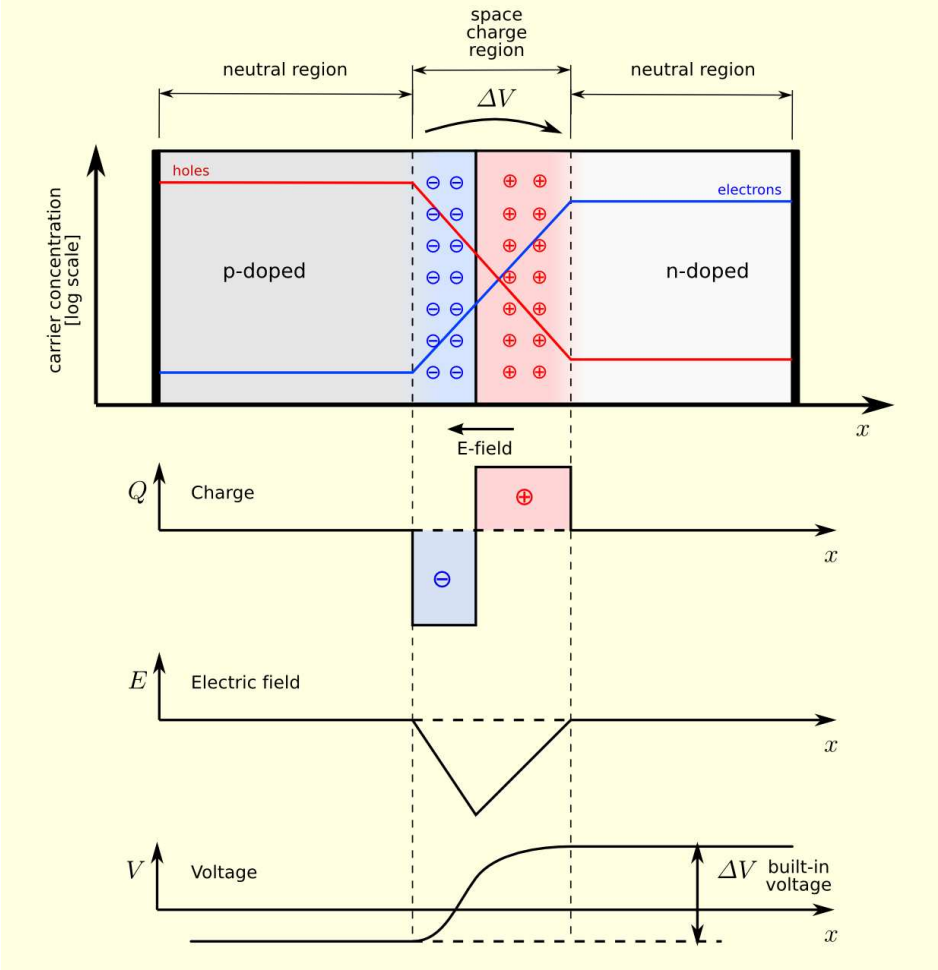

Figure 4: Charge Q or $n(x)$, electric field $E = -\nabla\phi$ and voltage V (or, equivalently, the electrostatic potential ϕ) for an abrupt p-n junction within the depletion approximation. Source: wikipedia, article on the *p-n junction*.

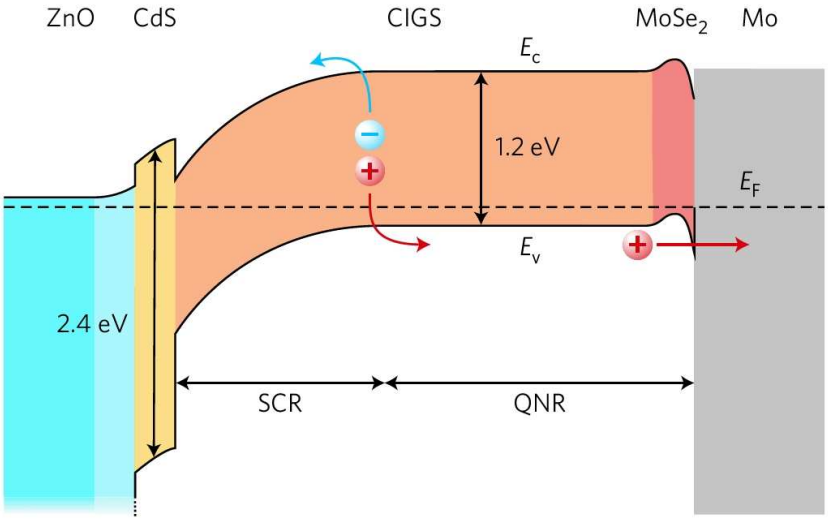

Figure 5: Schematic band diagram of a Cu(In,Ga)Se_2 heterojunction (from Ref. [22], reprinted by permission from Macmillan Publishers Ltd.). Five material layers are involved. The band edges E_C, E_V, the SCR (space charge region), quasi-neutral region (QNR), and the position of the Fermi level E_F are shown.

ZnO is a prototypical transparent conducting oxide (TCO) with many applications in photovoltaics and electronics. Between the ZnO window layer and the Cu(In,Ga)Se_2 absorber there is a very thin CdS buffer layer, commonly around 50 nm thick and deposited by chemical bath, while the thickness of the absorber is on the order of approximately one to two microns. The cell would work also without a buffer layer, but research has shown that the presence of an optimized buffer layer enhances the efficiency [19]. At least three reasons have been proposed for this observation [19]. First, the buffer layer protects against damages and chemical reactions resulting from the subsequent ZnO deposition. Second, it removes the natural thin oxide layer form the surface, which reestablishes the necessary positive charge needed for type inversion. And third, it removes remaining elemental selenium. Molybdenum is commonly used as the back contact material and a thin $MoSe_2$ layer has been observed to formduring deposition [20]. This $MoSe_2$ layer is understood to be responsible for the contact to be ohmic avoiding Schottky-type back contact barriers [20]. The band-gap is given as a constant of 1.2 eV in Figure 5, but in devices the band gap varies mainly due to a gradient of the indium versus gallium concentration [21]. This gradient is tuned to achieve the highest efficiency devices [22]. Detailed process engineering is necessary, which requires the exact control of copper, indium, gallium and selenium flow rates as a function of time. A three-stage coevaporation process has been the benchmark for absorber deposition for many years [21].

1.5 OPTIMIZING PHOTOVOLTAIC DEVICES: SOURCES OF EFFICIENCY LOSSES

1.5.1 *Efficiency limits and optimal gaps*

The limiting efficiency of a single-junction photovoltaic device is 40.8 % for an optimal band gap of 1.11 eV under direct illumination and 31.0 % with an optimal band-gap of 1.31 eV when diffuse light is used to generate the photocurrent [13]. Under real conditions, there is always a mixture between direct illumination by the sun and diffuse light, which is first scattered by the earths atmosphere before impinging onto the cell. The band gaps of silicon (1.1 eV) and Cu(In,Ga)Se_2 ($\approx$ 1.2 eV for [Ga]/[In+Ga]=0.3) meet the optimal band gap criterion quite closely. As a rule of thumb, the absorber band gap of an efficient device should lie within the range of 1.0 to 1.6 eV. It is rather straightforward to find materials with suitable band gaps for photovoltaics, but in order to achieve efficient devices many more factors need to be considered.

1.5.2 *Photocarrier recombination via defect states*

One of the main reasons for the limited efficiency of solar cells is the loss of photoexcited carriers, i.e. the recombination of electrons and holes via defect states in the band gap. Such states arise from defects such as point defects, dislocations, grain boundaries or at interfaces between different materials with lattice-mismatch. Recombination processes are often classified based on their location. For silicon solar cells they are often divided into the top (p-type) layer, the base (n-type) layer, recombination within the space charge zone and interface recombination. The classification is motivated by the fact that the character of defects is often different in the n- versus the p-type side, and the possible processes may depend also on the location of the Fermi level with respect to the band edges. In the literature on Cu(In,Ga)Se_2 cells a slightly different nomenclature is used. In this case, one distinguishes between recombination in the space charge zone (SCR) and in the quasi-neutral region (QNR) and additional recombination may occur in the buffer layer and at the buffer absorber interface as visualized in Figure 6. Interface recombination is a story of its own, but for our purposes it suffices to think about recombination at interfaces as defect-mediated processes via interface states in the gap. These may for example arise from broken bonds at an interface. Research has shown that all of the recombination processes in Figure 6 contribute to the loss of photocarriers in high-efficiency Cu(In,Ga)Se_2 cells, but recombination in the space-charge region seems to contribute the largest fraction [23]. The importance of defect-related loss processes for photovoltaics motivates the extensive efforts undertaken in this thesis to identify the relevant defects and their properties in Cu(In,Ga)Se_2 and to identify formation mechanisms of planar defects in silicon melt growth.

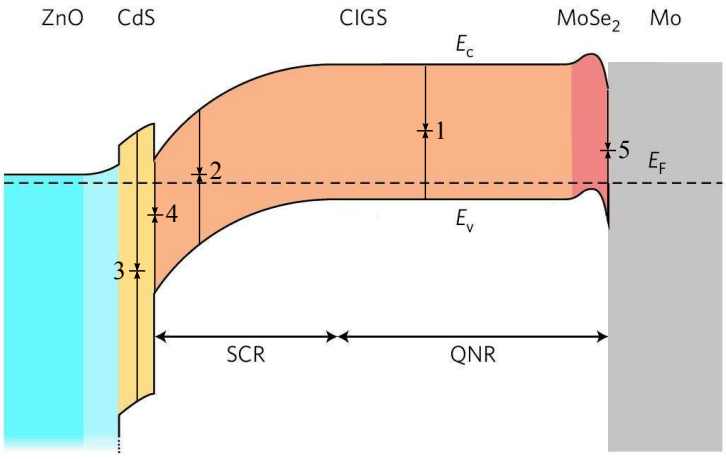

Figure 6: Recombination processes via defect states in $Cu(In,Ga)Se_2$ solar cells may occur in the quasi-neutral region (QNR) of the absorber bulk (1), in the space-charge region (SCR) (2), in the buffer (3), at the buffer-absorber interface (4) and at the absorber back-contact interface (5) (figure adapted by permission from Macmillan Publisher Ltd. from Ref. [22]).

1.5.3 *Band offsets*

Photovoltaic devices are also inefficient when the band offsets between the various layers in the band diagram are not optimally engineered. An efficient device requires suitable band offsets at the heterointerface as well as at the window layer, front and back contacts (Figure 5). The most important requirement to avoid loss of open-circuit voltage in $Cu(In,Ga)Se_2$ devices is that the conduction band offset at the p-n heterojunction interface is smooth or has only a minor spike that can be tunneled by electrons in the conduction band. In this case interface recombination can be avoided to a certain extent. Cliffs or big spikes will dramatically worsen the performance of the device.

1.5.4 *Lattice mismatch*

In order to avoid interface states in the band gap at heterocontacts it is required to choose similar lattice parameters. Low lattice mismatch generally leads to a favourable quality of the interface by reducing the density of interface states, which arise e.g. form misfit dislocations. The plot in Figure 7 shows the band gaps and lattice parameters of many ternary chalcopyrites and the lattice parameters of potential binary buffer materials. The image visualizes the compositional flexibility within the multinary chalgogenide family of compounds, which can be

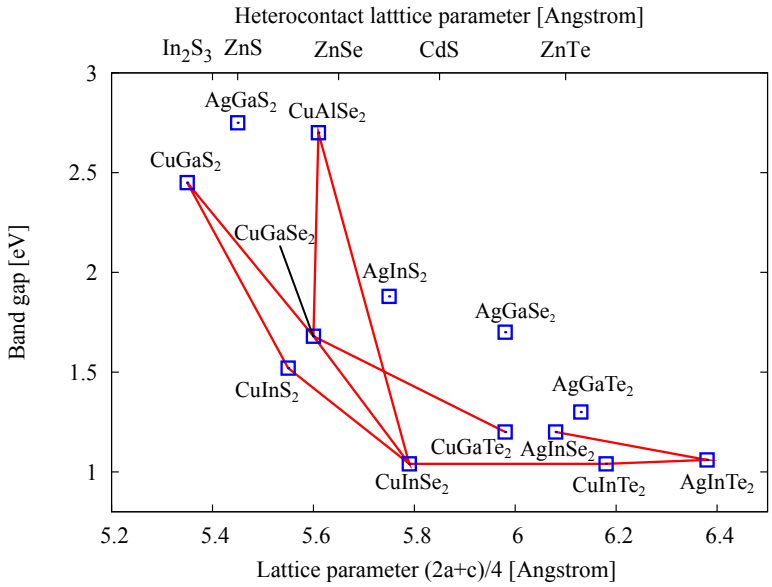

Figure 7: Lattice parameters and band gaps for various chalcopyrites. Lattice parameters for buffer materials are indicated at the top. The red lines between the compounds indicate miscibility. (Figure and data adapted from Ref. [11])

used to optimize the criteria of an optimal band gap and optimal lattice matching to the buffer simultaneously [11].

1.5.5 *Inhomogeneities and potential fluctuations*

Inhomogeneities in Cu(In,Ga)Se_2 have been identified to be a likely cause of efficiency limitation by several authors [24–27]. There can be different kinds of inhomogeneities: In general one distinguishes between fluctuations of the band gap and fluctuations of the electrostatic potential. Both of them can be induced by fluctuations in the composition. The fluctuations of the electrostatic potential, however, need charged defects to be present. It has been shown by Rau and Werner [24] that fluctuations of the band gap with a mean deviation of 100 meV can reduce the theoretical efficiency limit of solar cells by 6.1 per cent. This shows the significance of fluctuations for device optimization. However, the fluctuations of the electrostatic potential seem to be responsible for a larger reduction of the efficiency than the fluctuations of the band-gap in Cu(In,Ga)Se_2 cells [25, 26]. The fluctuations of the electrostatic potential have been measured to be on the order of 20 - 60 meV for Cu-poor $CuInSe_2$ and $CuGaSe_2$ [27] and have been estimated to be on the order of 140 meV at zero bias by Werner *et al* [25]. Control of inhomogeneities and potential fluctuations in Cu(In,Ga)Se_2 remains an active research topic and promises significant improvements of effi-

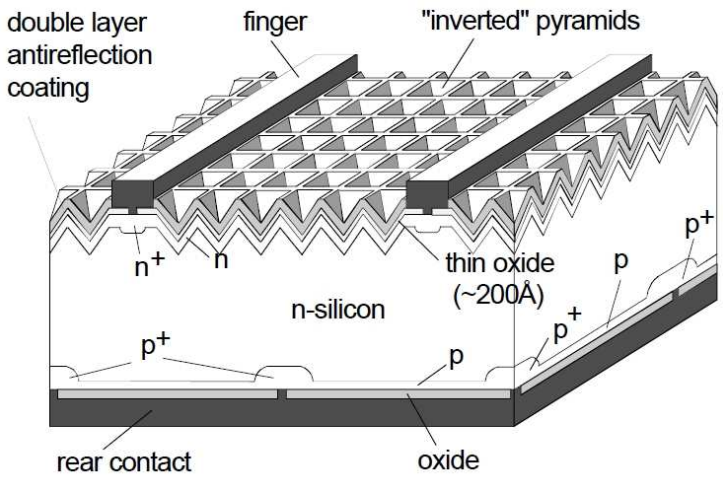

Figure 8: Example of a rear emitter n-type PERT cell structure (from Ref. [28], ©2006 IEEE, reprint with permission).

ciency. The relation of inhomogeneities to point defects should be pointed out here. Inhomogeneities in the intrinsic charged dopant profiles may partially be responsible for the electrostatic potential fluctuations. Point defects may thus exhibit indirect detrimental effects beyond recombination via defect states, but this point is hardly discussed in the literature.

1.6 REAL HIGH-EFFICIENCY DEVICES: SILICON VERSUS CU(IN,GA)SE_2

Even though the simple band diagram such as in Figure 3 is very useful to understand the basic device physics of a solar cell, it should also be mentioned that real silicon devices can be a lot more complicated. As an example, the schematics of a high-efficiency design for a single crystalline PERT (passivated emitter, rear totally-diffused) silicon solar cell is shown in Figure 8. One can clearly see that the geometry is very complex involving e.g. an anti-reflective surface structure and multiple p, p+, n and n+ layers. The shown design of a silicon device has reached record efficiencies up to 22.7 per cent [28].

The scanning electron micrograph image (SEM) of a real Cu(In,Ga)Se_2 thin film device is displayed in Figure 9. Obviously, such devices are highly polycrystalline with high-densities of grain boundaries and dislocations, not to mention the point defects and inhomogeneities due to variations in the indium and gallium concentrations, which can not be distinguished in the image. It should be obvious at this point that the band diagrams presented above, while being very useful concepts, are only approximate representations of real-world devices.

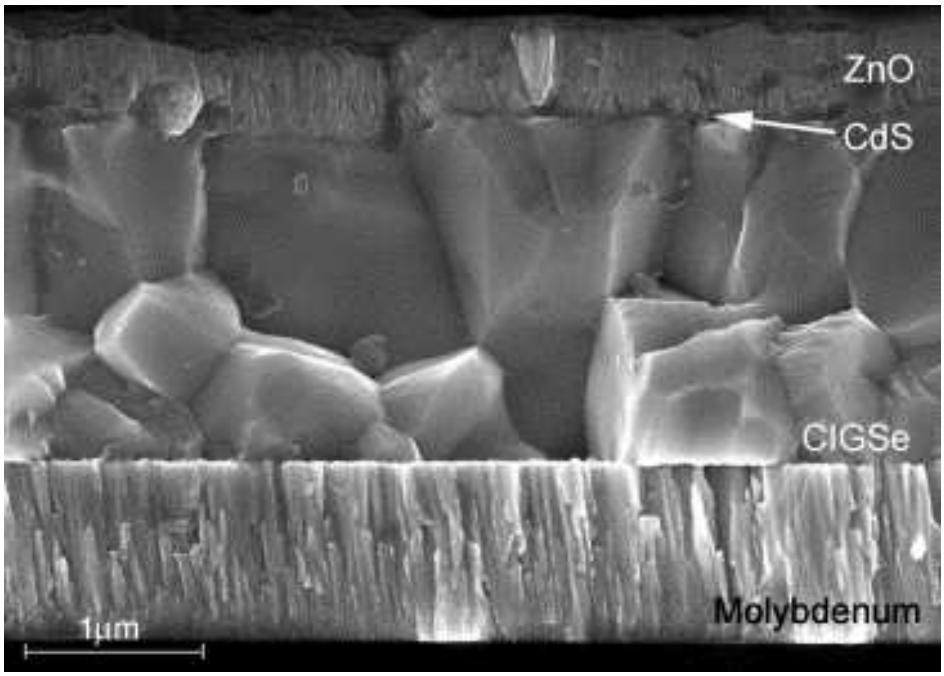

Figure 9: SEM micrograph of a cross-section of a Cu(In,Ga)Se_2 thin film solar cell deposited on a glass substrate (reprinted from Ref. [29] with permission from Elsevier).

2

$Cu(In,Ga)Se_2$: INTRINSIC POINT DEFECTS, PHASE DIAGRAM AND DIFFUSION

2.1 INTRODUCTION

This chapter will review the state of knowledge on some fundamental properties of the $Cu(In,Ga)Se_2$ absorber material itself focusing on the theoretical and experimental knowledge on intrinsic point defects, the phase diagram and copper diffusion. The reader who is not familiar with the thermodynamics of point defects may consult Chapter 5. All necessary concepts are reviewed there. The present chapter sets the stage for the detailed study of the intrinsic point defect physics in $CuInSe_2$ and $CuGaSe_2$ and copper diffusion mechanisms by means of screened-exchange hybrid density functional theory presented in Part III of this thesis. For excellent and more complete reviews of the properties of $Cu(In,Ga)Se_2$ with respect to its use as an absorber in thin-film solar cells the reader is also referred to Refs. [11] and [5].

2.2 INTRINSIC POINT DEFECTS

From a theoretical perspective, point defects in $CuInSe_2$ and $CuGaSe_2$ have mostly been studied using density functional theory within the supercell approach [8, 30–41]. The seminal paper by Zhang *et al.* [8] from 1998 on the defect physics in $CuInSe_2$ allowed to identify the defects responsible for intrinsic doping and gave a good first understanding of the defect physics in $CuInSe_2$ and subsequently in $CuGaSe_2$. The calculated high stability of the $In_{Cu} - 2V_{Cu}$ neutral defect complex was invoked to explain the stability of the so-called *ordered defect compounds* (ODCs, see also Section 2.3). In addition, the removal of the deep level of In_{Cu} upon pairing with the copper vacancies was presented as an explanation of the very good tolerance to large off-stoichiometries. The study represents the first work, which aims at a proper account of the point defect thermodynamics in terms of the chemical potentials of the constituent elements. This is essential since the formation enthalpies of point defects are strongly dependent on the chemical potentials and these are directly related to the preparation conditions of the material. The point defect formation energies

and the stability diagram of the study by Zhang *et al.* [8] are displayed in Figure 10. A prominent feature of these defect formation energy plots, which has often been cited in the literature, is that certain defects have negative formation energies over the entire range of the Fermi energy (e.g V_{Cu} at point B and Cu_{In} at point C). This is a consequence of the choice of chemical potentials, which were chosen as the extremum points A, B and C outside the stability region of $CuInSe_2$. For a physical interpretation of the thermodynamics of point defects, the chemical potentials should rather be chosen within the stability region of the phase to be considered. Methodologically, the study made use of the LDA functional and a static band gap correction. This correction scheme may not be accurate enough for reliable defect formation enthalpies, from today's point of view.

In 2004 the theoretical work on point defect physics in $CuInSe_2$ and $CuGaSe_2$ was picked up by Persson *et al* [33, 34]. While the work focused on the dopability of compounds, it also made use of improvements in the understanding of the corrections needed for accurate point defect enthalpies. For example the correction to the band edges was determined from LDA+U rather than using a static ad-hoc correction. The stability diagram as a function the chemical potentials and examples of the resulting point defect formation enthalpies are given in Figure 11. The plot allows to identify the Fermi level which results for the given chemical potentials. It is approximately determined by the point where copper vacancies and indium copper or gallium copper antisites, respectively, compensate each other $E_F^{n,comp}$. The exact equilibrium Fermi level E_F^{eq} as determined from the charge neutrality condition deviates only slightly from this exact point due to the contribution of free charge carriers (see Figure 11). Note that this picture of a compensated compound semiconductor, consistent with experiment, does not arise from the formation enthalpies as determined by Zhang *et al.* previously [8], since the relative formation enthalpies of copper vacancies versus indium antisites are largely different there such that a compensation Fermi level does not exist (see Figure 10). Persson *et al.* also found a Fermi pinning level due to the copper vacancy. This pinning level is located at the point where the formation energy of the copper vacancy as a function of the Fermi level is zero. When the formation energy is zero spontaneous formation of a high number of these defects can be expected, which results in the Fermi level being pinned, i.e. it can not be driven higher than the pinning level value.

Experimentally observed metastabilities have motivated the search for metastable point defects. Lany *et al.* suggested two intrinsic defects, which exhibit metastable properties: The selenium vacancy V_{Se} [35], or its complex with a copper vacancy $V_{Se} - V_{Cu}$ [36], and the intrinsic indium and gallium DX centers $(In, Ga)_{DX}$ [37].*

* DX centers in Cu(In,Ga)Se_2 can be regarded as In_{Cu} or Ga_{Cu} antisites, which are slightly displayed from their lattice site to the neighbouring threefold selenium coordinated site and carry two additional electrons, i.e. they are neutral. The denomination is motivated by extrinsic defects in GaAs with similar properties. See also the footnote on page 57.

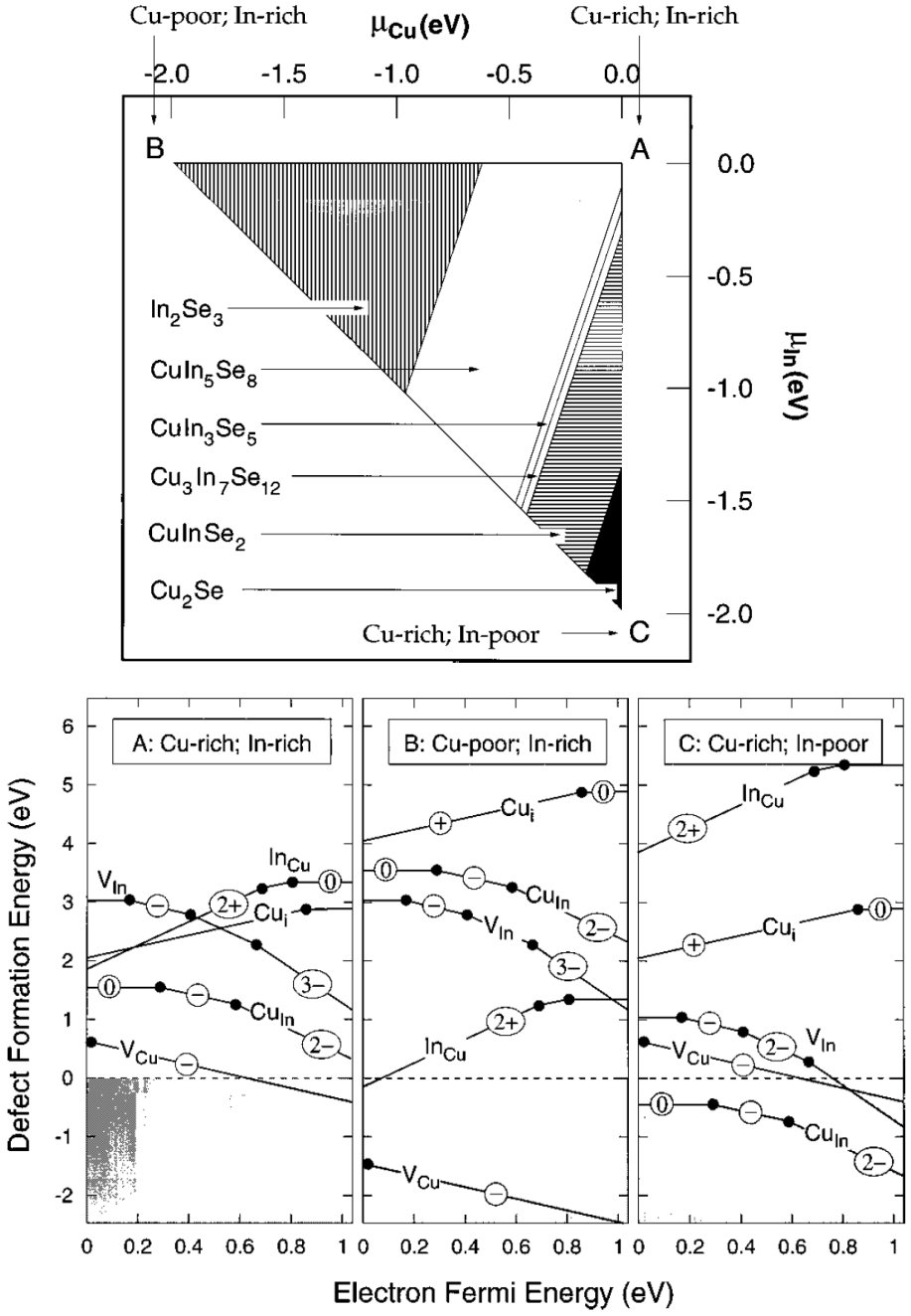

Figure 10: Point defect formation energies in $CuInSe_2$ and the stability diagram of the Cu-In-Se system (images from the work of Zhang *et al.* [8], ©1998 by the American Physical Society). The points A, B and C of the defect plots correspond to the extremum points in the stability diagram outside the stable region of $CuInSe_2$.

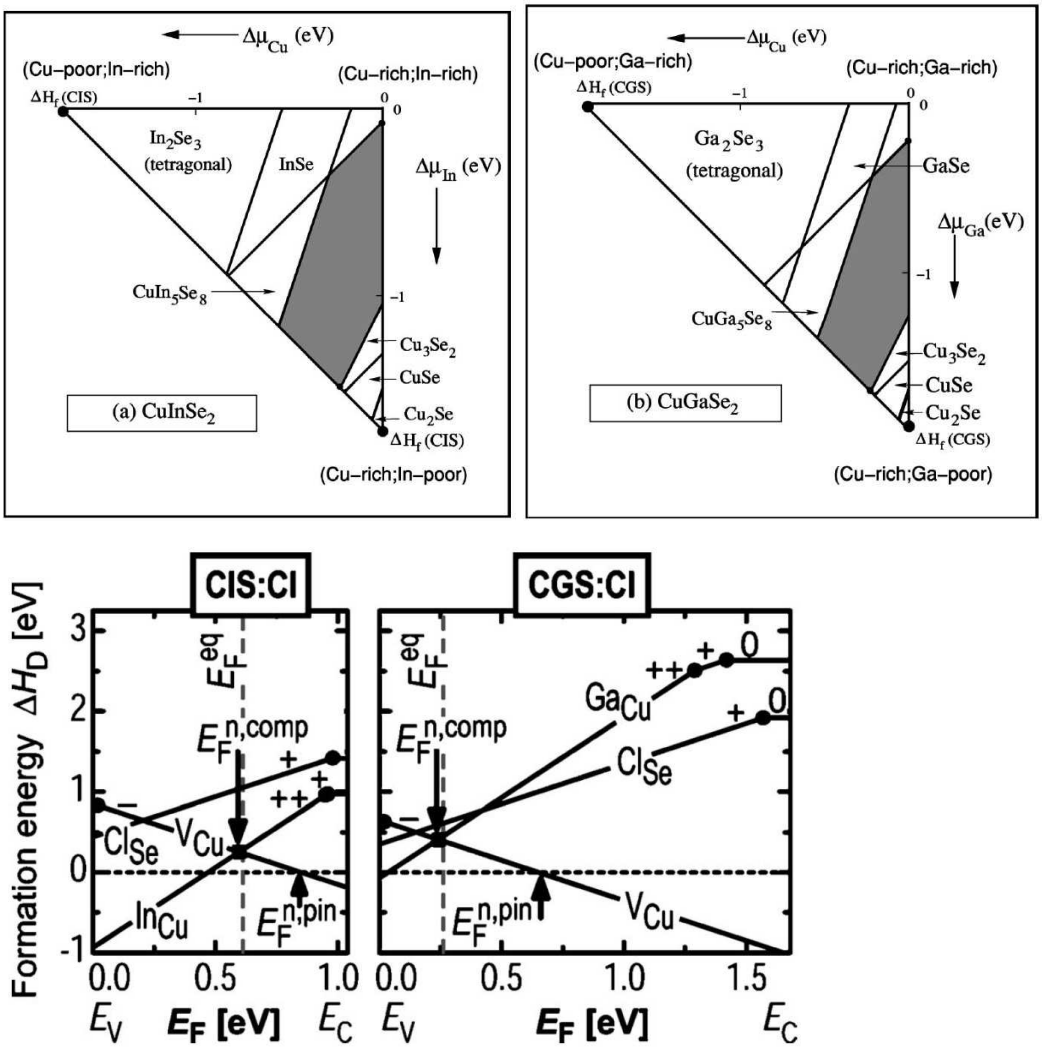

Figure 11: Stability diagrams for the Cu-In-Se and Cu-Ga-Se systems and point defect formation energy plots for $CuInSe_2$ and $CuGaSe_2$ containing the intrinsic point defects V_{Cu}, In_{Cu} and Ga_{Cu} (images from the work of Persson *et al.* [34], ©2005 by the American Physical Society). These intrinsic defects determine the compensation Fermi level $E_F^{n,comp}$ and the equilibrium Fermi level E_F^{eq}. The copper vacancies exhibit a pinning level $E_F^{n,pin}$. The formation energies are plotted for maximally indium and copper rich conditions, which correspond to maximum n-type conditions ($\Delta\mu_{In} = -0.07$ eV and $\Delta\mu_{Cu} = 0.0$ eV for $CuInSe_2$; $\Delta\mu_{Ga} = -0.21$ eV and $\Delta\mu_{Cu} = 0.0$ eV for $CuGaSe_2$).

A metastable point defect generally shows two different configurations separated by a large lattice relaxation, i.e. two configurations with clearly distinct atomic positions for the two different charge states separated by an energy barrier. In this case, the relative stability of the two different configurations depends on the Fermi level. When the Fermi level is changed such that the current configuration becomes unstable, the defect needs to relax over the energy barrier. During the time needed for relaxation the defect is thus metastable. Many different metastable effects have been experimentally observed in Cu(In,Ga)Se_2, such as persistent photoconductivity [42], the increase of the open-circuit voltage upon white-light soaking [43], an increase of the space-charge upon illumination [44] or reverse-biasing [45] accompanied with a decrease of the fill factor [46] as well as capacitance relaxation on long time scales after light-soaking [47]. However, it remains under debate, which, if any of these effects, can be assigned to metastable point defects [48, 49]. In the following, the metastable properties of V_{Se},$V_{Se} - V_{Cu}$ and $(In, Ga)_{DX}$ as proposed by Lany and Zunger [35–37] are briefly reviewed.

The selenium vacancy has been proposed as a metastable defect in $CuInSe_2$. It shows a large lattice relaxation at the +2/0 charge transition level at 0.08 eV (after Ref. [35]) which is associated with forming or breaking a bond between the adjacent indium atoms. Lateron it has been proposed that most of the selenium vacancies in $CuInSe_2$ actually exist as $V_{Se} - V_{Cu}$ complexes [36]. The metastable property of the selenium vacancy carry over to the the $V_{Se} - V_{Cu}$ complex. For the complex the metastable +1/-1 charge transition level† is located at 0.19 eV in $CuInSe_2$ and at 0.32 eV in $CuGaSe_2$ (Figure 12). This level can potentially explain certain metastabilities in Cu(In,Ga)Se_2 devices since the Fermi level is likely to be located below 0.2 eV in the absorber bulk material. When the device is biased or illuminated the Fermi level may be raised above the +1/-1 charge transition level such that the -1 charge state becomes stable. Two additional electrons would be trapped at the defect and this would increase the hole density. After the light or bias treatment is switched off, the defect could relax to its +1 ground state, but it has to overcome an energy barrier. Therefore, the relaxation process is slow such that the increased hole density can persist, which was proposed to explain persistent photoconductivity and other metastable effects [36]. This metastable process is conveniently visualized in a *configuration coordinate diagram* (Figure 13). It should be already noted at this point that the formation enthalpy of the $V_{Se} - V_{Cu}$ complex is relatively high even at favorable selenium-poor conditions (Figure 12). Therefore, the concentration of such defects in thermodynamic equilibrium could be expected to be rather low. Thus, it seems questionable if significant metastabilities, which require concentrations on the order of the free charge carrier density, can be attributed to $V_{Se} - V_{Cu}$.

† The charge of the copper vacancy of -1 adds to the charge of both configurations as compared to the +2/0 charge transition level of the sole V_{Se} defect.

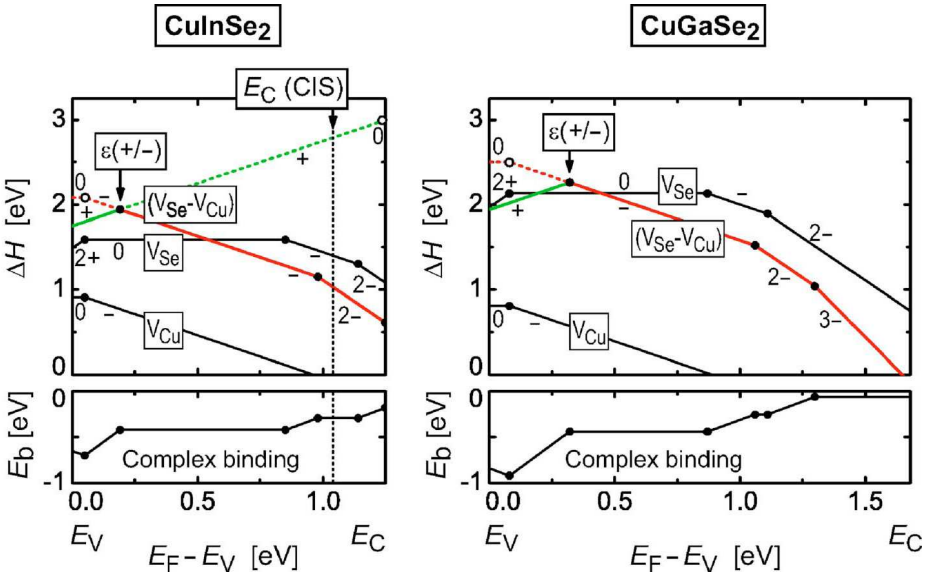

Figure 12: Defect formation enthalpy plot of the $V_{Se} - V_{Cu}$ complex (from the work of Lany and Zunger [36], ©2006 American Institute of Physics, reprint with permission). The important metastable charge transition level is indicated as $\epsilon(+/-)$

The In_{DX} and Ga_{DX} center have also been proposed as metastable defects in $CuInSe_2$ and $CuGaSe_2$ by Lany and Zunger [37]. The ground state configuration of these defects are plain In_{Cu}^{+2} and Ga_{Cu}^{+2} defects. When the Fermi level is raised above the DX pinning level E_{DX}^{pin} (0.92 eV in $CuInSe_2$, 0.84 eV in $CuGaSe_2$ [37]), however, the DX configurations were predicted to become energetically more favorable. The defects gain energy when they transform into the neutral DX configuration In_{DX}^{0} or Ga_{DX}^{0} by displacing the defect atom to the nearby threefold selenium-coordinated site and capturing two electrons (see Figure 15). The high Fermi level which is needed for the DX center to be stable suggests that it may only occur close to the buffer absorber interface where strong band bending occurs. The DX center then exhibits properties of a recombination center due to its defect state in the band gap (with single-particle energies ϵ_{DX} in Figure 14). It has therefore been suggested as a possible cause for the difficulty to maintain high efficiencies when gallium is alloyed in the absorber to increase the band gap [37]. The predicted metastable properties of the DX centers have been related to reversible changes of the fill factor in Cu(In,Ga)Se_2 solar cells as measured by admittance spectroscopy and capacitance-voltage characterization [37, 50].

A lot of defect-related experimental data exists from studies using many different spectroscopy methods such as e.g. photo- and cathodoluminescence, admittance and deep-level transient spectroscopy [51–53], photocapacitance measurements [54, 55], drive-level capacitance profiling [56], and Hall measurements

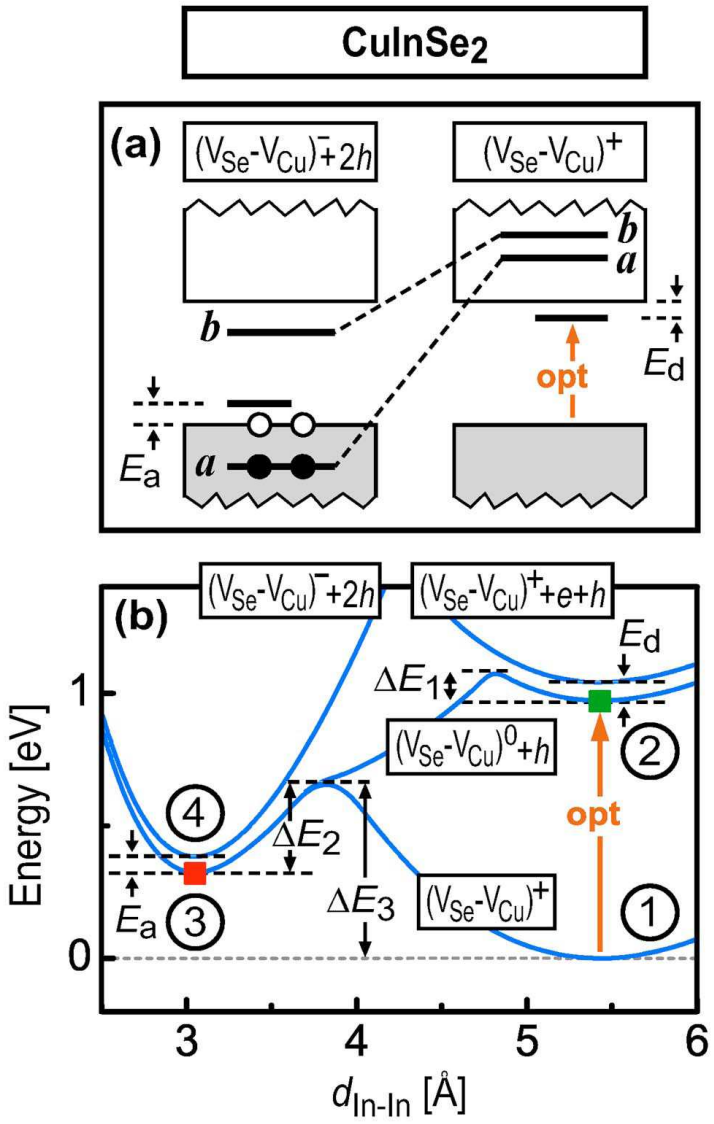

Figure 13: Configuration coordinate diagram of the $V_{Se} - V_{Cu}$ defect complex in $CuInSe_2$ (from the work of Lany and Zunger [36], ©2006 American Institute of Physics, reprint with permission). The trapping of optically excited electrons leads into the $(V_{Se} - V_{Cu})^-$ state (4). This state is potentially metastable and may persist, since the energy barrier ΔE_2 has to be overcome in order to relax to the $(V_{Se} - V_{Cu})^+$ state.

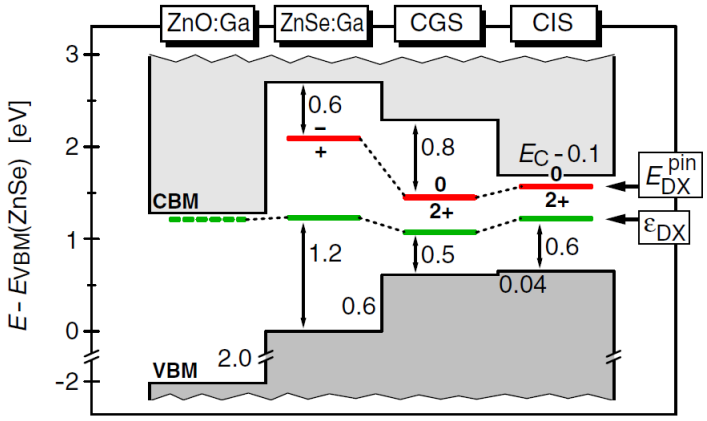

Figure 14: Pinning levels and single-particle energies of DX centers in $CuInSe_2$ and $CuGaSe_2$ as determined from LDA compared to pinning levels in other compounds (from the work of Lany and Zunger [37], ©2008 American Physical Society, reprint with permission).

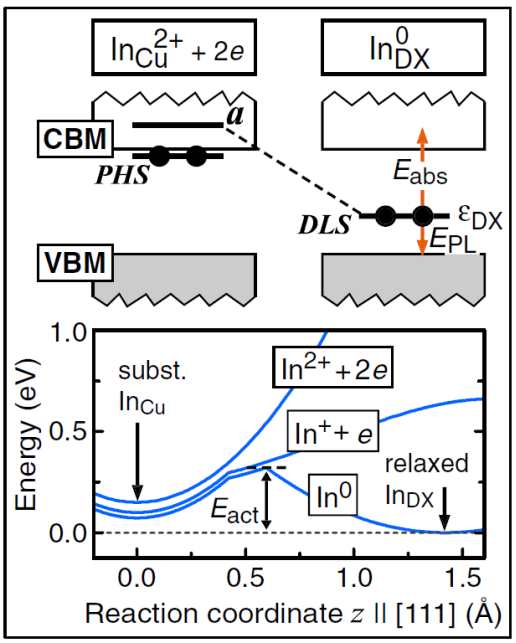

Figure 15: Configuration coordinate diagram for the metastable indium DX center in $CuInSe_2$ (from the work of Lany and Zunger [37], ©2008 American Physical Society, reprint with permission).

[57]. It is difficult to comprehensively summarize all of the experimental findings, but the data seem to support the existence of a deep level around 0.8 eV independent of Gallium content [54, 55] and of a hole trap level in the range between 0.15-0.35 eV in both $CuInSe_2$, $CuGaSe_2$ and its alloys [51–53, 57–61]. When measured using admittance spectroscopy, this level is often denominated as *N2*. For further reading, the reader is pointed to a recent review on shallow defects in $CuInSe_2$ and $CuGaSe_2$ [62]. Generally, the experimental data does not seem to be sufficient to assign any of the metastable phenomena to a certain metastable point defect.

2.3 PHASE DIAGRAM

Let us now turn to the discussion of the phase diagram of $CuInSe_2$ and $CuGaSe_2$. The phase diagram is essential for the understanding of diffusion and the interpretation of experimental results, e.g. when employing interdiffusion couples. The connection between the stability diagram (the grand-canonical zero temperature version of the common temperature-composition phase diagram), the chemical potentials of the constituent elements and the intrinsic point defects is an essential foundation of the present study. This fundamental connection will be further addressed in Part II of this thesis.

The ternary phase diagram of $CuInSe_2$ has been investigated in detail by Gödecke *et al* [63, 64]. Their pseudo-binary phase diagram is displayed in Figure 16. The stable solid phases in the ternary Cu-In-Se system are exclusively located on the Cu_2Se-In_2Se_3 pseudo-binary line. In addition to the boundary phases Cu_2Se and In_2Se_3 there are three phases, which are stable at room temperature α ($CuInSe_2$), δ_R ($CuIn_3Se_5$), γ_{T_R} ($CuIn_5Se_8$). The α phase corresponds to the common chalcopyrite crystal structure but may deviate significantly into the copper-poor composition up to 3 % at 600°C. A disordered high-temperature phase δ_H is stable over a wide concentration range and up to the melting point. The stable phases at room temperature are not consistently denominated in the literature. In this thesis, it is thus preferred to use the compositional description $CuInSe_2$, $CuIn_3Se_5$ and $CuIn_5Se_8$ to refer to these phases. The stability of $CuIn_3Se_5$ and $CuIn_5Se_8$, which are also referred to as ordered defect compounds (ODCs‡), has been suggested to result from the low formation enthalpy of $In_{Cu} - 2V_{Cu}$ defect complexes on the basis of local density functional theory [8, 30], but experimental studies do not seem to confirm the predicted long-range order [65]. The structure of the $CuIn_3Se_5$, $CuGa_3Se_5$ and their alloys has been debated [66, 67], but recently the debate seems to converge to a stannite-structure with $I\bar{4}2m$ space group [65]. The literature is not conclusive on the structure and the question of long-range order in $CuIn_5Se_8$ and $CuGa_5Se_8$. Many other compounds with stoichiometries between $CuInSe_2$ and $CuIn_5Se_8$ have been reported, but it is not

‡ The term *ordered vacancy compound* (OVC) is equivalently used in older papers.

clear whether they really exist as discrete phases in equilibrium [5]. In general, the Cu-Ga-Se system is much less well studied than the Cu-In-Se system.

2.4 COPPER DIFFUSION

Experimental determination of copper diffusion in $CuInSe_2$ yields diffusion coefficients varying over seven orders of magnitude from 10^{-13} to $10^{-7}cm^2/s$ at room temperature [68–72]. A pronounced dependence of the diffusion coefficient on copper concentration [71] and correlation with conductivity [70] has been found in experiments. Copper redistribution at the $CuInSe_2$/CdS interface has been proposed to be responsible for the voltage-bias induced metastable behavior of $CuInSe_2$ solar cells [45]. A model in which copper interstitials exhibit long-range field-induced drift from an interface into the bulk leaving negatively charged vacancies behind was formulated by Herberholz *et al.* [45], but direct evidence for this mechanism is still lacking today. Copper migration from the interface into the bulk has also been observed during deposition of the CdS buffer layer on $CuInSe_2$ at a certain Fermi pinning level citeKJ99, KFJ+00. Finally, external electric fields induce p-n junctions in p-type $CuInSe_2$ which is due to copper migration [71, 73–77]. For all of these phenomena, however, the atomistic details are not thoroughly understood. The diffusion of copper especially in relation to the formation of ODCs is not understood and therefore more detailed insights are desirable. The diffusion of copper via vacancy, interstitial and interstitialcy mechanisms and its consequences are addressed in chapters 7 and 8 of this thesis.

2.5 OPEN QUESTIONS

In Part III of this thesis, a complete recharacterization of the intrinsic point defect physics is carried out based on screened-exchange hybrid density functional theory and copper diffusion mechanisms are investigated. The improved accuracy of the method as compared to local density functional theory is one of the main motivations for this endeavor. It is intended to provide accurate answers to the following questions on the basis of the obtained data:

- What is the relation of the copper vacancy to the pinning of the Fermi level in the various compounds?
- Which are the most relevant intrinsic point defects in $CuInSe_2$ and $CuGaSe_2$, that can be contained in the absorber?
- Which defects represent relevant electron and hole traps?
- What are there experimentally observable activation energies?
- Which are the relevant mechanisms for copper diffusion in $CuInSe_2$?

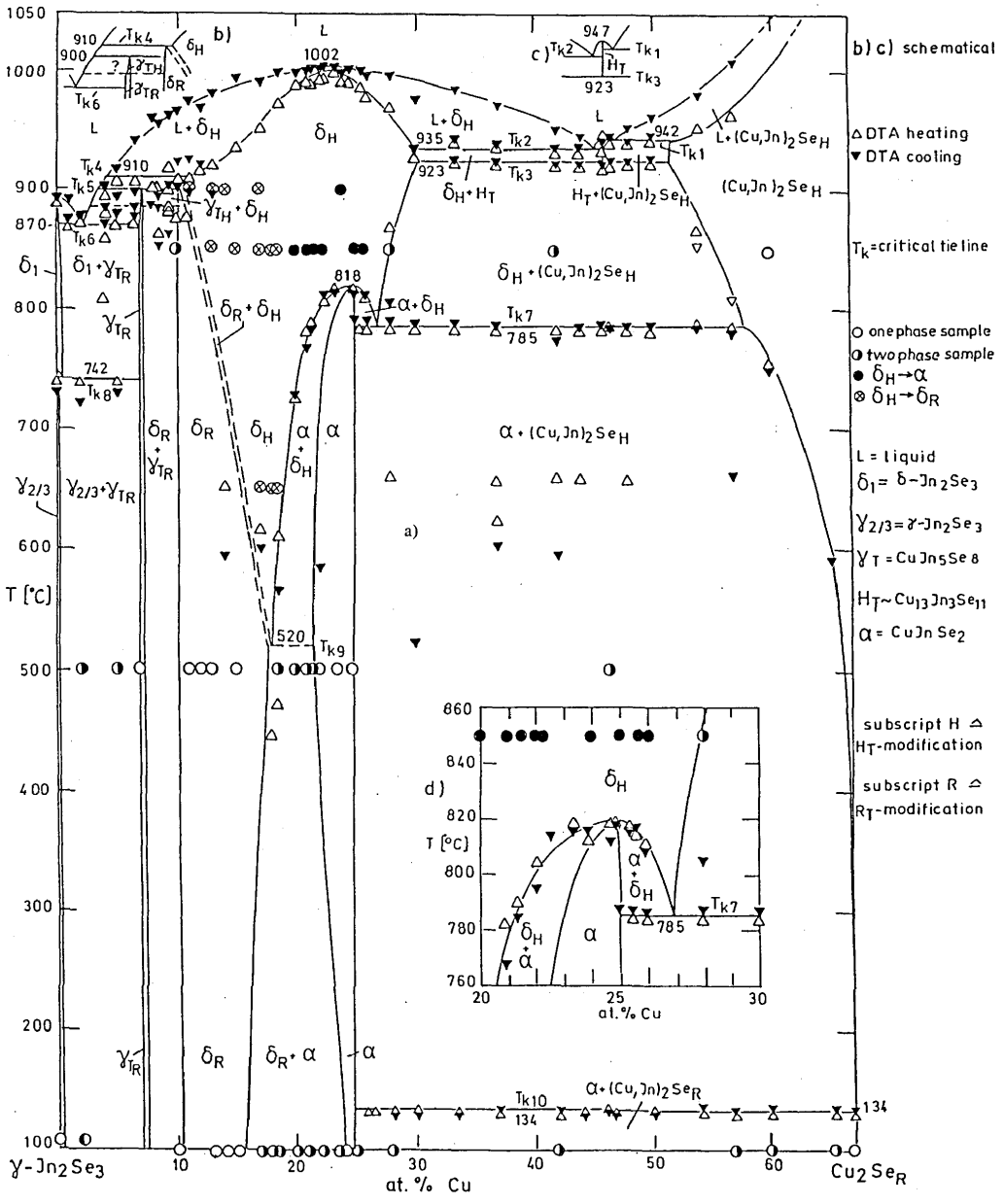

Figure 16: Experimentally determined pseudo-binary phase diagram along In_2Se_3-Cu_2Se (image from Ref. [64], reprint with kind permission of Carl Hanser Verlag.).

- What are corresponding activation energies?
- Which defects can potentially lead to metastabilities in the devices?
- What is the role of selenium vacancies and DX centers in this respect?
- What are the origins of the hole trap level at around 0.15-0.35 eV and of the 0.8 eV photocapacitance level?
- Which defects form complexes?
- What is the relation of the intrinsic point defect physics to the device performance?
- How do the preparation conditions have to be chosen in order to optimize the performance of devices with respect to the point defect physics?
- What are the differences to data obtained from local density functional theory in former studies? And is there some rationale for these differences?
- Can we gain a better understanding of the properties of intrinsic point defects in $CuInSe_2$ and $CuGaSe_2$ by using screened-exchange hybrid functionals?

Readers who want to skip the review of methodology (Part II) are directly referred to Part III for the full study and detailed answers. A brief summary of the answers is given on page 165.

3

SILICON: CRYSTAL GROWTH, INTERFACE KINETICS AND EXTENDED DEFECTS

3.1 INTRODUCTION

Wafers of crystalline silicon are used today in photovoltaics as well as in microelectronics. Silicon is *the* prototypical semiconductor and has been extensively studied. A lot of literature exists on defects in silicon and its properties. It is not the purpose to give a complete review here, since many good reviews on the properties of defects already exist [78, 79]. The formation of defects as a consequence of interface growth kinetics in silicon has been studied to a lesser extent. It is the purpose of Part IV of this thesis to understand the formation processes of twin boundaries, stacking faults and voids at the solid-liquid interface by atomic-scale simulations. In this chapter, the stage for this endeavour is set by reviewing two relevant methods for silicon crystal growth from the melt, the Czochralski process and edge-defined film-fed growth (EFG). Subsequently, the state of knowledge on the formation processes of twin boundaries, stacking faults and voids during silicon crystal growth from the melt is reviewed.

3.2 CRYSTAL GROWTH METHODS

Both photovoltaics and microelectronics require extremely pure and almost defect-free silicon. This poses stringent requirements on the crystal growth process. The most prominent single-crystal growth method for silicon is the Czochralski process. In this process, silicon is melted in a quartz crucible and a rotating seed crystal is slowly pulled from the melt with a velocity of only a couple of millimeters per second. The process allows to obtain highly pure silicon single-crystal ingots and is employed for this purpose on a large scale in the semiconductor industry today.

In EFG, the wafer is directly pulled from the melt. This has potential advantages in particular for silicon wafers for photovoltaics. The process is much faster than Czochralski growth with a velocity of up to meters per hour. EFG wafers are initially drawn from the melt as thin-walled polygonal tubes. Little cutting is necessary since the tubes already have the proper wafer thickness. The pro-

cedure thus saves scrap material, which is lost otherwise during slicing of the crystal into wafers. However, the obtained EFG-wafers are polycrystalline, i.e. they are not entirely defect free. Grain boundaries, twin boundries and other defects are present. The EFG procedure is thus suitable for photovoltaics, but not for microelectronics, which has stricter requirements on crystal quality.

3.3 INTERFACE GROWTH KINETICS

The atomic-scale processes at the moving liquid-solid growth interface play an important role during the crystal growth process [80]. When full thermodynamic equilibrium is not achieved, which in practice is the case for most crystal growth techniques, defects remain in the crystal. The concentration and distribution of these defects depend on the history of the crystal during growth. Despite the potentially great importance of interface growth kinetics our understanding of the relevant atomic-scale processes remains limited. Because atomic-scale processes at growth interfaces are extremely difficult to observe experimentally, computer simulations have become an important tool in this area [81].

Lattice Monte Carlo models were applied to study the equilibrium properties of silicon solid-liquid interfaces as well as crystal growth of silicon [82–88]. The general procedure of these simulations is to use a simple Ising-model with first or also second-nearest neighbour interactions as a model for the crystal where one state of a lattice site represents solid atoms, while the other state represents the liquid. The field term of the Ising-model may be used to represent a thermodynamic driving force $\Delta\mu$, a free energy difference driving the growth of the crystal. One of the universal feature of such models is the finding that the growth of the (111) interface is nucleation-limited. A two-dimensional nucleus at the planar interface is needed to provide the step to which further atoms can attach. This leads to a layer-by-layer growth of the (111) interface. Rough surfaces such as the (100) and (110) interface always have sites available to which atoms may attach and therefore growth on these interfaces is not nucleation but diffusion limited. Many of these simulations have been concerned with the roughening transition and preroughening transition of the (111) interface [82, 83, 85, 86]. The existence of the preroughening transition at (111) interfaces with only first nearest neighbour interactions seems to be a controversial issue [83, 85]. Other studies focus on the growth velocity versus undercooling relation [87, 88]. Generally, it has been understood from these simulations that the silicon (111) solid-liquid interface is atomically flat at the melting temperature, while other interfaces such as the (100) and (110) interfaces are atomically rough. The roughening transition of the silicon (111) interface occurs only above the melting temperature, while it occurs below the melting temperatures for the other interfaces. This behaviour is also reflected in the growth velocity versus undercooling curves, which show a linear relation for all rough interfaces, while for the (111) interface the relation

has an exponential shape. This is because growth of the (111) interface is limited by nucleation of two-dimenisonal seeds on the interface. For this reason, growth at the interface only occurs above a critical undercooling, which is experimentally estimated to lie between 1.5 K and 9 K [89–91]. A new model which incorporates twin boundaries and stacking faults into the Lattice Monte Carlo methodology is presented in Chapter 13 of this thesis.

3.4 TWIN BOUNDARIES AND STACKING FAULTS

Silicon does not grow as a perfect crystal under common growth conditions. Stacking faults and twin boundaries are very common defects with formation energies as low as approximately 30 J/m^2 (see Table 15 on page 151). The formation of twin boundaries is often observed in wafers produced by EFG and have historically been a problem in Czochralski growth also. Interestingly, it is experimentally found that wafer areas with a high twin density exhibit superior electrical properties in solar cells, i.e. a higher lifetime of excited charge carriers [92]. Therefore, an increase of the twin density in the wafers may lead to more efficient solar cells. In order to realize an increased twin density, however, a detailed understanding of the nucleation process of twin boundaries is essential.

The growth of parallel twins in small crystallites can be explained by the reentrant-corner Hamilton-Seidensticker growth mechanism [93]. This mechanism, however, explains only the continous growth, after twins already have formed. It does not address the nucleation of twin boundaries. Twin formation in silicon growth from the melt has been extensively studied experimentally and several formation models have been proposed [94–98]. Still, the nucleation process of the twin boundaries has not been directly observed and several twin formation mechanisms have been proposed in the past. It has been reported in recent papers that parallel twins can form at (111) microfacets [94, 95] as well as that they may form at grain boundaries [96]. Moreover, twins may already be present in small nuclei formed in the melt [97], or may form at a later stage [98]. Recently, it has been stated that carbon impurities may also induce twin formation in silicon [99]. It has been recognized by Billig [100], that twinning in Czochralski growth occurs on (111) facets that form at the three-phase boundary between crystal, melt and ambient. A thermodynamic model to explain this behaviour has been devised by Hurle [101] based on ideas of Voronkov [102]. A clear understanding of the atomic processes responsible for twin boundary formation has, however been lacking. The twin formation mechanism at grain boundaries is revealed in Chapter 11 of this thesis.

3.5 VOID FORMATION

Voids of up to 100 nm in diameter are typically observed in silicon ingots grown from the melt [103]. Among these, octahedral voids often occur as twin-type, i.e. two voids very close to each other [104]. Since electronic devices shrink to ever smaller sizes, even the presence of these very small voids represents a significant challenge for the reliability of electronics built from silicon wafers [78]. Much progress has been made in the past decade in understanding the formation of voids and dislocation loops [78, 105] and it is widely accepted that void formation in silicon is due to the condensation of single vacancies from a supersaturated crystal [78]. The origin of double void formation is, however, still a matter of debate. In general, thermodynamic models assume, that depending on the ratio of growth velocity and temperature gradient, excess vacancies or interstitials are incorporated at the growth front [106–110]. When the crystal is cooled to temperatures below 1100 °C these excess vacancies may condense and nucleate voids, while excess interstitials form interstitial loops. Modeling approaches using kinetic Monte-Carlo methods [106, 111–115] or continuum models [116, 117] have supported this picture. In Chapter 12, an alternative mechanism for void and double void formation based on kinetic effects at the growth interface is presented.

3.6 OPEN QUESTIONS

The open questions related to silicon crystal growth from the melt and the formation processes of defects to be investigated in the present thesis are summarized as follows:

- What is the nucleation mechanism of twin boundaries in silicon grown from the melt? (Ch. 11)
- How can twin nucleation be influenced? (Ch. 11)
- What is the nucleation mechanism of nanovoids in silicon grown from the melt? (Ch. 12)
- Is there a role of interface kinetics in void formation in addition to the common models based on vacancy condensation? (Ch. 12)
- How does the the twin formation energy influence the formation of faulted islands at the (111) growth interface? How does it depend on undercooling? (Ch. 13)
- How can we efficiently model stacking faults at the interface on longer length and time-scales? (Ch. 13)

The reader is referred to the Summary (page 165) for brief answers and to the chapters in Part IV for detailed descriptions of how the questions were tackled.

Part II

METHODS

The following methodological part introduces the toolkit of atomistic simulations. Starting from statistical and quantum physics, the atomistic methods for total energies as well as for sampling equilibrium and the calculation of time trajectories of interacting ensembles of atoms are introduced. Special emphasis is put on the thermodynamics of point defects, a necessary foundation for the extensive study of intrinsic point defects in $CuInSe_2$ and $CuGaSe_2$ in Part III.

4

ATOMIC-SCALE SIMULATION METHODS

4.1 THE FUNDAMENTAL PICTURE

Atomic-scale simulations of defects in semiconductors have become an emerging field over recent years. This is not only because of the increasing availability of more powerful computers, but mostly due to the development of refined theoretical methods. The foundation of atomic-scale simulations relies on two fundamental physical theories: Statistical mechanics and quantum mechanics.

The fundamental connection of statistical mechanics to thermodynamics as discovered by Boltzmann relates the entropy S to the number W of microstates of the system:

$$S = k_B \ln W. \tag{4.1}$$

This definition of entropy, however, applies only for closed systems, such as for example the universe as a whole, in which all possible states have equal probability and energy is conserved. In thermodynamics, one is more often interested in subsystems, which are not necessarily closed and the microstates may have varying probability. Therefore, it is more appropriate to work with the generalized Gibbs entropy,* which allows to attribute arbitrary probability p_i to each microstate i:

$$S = -k_B \sum_i p_i \ln p_i. \tag{4.2}$$

In statistical mechanics, an *ensemble* is defined defined by fixing three of the extensive thermodynamic variables. For the simulation of physical systems, which can be considered to be in contact with a heat bath and can not exchange particles with the environment, the canonical ensemble is one possible and useful choice. This ensemble assumes fixed particle number N, volume V and temperature T. For this case, the probability of a certain microstate i depends on its energy E_i and is given by the Boltzmann probability $p_i = \exp\left(-\frac{E_i}{k_B T}\right)$. Furthermore, in statistical mechanics, a partition function for each ensemble is defined

* see Ref. [118] for a discussion of the Gibbs entropy versus the Boltzmann entropy

by a sum over the probabilities of the microstates. For example, the canonical partition function Z_C is a sum over all possible states i weighted with respect to the state's probability, i.e.

$$Z_{\mathrm{C}} = \sum_i \exp\left(-\frac{E_i}{k_{\mathrm{B}}T}\right). \tag{4.3}$$

Knowledge of the partition function allows to construct the thermodynamic potential of the chosen ensemble, which is the Helmholtz free energy in the canonical case

$$F(T,V,N) = U(T,V,N) - T \cdot S(T,V,N) = -k_B T \ln Z_{\mathrm{C}}. \tag{4.4}$$

All thermodynamic properties of a canonical system in equilibrium can be derived from this thermodynamic potential. Therefore, if we knew the energy E_i of every possible state i of a system, one would have access to any desired thermodynamic property of the system. So how can we access the energy of a certain state?

In the classical picture it is straightforward to write down the interaction of any ensemble of particles if the state is specified by the positions and velocities of the particles. For example, if there is only electrostatic interaction between the particles, this would simply be a sum over all pairs of particles with the potential energy given by Coulomb's law, i.e.

$$\frac{q_i q_j}{4\pi e_0 r_{ij}}, \tag{4.5}$$

where q_i and q_j are the charges of particles i and j, and r_{ij} is their distance.

Although calculating the trajectories of such a classical many-body problem can already become difficult when the number of particles is increased beyond three, it is relatively straightforward to calculate the total energy for any given state. The calculation of a specific thermodynamic property then becomes mainly a problem of sufficient sampling of the phase space for determining the ensemble average.

However, we know that classical mechanics is not sufficient to understand the properties of matter. Quantum theory lies at the very heart of solid state physics and is crucial in order to understand most properties of solids, including the total energy of a system of atoms. We thus need to turn to modern quantum theory in order to calculate the total energy of any system from first-principles. The answer is contained in the Schrödinger equation, which in its simplest time-independent form can be written as the eigenvalue problem

$$\hat{H}|\psi\rangle = E|\psi\rangle. \tag{4.6}$$

In this representation, the interactions of the particles of the system are still hidden in the Hamilton-Operator $\hat{H}$, which acts on the many-body wavefunction

$|\psi\rangle$, represented here in the general form of a ket-vector from Hilbert space [119]. Solving the eigenvalue problem yields the energy E_n belonging to the eigenstate $|\psi_n\rangle$. With explicit interactions in real-space representation for a system of atoms with fixed positions of the classically treated nuclei $R_{I,J}$ (Born-Oppenheimer approximation) the equation reads

$$\left[-\frac{\hbar^2}{2m}\frac{\partial^2}{\partial r^2} + \frac{e^2}{2}\frac{Z_I Z_J}{|R_I - R_J|} - \frac{Z_I e^2}{|r_i - R_I| + \frac{e^2}{2}\frac{1}{|r_i - r_j|}} \right] \psi(r) = E\psi(r). \qquad (4.7)$$

In this equation the first-term is the kinetic energy operator of the electrons and the following three terms are the potential energy operators of the ion-ion, ion-electron and electron-electron interactions, respectively.† This equation is impossible to solve analytically, except for very simple cases such as the hydrogen atom [119]. Systems such as solids, even if just a few atoms are considered, are impossible to solve numerically based on this rigorous approach. Therefore, advanced computational methods and approximations are necessary for the simulation of larger systems. The more approximations are used the larger are the system sizes and time scales that can potentially be accessed (Figure 17), which of course is not possible without reducing accuracy. Density functional theory (DFT), which is introduced in more detail below, nowadays is a very popular approach to approximatively solve the Schrödinger equation to obtain the total energy. When we are interested in thermodynamic quantities of a system, where we basically have to sum over infinitely many states to obtain an ensemble average, we would basically have to solve the Schrodinger equation infinetely many times to solve the problem exactly from first principles. This is obviously impossible. It should now be clear that we need advanced approximations and algorithms to simulate physical systems on the basis of statistical mechanics, both for total energy computations and for sampling the phase space. In practice there exist various levels of approximations in both of these areas. In the following, the total energy computation will be described starting out from density functional theory with its various levels of approximations going to the coarser approximations such as the descripition of interacting atoms via empirical potentials and lattice hamiltonians, which do not treat electrons explicitly anymore. With respect to atomistic methods needed to sample the phase space with the goal of obtaining thermodynamic information or to calculate trajectories in phase space, we briefly introduce the molecular dynamics method as well as Metropolis Monte Carlo sampling and the Kinetic Monte Carlo algorithm in the following sections. In principle, atomic-scale data can be used in continuum models, to bridge the length-scale further up to the macroscopic scale. The appropriate choice of methods from this atomic-scale simulation *toolkit* is essential

† r_i and r_j are the position operators of the electrons, while R_I and R_J represent the ones of the ions. Z_I and Z_J are the charges of the ions. The sums over electrons and ions are not explicitly written (Einstein's sum rule).

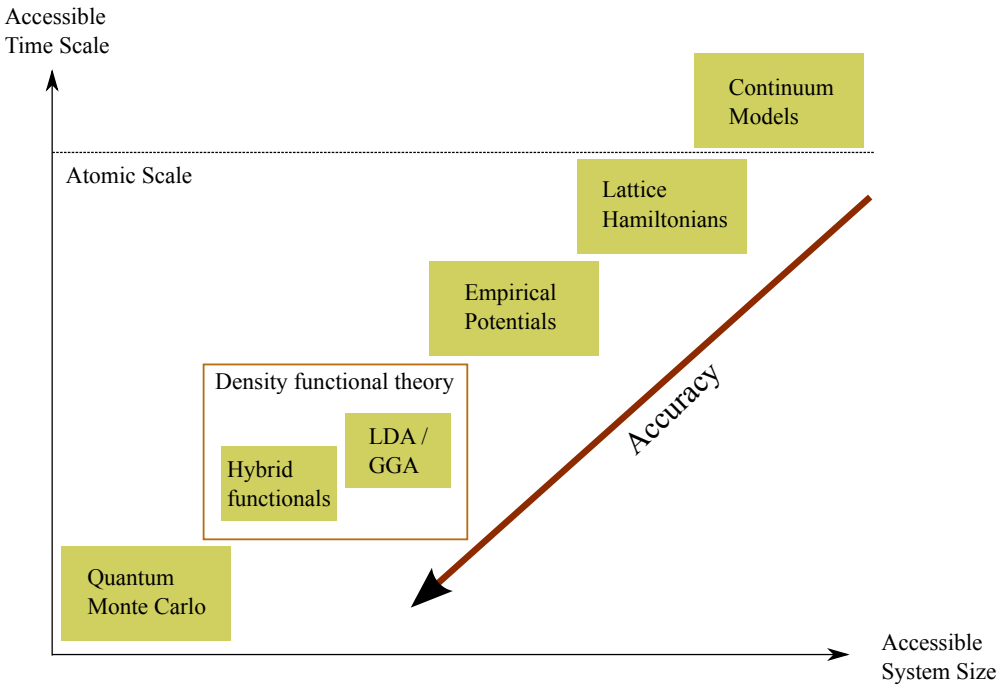

Figure 17: Atomic-scale total energy methods with respect to accessible time scales and system sizes. Accessing the time dimension requires to couple the total energy methods as displayed in the figure to an algorithm for the calculation of time trajectories such as molecular dynamics or Kinetic Monte Carlo (see Section 4.3). Therefore, the above representation shoud be understood as an approximative classification.

and depends on the question to be solved. The limiting factor is most often the necessary amount of computational resources. Every problem has its requirements with respect to the necessary system size and time scale, which in turn constrain the achievable accuracy. Many problems which in principle can be tackled by atomic-scale simulation methods can in practice only be solved with a good amount of creative thinking about how to combine the available tools in the most sensible way.

Following the introduction of the full suite of atomic-scale simulations methods in the present chapter, the necessary concepts for the calculation and interpretation of the thermodynamics of point defects are introduced in Chapter 5.

4.2 METHODS FOR TOTAL ENERGIES

4.2.1 *Density functional theory (DFT)*

4.2.1.1 *Basics*

In density functional theory (DFT), the complexity of a many-body system of N interacting electrons in the presence of ionic cores is reduced to the optimization of an electron density, which depends only on three spatial coordinates independent of the number of electrons. Hohenberg and Kohn showed in 1964 [120] that the energy E of an interacting electron gas in an external potential $V(\mathbf{r})$ due to ionic cores and external fields can be expressed by a functional $F[n(\mathbf{r})]$ of the electron density $n(\mathbf{r})$ and that the ground state energy is equivalent to $E_{\mathrm{GS}} = \min\{\int V(\mathbf{r})n(\mathbf{r})d\mathbf{r} + F[n(\mathbf{r})]\}$. The proof itself, however, does not provide a recipe of how to construct an explicit functional $F[n(\mathbf{r})]$. Later, Kohn and Sham showed that the problem of many interacting electrons may be transformed into a problem of non-interacting particles moving in an effective potential, which may in principle include all many-body effects including exchange and correlation, and is only a functional of the electron density [121]. Within the Kohn-Sham method, the ground-state total energy E for a collection of electrons interacting with one another and with an external potential V_{ext} (including the interaction of the electrons with the nuclei) can be written as

$$E[n] = \sum_{\alpha} f_\alpha \langle\psi_\alpha| \left(\frac{1}{2}\boldsymbol{\nabla}^2 + V_{\mathrm{ext}} + \frac{1}{2}\int \frac{n(\boldsymbol{r}')dr'^3}{|\boldsymbol{r}-\boldsymbol{r}'|} \right) |\psi_\alpha\rangle + E_{\mathrm{xc}}[n] + E_{\mathrm{II}},$$

where f_α is the occupation of a single-particle state $|\psi_\alpha\rangle$ usually taken from a Fermi-function, while E_{II} describes the ion-ion interaction. All many-body effects are hidden in the exchange-correlation $E_{\mathrm{xc}}[n]$ term.

By construction, density-functional theory is an exact theory given that the exchange-correlation functional is known. In praxis, however, the functional has to be approximated. Since the foundations of density-functional theory have been completed with the Hohenberg-Kohn theorem and the Kohn-Sham ansatz, subsequent progress in the theory has focused on efficient numerical implementations and improved exchange-correlation functionals [122].

4.2.1.2 *Basis Sets*

Finding a mathematically convenient basis set representing the Kohn-Sham orbitals within density functional theory calculations is essentially a balance of computational performance and accuracy. Any basis can be made more complete and therefore more accurate by adding more basis functions. For a plane-wave or real space basis this can be systematically done by simply increasing the spectral range. Usually, core electrons, for which the wave-functions exhibit strong oscillations, are excluded and replaced by so-called pseudo-potentials representing

the combined potential of the ionic core and core electrons. Exclusion of the core electrons results in an improved performance, especially for plane-wave basis sets, and is often a prerequisite for treating extended systems. Using a localized basis set, such as for example a Gaussian or numerical atomic orbital basis function, may have advantages concerning the scalability of the method with respect to the system size. However, in that case, more effort is needed to check the completeness of the basis set. A combination of a localized basis and a plane-wave representation is the full potential linearized augmented plane wave (FP-LAPW) method, which represents an accurate yet efficient all-electron approach [123].

4.2.1.3 *Functionals for Exchange and Correlation*

LOCAL APPROXIMATIONS:

In the local density approximation (LDA), the exchange-correlation energy as a functional of the density is described by a homogeneous electron gas. The correlation energy of the homogeneous electron gas can be obtained by highly accurate Quantum Monte-Carlo simulations [124], while the exchange energy is known analytically. The LDA is sufficiently accurate for many problems in solid-state physics, especially for describing electrons in simple metals, which behave very much like free electrons. Because of its simplicity and limited computational costs, the LDA is very useful for describing large systems as well as for obtaining approximate energies and wave functions that can then be refined by more sophisticated levels of theory. An improvement of the LDA has been achieved by recognizing that the exchange-correlation energy can be described more accurately by including gradients of the electron density. In contrast to LDA, different variants exist of how the gradient is included. Nowadays, however, the generalized gradient approximation (GGA) by Perdew, Burke and Ernzerhof [125] (PBE-GGA) is most widely used.

Although improving on many calculated material properties in comparison with the local approximation, the GGA still has deficiencies in various aspects. Most importantly, both the LDA and the GGA fail to reasonably describe the fundamental band gap, which is generally underestimated (sometimes by more than 50%) in both approximations. This issue is known as the band-gap problem in DFT. Approaches to improve the exchange-correlation energy by including higher derivatives of the electron density have failed, and it is now generally accepted that improvements require to properly account for non-locality.

LDA+U AND GGA+U:

A direct extension of the LDA and the GGA functional is obtained by adding an on-site Coulomb repulsion term to specific orbitals representing the electrostatic repulsion between localized electrons. This approach is motivated by the lattice -based Hubbard model [126], which describes the repulsion of electrons within a narrow band, i.e. electron correlation, by an empirical parameter U. Sim-

ilarly, a density functional that partially corrects specific localized orbitals for the electron correlation can be designed by introducing the repulsion parameter U (LDA+U or GGA+U) [127].

The +U method has become a popular approach, which allows for a partial correction of the correlation and self-interaction error of the LDA and significantly improves the description of Mott insulators, such as transition metal oxides. Nowadays, the method is widely applied due to its relative accuracy at very reasonable computational costs. As a byproduct, the calculated band gaps of semiconductors can be improved by using the +U approach, because the increased repulsion between specific orbitals leads to an enhanced localization. However, LDA+U and GGA+U still underestimate the band gap. In addition, it is often not a priori clear how and for which orbitals U parameters should be applied. Further details on the LDA+U method can be found in a review by Anisimov [128].

HYBRID FUNCTIONALS:

The LDA and the GGA functional considerably underestimate the exchange energy, but properly account for the correlation energy. The Hartree-Fock method by definition properly accounts for the exchange interaction, but in turn can not access the correlation energy. Therefore, one may conclude that the true answer to the problem must lie somewhere in between. This is the starting point for the development of hybrid functionals. The basic idea for hybrid functionals is thus to mix the exchange-correlation energy of the traditional LDA or GGA functionals with a fraction of exact or Hartree-Fock exchange. In recent years, it turned out that hybrid functionals are indeed able to give a much better description of the exchange and the correlation energy than traditional functionals. Also, the band gaps are significantly improved. This, however, comes at a price: Hybrid functionals are computationally at least two orders of magnitude more expensive than their local or semi-local counterparts. Typical examples of hybrid functionals that have been engineered in such a way are B3LYP [129], PBE0 [130] and HSE06 [131, 132]. A review on hybrid functionals applied to solids and an assessment of their accuracy in comparison to experiment has recently been given by Marsman et al. [133]. Another review focusing more on the general theoretical framework has been authored by Kümmel and Kronik [134], who also discuss the issue of the band-gap problem in case of hybrid functionals.

Hybrid functionals can further be distinguished by whether they use a global approach to mix the exchange correlation energy E_{xc} from a nonlocal Hartree-fock type exact exchange E_x^{HF} and a semi-local PBE-GGA contribution E_x^{GGA}, such as

$$E_{xc}^{hybrid} = E_{xc}^{GGA} + x_{HF}(E_x^{HF} - E_x^{GGA}), \tag{4.8}$$

or whether a range-separated screened hybrid functional such as HSE06 is used [135]. This functional splits the electron-electron interaction into a short-range and a long-range part. For the short range part 25 % short-range (SR) exact exchange is mixed with 75 % short-range GGA exchange, while the long-range part (LR) is treated purely on the basis of GGA:

$$E_{\mathrm{xc}}^{\mathrm{HSE}} = \frac{1}{4} E_{\mathrm{x}}^{\mathrm{HF,SR}}(\omega) + \frac{3}{4} E_{\mathrm{x}}^{\mathrm{GGA,SR}}(\omega) + E_{x}^{\mathrm{GGA,LR}}(\omega) + E_{\mathrm{c}}^{\mathrm{GGA,LR+SR}} \tag{4.9}$$

The range separaration can be tuned using the exchange screening parameter ω. The standard value for the HSE06 functional is $\omega = 0.2$ Å^{-1}. HSE06 can be considered as a generalized functional in the sense that for $\omega = 0$ HSE06 reduces to the PBE0 functional, and when ω approaches infinity the short-range non-local exact exchange vanishes and it reduces to standard PBE-GGA. The most notable success of HSE06 is the fact that it is able to give much better band gaps for solids compared to local and semi-clocal as well as to global hybrid functionals [133]. This makes HSE06 particularly suitable for point defect calculations of semiconductors, and is therefore the method of choice in Part III of this thesis. The implications of the exchange screening parameter ω and the fraction of exact exchange for the band gaps of chalcopyrite solids will be discussed in Chapter 6.

For a more detailed general introduction into ab-initio total-energy calculations we refer the reader to a review paper by Payne et al. [136]. A highly recommendable full treatise on electronic structure calculations including recent developments in DFT methods can be found in a recent book by R. Martin [122]. The different approximative functionals in density-functional theory may be ordered into a hierarchy starting with the most basic, the local density approximation and then increasing in accuracy. Such a hierarchy is sometimes called the Jacobs ladder of DFT. A table which puts the different ab-initio methods and functional approximations into such a scheme is shown in Table 1.

4.2.2 *Quantum Monte Carlo*

Quantum Monte Carlo (QMC) is another ab-initio method for solving the Schrödinger equation. It is a ground-state method based solely on the many-body wave function as the basic object. Therefore, it takes a fundamentally different approach to the problem of electron correlation compared to the methods described before, which are all based on the electronic density. The basic idea is to sample the many-body wave function using random numbers. Quantum Monte Carlo is in principle able to give the correct total energy and therefore an exact treatment of exchange and correlation is possible. However, this is only true for infinite statistical sampling. The error in the total energy of a system given by QMC is an entirely statistical error, which scales as the inverse square root of the number of sampling steps. It is the extreme computational cost of this method,

Method	Description	Ref.
Density Functional Theory		
Local and Semi-local Functionals		
Local density approximation (LDA)	A local functional describing exchange-correlation energy that depends only on the local electron density and is obtained from the solution for the homogeneous electron gas	[124]
Generalized gradient approximation (GGA)	The exchange-correlation energy also depends on the gradient of the electron density.	[125]
Orbital-dependent and Hybrid Functionals		
LDA+U / GGA+U	An on-site coulomb repulsion term, represented by the parameter U is included for specific orbitals. Description of exchange and correlation is improved if U is chosen properly.	[127]
Hybrid Functionals (HSE06, PBE0, B3LYP, etc)	Improved accuracy of the exchange-correlation energy by mixing local or semi-local functionals with a fraction of exact exchange or Hartree-Fock exchange. Provides a good alternative to local and semi-local functionals, but is computationally more expensive. In certain cases, hybrid functionals alleviate the band-gap problem.	[133, 134]
Wave function based		
Quantum Monte Carlo (QMC)	True many-body wave function approach, highly accurate but also computationally expensive, currently forces are still hard to obtain	[137]

Table 1: Overview of ab-initio total energy methods.

which limits its usefulness in practice. For very small systems it can, however, be a very valuable tool if very accurate total energies are needed. In praxis, the forces on the ions are hard to obtain and computationally much more expensive than the total energy, which make structural relaxations difficult. A concise review on Quantum Monte Carlo methods has been given by Foulkes *et al.* [137].

4.2.3 *Classical interatomic potentials*

The description of the potential energy of a system of atoms by classical interatomic potentials represents a coarse graining step, which can save a significant amount of computation time. It relies on the fact that it is often a good enough approximation to write down an expression for the potential energy of a system, which only depends on the nuclear coordinates of the atoms. This approach abstracts completely from the existence of electrons, but their contribution is implicitly contained in the mathematical expressions of the potential. Total energy data from more accurate methods, which explicitly treat the interactions of electrons, such as density functional theory, can be used to develop empirical potentials and test their accuracy and transferability.

In the following, we explain two popular formalisms for elemental semiconductors, the Stillinger-Weber [138] and the Tersoff [139] potential. These have historically been the two most important classical interatomic potentials to model silicon and the first to achieve a sufficient degree of transferability. Being able to use the same set of parameters for the silicon crystal and the melt is a requirement, e.g. to reliably model crystallization processes. The Stillinger-Weber and the Tersoff formalisms have been the basis for developing accurate and transferable interatomic potentials for more complex systems such as multicomponent semiconductors [140]. Note that there is a large number of other analytical forms of potentials available and the terminology varies within different research areas. We favour to use the notion of *classical interatomic potentials*, but the terms *many-body potential* and *empirical potential* are often used interchangeably, and chemists often speak of *force fields*. The latter notion, however, refers mostly to formalisms, which lack the dependence of the parameters on the local environment and are therefore hardly transferable.

The Stillinger-Weber potential is based on the idea, that the tetrahedral bonds in covalently bonded systems require to go at least to three-body interactions [138]. The most general form of the potential energy function for this case is

$$V(\{\boldsymbol{r}_i\}) = \sum_i v_1(\boldsymbol{r}_i) + \sum_{i,j} v_2(\boldsymbol{r}_i, \boldsymbol{r}_j) + \sum_{i,j,k} v_3(\boldsymbol{r}_i, \boldsymbol{r}_j, \boldsymbol{r}_k) \tag{4.10}$$

with 1-, 2- and 3-body terms. The pair interaction is a rather trivial function of the atomic pair distance r_{ij}:

$$v_2(r_{ij}) = \begin{cases} A(Br_{ij}^{-p} - r_{ij}^{-q}) & \mathrm{r_{ij} < a} \\ 0 & \mathrm{r_{ij} \geq a} \end{cases}. \tag{4.11}$$

It depends on the parameters A, B, p, and q and smoothly goes to zero at the cut-off radius a making sure that the derivative of the function is continous. This is a requirement for reliable forces and for the use of the potential in molecular dynamics simulations.

The 3-body interaction then needs to incorporate the angular interaction responsible for the tetrahedral symmetry of the cubic diamond phase of silicon. For these reasons of symmetry Stillinger and Weber suggested to define v_3 in terms of an auxilary function $h(r_{ij}, r_{ik}, \theta_{jik})$ dependent on the interatomic distances of the pairs and the angle θ_{jik} between them centered at atom j as

$$v_3(\boldsymbol{r}_i, \boldsymbol{r}_j, \boldsymbol{r}_k) = h(r_{ij}, r_{ik}, \theta_{jik}) + h(r_{ji}, r_{jk}, \theta_{ijk}) + h(r_{ki}, r_{kj}, \theta_{ikj}) \tag{4.12}$$

with

$$h(r_{ij}, r_{ik}, \theta_{jik}) = \lambda \exp\left(\gamma(r_{ij} - a)^{-1} + (r_{ik} - a)^{-1}\right)\left(\cos\theta_{jik} + \frac{1}{3}\right)^2 \tag{4.13}$$

This expression makes sure that h and therefore v_3 vanish for the perfect tetrahedral angles for which $\cos\theta_{jik} = -\frac{1}{3}$.

The Stillinger-Weber potential is designed to model crystalline silicon and is rather reliable for that purpose. However, it was not designed for conditions in which the local coordination deviates from its crystalline value of four and can become problematic in these case. Such a situation can occur for non-tetrahedral polytypes, at surfaces, defects or in the liquid phase. The Tersoff formalism improves the description at varying local coordination by incorporating the *bond-order* concept. Within this concept, the total energy V is a sum over single bonds with pair bond energies V_{ij}:

$$V(\{\boldsymbol{r}_i\}) = \frac{1}{2}\sum_{i \neq j} V_{ij}. \tag{4.14}$$

The bond energy is defined by the equation

$$V_{ij} = f_C(r_{ij})[V_R(r_{ij}) + b_{ij}(\{\boldsymbol{r}_i\})V_A(r_{ij})]. \tag{4.15}$$

This bond energy is the sum of an attractive and a repulsive pair potential $V_A(r_{ij})$ and $V_R(r_{ij})$, respectively. The resulting potential is a many-body potential since the bond-order coefficients b_{ij} depend on the local coordination, i.e. not

every bond contributes the same constant energy. The coeffcients are commonly taken such that bonds become weaker with higher coordination. $f_C(r_{ij})$ is a cutoff function to limit the range of the potential. The Erhart-Albe version of the Tersoff formalism is used in part IV of this thesis for modelling silicon growth from the melt [140]. The Tersoff formalism is suitable for modelling silicon crystallization, since it takes into account the different local environments in the crystal, the melt, and at the solid-liquid interface, which ensures the necessary transferability.

The expressions for the repulsive and attractive pair potentials within in the Erhart-Albe formalism are [140]

$$V_R(r_{ij}) = \frac{D_0}{S-1} \exp\left[-\beta\sqrt{2S}(r_{ij} - r_0)\right] \tag{4.16}$$

and

$$V_A(r_{ij}) = \frac{SD_0}{S-1} \exp\left[-\beta\sqrt{2/S}(r_{ij} - r_0)\right]. \tag{4.17}$$

D_0 and r_0 have the physical meaning of dimer energy and bond length. β and S are fitting parameters. The cutoff function is given as

$$f_C(r) = \begin{cases} 1 & \mathrm{r} < \mathrm{R} - \mathrm{D} \\ \frac{1}{2} - \frac{1}{2}\sin\left(\frac{\pi}{2}\frac{r-R}{D}\right) & |\mathrm{R} - \mathrm{r}| \leq \mathrm{D}\,, \\ 0 & \mathrm{R} + \mathrm{D} < \mathrm{r} \end{cases} \tag{4.18}$$

where R and D specify the position and width of the cutoff region.

Finally, the bond order is defined as

$$b_{ij} = (1 + \chi_{ij})^{-1/2}, \tag{4.19}$$

with

$$\chi_{ij} = \sum_{k \neq i,j} f_C(r_{ik}) \exp\left[2\mu(r_{ij} - r_{ik})g(\theta_{ijk})\right], \tag{4.20}$$

and the angular function

$$g(\theta) = \gamma\left(1 + \frac{c^2}{d^2} - \frac{c^2}{d^2 + [h + \cos\theta]^2}\right). \tag{4.21}$$

There is a total of nine adjustable parameters μ, γ, c, d and h, in addition to β, S, R and D , which all depend on the atom type and which have to be determined by fitting. The improved description taking into account the dependence on varying local coordination within this approach leads to improved transferability. It comes at the price of the increased effort, which is necessary to fit the above expressions in order to obtain reliable parameter sets.

4.2.4 *Lattice Hamiltonians*

Another level of approximative description of the interactions between atoms is to restrict the positions of the atoms to discrete lattice sites. Although this may seem like a severe restriction, it is a reliable and very useful approximation for many applications such as ordering phenomena in multinary alloys, phase diagram calculations of alloys and epitaxial growth. In fact, lattice-based models may even work quite well for certain applications which involve liquids or gases such as modeling growth from the melt or solid-gas transport. This flexibility of a lattice model is often due to the fact that many properties, which would require deviations from the lattice sites, such as vibrational properties may be encoded in the effective interactions of the lattice model. The merit of the lattice constraint is a huge reduction of the phase space to be sampled when thermodynamic information is to be obtained. Historically, the Ising model is the most famous example of a lattice Hamiltonian with simple pair interactions in statistical mechanics [141]. It was originally proposed as a model for ferromagnetism and is probably one of the most studied models in statistical physics [142]. Initially, the model was studied only in one spatial dimension and was concluded not to be able to explain ferromagnetic phase transitions by Ising himself [141]. It was Peierls who first realized that the model thus indeed lead to phase transitions in two or three dimensions [143]. The Ising model may not only be employed as a model for ferromagnets, but also as one for binary alloys, for crystal growth and for many other applications [142]. The model consists of spins S on a crystal lattice. These spins interact only with their nearest neighbours with the interaction constant J and have two possible states: up and down, i.e. $S = +1$ or $S = -1$. The Ising model is described by the following Hamiltonian:

$$H = -J \sum_{i \neq j} S_i S_j - h \sum_i S_i. \tag{4.22}$$

The first term of this Hamiltonian is basically a sum over all nearest neighbour pair interactions, while the second part represents the interaction energy of the spins with an external magnetic field h. The Ising model is able to provide a simple and intuitive explanation for ordering phenomena such as the existence of an order-disorder phase transition of the ferromagnet at a critical temperature. However, there is no exact analytical solution for the Ising model in three dimensions. Fortunately, Monte Carlo simulations can provide reliable numerical solutions for the Ising model. A lattice Hamiltonian of the form above represents a very efficient model for describing short-ranged interactions, but also introduces significant approximations.

In practice, it is often necessary to go to more refined lattice Hamiltonians including more distant pair interactions or higher order many-body interactions. The cluster expansion formalism is an advanced interaction scheme formally

including arbitrary many-body terms and long-range interactions. It can e.g. be written as

$$H = J_0 + J_1 \sum_i S_i + J_2 \sum_{i \neq j} S_i S_j + J_3 \sum_{i \neq j \neq k} S_i S_j S_k + ... \tag{4.23}$$

In principle, such model Hamiltonians have been shown to be able to match the true interactions of any multicomponent alloy exactly when the expressions are not truncated [144]. However, in order to make the cluster expansion numerically treatable only a finite number of *effective* cluster interactions (ECIs) can be included [145]. This means that the applicability of the approach requires sufficiently rapid convergence with respect to the the number of ECIs [145]. The effective cluster interactions J_i, are usually fitted to total lattice energies of certain lattice configurations that are obtained by DFT calculations or other total energy methods [145]. When M figures are included in the cluster expansion fit, then the energy of at least M ordered structures has to be known from DFT calculations. The cluster expansion formalism has been successfully applied in particular for modelling bulk properties of binary metallic alloys. However, the method has its drawbacks, e.g. it can not easily be generalized to model nanoparticles due to the lack of symmetry and the convergence of the expansion can sometimes be an issue [146].

4.3 METHODS FOR TIME EVOLUTION AND SAMPLING EQUILIBRIUM

4.3.1 *Molecular dynamics*

Molecular dynamics simulations refer to the numerical solution of the classical equations of motions of a set of interacting atoms in the time domain. This coupled set of Newtonian partial differential equations for an ensemble of N atoms can be written as

$$\boldsymbol{F}_i = -\boldsymbol{\nabla}_i V(\boldsymbol{r_1}, ..., \boldsymbol{r_N}) = m_i \frac{\partial^2 \boldsymbol{r}_i}{\partial t^2} \quad \text{for i} = 1, ..., \text{N}. \tag{4.24}$$

Here, the force $\boldsymbol{F}_i$ on atom i is the negative derivative of the potential energy V with respect to the position coordinates of atom i. The potential energy can be obtained from any total energy method, which is capable of giving a total energy for a system of atoms in terms of their position coordinates. When the total energy is derived from density functional theory, large efficiency gains are possible when the wave-function is not solved for from scratch at every time-integration step, but when it is predicted by a classical equation of motion [147]. In that case, we speak of *Car-Parinello molecular dynamics*[147], which is what is usually meant when people speak of *first-principles molecular dynamics* today. It should be kept in mind that the nuclei are treated classically within this approach.

Most of the time, however, the molecular dynamics method is used in conjunction with classical interatomic potentials. This approach allows to simulate ensembles of up to millions of atoms on timescales up to nanoseconds. Many molecular dynamics codes are available today and they implement a variety of classical interatomic potentials for all kinds of materials. One of the most flexible and most widely used codes today is LAMMPS [148]. It is also used for the simulation in part IV of the present thesis.

4.3.2 *Metropolis Monte Carlo*

Since the original work *Equation of State Calculations by fast Computing Machines* by Nicholas Metropolis in 1953 [149] the Metropolis Monte Carlo method has become a widely applied standard method in statistical physics as well as in solid state physics and beyond. The idea of this algorithm is to perform an integration in phase space to determine thermodynamic quantities in an efficient way by importance sampling. In the Metropolis Monte Carlo method the points in phase space are chosen with a certain probability that corresponds to a Boltzmann distribution. By using such a probability the states that contribute most to the integral are chosen more frequently than others, which speeds up the calculation.

The time-dependent behaviour of a system, i.e. its evolution towards equilibrium, can be described by a master equation

$$\frac{\partial P_n(t)}{\partial t} = -\sum_{n \neq m} \left[P_n(t) W_{n \to m} - P_m(t) W_{m \to n} \right], \tag{4.25}$$

where $P_n(t)$ is the probability to find the system in state n at time t, and $W_{n \to m}$ is the transition rate for going from state n to state m. One straightforward way to ensure the master equation is to choose

$$P_n(t) W_{n \to m} = P_m(t) W_{m \to n}. \tag{4.26}$$

This equation is commonly known as the *detailed balance* condition. Great care is generally taken in Monte Carlo simulation schemes to ensure this condition, because otherwise the laws of equilibrium thermodynamics could be violated.

The probability of the n-th state occuring in a classical system is given by

$$P_n(t) = e^{-E_n / k_B T} / Z, \tag{4.27}$$

where Z is the partition function. The absolute value of $P_n(t)$ is usually not exactly known because of the partition function Z in the denominator. However, this problem may be avoided if we just generate every new state m from the

preceeding state n. This gives us a *Markov chain* of states. Now, the relative probability between the old and the new state is given by

$$\frac{P_n(t)}{P_m(t)} = \frac{W_{m\to n}}{W_{n\to m}} = e^{-(E_n - E_m)/k_B T}. \tag{4.28}$$

The partition funtion Z has cancelled out and we need to know only the energy difference $\Delta E = E_n - E_m$ between the initial and the final state. Any choice of the transition rate that satisfies the above detailed balance condition is allowed. The most prominent choice is certainly the one of the original Metropolis method, i.e.

$$\begin{aligned} W_{n\to m} &= e^{-\Delta E/k_B T} && for\ \Delta E > 0 \\ &= 1 && for\ \Delta E < 0 \end{aligned} \tag{4.29}$$

In praxis, the application of a Metropolis Monte Carlo algorithm consists of a few simple steps. First, we have to choose a new state, for example by translating a randomly chosen atom by a certain amount, and then calculate the energy difference between the old and the new state ΔE, for example by using a model Hamiltonian or analytical potentials. We may then calculate the transition probability from Eq. (4.29). If $\Delta E < 0$, i.e. the total energy of the system is lowered, then the new state is always accepted. If $\Delta E > 0$ then a uniformly distributed random number is drawn, and the new state will only be accepted if this random number is smaller than $e^{-\Delta E/k_B T}$. If the random number is bigger, the new state will be rejected and the translation of the considered atom will not be applied. Repeating these steps will finally evolve the system into thermodynamic equilibrium.

4.3.3 *Kinetic Monte Carlo*

The Metropolis Monte Carlo algorithm described in the preceeding section can be considered as a ground state search. The Kinetic Monte Carlo approach extends the concepts of Metropolis Monte Carlo in a way that the time evolution of a system can be described. The evolution through phase space may then be considered as physical, with a physical time being well defined. Kinetic Monte Carlo is especially suitable to study all kinds of atomic diffusion, which may be mapped onto a lattice. A good introduction to the Kinetic Monte Carlo method may be found in Ref. [150] and its thoretical foundations have been discussed in Ref. [151].

All atomic diffusion processes may be considered to have a finite energy difference between their initial and final state. This energy difference can be calulated from a lattice Hamiltonian, the same way as when using a lattice-based Metropolis Monte Carlo method. But when an atom is jumping from its initial to its final state it not only needs the energy difference between the initial and the final state,

but also an additional migration barrier E_m. According to transition-state theory the rate R_{ij} at which the diffusion process from the initial state i to the final state j occurs is given by

$$R_{ij} = \nu_0 e^{-(\Delta E_{ij} + E_{m,ij})/k_B T} \qquad \text{for } \Delta E_{ij} > 0 \tag{4.30}$$

$$R_{ij} = \nu_0 e^{-E_{m,ij}/k_B T} \qquad \text{for } \Delta E_{ij} < 0, \tag{4.31}$$

where ΔE_{ij} is the energy difference between state i and state j and ν_0 is the attempt frequency. The migration barrier $E_{m,ij} = E_{m,ji}$ for a process $i \rightarrow j$ has to be the same for the reverse process $j \rightarrow i$ in order to fulfill the detailed balance condition [151]. If the same barrier for all processes is assumed, the Kinetic Monte Carlo method reduces to the Metropolis Monte Carlo algorithm. In that case, the trajectory through phase space within the Metropolis Monte Carlo method may be interpreted as physical and a time scale can be defined.

4.4 METHODS FOR SADDLE POINT SEARCH

Saddle point energies are important ingredients for the modelling of diffusion processes in materials science as well as in chemical reactions and other fields [152]. A variety of methods are available to search for saddle points and for obtaining their energies, such as e.g. the Ridge, the Conjugate Peak Refinement or the Dimer method [152]. If the initial and final state are known in terms of the atomic coordinates and a reasonable guess for a diffusion path is available, the climbing-image nudged elastic band method (CI-NEB) is a very useful method to obtain the saddle point configuration and its energy [153, 154]. This method can be conveniently coupled to the total energy methods described in Section 4.2 and is applied to obtain migration barriers for atomic diffusion in Chapters 7 and 8 of this thesis.

4.4.1 *Nudged-elastic band method*

In the nudged-elastic band method (NEB) a discrete set of images, i.e. a set of atomic position coordinates, which define a path form the initial to the final state, is connected with springs [152]. These images are then relaxed to the minimum energy path by an optimization algorithm. The method takes care that the set of images does not evolve away from the minimum energy path by using advanced numerical schemes. Within this approach the images close to the saddle point tend to slide to lower energies. This is prevented in the advanced *climbing-image* nudged elastic band method (CI-NEB) [154]. This method converges the highest energy image exactly to the saddle point by zeroing the spring force on this image and including only the inverted parallel component of the true force [152].

4.5 METHODOLOGICAL CONSIDERATIONS FOR THE TOPICS OF THIS THESIS

Within the present dissertation, two different topics related to the defect physics in Cu(In,Ga)Se_2 and in silicon are investigated based on the atomic-scale simulation tools explained above.

- In part III, the intrinsic point defects in Cu(In,Ga)Se_2 are investigated using screened-exchange hybrid density functional theory
- In part IV, the formation of twin boundaries, stacking faults and voids is investigated by molecular dynamics using the Albe-Erhart bond-order potential [140] and lattice Monte Carlo techniques

This choice of methods is motivated by the requirements on systems sizes, time scales and accuracy. In case of point defects in Cu(In,Ga)Se_2, we are interested in point defect formation energies as well as in their electronic properties. For this purpose, it is essential to resort to a method which retains an adequate description of the electronic system such as density functional theory. Since many open questions remain concerning the point defects Cu(In,Ga)Se_2, and LDA has recently been found to give rather inaccurate results in some cases, the present approach is to go a level beyond the accuracy of the LDA. In order to achieve consistent results the present study of the intrinsic point defects in Cu(In,Ga)Se_2 is carried out by using the Heyd-Scueria-Ernzerhof screened-exchange hybrid density functional [155, 156]. The additional concepts needed to derive point defect formation energies and other properties from ab-initio methods are introduced in Chapter 5.

The atomic-scale simulation of extended defect formation in silicon growth from the melt has to be tackled from a different angle. In this case, it is important to observe defect formation during growth, which requires time scales of at least nanosecond and system sizes of 200.000 atoms or more. This is not achievable using first-principles methods. Molecular dynamics in conjunction with a classical interatomic bond-order potential represents a feasible approach which retains sufficient accuracy for the problem. In order to simulate even bigger systems up to millions of atoms and to reach up to the time scale of seconds we develop a new lattice model to simulate silicon crystal growth from the melt including possible stacking fault formation at the interface in Chapter 13. The disadvantage is to loose the ability to simulate grain boundaries due to the lattice approximation.

5

AB-INITIO CHARACTERIZATION OF POINT DEFECTS

5.1 INTRODUCTION

In order to see the necessity of first-principles calculations in the context of point defects it is worth mentioning some quantities of interest, which can be calculated. The formation energies of intrinsic defects like vacancies, interstitials, antisites or more complex defect arrangements can be compared in order to identify the predominant defect species. In the case of extrinsic impurities, the calculated formation energies provide insights into the solubility of the impurities. The stable charge states of intrinsic or extrinsic defects can be obtained, which in turn classify the defects as acceptors or donors in a specific host material. Furthermore, the activation energies for changing the charge state, i.e. the ionization energies of the defects can be obtained and therefore allow to identify appropriate donors and acceptors for device development. In this context, ab-initio methods have made significant contributions to the understanding of AX and DX centers* in II-VI semiconductors and particulary in GaAs [158–160].

Defect induced states within the band gap affect the optical properties, e.g. in the case of color centers, or can act as recombination centers. The assignment of these levels to specific defects is experimentally difficult but possible with the aid of DFT calculations. Apart from the thermodynamic stability also the mobility of point defects can be assessed. The free energy of defect migration determines the kinetic stability of intrinsic point-defects and impurities under non-equilibrium conditions. In the case of more than just one defect, their interactions can be studied by calculating binding energies. The characteristics of extrinsic point defects are sometimes heavily influenced by the presence of intrinsic point-defects, e.g. due to defect association.

* A DX center is a substitutional donor which may behave like an acceptor depending on the position of the Fermi level. Similarly, an AX center is an acceptor, which may behave like a donor. This behaviour is usually associated with large lattice relaxations and bond breaking. In the AX and DX denomination, A stands for acceptor and D for donor. These substitutional donors and acceptors were previously thought to associate with unkown point defects, represented by the symbol X, which was not confirmed later. The denominations AX and DX center, however, remained [157].

Also, the association of solely intrinsic point-defects is a key for understanding the materials behavior as it is the case for chalcopyrites [161]. Another important application is the determination of doping limits, which can be estimated by first-principles calculations. Alternatively it is possible to choose one specific defect and even focus on a single certain charge state in order to calculate properties of interest which in turn can be used for the experimental identification or characterization of this specific defect.

Various experiments capable of identifying point defects can be simulated from first-principles with, however, varying reliability. For example, it is possible to calculate the formation volume of defects to study their impact on the crystal lattice parameter [162]. Calculating ionization energies enables to estimate the conductivities which can then be measured [163]. It is possible to identify the defect related magnetic moment and derive parameters for electron paramagnetic resonance measurements [164]. It is even possible to model the positronic trapping state at a defect location and derive from it the characteristic lifetimes in order to compare them with results obtained by positron annihilation spectroscopy [165].

In the case of localized defect related states, optical spectra are the primary means for defect identification. The calculation of optical properties is, however, often difficult in the case of solids. Using simple LDA/GGA-DFT in most cases it is at least possible to identify whether an absorption feature can be expected or not. The absorption energy on the other side is clearly an excited state property and affected by the difficulties mentioned above. A good example for the calculation of a defect excitation can be found in Ref. [166], where the full methodology of many-body perturbation theory was applied to the excitation of a negatively charged nitrogen-vacancy color center in diamond.

In the following section, the calculation of the formation energies of intrinsic point defects for a two component system is explained in order to give a basic understanding of the concept of ab-initio point defect calculations.

5.2 THERMODYNAMICS OF POINT DEFECTS

The key quantity for accessing the thermodynamics of point-defects in solids is the Gibbs free energy of defect formation (ΔG_f). Ultimately, one is interested in defect concentrations which can be calculated from the formation energy for the dilute limit ($c < 10^{-3}$) through

$$c = c_0 \exp\left(-\frac{\Delta G_\mathrm{f}}{\mathrm{k_B} T}\right) = c_0 \exp\left(-\frac{\Delta E_\mathrm{f} + p\Delta V_\mathrm{f} - T\Delta S_\mathrm{f}}{\mathrm{k_B} T}\right). \tag{5.1}$$

Here, c_0 is the concentration of available positions for the defect in the lattice, $\mathrm{k_B}$ is the Boltzmann constant and T the temperature. The quantities ΔE_f, ΔV_f and ΔS_f are the formation energy, formation volume and formation entropy of

the corresponding defect. The discussion now focusses on the formation energy, which is usually the dominating contribution and sufficient for low temperature and low pressure conditions. The other two contributions can, however, also be calculated within electronic DFT.

At this stage, two systematic paths can be followed. It is possible to construct defect pairs or clusters which are charge neutral and conserve the particle numbers. This method leads to the well known Kröger-Vink notation of defect reactions. A typical example is the so-called Schottky defect equilibrium which in the case of a simple metal oxide (MO) could be

$$0 \rightleftharpoons \mathrm{V}_\mathrm{O}^{2+} + \mathrm{V}_\mathrm{M}^{2-} \ . \tag{5.2}$$

The defect equilibrium and therefore the concentrations can be expressed in terms of Gibbs free energy of defect formation $\Delta G_\mathrm{Schottky} \approx \Delta E_\mathrm{Schottky}$. The strength of this method is that by conserving charge as well as particle numbers, the formation energy does not depend on external reservoirs other than the material itself. In the case of a first-principles approach, $\Delta E_\mathrm{Schottky}$ is calculated by constructing a super-cell of the MO, remove a cation and an anion from arbitrary positions, and calculate the formation energy $\Delta E_\mathrm{Schottky}$ from total energy differences via

$$\Delta E_\mathrm{f} = E^Z_\mathrm{defect} - E^Z_\mathrm{ideal} \ . \tag{5.3}$$

Here, E^Z_ideal and E^Z_defect are the total energies as obtained by a total energy calculation for the super-cells containing the defect and the ideal structure. This approach uses only the DFT total energies and returns relatively accurate numbers. There are, however, some pitfalls using this approach. Apparently, the charge states in Equation 5.2 were simply guessed and could well differ from $q = \pm 2$. It is of course possible to check the charge state via the electron density output of the DFT code which is always available. In case the charge state is different for either the oxygen or cation vacancy (the oxygen vacancy could be a color center or single donor), this super-cell calculation can not represent the ground state of the defect. For the case that $\mathrm{V_O}$ is only singly charged, one could insert two $\mathrm{V_O}$ in order to reestablish the ground state. Then, the conservation of particle numbers has to be omitted. In complex oxides (e.g. in sesquioxides), defect reactions are even more complicated as exemplified by the following reaction:

$$0 \rightleftharpoons 3\mathrm{V}_\mathrm{O}^{2+} + 2\mathrm{V}_\mathrm{M}^{3-} \ . \tag{5.4}$$

It can be seen that the number of defects (five in this case) increases dramatically with the complexity of the materials stoichiometry. Considering typical cell sizes accessible by present DFT calculations ($50 < N_\mathrm{atoms} < 1000$) the assumption of dilution is not fulfilled, and the resulting numbers will surely depend on the actual arrangement of the defects within the cell. Therefore, this approach is

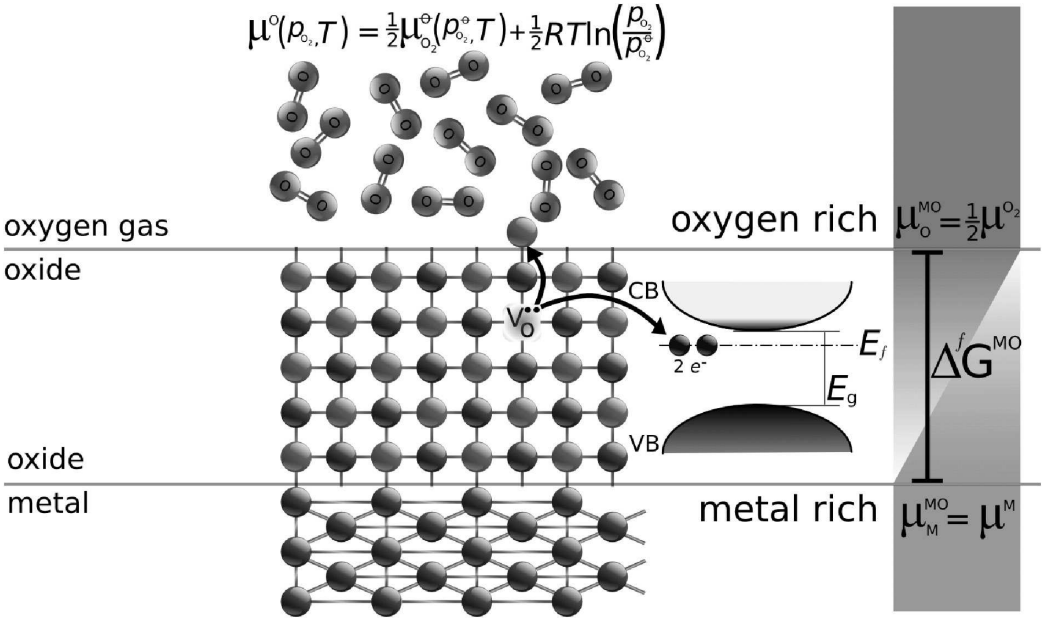

Figure 18: Defective metal oxide and possible reservoirs for anions, cations and electrons. Here, as an example, we show the case of an oxygen vacancy in charge state $q = +2$, which is formed by releasing a neutral oxygen atom to the gas reservoir with chemical potential $\mu_O^{MO} = \frac{1}{2}\mu^{O_2} = \mu^O(p_{O_2}, T)$ and by moving two electrons into the electron reservoir with the Fermi energy E_f.

neither unique nor flexible. Following the ideas of Zhang and Northrup [167] it is more efficient to calculate the formation energies of individual defects sequentially and in different charge states, so that charge as well as particle conservation do not need to be fulfilled. Defect reactions are constructed at a later stage from the individual defects with the lowest formation energies. Since the constraints of constant particle numbers and charge are neglected, the free energy of defect formation depends on the chemical potentials and electrochemical potential of the reservoirs:

$$\Delta G_\mathrm{f} = \Delta E_\mathrm{f} + p\Delta V_\mathrm{f} - T\Delta S_\mathrm{f} - \sum_i n_i \mu_i + qE_\mathrm{F} \; . \tag{5.5}$$

Here, n_i are the number of exchanged particles of type i in order to construct the defect and μ_i are the corresponding reference chemical potentials. The reference electrochemical potential for the electrons is the Fermi energy E_F, and q is the charge state of the defect.

Figure 18 illustrates the process of defect formation as a subsequent exchange of (neutral) atoms and electrons with their respective reservoirs. The chemical potentials of the relevant atomic species μ_i and the Fermi energy E_F are experi-

mental control variables. The Fermi energy is also sometimes referred to as the chemical potential of the electrons. Conceptually, the Fermi energy can be controlled or influenced by dopants and impurities. The control over the chemical potentials is often difficult to establish, experimentally. The chemical potentials μ_i are related to the species activities a_i via $\mu_i = \mu_i^{\ominus} + RT \ln a_i$, where $\mu_i^{\ominus}$ is the reference chemical potential in the chemical standard state. In case of a reference reservoir in the gas phase the chemical potential may be related to the partial pressure p_i via the ideal gas law. For the oxygen gas phase, e.g., this allows to relate the chemical potential of oxygen μ^{O} to the oxygen partial pressure p_{O_2} via $\mu^{\mathrm{O}}(p_{\mathrm{O}_2}, T) = \frac{1}{2}\mu^{\ominus}_{\mathrm{O}_2}(p^{\ominus}_{\mathrm{O}_2}, T) + \frac{1}{2}RT \ln\left(\frac{p_{\mathrm{O}_2}}{p^{\ominus}_{\mathrm{O}_2}}\right)$, where $p^{\ominus}_{\mathrm{O}_2}$ refers to the partial pressure in the standard state. In the case that the reference chemical potentials are the ones of solid phases it is difficult to establish precise experimental control. However, the activities and therefore the chemical potentials are always closely related to the availability of the respective species during production of the material. In applied studies the chemical potential of metallic species is therefore often treated as a free parameter, expressed as deviations from the cohesive energies $\mu_i = \mu_i^{el} + \Delta\mu_i$ of the most stable elemental reference phases μ_i^{el}. The chemical potential of the solid phase is equal to its cohesive energy and serves as a reference for the metal rich limit ($\mu_{\mathrm{M}}^{\mathrm{MO}} = \mu^{\mathrm{M}}$ in Figure 18). The maximal deviations from the elemental reference values are restricted by the heat of formation of the compound ΔH_{f}, which can also be calculated from first-principles:

$$\Delta H_{\mathrm{f}}^{\mathrm{MO}} = \Delta\mu_{\mathrm{M}} + \Delta\mu_{\mathrm{O}}. \tag{5.6}$$

It is common to plot the defect formation energies as a function of the Fermi energy at specific chemical potentials of interest.

At this stage, it may appear irritating that the defect stability, which depends on the Fermi energy, influences the Fermi energy itself, as defects are charged. Once the formation energies of all (predominant) defects are known the determination of the concentrations is achieved as follows: First, a specific environment is chosen by fixing the atomic chemical potentials. Next, the formation energies and concentrations are expressed as a function of the Fermi energy. The actual value of the Fermi energy is obtained by additional physical constraints. At the resulting Fermi energy, the total charge (including also free charge carriers and dopants) should vanish (charge neutrality), and none of the defects should have a negative formation energy. A detailed description of this process is given in Ref. [163].

Although the Fermi energy always assumes a fixed value in thermodynamic equilibrium, it is instructive to plot the formation energies of all defects as a function of this parameter. In this representation it is most convenient to discuss the changes of the defect equilibria upon extrinsic doping and changes of the environment.

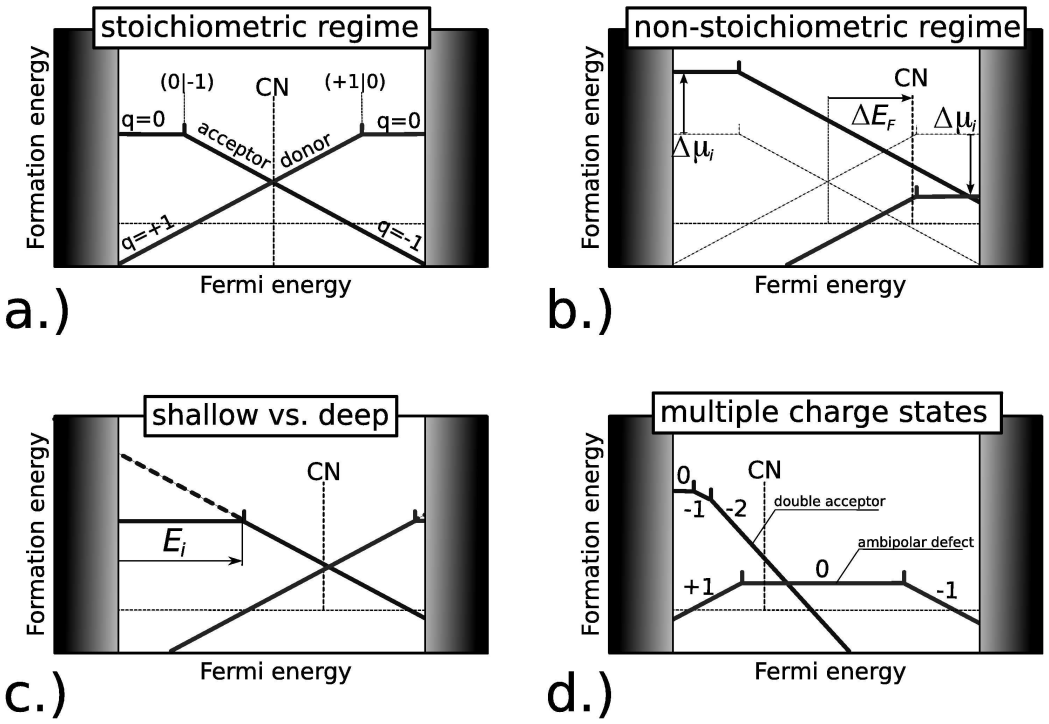

Figure 19: Examples for prototype defects: (a) A Schottky/Frenkel defect-pair and stoichiometric defect reaction. (b) Shift towards a non-stoichiometric regime due to changes of the μ_i. (c) A deep acceptor and a shallow donor defect. (d) Examples for multiple charge states, e.g. an ambipolar defect and a double acceptor defect. The (approximate) point of charge neutrality (CN) is indicated for all examples.

In Figure 19, several well known defect equilibria are translated into this representation. The first panel (a) represents the Schottky reaction of Equation 5.2. The slope of each line represents the charge state of the defect (Equation 5.5). In this case, the acceptor and donor formation energies are totally symmetric with respect to each other and the charge neutrality (CN) is easily found at the point where the formation energy of both defects has the same value. Charge states can change as it is denoted by the changing slopes of the defects. The apparent symmetry between donor and acceptor formation energies is not necessarily present in real materials. The situation changes especially when a different environmental condition ($\Delta\mu_i$) is chosen.

In the case of our metal oxide the second panel (b) of Figure 19 shows the effect of a lower oxygen pressure and/or higher temperature and a consequently lower chemical potential of oxygen and a correspondingly higher chemical potential of the metal. Under these conditions, the formation energy of the oxygen vacancy is lower and that of the cation vacancy higher. The Fermi energy necessarily shifts to the right (n-type) since negative formation energies are unphysical. The charge neutrality is now more difficult to determine since three species significantly contribute to it. Positive charge carriers are the oxygen vacancies whereas cation vacancies and electrons in the conduction band (CB) are negative compensating charges. The exact numbers have to be determined numerically and now also depend on the density of states in the conduction band. We also see that in this case, the fact that the oxygen vacancy can transform into a neutral color center may further affect the charge neutrality.

The third panel (c) displays the situation when the ionization energy of the acceptor and donor differ from each other. The ionisation energy of the defect is given by the distance of the charge-state transition energy to the VBM for acceptors and to the CBM for donors. The donor is shallow (low ionization energy), while the acceptor is deep (high ionization energy). Only very shallow donors are able to keep their charge even at a Fermi energy close to the band edges. These defects are generally good candidates to produce free charge carriers. This is a necessary but not a sufficient condition. In order to obtain the free charge carriers the defects of opposite charge should additionally have high formation energy. In Figure 19.c, for example, this is not the case. The point of charge neutrality is well below the CBM. In this situation, even with the help of additional extrinsic donors, the Fermi level can hardly move higher. This is because the formation energy of the acceptor becomes negative for a Fermi energy well below the CBM. This is usually referred to as Fermi-level pinning, a situation which leads to difficulties of $n-$type doping, e.g. in chalcopyrites due to the presence of negatively-charged copper vacancies. The probability for the existence of such pinning levels generally increases with larger band gaps. Therefore, the larger the band gap, the fewer materials can be found which are still dopable to a significant extent. This is because the intervals of the Fermi-level for which negative defect formation energies occur, are potentially larger

for wide-gap materials. While small band-gap materials like silicon or GaAs can usually be doped $n-$ as well as $p-$type, one type of doping usually predominates for wide-gap materials, while the other is more difficult or even impossible to achieve. Finally, for insulating materials often neither $n-$ nor $p-$type doping can be achieved.

In the last example (Figure 19.d) it is shown that defects can potentially exist in multiple charge states. It is possible that donors and acceptors have two or more ionization levels. Consequently, they exhibit two or more different charge states. It is further also possible that defects exist in negative as well as positive charge states are, i.e. ambipolar defects. Important defects of this class are for example vacancies and interstitials in silicon, as well as hydrogen in many semiconductores. In the case of hydrogen, the switching from donor to acceptor does not occur via a neutral charge state. The omission of a charge state is called a negative U behavior and is usually related to large structural relaxations and conformational changes of the defect.

5.3 FORMATION ENERGIES FROM AB-INITIO CALCULATIONS

After giving some examples, we now show the process of obtaining the formation energies of point-defects from the output of first-principles calculations. First, an appropriate variant of first-principles methodology is chosen, which reproduces most of the relevant properties of the bulk material and still allows to calculate at least 100 atoms. Bulk calculations are performed, and the accuracy of the (DFT) method is tested with the semiconductor and all relevant reference phases. From a band structure calculation of the host semiconductor, the position of the VBM and CBM and their corresponding energies are determined.

In the next step, neutral defects are placed into a supercell of a sufficient size and the structures are optimized usually at constant volume conditions. The size of the supercell should be as large as possible. However, this sensitively depends on the material, the method and available computational resources. The calculations are usually conducted within periodic boundary conditions and the defects in the supercells should be separated by at least two neighboring shells. The defects are subsequently charged, and the total energies are calculated for each charge state. When periodic boundary conditions are used, a homogeneous counter charge is added to avoid energy divergence. Unfortunately, this measure introduces spurious cell size effects. In the case of potentially magnetic defects, additional spin-polarized calculations have to be conducted in order to avoid spin contamination.

Afte running the necessary total energy calculations and carrying out the necessary corrections, the formation energies for each charge q state can be obtained as

$$\Delta H_{\mathrm{f}}^{q} = \Delta E_{\mathrm{def}} + \sum_{i} \Delta n_i \Delta \mu_i + q(\epsilon_{\mathrm{VBM}} + E_{\mathrm{F}}), \tag{5.7}$$

where ΔE_{def} is the calculated energy difference between the system with and without defect, $\mu_i = \mu_i^{\mathrm{ref}} + \Delta\mu_i$ is the chemical potential of the element i, ϵ_{VBM} is the energy of the valence band maximum (VBM) obtained from the calculation and E_{F} is the Fermi energy.

Normally, only the line segments for the charge states with the lowest formation energy are plotted for each defect (see Figure 19). As discussed above, defect formation energies are usually plotted under specific chemical potentials of its constituents, which are of interest. It is often instructive to plot the formation energies under the most extreme conditions, which give upper and lower limits to the formation energies of specific defects. In the case of the metal oxide (see Figure 18) this would be $\Delta\mu_{\mathrm{O}} = 0; \Delta\mu_{\mathrm{M}} = H_{\mathrm{f}}^{\mathrm{MO}}$ in the oxygen-rich (high oxygen pressure) limit whereas $\Delta\mu_{\mathrm{O}} = H_{\mathrm{f}}^{\mathrm{MO}}; \Delta\mu_{\mathrm{M}} = 0$ in the reducing limit (low oxygen pressure)†.

5.4 CORRECTION SCHEMES

Standard local density functional calculations for point defects are prone to various sources of errors. Today it seems accepted, that two sources of error are most important for point defect calculations using the supercell approach and have to be corrected for: The first of which arises from the spurious interaction of the charged defect cell with its periodic image. This error is commonly corrected for by two separate corrections, the pure electrostatic correction, i.e. a Makov and Payne type image charge correction [168], and a potential alignment correction [34]. For the image charge correction, it has been proposed that the pure monopole term should be scaled down with a constant factor, since the quadrupole contributions effectively show the same scaling with opposite sign [169, 170]. Very recent studies confirm that the pure Makov and Payne monopole correction generally overestimate the correction unless for point charge like defects [171]. The second important error in DFT point defect calculations arises from the band-gap correction, which is necessary when local functionals are used. The band-gap problem is long known in density-functional theory and consists of the fact that local and semilocal functionals severely underestimate the band-gap of most compounds. Today it is understood that for accurate point defect calculations not only the band gap needs to be accurate, but also the individual

† The Gibbs free energy of formation G_{f} is equal to the formation enthalpy H_{f}, when the entropy of formation is neglected. This is usually a safe approximation at room temperature.

band edges need to be correctly positioned on an absolute energy scale [172, 173]. This is easy to understand since the position of the valence band edge directly enters the formation energy of charged defects. When an absolute reference potential is considered, many localized defect states are approximately constant on an absolute scale, but not as referenced to the valence band edge [173]. This, however, does not necessarily have to be the case for defects, which are not atomically localized or which interact with the band edges. Such defect states may shift with the band edges to an unknown degree. A localized defect state may relatively easy be recognized based on the analysis of the density of states, if the defect state lies within the predicted gap. In this respect, hybrid functionals can be of great help, since they allow localized defect states over the whole band gap to be observed. As a consequence, they allow to determine whether defect states shift with the band edges once the underestimated band gap as given by local functionals opens up. In such cases, static corrections to the band gap are bound to fail even if the correct position of the valence band edge is known [169, 173].

Part III

INTRINSIC POINT DEFECT PHYSICS IN $Cu(In,Ga)Se_2$

This part of the thesis is concerned with a detailed characterization of the intrinsic point defect physics of $CuInSe_2$ and $CuGaSe_2$ based on screened-exchange hybrid density functional theory. First, in chapter 6, the method is calibrated, i.e. the exchange screening parameter is optimized to reproduce the band gaps of various chalcopyrite phases and the structural parameters and other material properties are calculated in order to assess the accuracy of the method. In chapter 7 and 8 the properties of copper vacancies and copper interstitials are investigated. The consequences of these properties are discussed primarily with respect to fast copper migration and Fermi-level pinning in the material. In Chapter 9, the focus is put on the trap properties of cation antisite defects, the metastable $V_{Se} - V_{Cu}$ complex, and metastable DX centers. The electron trap properties of Ga_{Cu} are confirmed by photoluminescence measurements. As the final step, all pieces of the puzzle are put together. The properties of all remaining intrinsic defects are obtained and the complete intrinsic point defect physics in $CuInSe_2$ and $CuGaSe_2$ and its consequences for devices are discussed in chapter 10. This leads to an accurate, complete and consistent picture of the intrinsic point defect physics. In order to clarify the situation with respect to literature data, a detailed comparison is carried out and the origins of deviations from literature data are discussed.

6

SCREENED-EXCHANGE HYBRID DENSITY FUNCTIONAL THEORY CALCULATIONS FOR CHALCOPYRITES

6.1 HSE06: EXCHANGE SCREENING VS. FRACTION OF EXACT EXCHANGE

In order to test the accuracy of screened-exchange hybrid density functional theory for defect calulations in chalcopyrites, we first tested and calibrated the HSE06 functional. This functional entails the range separation parameter ω as described in Section 4.2.1.3. The fraction of exact exchange can be tuned as well. Since accurate band gaps are necessary for accurate defect calculations (see Chapter 5), it is straightforward to tune one of the two available parameters to match the band gap of the compound of interest.

For this purpose we calculated the single-particle eigenvalue spectrum of the relaxed structure of $CuInSe_2$ as a function of these two parameters of the functional. Details of the computation are as described in Section 6.3. In Figure 20, the band edge energies and the resulting band gap of $CuInSe_2$ is plotted. When tuning the screening parameter ω, while keeping the fraction of exact exchange at its standard value of 0.25, it is found that $\omega = 0.13$ Å^{-1} reproduces the band gap of $CuInSe_2$ very well (Figure 20, top). Furthermore, this parameterization also gives almost exact band gaps for many other chalcopyrite compounds without additional fitting as displayed in Table 2. This shows that the procedure captures a lot of the essential band structure physics and is not just arbitrary fitting. We therefore decided, that all calculations based on the screened-exchange hybrid functional in this thesis are carried out using $\omega = 0.13$ Å^{-1}. It is important to use only one parameter setting for all calculations in order to obtain consistent results. The following section provides further evidence of the accuracy of this choice for the calculation of bulk properties of various chalcopyrite phases. For comparison, the band edge energies and the band gap of $CuInSe_2$ was also calculated and plotted for varying fractions of exact exchange in Figure 20 (bottom), while keeping ω at its standard value of 0.2 Å^{-1}. In this case, a fraction of exact exchange of 0.3 is found to reproduce the band gap of $CuInSe_2$ equally well.

While the comparison of band gap energies is trivial, It may not be evident, if it is valid to compare band edge energies for different functional parameterizations

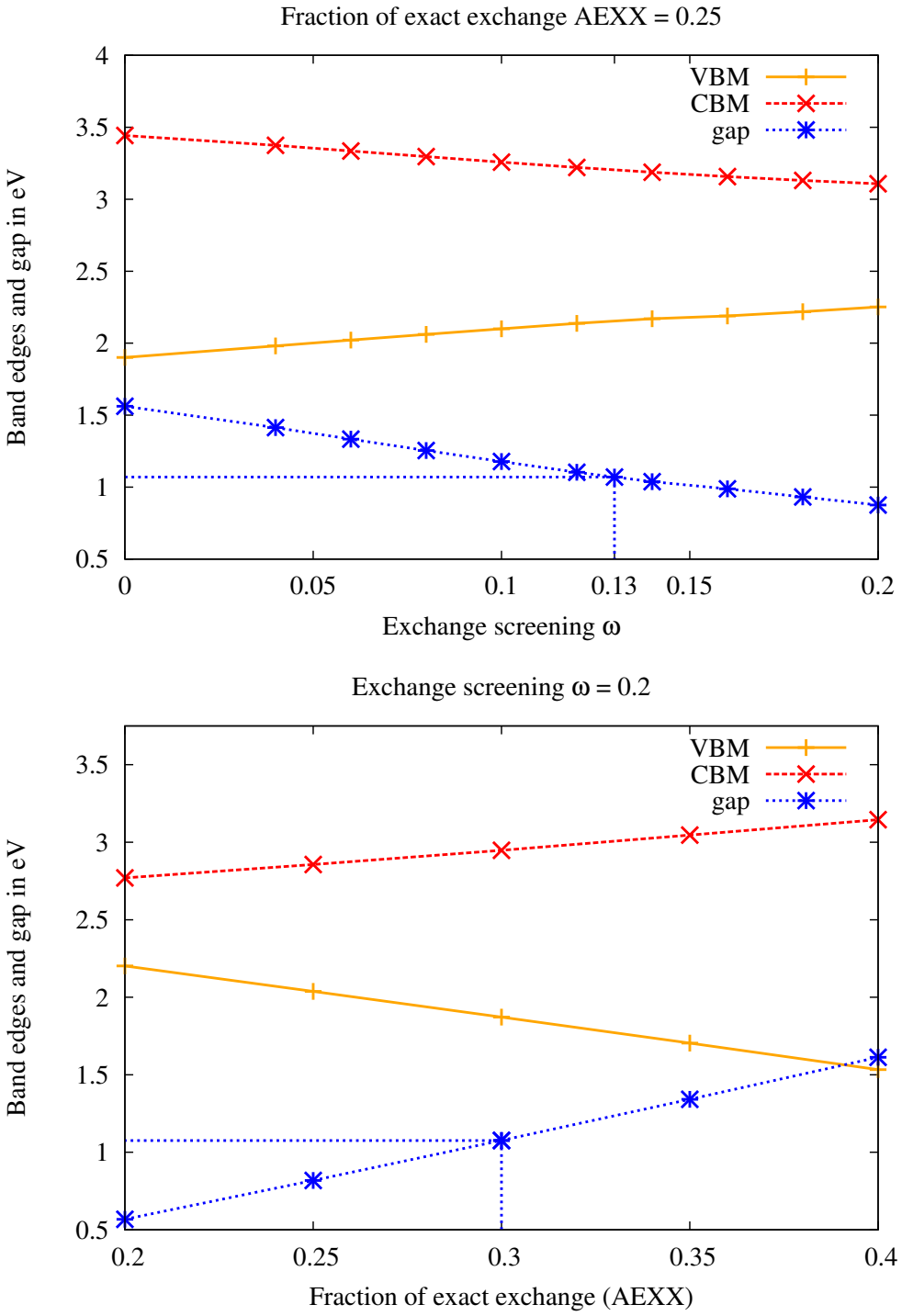

Figure 20: Top: Position of conduction and valence band edges and the resulting band gap of $CuInSe_2$ as a function of exchange screening parameter ω with the fraction of exact exchange fixed to 0.25. Bottom: Same plot as a function of the fraction of exact exchange with the exchange screening parameter fixed to $\omega = 0.2$ Å^{-1}.

on an absolute scale. However, in the case of differently parameterized hybrid functionals applied to the same material, it is justified to use the average local electrostatic potential as a reference level [172, 173]. When the same pseudopotential is used, this average of the electrostatic potential is trivially zero within the VASP implementation [174], such that the trends of the band edges in Figure 20 are physically meaningful. For our choice of $\omega = 0.13$ Å^{-1} and 0.25 fraction of exact exchange, the valence band edge of $CuInSe_2$ is positioned 0.51 eV lower as compared to plain PBE-GGA. The difference in the position of the valence band edge explains an important fraction of the differences in the formation energies of charged defects obtained with different functionals [173].

6.2 BULK PROPERTIES

The calculated structural parameters, i.e. the lattice constants a, c, the c/a ratio, the internal displacement parameter u^* as well as the bulk modulus B obtained from a fit to the Birch-Murnaghan equation are shown in Table 2. These properties were calculated using the 16-atom tetragonal unit cell and a k-point grid of 4x4x2 for both functionals. Other technical details of the calculations are as in Section 6.3.

From Table 2 it can be seen, that in addition to the accurate band gaps, the hybrid functional improves almost all calculated material parameters towards the experimental values in comparison to standard GGA calculations. Particularly, the c/a ratio and displacement parameter u are significantly improved. The well-described band gaps and the improved structural parameters show that the screened-exchange hybrid functional with $\omega = 0.13$ Å^{-1} provides very good accuracy beyond standard LDA/GGA functionals for the present chalcopyrite selenides and sulfides.

* The chalcopyrite crystal structure has a degree of freedom for ionic displacement of the two crystallographically inequivalent selenium sites. This displacement is usually denominated as u.

Hybrid	E_{gap}	a	c/a	u	B
$CuInSe_2$	1.07	5.839	2.013	0.2259	57.9
$CuGaSe_2$	1.68	5.650	1.965	0.2508	66.7
$CuInS_2$	1.53	5.572	2.010	0.2266	68.8
$CuGaS_2$	2.44	5.366	1.967	0.2537	79.3
$CuIn_5Se_8$	1.31	5.743	1.978	0.2111	-
Exp.	E_{gap}	a	c/a	u	B
$CuInSe_2$	1.04 [4]	5.814	2.001	0.2258 [175]	54 [176], 72 [177]
$CuGaSe_2$	1.68 [4]	5.614	1.964	0.250 [178]	71 [179]
$CuInS_2$	1.53 [4]	5.561	1.999	0.2295 [180]	71 [176], 75 [177]
$CuGaS_2$	2.43 [4]	5.350	1.959	0.2593 [180]	94 [181], 96 [182]
$CuIn_5Se_8$	1.32 [183]	5.748	2.008	-	-
GGA	E_{gap}	a	c/a	u	B
$CuInSe_2$	0.01	5.880	2.012	0.2177	55.8
$CuGaSe_2$	0.01	5.687	1.984	0.2438	59.3
$CuInS_2$	0.02	5.609	2.008	0.2179	65.3
$CuGaS_2$	0.62	5.388	1.980	0.2471	77.6
$CuIn_5Se_8$	0.0	5.688	1.989	0.2036	-

Table 2: The band gaps E_{gap}, lattice parameter a, c/a ratio, displacement parameter u and the bulk modulus B calculated using the screened-exchange hybrid functional with $\omega = 0.13$ Å^{-1} (Hybrid) in comparison to experimental data (Exp.) and to calculations using the PBE-GGA functional (GGA). An overall improvement when using the hybrid functional, especially of the band gaps, the anion displacement parameter u and the c/a ratio is evident. E_{gap} is given in eV, a and u are given in Å, The bulk modulus B is given in GPa.

6.3 SETUP FOR BULK AND DEFECT CALCULATIONS

In the following chapters, ab-initio calculations for point defects are carried out based on the HSE06 and the GGA functional. The parameters and technical details for these calculations are summarized as follows:

- The Vienna ab-initio simulation package (VASP) [174] was used for all calculations.
- All calculations within HSE06 use an exchange-screening parameter ω of 0.13 $Å^{-1}$ and a fraction of exact exchange of 0.25.
- For the calculation of bulk properties in the tetragonal unit cell of 16 atoms, a Γ-centered 4x4x2 k-point grid was used.
- Unless stated otherwise, 2x2x1 supercells of the tetragonal 16-atom chalcopyrite unit cell, i.e quasi-cubic supercells of 64 atoms, were used for the defect calculations.
- For these cells, a Γ-centered 2x2x2 k-point grid was used both for HSE06 and GGA calculations. The defect formation energies were found to be converged to within a few meV as compared to a 4x4x4 grid.
- PBE projector-augmented wave potentials (PAW) were used.
- A plane-wave energy cutoff of 350 eV was used for all calculations.
- Ions were fully relaxed to Hellmann-Feynman forces below 0.05 eV/Åfor supercells of 64 atoms.
- For a few defects, 3x3x3 supercells of 216 atoms, based on the primitive 8-atom monoclinic unit cell, were used together with the HSE06 functional. For these computationally intensive calculations a Γ-centered 2x2x2 k-point grid was used as well, but forces were relaxed to below 0.2 eV/Å.

7

COPPER VACANCIES IN $CuInSe_2$, $CuGaSe_2$, $CuInS_2$ AND $CuGaS_2$

7.1 INTRODUCTION

The copper vacancy is known to be the most prominent defect in $CuInSe_2$, $CuGaSe_2$, $CuInS_2$ and $CuGaS_2$ [184]. For the selenides $CuInSe_2$ and $CuGaSe_2$ this has been formerly shown by density-functional theory (DFT) calculations [8, 34, 184]. The very low formation energy of the negatively charged copper vacancy may lead to the formation of ordered defect compounds (ODCs) [30], also known as ordered vacancy compounds (OVCs), and is also the reason for Fermi-level pinning [34, 185, 186]. The formation of n-type ordered vacancy compounds (OVCs) and thus the formation of a $CuInSe_2$/OVC p-n-heterojunction occurs at the CdS/$CuInSe_2$ buffer/absorber interface and is supposed to improve the device performance [187]. Copper vacancies are also present in the sulfides $CuInS_2$ and $CuGaS_2$, but theoretical data is more scarce in that case. Simple models such as the macroscopic cavity model, however, suggest very similar formation energies of the neutral copper vacancy in the selenides as compared to the sulfides [188]. Formation of copper-poor phases has been observed also at $CuInS_2$ surfaces [189], but to our knowledge no direct evidence of a $CuInS_2$/ODC p-n-heterojunction does exist in the literature. ODCs are copper-poor but indium-rich compared to the bulk 1:1:2 stoichiometry. In order to form an ODC at an interface, diffusion of copper and indium is therefore necessary. Experimental determination of copper diffusion in $Cu(In,Ga)(Se,S)_2$ yields diffusion coefficients varying over seven orders of magnitude from 10^{-13} to 10^{-7} cm^2/s at room temperature [68–72]. A pronounced dependence of the diffusion coefficient on copper concentration [71] and correlation with conductivity [70] has been found in experiments. The diffusion of copper in these materials, especially in relation to the formation of ODCs is not understood and therefore more detailed insights are desirable.

	$\Delta H_f^{V_{Cu}^-}$ in eV				ΔE_m in eV	
	Hybrid	GGA	LDA (+U) [34]	cavity [188]	Hybrid	GGA
$CuInSe_2$	1.27	0.43	0.85	1.04	1.26	1.13
$CuGaSe_2$	1.21	0.23	0.61	0.94	1.21	1.03
$CuInS_2$	1.74	0.61	-	1.06	1.46	1.23
$CuGaS_2$	1.65	0.36	-	1.01	1.28	1.05

Table 3: Formation energies $\Delta H_f^{V_{Cu}^-}$ and migration barriers ΔE_m of the negatively charged copper vacancy (q=-1) obtained from the hybrid functional calculations in comparison with GGA calculations, calculations of Persson *et al.* [34] using LDA with a posterior +U correction (LDA (+U)) and values obtained from the macroscopic cavity model [188] (cavity) for the *neutral* copper vacancy.

7.2 DEFECT FORMATION ENERGIES

We have calculated the formation energies of the copper vacancies according to the equation

$$\Delta H_f^{V_{Cu}} = \Delta E_{V_{Cu}} + \mu_{Cu} + q(\epsilon_{VBM} + \epsilon_F), \tag{7.1}$$

where $\Delta E_{V_{Cu}}$ is the calculated energy difference between the system with and without the copper vacancy, $\mu_{Cu} = \mu_{Cu}^{ref} + \Delta\mu_{Cu}$ is the chemical potential of copper, q is the charge state of the vacancy, ϵ_{VBM} is the energy of the valence band maximum (VBM) obtained from the calculation and ϵ_F is the Fermi energy. The reference chemical potential of copper μ_{Cu}^{ref} is taken from a separate calculation of the face-centered cubic copper phase. We restrict the chemical potential difference $\Delta\mu$ to the stability range of the chalcopyrite phase. $\Delta\mu_{Cu} = 0$ is the appropriate upper bound, while the lower bound is given by the value where the transition to the defect phases $CuIn_3Se_5$, $CuGa_3Se_5$, etc. occurs.

The calculated formation energies of the copper vacancy in charge state $q = -1$ at maximally copper-rich conditions ($\Delta\mu_{Cu} = 0.0$) for a Fermi energy at the valence band maximum are given in Table 3 and the data is plotted as a function of the Fermi energy in Figure 21 and 22 for copper-rich as well as copper-poor conditions ($\Delta\mu_{Cu} = -0.5$ eV), respectively. The value of 1.27 eV obtained for the negatively-charged copper vacancy in $CuInSe_2$ using the hybrid functional is somewhat higher than the value of 0.85 eV calculated by Zunger *et al.* using LDA with an a posteriori valence band correction obtained from LDA+U [34]. For $CuGaSe_2$ we obtain 1.21 eV, which is also higher than their value of 0.61 eV.

For the sulfides, however, we obtain higher copper vacancy formation energies than for the selenides: 1.74 eV for $CuInS_2$ and 1.65 eV for $CuGaS_2$. The formation energy of the copper vacancy is thus very similar in $CuInSe_2$ and in $CuGaSe_2$, but it is approximately 0.5 eV higher in the sulfides $CuInS_2$ and $CuGaS_2$. This

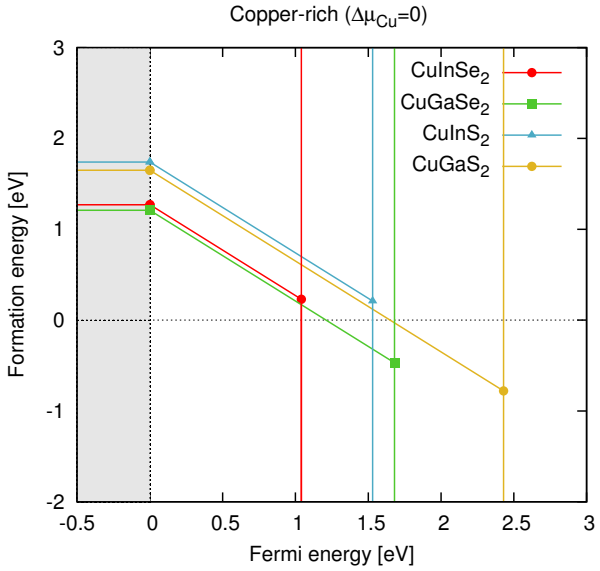

Figure 21: Fermi-level dependent copper vacancy formation energies from the hybrid functional under copper-rich conditions: $\Delta\mu_{\mathrm{Cu}} = 0$. The valence band maxima have been aligned and the formation energies have been plotted only up to the conduction band using the experimental band gap.

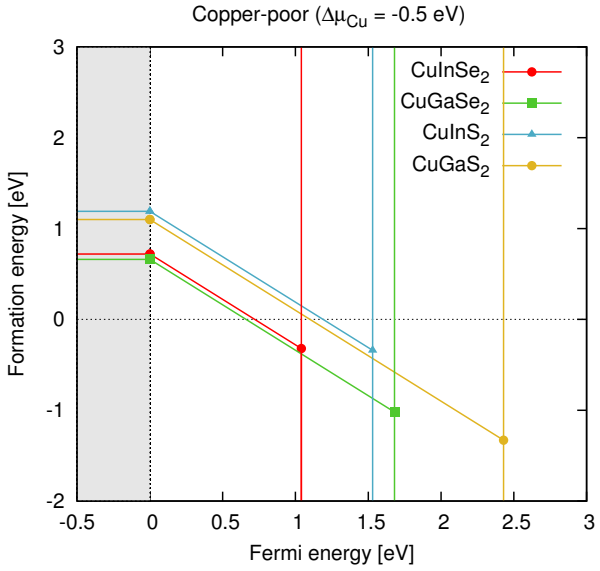

Figure 22: Fermi-level dependent copper vacancy formation energies from the hybrid functional under copper-poor conditions: $\Delta\mu_{\mathrm{Cu}} = -0.5$ eV. All materials show a Fermi pinning level.

is in contrast to the macroscopic cavity model proposed in Ref. [188] as well as standard GGA calculations (see Table 3), which both give very similar formation energies for both the selenides and the sulfides. This underlines the importance of an accurate treatment of electron exchange and correlation for total energy defect calculations in chalcopyrite selenides and sulfides.

7.3 FERMI-LEVEL PINNING

The Fermi pinning level that results from copper vacancy formation is given by the Fermi level at which the copper vacancy formation energy turns zero and depends on the copper chemical potential: $E_{\mathrm{F,pin}} = \Delta H_f^{\mathrm{V_{Cu}^-}} + \Delta\mu_{\mathrm{Cu}}$. Under copper-rich conditions ($\Delta\mu_{\mathrm{Cu}} = 0$), no Fermi pinning levels are obtained for $CuInSe_2$ and $CuInS_2$ (see Figure 21). However, photovoltaic p-type material is grown under copper-poor conditions such that the results should rather be interpreted at $\Delta\mu_{\mathrm{Cu}} = -0.5$ eV [190] (see Figure 22). Using this copper chemical potential, Fermi pinning levels are obtained for all materials considered ($CuInSe_2$: 0.77 eV, $CuGaSe_2$: 0.71 eV, $CuInS_2$: 1.24 eV, $CuGaS_2$: 1.15 eV). These Fermi-pinning levels are comparable to the experimental levels of around 0.85 eV associated with the formation of copper-poor interface phases reported by Klein *et al.* [185, 186]. The higher formation energy of the copper vacancy in $CuInS_2$ and $CuGaS_2$ leads to significantly higher Fermi pinning levels at 1.24 eV and 1.15 eV, respectively. This explains why copper diffusion related Fermi level pinning has so far not been reported in these sulfide compounds, since such high voltages were not applied in the respective experiments. The higher formation energy of the sulfides also indicates a reduced tendency to form ordered defect compounds at interfaces in photovoltaic cells.

7.4 MIGRATION BARRIERS AND DIFFUSION

The migration barriers of copper vacancies were calculated using the climbing-image nudged elastic band method (Section 4.4.1). These migration barriers ΔE_m are generally of the same order of magnitude for all examined chalcopyrite phases (see Table 3). The hybrid functional generally gives somewhat higher barriers for all phases (+ 0.13 to 0.23 eV). As a chemical trend we find that substituting In with Ga slightly decreases the migration barrier, while substituting Se with S slightly increases it.

Today's literature on copper diffusion coefficients in $CuInSe_2$ is not conclusive. Activation barriers ranging from 0.2 eV up to 1.25 eV have been reported for $CuInSe_2$ as well as widely varying prefactors. In the following, we estimate the temperature-dependent self-diffusion coefficient of $CuInSe_2$ and compare to experimental data. From the obtained copper vacancy migration barriers we may

estimate the self-diffusion coefficient D_{Cu}, ignoring anisotropic diffusion due to deviations from the ideal c/a ratio (c/a=2), using

$$D_{\mathrm{Cu}} = \frac{1}{6} z \nu c_{\mathrm{V_{Cu}}} d^2, \tag{7.2}$$

where z is the number of nearest neighbours (in our case $z = 4$),

$$d = \sqrt{(a/2)^2 + (c/4)^2} \approx \frac{1}{\sqrt{2}} a \tag{7.3}$$

is the copper ion nearest-neighbour distance, $c_{\mathrm{V_{Cu}}}$ is the copper vacancy concentration, and the total jump frequency ν on a specific neighbour site is given by

$$\nu = \nu^* \exp\left(-\Delta H_{\mathrm{m}} / \mathrm{k_B T}\right). \tag{7.4}$$

The frequency $\nu^* = \nu_0 \exp \Delta S_{\mathrm{m}} / \mathrm{k_B}$ contains the migration entropy ΔS_m and is typically estimated to be of the order $\nu^* \approx 10^{13} \mathrm{s}^{-1}$. We assume a total copper vacancy concentration of 1 atomic percent, which translates to a concentration of $c_{\mathrm{V_{Cu}}} = 0.04$ of copper vacancies on the copper sublattice. Note that the concentration is not given by an exponential Boltzmann term in the case of athermal vacancies and vacancies introduced by non-stoichiometry, but may be assumed to be fixed.

This results in a diffusion coefficient of

$$D = 4.64 \cdot 10^{-4} \mathrm{cm}^2/\mathrm{s} \cdot \exp(-1.26\ \mathrm{eV}/k_B T). \tag{7.5}$$

This self-diffusion coefficient is lower than the ones measured in experimental studies so far (see Figure 23). The result compares best with the NMR diffusion coefficient as determined by Becker and Wagner [191, 192] (compare BW83 in Fig. 23). Wagner assumed the same activation energy for $CuInSe_2$ as measured for $CuInS_2$ [192], i.e. 1.25 eV, which agrees excellently with our value of 1.26 eV for $CuInSe_2$ and reasonably with the one for $CuInS_2$ of 1.46 eV. Our estimate of the diffusion coefficient is also in reasonable agreement with the radio tracer diffusion coefficient by Gartsman et al. [69] when using a volume source by activating copper ions with deuterium irradiation (see GCL+97 vol. in Fig. 23). In this case our value is about three orders of magnitude lower. When using the more common thin-film radio tracer technique, they measured a value of around $10^{-8} \mathrm{cm}^2/\mathrm{s}$ at 430°C (GCL+97 surf. in Fig. 23), i.e. about 5 orders of magnitude higher than our estimate. This thin-film tracer diffusion coefficient has been interpreted as a chemical diffusion coefficient, while the one from the volume source was interpreted as the self-diffusion coefficient. However, in order to expect a significant concentration gradient using the first of the two methods and therefore chemical diffusion, an interstitial diffusion mechanism has to be

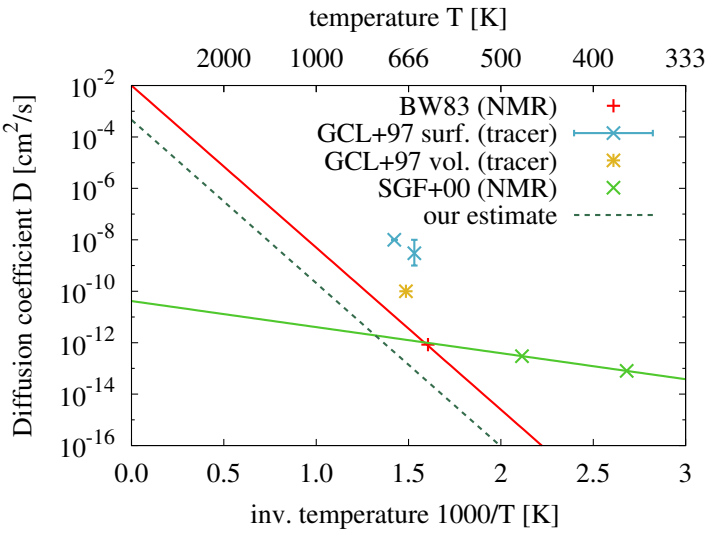

Figure 23: The self-diffusion coefficient of $CuInSe_2$ as estimated based on copper vacancy diffusion (see text) compared to experimental measurements by the most direct methods, i.e. radio tracer diffusion (GCL+97: Ref. [69]) and nuclear magnetic resonance (BW83: Ref. [191], Ref. [192] and SGF+00: Ref. [193]).

assumed if there is no concentration gradient in the initial sample. More recent NMR data by Stallworth and others give a diffusion coeffcient of the order $10^{-13}cm^2/s$ at 373 K [193], which is about 14 orders of magnitude higher than our estimate suggests (compare SGF+00 in Fig. 23). Their activation energy of 0.2 eV is much lower than our value of 1.26 eV. This large disagreement may be related to the non-stoichiometry of the samples in the NMR experiments (2 percent excess Se/S, i.e. copper-poor). There is also an extensive literature that measures chemical diffusion coeffcients using indirect methods such as p-n junction motion [75, 194–197], potentiostatic current decay [70, 71] and transient ion drift [68] (see Ref. [72] for a review), which we do not discuss here in detail. These methods generally yield much higher diffusion coefficients. The analysis of the data using indirect methods is complicated by internal and external electric fields [72]. We only want to mention the work of Tell et al. [198] who obtained an activation energy of 1.19 eV for $CuInSe_2$ by p-n junction motion in good agreement with our result. A possible reason for largely varying diffusion coefficients that is present in direct as well as indirect methods is the varying stoichiometry of the material. While stoichiometric samples have been measured in Ref. [191], which agrees best with our estimate, samples of $CuInSe_2$ are usually prepared copper-poor. From the very low copper vacancy formation energies and the phase diagram it can be assumed that these samples have a large concentration of copper vacancies up to several percent or more, such that diffusion can not be analyzed in the dilute vacancy limit. Furthermore, from the proposed phase diagrams (e.g.

Ref. [199]) it may be inferred that phase segregation of an ODC phase at low temperatures might be possible if copper is understoichiometric. For these two reasons, diffusion is likely to vary strongly with composition, which has been formerly measured by Dagan *et al.* [71]. Furthermore, grain boundary diffusion may play a role in polycrystalline samples. An exact estimate of the diffusion in such samples is not possible from the data presented here. However, the estimate given is valid for stoichiometric or slightly copper-poor single crystal samples in the absence of electric fields and does indeed compare to such experimental data within the accuracy of the estimate of the prefactor when direct experimental methods are used.

7.5 SUMMARY

In conclusion, we have calculated the defect formation energies and migration barriers of the copper vacancy in $CuInSe_2$, $CuGaSe_2$, $CuInS_2$ and $CuGaS_2$. The formation energies of copper vacancies under copper-rich conditions are around 0.5 eV higher for the sulfides than for the selenides. In contrast, substituting indium with gallium has a negligible effect on the formation energies. The higher formation energies in the sulfides imply that the sulfides may tolerate a higher Fermi level at the buffer absorber interface. The migration barriers of the copper vacancy were found to be very similar, i.e. 1.26 eV for $CuInSe_2$ and of comparable magnitude for the other materials. We conclude that copper diffusion in all studied stoichiometric or slightly copper-poor materials in the absence of electric fields is significantly slower than commonly expected. Much higher experimentally measured diffusion coefficients may be attributed to a variety of effects, e.g. the presence of internal and external electric fields, non-ideality of vacancies, i.e. the breakdown of the dilute limit of copper vacancies in non-stoichiometric samples, and grain boundary diffusion in polycrystalline sample. In addition, other diffusion paths seem likely to be present. In the following chapter, we show the importance of copper interstitials in $CuInSe_2$ for diffusion.

8

COPPER INTERSTITIALS IN $CuInSe_2$

8.1 INTRODUCTION

The fact that the copper vacancy diffusion mechanism cannot account for fast ion conductivity and is insensitive to drift from electric fields due to its rather high migration barrier, motivates the investigation of alternative copper diffusion mechanisms, such as copper interstitial diffusion.

In addition, several phenomena which require fast copper diffusion are known to exist in $CuInSe_2$. Copper redistribution at the $CuInSe_2$/CdS interface has been proposed to be responsible for the voltage-bias induced metastable behaviour of $CuInSe_2$ solar cells [45]. A model in which copper interstitials exhibit long-range field-induced drift from an interface into the bulk leaving negatively charged vacancies behind was formulated by Herberholz et al. [45], but direct evidence for this mechanism is still lacking today. Copper migration from the interface into the bulk has also been observed during the deposition of the CdS buffer layer on $CuInSe_2$ at a certain Fermi pinning level [185, 186]. Finally, external electric fields induce p-n junctions in p-type $CuInSe_2$ which is due to copper migration [71, 73–77]. For all of these phenomena, however, the atomistic details are not thoroughly understood.

Local DFT calculations with static band-gap corrections report formation energies larger than 2 eV for the copper interstitial [8, 32], which makes a significant contribution of interstitials to the copper diffusion unlikely. In this chapter, however much lower than previously reported formation energies for copper interstitials are obtained by using the hybrid functional HSE06 and two particularly fast copper interstitial diffusion mechanisms are identified.

8.2 METHOD

The setup for defect calculations as in Section 6.3 was applied. In case of the hybrid functional, ionic relaxation has been carried out with a truncated Fock operator. After full ionic relaxation, the wavefunctions were converged using the full Fock operator. The correction to the formation energies when treating the same ionic configuration and the reference cell with the full Fock operator as

compared to the truncated one adds up to a difference in the defect formation energies of not more than 15 meV, which shows that truncation of the Fock operator is a safe approximation due to good error cancellation. The electrostatic correction has been carried out within the scheme developed by Freysoldt et al. [200] This correction amounts up to 0.15 eV for single charged copper interstitials. Migration barriers have been calculated by the climbing-image nudge-elastic band method (CI-NEB) (see Section 4.4.1) using 3 images for the direct and indirect interstial mechanism and 11 images for the Frenkel pair formation process. The defect formation energies of the copper interstitials according to Equation 5.7 are

$$\Delta H_f^{\mathrm{Cu_i}^q}(\Delta\mu_{\mathrm{Cu}}, \epsilon_{\mathrm{F}}) = \Delta E_{\mathrm{def}} - \mu_{\mathrm{Cu}} + q(\epsilon_{\mathrm{VBM}} + \epsilon_{\mathrm{F}}), \tag{8.1}$$

where ΔE_{def} is the calculated energy difference between the system with and without the copper interstitial, $\mu_{\mathrm{Cu}} = \mu_{\mathrm{Cu}}^{\mathrm{ref}} + \Delta\mu_{\mathrm{Cu}}$ is the chemical potential of copper, q is the charge state of the interstitial, ϵ_{VBM} is the energy of the valence band maximum obtained from the calculation and ϵ_F is the Fermi energy.

8.3 RESULTS

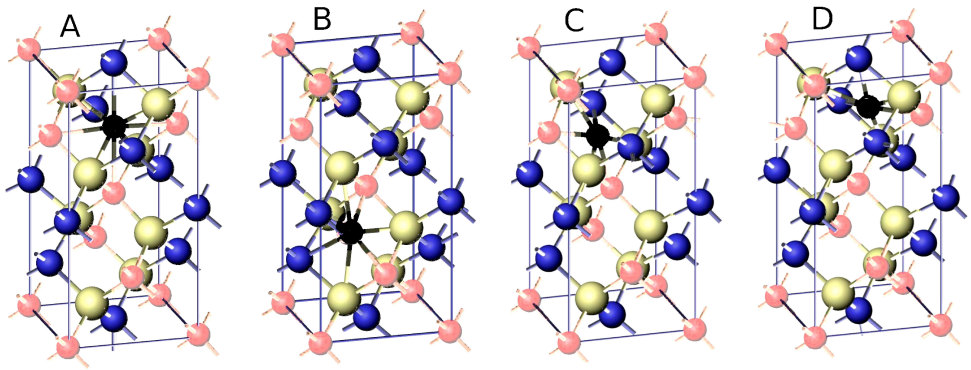

Figure 24: The copper interstitial atom (black) can relax in four different configurations. The octahedral (with respect to the cations) site A, which is the ground state using HSE06, the tetrahedral site B, which is the saddle point configuration of the direct migration mechanism, and the two trigonal planar sites C and D. Site C is the ground state within GGA. Compare also Figure 25. *Copper: (red/light grey), indium: (blue/dark grey), selenium: (yellow/white) (colour online/print). Images created with OVITO [201].*

The copper interstitial in $CuInSe_2$ can occur in distinct stable configurations on four different crystallographic sites (see Figure 24 and 25). These positions are the octahedral (with respect to the cations) site A, the tetrahedral site B, and the two trigonal planar sites C and D, where an interstitial at site C has two nearest copper neighbours and one nearest indium neighbour and the interstitial at site

	This work			Refs.		
$\mathbf{Cu}_i^+$	HSE06	GGA				LDA [8] +static
site A	0.17	0.94				2.04*
site B†	0.38	1.07		-		
site C	0.20	0.91		-		
site D	0.21	0.96		-		
$\mathbf{Cu}_i^0$	HSE06	GGA	GGA +gap	GGA [32]	GGA [32] +gap	LDA [8] +static
site A	1.21 (1.68)	1.52	2.56	1.67	2.67	2.88*
site B†	1.41 (1.88)	1.67	2.71	1.76	2.76	-
site C	1.25 (1.72)	1.52	2.56	-	-	-
site D	1.24 (1.71)	1.55	2.59	-	-	-
Frenkel pair	1.45	1.21				

Table 4: Copper interstitial and Frenkel pair formation energies $\Delta H_f(\Delta\mu_{Cu} = 0, \epsilon_F = 0)$ (see Equation 8.1) in eV. The values in brackets do not include the band-filling correction. All reported values include the electrostatic correction. The GGA values for the neutral defect are reported with and without a static band gap correction to the conduction band (GGA + gap), but without band-filling correction.

D has one nearest copper neighbour and two nearest indium neighbours. The sites A and B have been treated in Ref. [32], while calculations for sites C and D have not yet been reported.

In the following, the formation energies of the single positively charged and neutral copper interstitial at the different sites are quoted for $\Delta\mu_{Cu} = 0$ and a Fermi-level position at the valence band maxium ($\epsilon_F = 0$) as the reference state (Table 4). The chosen values may be translated to other conditions using Equation 8.1. With the GGA functional the trigonal planar site C is actually the ground state of the single positively charged copper interstitial (see Table 4). Its formation energy, however, is only 0.03 eV lower compared to the octahedral site A. The GGA values without band gap correction for sites A through D are all very similar and close to 1 eV. When adding the value of the band gap of 1.04 eV, the interstitial formation energies within GGA are comparable to the value of 2.04 eV given in Ref. [8]. Using the hybrid functional HSE06 with adapted screening parameter, however, we find significantly lower formation energies from 0.17 to 0.38 eV. The hybrid functional values reverse the energetic order between site A and C, i.e. the octahedral site A is the ground state for HSE06, while the trig-

* We assume that the value is for the octahedral site A.
† Site B is a saddle point configuration.

	Cu_i^+ HSE06	Cu_i^0 HSE06	Cu_i^+ GGA	Cu_i^0 GGA	Frenkel pair GGA
direct mechanism	0.22	0.20	0.13	0.09	1.26
indirect mechanism	0.34	0.30	0.30	0.26	1.43

Table 5: Migration barriers ΔH_m for the positive and neutral charge state of the copper interstitial diffusion mechanisms in $CuInSe_2$ and the activation barrier of Frenkel pair formation (Frenkel pair GGA) in eV.

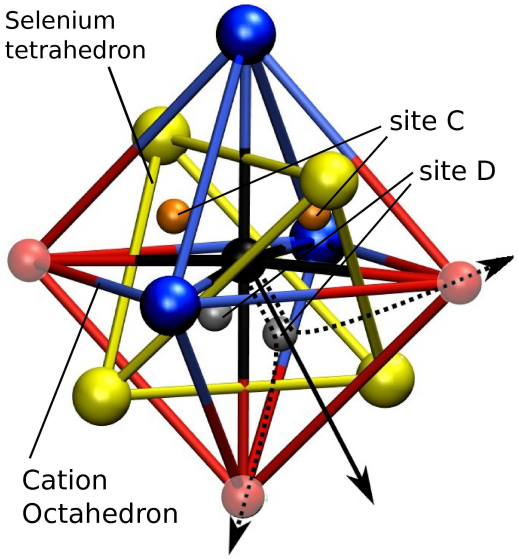

Figure 25: The octahedral copper interstitial atom on site A (central black) can migrate via a direct mechanism (straight arrow) and an indirect interstitialcy mechanism (dashed arrows). On the cation octahedron indium (blue/dark) is displayed larger than copper (red/light grey), (colour online/print).

onal planar sites C and D are 0.04 eV higher in energy. Although these energy differences are small, an accurate treatment of the exchange-corrleation energy therefore is important for obtaining the correct ground state in the case of the copper interstitial. The very similar formation energies of sites A, C and D show that the octahedral copper interstitial has significant freedom to move within the selenium tetrahedron (see Figure 24). The low formation energies obtained from the hybrid functional compared to the uncorrected GGA values originate from two sources: First, the use of the hybrid functional leads to a down shift of the valence band maximum, while the static band gap correction basically assumes that only the conduction band shifts upwards. Second, the more accurate treatment of the exchange-correlation energy in the hybrid approach leads to a smaller difference in the total energies. The dominating first effect enters Equation 8.1 via ϵ_{VBM}, while the second effect enters via ΔE_{def}. Comparing the

formation energies of the positive copper interstitial from the uncorrected GGA functional and from HSE06, we can split up the difference into the contribution of the valence band shift $\Delta\epsilon_{\mathrm{VBM}} = 0.51$ eV and the difference in the total energies of the defects containing the exchange correlation energy difference $\Delta E_{\mathrm{def}} = 0.32$ eV. For comparison, in Ref. [34] a valence band shift of $\Delta\epsilon_{\mathrm{VBM}} = 0.37$ eV has been determined when using LDA+U vs. LDA, but the formation energy of the copper interstitial has not been determined. The copper interstitial formation energy of 2.04 eV obtained from LDA in Ref. [8] suffers from an inappropriate static correction, which is not equivalent to Equation 8.1 and the corresponding expression in Ref. [34] and uses the position of the conduction band as the reference for donors. Therefore, it results in particularly large errors for donor defects in all charge states, which are approximately the band gap times the dominating charge state in magnitude. This explains the large difference in formation energies of the $\mathrm{In_{Cu}}$ anti-site defect in Ref. [8] obtained from LDA with the static band-gap correction as compared to Ref. [34] using an LDA+U corrected position of the valence band maximum, which amounts up to 2.53 eV for the charge state +2 and is of similar magnitude for other charge states.

The formation energies as well as the analysis of the eigenvalues show that the copper interstitial is a shallow donor, which does not create deep states in the band gap. The shallow donor behaviour and the rather small k-point grid make a relatively large band-filling correction necessary (Table 4, see Ref. [34] for a discussion of the band-filling correction). This is only necessary for the neutral charge state, for which the conduction band is populated.

Two possible migration mechanims of the copper interstitial were identified. A direct mechanism, where the octahedral copper interstitial (site A) migrates via the tetrahedral saddle point site (site B), and an indirect interstitialcy mechanism, where the octahedral interstitial knocks out a copper atom from a lattice site to the next octahedral site (see Figure 25). The hybrid functional gives a migration barrier of $\Delta H_{\mathrm{m}} = 0.22$ eV for the direct mechanism and a barrier of 0.34 eV for the indirect mechanism in case of the positive charge state (see Table 5). Similar to the case of copper vacancies in the previous chapter, the GGA functional gives slightly lower migration barriers. Note, however, that the reported GGA migration barriers are measured from a different ground state configuration (site C).

As photo-enhanced copper diffusion may occur, it is also interesting to compare the migration barriers for different charge states. We find that the migration barriers of the neutral charge state are only reduced by at most 0.04 eV in comparison to the positive charge state, which is unlikely to account for a significant enhancement of copper diffusion. However, illumination-enhanced copper diffusion may also originate from space-charge induced electric fields, when the illumination changes the magnitude of the field. The occurence of direct and indirect diffusion paths is in line with the finding of Cahen *et al.* [69], who stated that the better than expected stability of p-n junctions in $\mathrm{CuInSe_2}$ may be ex-

plained by more than one active diffusion mechanism. Activation energies of the two mechanisms are given by $E_a^{Cu_i^+} = \Delta H_f^{Cu_i^+} + \Delta H_m^{Cu_i^+}$. Using Equation 8.1 we can write

$$E_a^{Cu_i^+} = \Delta H_f^{Cu_i^+}(0,0) - \Delta\mu_{Cu} + \epsilon_F + \Delta H_m^{Cu_i^+}. \tag{8.2}$$

For typical copper-poor p-type high-grade photovoltaic material, the typical Fermi level is $\epsilon_F \approx 0.25$ eV and $\Delta\mu_{Cu} \approx -0.5$ eV [190], which gives an approximate activation energy of 1.14 eV for the direct and 1.26 eV for the indirect diffusion mechanism, both being close to the activation energy of 1.26 eV for the vacancy mechanism [38]. This shows that all three mechanisms similarly contribute to the copper self-diffusion in high-grade photovoltaic $CuInSe_2$, which poses a challenge to their experimental detection. The model proposed by Herberholz *et al.* [45] for long-range copper migration at interfaces requires atoms to leave their lattice sites close to the interface, thereby creating Frenkel pairs. The activation barrier for Frenkel pair formation for both a direct and an indirect mechanism have been calculated only with the GGA functional as these calculations are rather expensive due to 11 images used for this process in the CI- NEB calculation. Similarly to the diffusion processes, a Frenkel pair can be created via a direct mechanism, i.e. an atom is displaced from its lattice position to an interstitial site, or an indirect mechanism, i.e. it kicks out one of its nearest neighbour copper atoms. The activation barrier of the direct and indirect Frenkel pair formation process as obtained from the GGA-NEB calculation are 1.26 eV and 1.43 eV. This barrier has to be thermally overcome before copper interstitials may exhibit fast diffusion under the influence of an interface space charge or external electric field. For copper-poor samples, however, frequent recombination with vacancies is expected to inhibit fast copper interstitial diffusion to some degree.

8.4 SUMMARY

In conclusion, we have calculated the formation energies and migration barriers of the copper interstitial and Frenkel pairs from the screened exchange hybrid functional HSE06 and the GGA functional. Both, the rather low formation energies and the low migration barriers clearly show that not only the copper vacancy but also the interstitial is an important defect driving copper diffusion phenomena in $CuInSe_2$. A direct and an indirect migration mechanism with migration barriers as low as 0.22 and 0.34 eV make the copper interstitial susceptible to space-charge induced drift. In contrast, a significant dependence of the migration barriers on the charge state has been ruled out. The formation energies and energy barriers for the migration and Frenkel pair formation processes are consistent with a number of physical models that have been invoked for different phenomena related to copper diffusion in the literature.

9

ANTISITE TRAPS AND METASTABLE POINT DEFECTS IN $CuInSe_2$ AND $CuGaSe_2$

9.1 INTRODUCTION

This chapter focuses on the computational characterization of the cation antisite defects, the metastable DX centers, and $V_{Se} - V_{Cu}$ complexes. We will investigate their localization properties in detail and compare to photoluminescence masurements before turning to the full picture of the intrinsic point defect thermodynamics in chapter 10. The localization properties of antisites have not been formerly studied. In contrast, the intrinsic indium and gallium DX centers $(In, Ga)_{DX}$ [37] and the selenium vacancy V_{Se} [35] or selenium vacancy–copper vacancy complex $V_{Se} - V_{Cu}$ [36] were formerly found to exhibit metastable behaviour and localized states in the band gap. These theoretical results have been invoked [202–204] to explain the experimentally observed light and voltage-bias induced metastabilities. However, metastable point defects are not the only possible explanation. Copper migration in the space charge region [205, 206], deep acceptor levels in the CdS buffer layer [207], an electron-injection dependent barrier at the molybdenum back-contact of the device [48], or the presence of a p+-layer in conjunction with a shallow donor level at the buffer absorber interface [208] have all been put forward as possible explanations. Therefore, metastabilities in Cu(In,Ga)Se_2 based devices and their possible relation to the N2 and N1 levels remain puzzling and it is not clear whether a single explanation is sufficient to explain all of the observed phenomena [26, 48].

To recall some of the key experimental findings: A hole trap level in the range between 0.15-0.35 eV, often named N2, has been observed using admittance and deep-level transient spectroscopy (DLTS) and Hall measurements in $CuInSe_2$ [51–53], $CuGaSe_2$ [52, 53, 57, 60, 61] and Cu(In,Ga)Se_2 [51, 52, 56, 58, 59]). In addition, a deep defect around 0.8 eV independent of Ga content has been observed served using photocapacitance spectroscopy [54, 55]. A measured activation energy between 0.05-0.20 eV, has been attributed to an interface defect in Cu(In,Ga)Se_2 and was named N1 [58], although this denomination is ambiguously used and it is unclear whether the N1 response is associated to a defect at all [48]. Indeed, various metastable effects have been observed in Cu(In,Ga)Se_2 devices such as

persistent photoconductivity [42], the increase of the open-circuit voltage upon white-light soaking [43], an increase of the space-charge upon illumination [44] or reverse-biasing [45] accompanied with a decrease of the fill factor [46] as well as capacitance relaxation on long time scales after light-soaking [47].

In this chapter, it is shown that $Cu_{In,Ga}$ antisites create two hole trap levels in the gap of both $CuInSe_2$ and $CuGaSe_2$, while Ga_{Cu} antisites create an electron trap level in $CuGaSe_2$. The results are put in context to photoluminescence measurements of $CuGaSe_2$ thin-film solar cells carried out by Thomas Unold and colleagues at the Helmholtz center Berlin (HZB). The implications of the localized defect states and the thermodynamics of the defects for the performance of $Cu(In,Ga)Se_2$ solar cells are discussed.

9.2 METHOD

Again, the HSE06 functional [155, 156] was used with the setup as in Section 6.3. Ion positions were relaxed until forces were converged to below 0.05 and 0.1 eV/Å, for supercells of 64 and 216 atoms, respectively. Spin polarization was considered for unpaired electrons in 64 atoms cells and in case of Cu_{Ga}^{-1} in a cell of 216 atoms, but was found to have only a small effect on the total energy, e.g. 24 meV total energy difference compared to the non-spin-polarized result in the latter case. The computationally costly calculation of supercells of 216 atoms with a 2x2x2 k-point grid was necessary in order to observe unambiguously localized defect levels of $Cu_{In,Ga}^{0}$ and Ga_{Cu}^{0}. All reference phases presented in the stability diagram (Fig. 26) were calculated using the same functional. The point defect formation energies were calculated as a function of the chemical potentials of the constituents $\Delta\mu_i$ referenced to the elemental phases and the Fermi energy ϵ_F according to Equation 5.7. The potential alignment and image charge corrections have been carefully carried out as described in Ref. [169]. Numerical data of the formation enthalpies of bulk phases for construction of the stability diagram and calculated defect formation energies for all defects and charge states are reported in detail Chapter 10.

9.3 RESULTS AND DISCUSSION

Since high-efficiency $Cu(In,Ga)Se_2$ absorber material is prepared under a highly selenium-rich atmosphere, e.g. with a selenium to metal flux ratio of 5 [209], it is instructive to interpret the defect physics for this material under selenium-rich conditions on the Se-$Cu(In,Ga)Se_2$ phase boundary in the calculated stability diagram (point A in Fig. 26). In contrast to a previously calculated stability diagram [34], our calculations show a phase boundary between Cu_2Se and $CuInSe_2$, which is in line with the experimental phase diagram and the observation of Cu_2Se precipitates under certain processing conditions [63] (point B). For Cu-

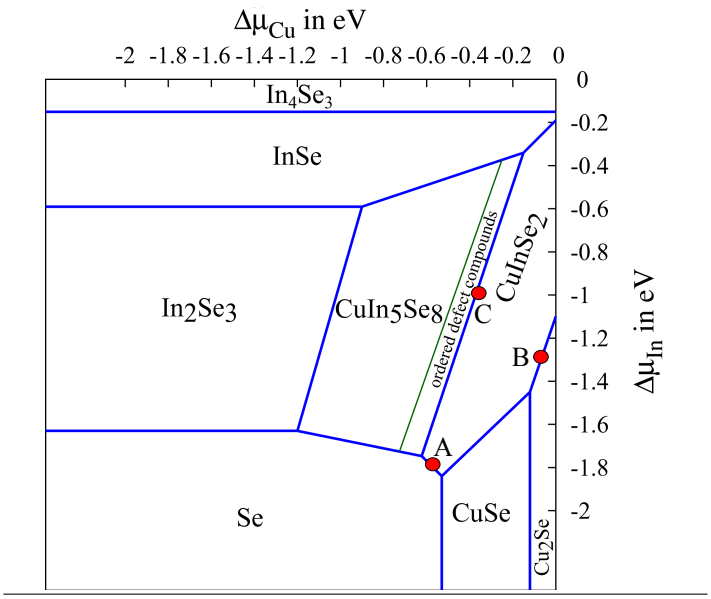

in eV	$CuInSe_2$		$CuGaSe_2$	
	$\Delta\mu_{Cu}$	$\Delta\mu_{In}$	$\Delta\mu_{Cu}$	$\Delta\mu_{Ga}$
A	-0.5	-1.87	-0.5	-2.17
B	-0.1	-1.3	-0.1	-1.5
C	-0.4	-1.0	-0.3	-1.0

Figure 26: Stability diagram for $CuInSe_2$. The defect formation energies in Figure 27 are discussed in terms of the chemical potential at points A, B and C. The stability range for $CuGaSe_2$ (not shown) has the same shape, but a somewhat larger extent due to its higher formation enthalpy ($CuInSe_2$: -2.37 eV, $CuGaSe_2$: -2.67 eV). Numerical values for point A, B and C are given in the table.

poor compositions, which yield the highest conversion efficiency, Cu(In,Ga)Se_2 is a highly compensated semiconductor. In this case, the charge neutrality condition and thus the Fermi-energy is essentially determined by the concentration of donors and acceptors with the lowest formation energies (see Figure 27). For the chemical potentials at points A, B and C the material turns out to be p-type, while it becomes n-type for maximal Cu- and In-rich conditions (not shown). Figure 27 shows the calculated defect formation energies for the various chemical potentials.

One of the most intriguing result is that $Cu_{In,Ga}$ antisites in both materials, $CuInSe_2$ and $CuGaSe_2$, can have equally low formation energies as copper vacancies and may thus also act as compensating defects. This finding is consistent with large concentrations of Cu_{In} in $CuInSe_2$ recently reported using wavelength dispersive x-ray diffraction even for copper-poor material [210]. However, when the chemical potentials are shifted towards metal-rich conditions (e.g. point C), it is seen that the defect formation energy of $Cu_{In,Ga}$ at the intrinsic Fermi level (vertical arrow) increases, while it does not change much for $(In, Ga)_{Cu}$ and V_{Cu}.

The analysis of the density of states of $Cu^0_{In,Ga}$ reveals an empty narrow defect band above the VBM for Cu_{In} in $CuInSe_2$ (at 0.27 eV) and Cu_{Ga} in $CuGaSe_2$ (at 0.36 eV, Figure 28 and 30), which represents two trapped holes (the hole density of the empty single-particle defect state of Cu_{Ga} as obtained from the calculation is displayed in Fig. 29). Similarly, it is observed that $Cu^{-1}_{In,Ga}$ traps single holes in the minority spin channel. Holes trapped by $Cu_{In,Ga}$ defects have Cu *d*-Se *p* character and can be classified as intermediate between deep and shallow based on their localization, which extends to the nearest copper neighbors. The defect shows negligible lattice relaxation below 0.01 Å. Furthermore, a localized electron trap level emerges for Ga^0_{Cu} at a single-particle energy of 1.17 eV above the VBM in $CuGaSe_2$ (see also Figure 28 and 29). The complexes $Ga_{Cu} - V^-_{Cu}$ and $(Ga_{Cu} - 2V_{Cu})^{-2}$ show defect levels at the same position. The defect level of In^0_{Cu} is found to be resonant within the CB for $CuInSe_2$ at 1.48 eV and for $CuGaSe_2$ at 1.46 eV in the gap approximately independent of gallium content. This finding is in contrast to Ref. [8], in which deep In_{Cu} levels were found in $CuInSe_2$, which were removed by pairing the defect with copper vacancies.

It should be noted that defect calculations on Cu(In,Ga)Se_2 have so far been performed with supercells smaller or equal to 64 atoms [8, 34, 37]. However, very disperse defect bands appear within the gap for the cells with 64 atoms for the antisite defects (see Figure 28), which indicates significant self-overlap of the defect wavefunctions. Within GGA, delocalization even occurs in large supercells up to 216 atoms, which explains why localized antisite hole traps have not been identified in the past. This proves that an accurate nonlocal treatment of exchange and correlation and large supercells are crucial for obtaining the correct localization behavior of the $Cu_{In,Ga}$ defect.

The fact that $Cu_{In,Ga}$ antisites localize holes, are abundant under typical preparation conditions (up to $10^{20}cm^{-3}$ at 850 K deposition temperature) and the cal-

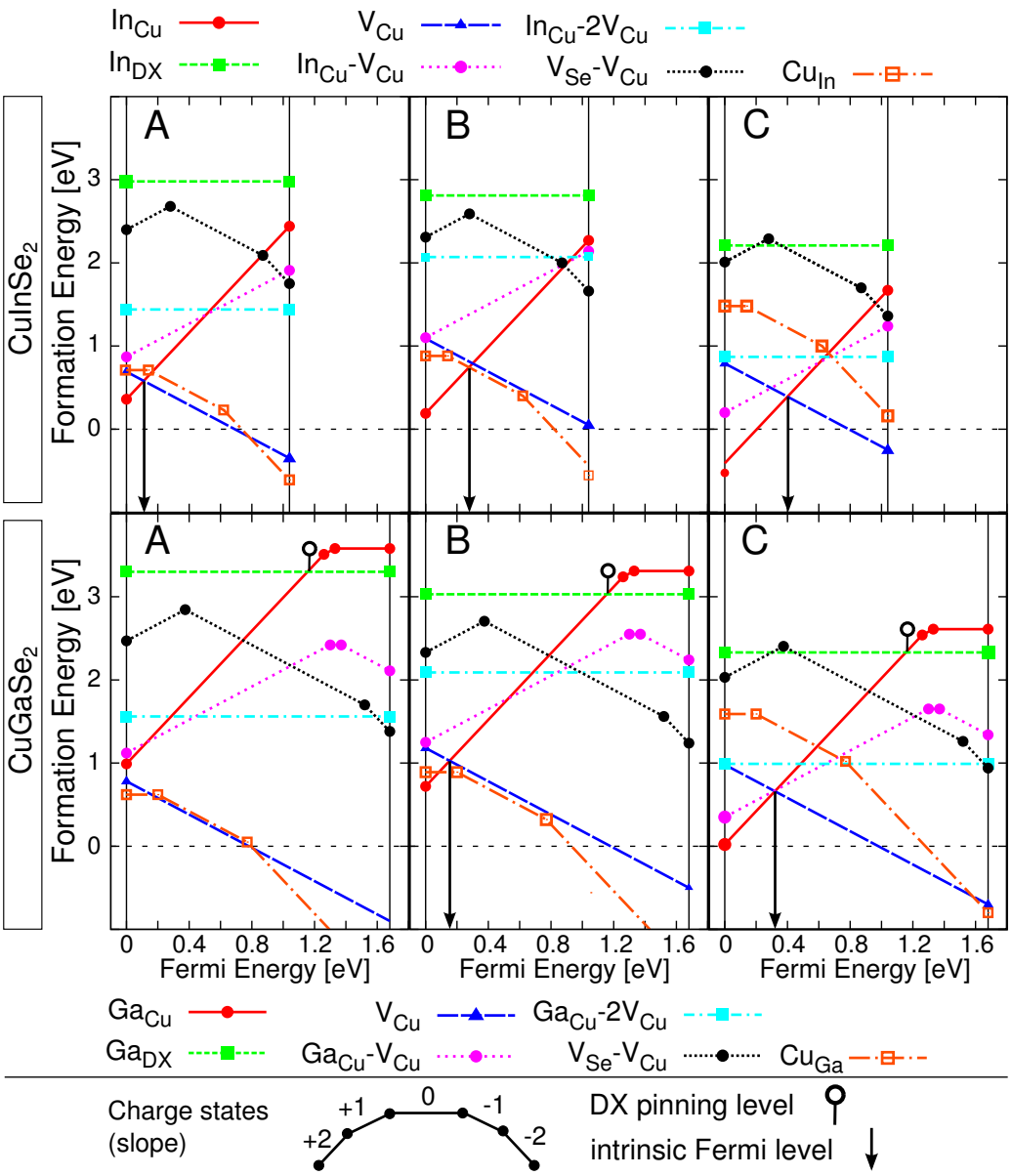

Figure 27: Defect formation energies, charge transition levels and the determined intrinsic Fermi levels in $CuInSe_2$ and $CuGaSe_2$ for chemical potentials corresponding to points A, B and C in Figure 26. Numerical data is given in Chapter 10.

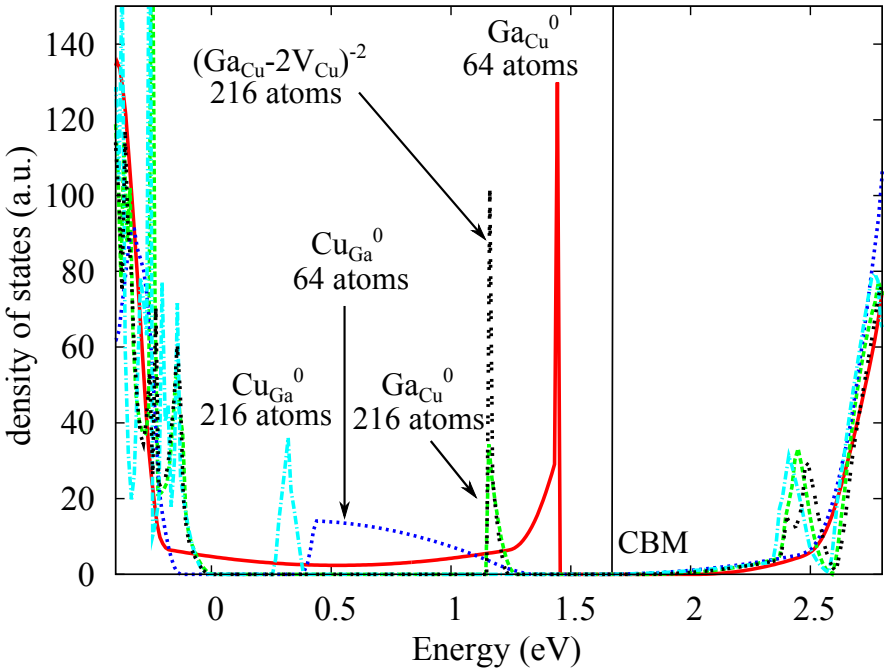

Figure 28: Aligned density of states of $CuGa^0$, Ga^0_{Cu} and $(Ga^0_{Cu} - 2V_{Cu})^{-2}$ in $CuGaSe_2$ in supercells of 64 and 216 atoms as obtained with the adapted HSE06 functional.

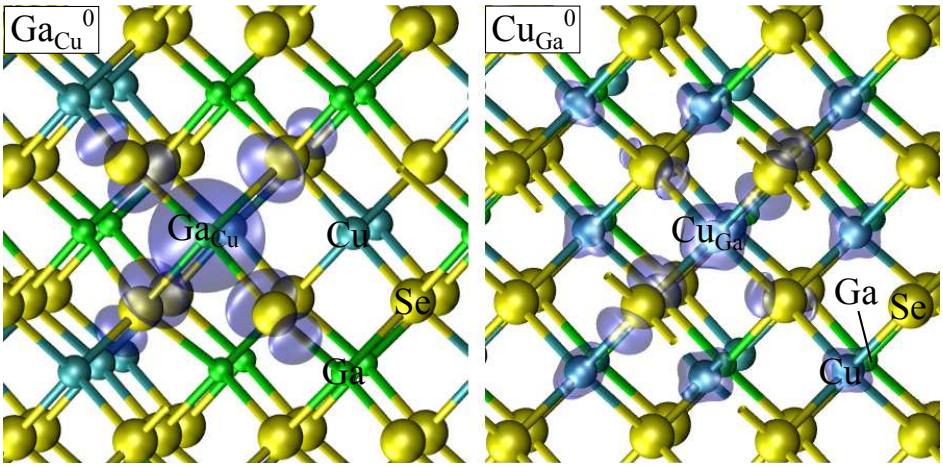

Figure 29: Defect level electron charge density of Ga^0_{Cu} (left: isosurface 0.03 eÅ^{-3}) and hole density of Cu^0_{Ga} (right: isosurface 0.02 eÅ^{-3}) as obtained in supercells with 216 atoms.

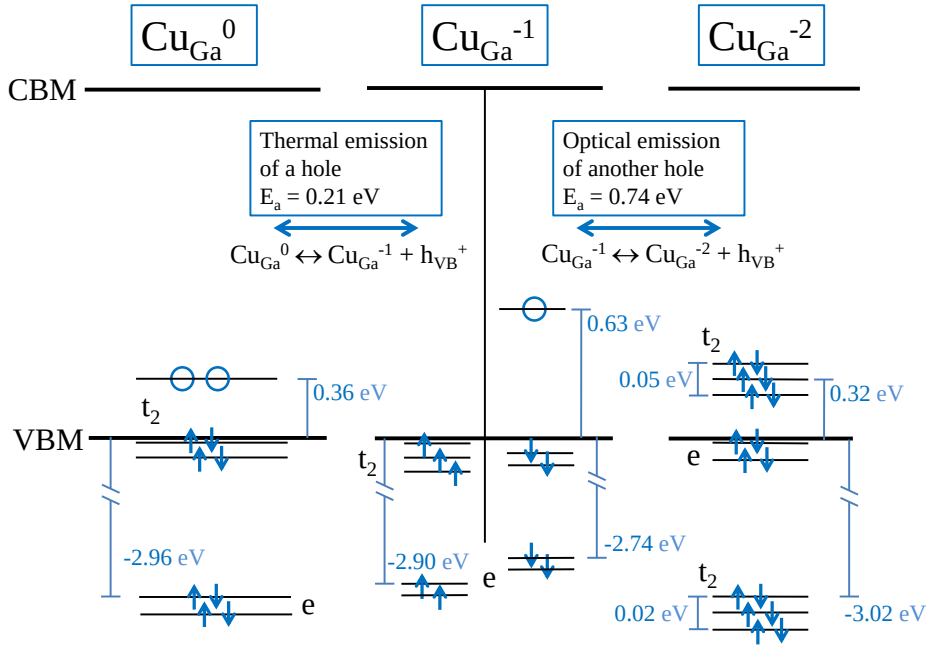

Figure 30: Schematic representation of the localized single-particle defect levels of Cu_{Ga} in $CuGaSe_2$ as obtained by analysis of the local density of states for supercells of 216 atoms and hole emission processes as discussed in the text.

culated thermal transition energy for the process $Cu^0_{Ga} \rightarrow Cu^-_{Ga} + h^+_{VB}$ (Figure 30) of 0.21 eV agrees with experimental measurements (e.g. 0.1-0.3 eV in Ref. [56] and 0.1-0.2 eV in Ref. [59]) make it safe to conclude that the N2 hole trap level is due to the $Cu_{In,Ga}$ antisite. The fact that this level does not occur in all samples can be explained with differing formation energies relevant for different preparation conditions (compare points A, B, C in Fig. 27). $Cu_{In,Ga}$ is also the source of a second, deeper hole trap level around 0.8 eV as observed in photocapacitance measurements [54], since the calculated transition energy for the emission process of a single trapped hole $Cu^{-1}_{Ga} \rightarrow Cu^{-2}_{Ga} + h^+_{VB}$ (0.74 eV, see Figure 30) agrees well. This leads to the experimentally verifiable conclusion that the N2 defect signal and the 0.8 eV photocapacitance signal should correlate. The analysis of the local density of states reveals significant changes of the defect wave function upon emission of the single trapped hole. Cu^{-2}_{Ga} shows three localized defect states with t_2 symmetry at 0.32 eV above the VBM and two states with e symmetry right at the VBM (see Figure 30). For Cu^{-1}_{Ga} and Cu^0_{Ga} the t_2 states trap the holes. Additional defect-localized states are located roughly 3 eV below the VBM (see Figure 4), with t_2 symmetry for Cu^{-2}_{Ga} but e symmetry in case of Cu^{-1}_{Ga} and Cu^0_{Ga}. $Cu_{In,Ga}$ antisites therefore show interesting defect physics arising from valence band-defect due to interactions of full cation d shells and anion p orbitals at the VBM, which can not be understood in terms of single orbital defect states in the gap and which leads to two different hole trap levels without considerable lattice relaxation.

The Ga^0_{Cu} antisite, in contrast, shows a clearly localized electron trap state at a single-particle energy of 1.17 eV above the VB in $CuGaSe_2$ and at 1.07 eV in $CuInSe_2$ very close to the CBM. Therefore this antisite defect becomes increasingly deep when Ga is alloyed into $CuInSe_2$, due to the rising CB. Since Ga_{Cu} is expected to occur in large quantities in $Cu(In,Ga)Se_2$ due to its low formation energy, it may limit solar cell efficiency when Ga alloying is used to increase the band-gap: When the CBM is raised above the position of the Ga_{Cu} defect level, recombination through this defect may limit the open-circuit voltage. Since the associates of Ga_{Cu} with copper vacancies display the same single-particle defect level as the non-complexed antisite, the complexes may cause the same limitations.

To confirm the theoretical results for the Ga_{Cu} defect, temperature-dependent photoluminescence measurements were carried out by Thomas Unold and coworkers at the Helmholtz Center Berlin (HZB). $CuGaSe_2$ thin-film solar cells were prepared by a three-stage coevaporation process, as used for high-efficiency chalcopyrite solar cell devices [211]. For the thin film absorber investigated, a ratio [Cu]/[Ga] = 0.87 was measured by x-ray fluorescence analysis and the accompanying solar cell showed a device efficiency of 7%. Photoluminescence (PL) was measured using a 670 nm diode-laser as excitation source and a thermoelectrically-cooled InGaAs array coupled to a 0.5 m spectrograph for luminescence detection, with the sample placed in a closed-cycle helium cryostat. A photoluminescence

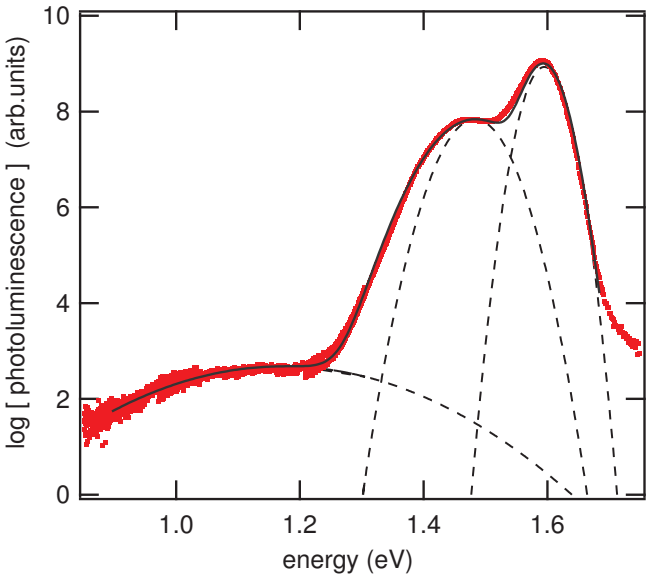

Figure 31: Photoluminescence spectrum at T=15 K measured for $CuGaSe_2$ thin films. The black solid line indicates a fit consisting of three gaussian-shaped transitions at E1 = 1.6 eV, E2 = 1.48 eV and E3 = 1.17 eV (dashed lines).

spectrum obtained at 15 K is shown in Figure 31. Three recombination peaks located at 1.6 eV, 1.48 eV and 1.17 eV can be clearly distinguished. The temperature and excitation intensity dependence of these peaks is consistent with an assignment of the peak at 1.6 eV to a tail-to-band transition, commonly observed in Cu-poor chalcopyrites [212], and the assignment of the peak at 1.48 eV to a free-to-bound transition. The latter transition energy is in excellent agreement with the calculated optical emission energy for the recombination process $Ga_{Cu}^{+} + h_{VB}^{+} \rightarrow Ga_{Cu}^{++}$ in $CuGaSe_2$ (1.44 eV). The temperature and excitation dependence of the third broad peak observed at about 1.17 eV is consistent with a donor-acceptor transition. A possible candidate for this transition is the process $Ga_{Cu}^{+} + Cu_{Ga}^{0} \rightarrow Ga_{Cu}^{2+} + Cu_{Ga}^{-1}$, i.e. the recombination of a single electron localized on a Ga_{Cu} antisite with a neighboring Cu_{Ga} hole trap by radiative tunneling, which has a calculated transition energy of 1.02 eV.

For metastabilities originating from intrinsic DX centers to occur, it is necessary that a DX pinning level exists within the gap [37]. From our results (Figure 27), we conclude that such a pinning level only occurs for Ga_{Cu} antisites in $CuGaSe_2$ ($E_{DX,pin}^{CuGaSe_2} = 1.16$ eV), but not for In_{Cu} antisites in $CuInSe_2$ ($E_{DX,pin}^{CuInSe_2} = 1.31$ eV, well above the CB and in contrast to Ref. [37]). Therefore, Fermi-level pinning and metastable effects due to intrinsic DX centers may occur in larger band gap $Cu(In,Ga)Se_2$ above approximately 30 per cent Ga content, but not for the ternary $CuInSe_2$.

In order to assess the energy differences responsible for the different DX pinning levels as compared to Ref. [37], it is instructive to compare the *uncorrected* formation energies of In_{Cu}^{2+} and In_{DX} in $CuInSe_2$ within our approach to the ones obtained from LDA applying only the static +U valence band correction of Ref. [37], which we were able to reproduce. The uncorrected formation energy of In_{Cu}^{2+} within our approach is 0.4 eV lower, while the one of In_{DX} is 0.32 eV higher. These energy differences, which result from the different treatments of exchange and correlation within HSE06 as compared to the LDA, mostly the improved description of the Cu *d* electrons, directly cause the change in the DX pinning levels.

We have also investigated $V_{Se} - V_{Cu}$ vacancy pairs, which have been held responsible for a variety of metastability phenomena in $Cu(In,Ga)Se_2$. With respect to this defect pair our hybrid functional calculations yield comparable charge transition levels (+/-) and metastable relaxation behavior as previously found in LDA-based calculations [36]. However, the formation energies of this defect complex are higher than 2 eV at the relevant Fermi levels at points A, B and C in Figure 27). Thus, under thermal equilibrium conditions, $V_{Se} - V_{Cu}$ associates should occur only in minor quantities (below 10^{12} cm^{-3} at 850 K deposition temperature as estimated from the defect formation energy). Thus, these defects can only cause metastable phenomena if the material is prepared with high $V_{Se} - V_{Cu}$ content due to far-from-equilibrium growth conditions.

9.4 SUMMARY

We have shown that $Cu_{In,Ga}$ defects create two localized hole trap levels in both $CuInSe_2$ and $CuGaSe_2$, which are related to the experimentally observed N2 level and a deep response in photocapacitance measurements. In contrast, Ga_{Cu} antisites exhibit an electron trap level in $CuGaSe_2$ which was confirmed within good accuracy by photoluminescence measurments. Ga_{Cu} antisites also display metastable DX behaviour, although at a higher Fermi level than previously found, while In_{Cu} antisites are very shallow and do not display metastable DX behaviour. We will return to and elaborate on many aspects of the defects investigated so far in the following chapter completing the full picture of the physics of intrinsic point defects in $CuInSe_2$ and $CuGaSe_2$ and giving verbose numerical data.

10

THE COMPLETE INTRINSIC POINT DEFECT PHYSICS OF $CuInSe_2$ AND $CuGaSe_2$

10.1 INTRODUCTION

The remaining intrinsic point defects are characterized in this chapter and the full picture of the intrinsic defect physics in $CuInSe_2$ and $CuGaSe_2$ is presented. Only a complete assessment of all relevant defects under realistic chemical potentials allows to accurately determine the relevant intrinsic defects, their concentrations, transition levels and the Fermi level in the material. The calculations are carried out in a self-contained manner with the same hybrid functional as before in order to obtain consistent results. Extensive reference to literature data is made and possible sources of deviations are pointed out in order to clarify the theoretical perspective on point defects in $Cu(In,Ga)Se_2$ to the reader.

The chapter is organized as follows: The methodology is explained in Section 10.2 and the resulting stability diagrams, defect formation energies, charge transition levels and single-particle defect states are introduced in Section 10.3. A detailed discussion of the properties of individual point defects follows in Section 10.4. The issue of whether metastable defects can be assigned to experimentally observed metastabilities is discussed in Section 10.5. In Section 10.6 we provide evidence that defect complexes with copper vacancies are not relevant in $Cu(In,Ga)Se_2$ and discuss opposite findings in the literature. A detailed comparison of our results with literature data based on local functionals and a discussion of the prevailing trends follows in in Section 10.7, while the predicted defect physics are compared to experimental findings in Section 10.8. Theory-based guidance to solar cell device optimization is given in Section 10.9. Finally, connections of the present results to other materials are pointed out in Section 10.10.

10.2 METHOD

The methodology is similar to the previous chapters and we used the basic setup as in Section 6.3. In some cases, when the localization behaviour of the defect in the smaller cell was not conclusive, super cells of 216 atoms were used. The im-

age charge correction was carried out as described in Ref. [169] using a fraction of 0.66 of the monopole correction and the potential alignment correction was applied by aligning the core-averaged electrostatic potentials far from the defect [171]. Spin-polarization was considered for charge states with unpaired spins, but was generally found not to affect the total energies significantly.

As in the previous chapters, the defect formation energies were calculated according to Equation 5.7, i.e.

$$\Delta H_f^q = \Delta E_{def} + \sum_i \Delta n_i \Delta \mu_i + q(\epsilon_{VBM} + E_F). \tag{10.1}$$

10.3 RESULTS

10.3.1 *Stability diagrams*

	ΔH_f HSE06	ΔH_f GGA	crystal structure	Exp. eV per f.u. (kJ/mol per f.u.)
$CuInSe_2$	-2.37	-1.79	Chalcopyrite	-2.12 (-204) [213]
$CuGaSe_2$	-2.67	-2.33	Chalcopyrite	-2.75 (-264) [214]
$CuIn_5Se_8$	-9.37	-7.04	ODC CH-type [8]	-
$CuGa_5Se_8$	-10.96	-7.97	ODC CH-type [8]	-
CuSe	-0.53	-0.27	Klockmannite [215]	-0.42 [213]
Cu_2Se	-0.68	-0.02	antifluorite [216]	-0.61 (-59) [213]
Cu_3Se_2*	-1.12	-0.58	umangite [217]	-1.03 (-99) [218]
InSe	-1.28	-1.05	layered structure [219]	-1.22 (-117) [213]
In_2Se_3	-3.25	-2.46	β-In_2Se_3 [220]	-3.57 (-343) [213]
In_4Se_3	-3.55	-3.09	layered structure [221]	-3.79 (-364) [222]
GaSe	-1.47	-1.14	layered structure [223]	-1.65 (-159) [213]
Ga_2Se_3	-3.62	-2.99	defect zincblende [224]	-4.56 (-439) [213]

Table 6: Calculated formation enthalpies of the phases displayed in the grand-canonical zero temperature phase diagram in eV per formula unit as compared to experimental values. The crystal structures used in the calculations are also given.

The stability diagrams shown in Figure 32 were calculated from the formation enthalpies of the compound obtained within the adapted HSE06 functional as displayed in Table 6. In order to assess the effect of phase stability and the chemical conditions on the defect physics in more detail than in Chapter 9, six combinations of chemical potentials are specified (points A to F in Figure 32) and will be used in order to discuss trends in the defect physics. The chemical

* The structure is metastable when HSE06 values are considered (in contrast to GGA values) and does not show up in the stability diagrams.

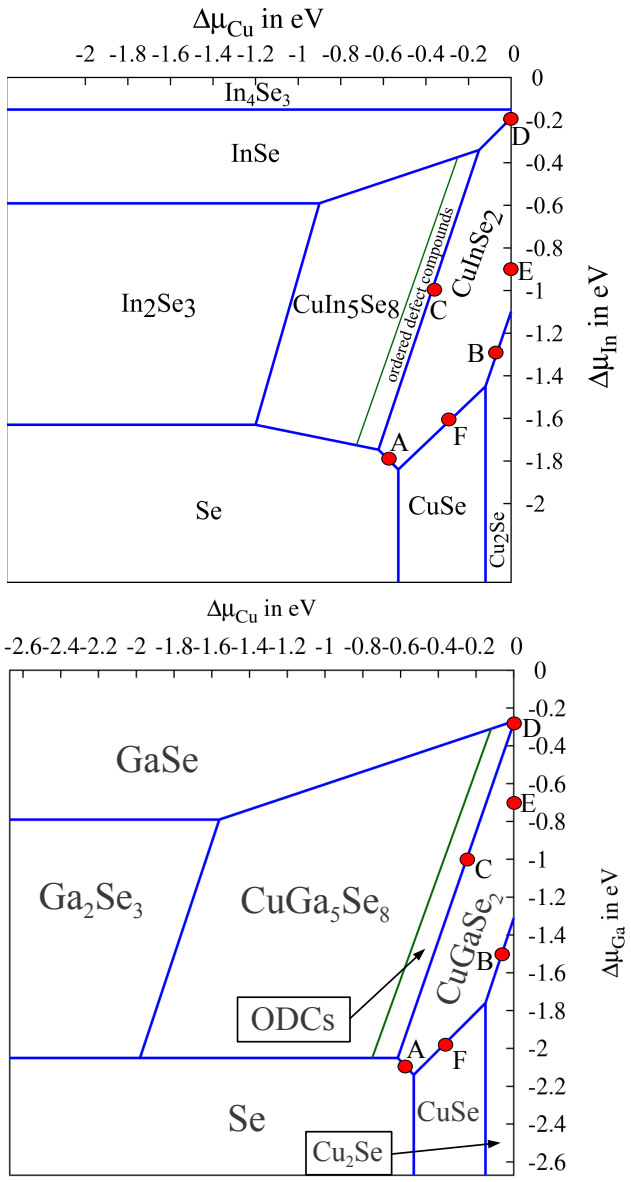

in eV	$CuInSe_2$		$CuGaSe_2$	
	$\Delta\mu_{Cu}$	$\Delta\mu_{In}$	$\Delta\mu_{Cu}$	$\Delta\mu_{Ga}$
A	-0.5	-1.87	-0.5	-2.17
B	-0.1	-1.3	-0.1	-1.5
C	-0.4	-1.0	-0.3	-1.0
D	0.0	-0.2	0.0	-0.3
E	0.0	-0.9	0.0	-0.7
F	-0.4	-2.0	-0.3	-1.6

Figure 32: Stability diagram for $CuInSe_2$ and $CuGaSe_2$ as derived from the data in Table 6. The defect formation energies in Figure 33 are discussed in terms of the chemical potentials at the given points A to F.

potentials of the constituent elements as referenced to their elemental phase are related by the condition that their weighted sum must add up to the formation enthalpy of the compound, e.g. for $CuInSe_2$:

$$\Delta\mu_{Cu} + \Delta\mu_{In} + 2\Delta\mu_{Se} = \Delta H_f^{CuInSe_2}. \tag{10.2}$$

We choose to fix $\Delta\mu_{Cu}$ and $\Delta\mu_{In}$, $\Delta\mu_{Se}$ is then given by the above condition. In the following, a little more rationale is provided of which conditions of the chemical potentials, i.e. which points in the stability diagrams, are suitable to interpret the defect physics in solar cell absorber material.

Since high-efficiency $Cu(In,Ga)Se_2$ absorbers are prepared under a highly selenium-rich atmosphere, e.g. with a selenium to metal flux ratio of 5:1 [209], it is instructive to interpret the defect physics for this material under selenium-rich conditions on the Se-$Cu(In,Ga)Se_2$ phase boundary in the calculated stability diagram (point A in Fig. 32). In addition, this point also agrees very well with a measured value of the copper-chemical potential of -0.45 to -0.5 eV in high-quality $Cu(In,Ga)Se_2$ [190]. The reader is also referred to the discussion on suitable chemical potential conditions in Ref. [225], which supports that the true preparation conditions for high-quality absorber material can be expected to be close to point A. Under copper-rich conditions, when Cu_2Se precipitates are likely to occur [63], the defect physics should rather be discussed at the Cu_2Se phase boundary, i.e. at point B in the stability diagrams. For most chemical potentials in $CuInSe_2$ and for any valid combination of chemical potentials in $CuGaSe_2$ the material turns out to be p-type. $CuInSe_2$ can also be prepared n-type for maximal Cu- and In-rich conditions (at point D in Figure 33) in agreement with the findings of Persson *et al.* [34] and experimental observations of n-type $CuInSe_2$ crystals [226].

It is of general interest to compare the formation enthalpies of the compounds within our approach to the experimental ones and the ones obtained by GGA (Table6) in order to assess the applicability of the HSE06 functional for thermochemistry [227]. GGA turns out to generally underestimate the formation enthalpies, while HSE06 gives values, which are generally in much better agreement with experiment. In contrast to GGA, HSE06 somewhat overestimates the formation enthalpies of the copper containing compounds, while it still underestimates the ones which do not contain copper. A particular pathologic case seems to be Cu_2Se, which has an almost vanishing formation enthalpy within GGA, while HSE06 dramatically improves the agreement with the experimental value. This explains why formerly calculated phase stability diagrams using local functionals display Cu_3Se_2 as a neighbouring phase to $CuInSe_2$ [34, 204], but not Cu_2Se, which disagrees with the experimentally determined phase diagram and observations of Cu_2Se precipitates in $CuInSe_2$ [63]. The largely improved formation enthalpies of the copper containing compounds as compared to the experimental values are likely to originate from the improved description of the localized

copper *d* electrons within HSE06 and suggest that HSE06 is particularly suitable to study copper containing compounds and other compounds containing closed *d* shell transition metal ions.

10.3.2 *Point defect formation energies*

The calculated formation energies of the intrinsic point defects in $CuInSe_2$ and $CuGaSe_2$ are plotted as a function of the Fermi energy for the six representative combinations of chemical potentials A to F in Figure 33. The underlying numerical data, i.e. the formation energies for $E_F = 0$ and $\Delta\mu_{Cu} = 0, \Delta\mu_{In} = 0$ and $\Delta\mu_{Se} = 0$ for all relevant charge states q are given in Tables 7 and 8. Note that this choice does not correspond to a physically meaningful situation, but it is a convenient choice for citing the data and in order to compare to literature values. The physical interpretation of the defect formation energies, however, requires the choice of chemical potentials within the stability region of $CuInSe_2$ and $CuGaSe_2$ as in Figure 32 and consistent determination of the Fermi level E_F. The intrinsic Fermi energy for the different preparation conditions was qualitatively determined by considering the charge neutrality condition. For accurate quantitative predictions of the intrinsic Fermi energy, it is necessary to numerically solve the charge neutrality condition. The present procedure, however, is accurate enough for our purpose.

One of the most important issues to consider is to identify the defects, which are contained in high quantities in the material such that they influence its properties. This depends on the chosen chemical potentials, which are connected to the preparation conditions. From Figure 33 it is seen that the defects which have low formation energies below approximately 1 eV in $CuInSe_2$ are the antisite In_{Cu}, the copper vacancy V_{Cu}, the Cu_{In} antisite and the copper interstitial Cu_i. The situtation is analogous in $CuGaSe_2$ with the defects Ga_{Cu}, V_{Cu}, Cu_{Ga} and Cu_i. Doping and self-compensation in $CuInSe_2$ and $CuGaSe_2$ have been understood to be due to In_{Cu} and V_{Cu} in $CuInSe_2$ and Ga_{Cu} and V_{Cu} in $CuGaSe_2$ in the past [34]. However, our results show that Cu_{In}, Cu_{Ga} and Cu_i may substantially contribute to doping and compensation under certain preparation conditions, such as e.g. at points B and F for $CuInSe_2$ and points B,C,E and F for $CuGaSe_2$. This implies that the properties of these four intrinsic defects may significantly influence the properties of the material.

Other defects than the ones mentioned above should only be contained in small quantities based on the obtained formation energies in an equilibrium picture, such that they should not significantly alter the properties of $CuInSe_2$ and $CuGaSe_2$. However, significant amounts of these defects could arise if the material is prepared far from quilibrium and they could contribute to mass transport at high temperatures. Furthermore, they may exhibit interesting properties from

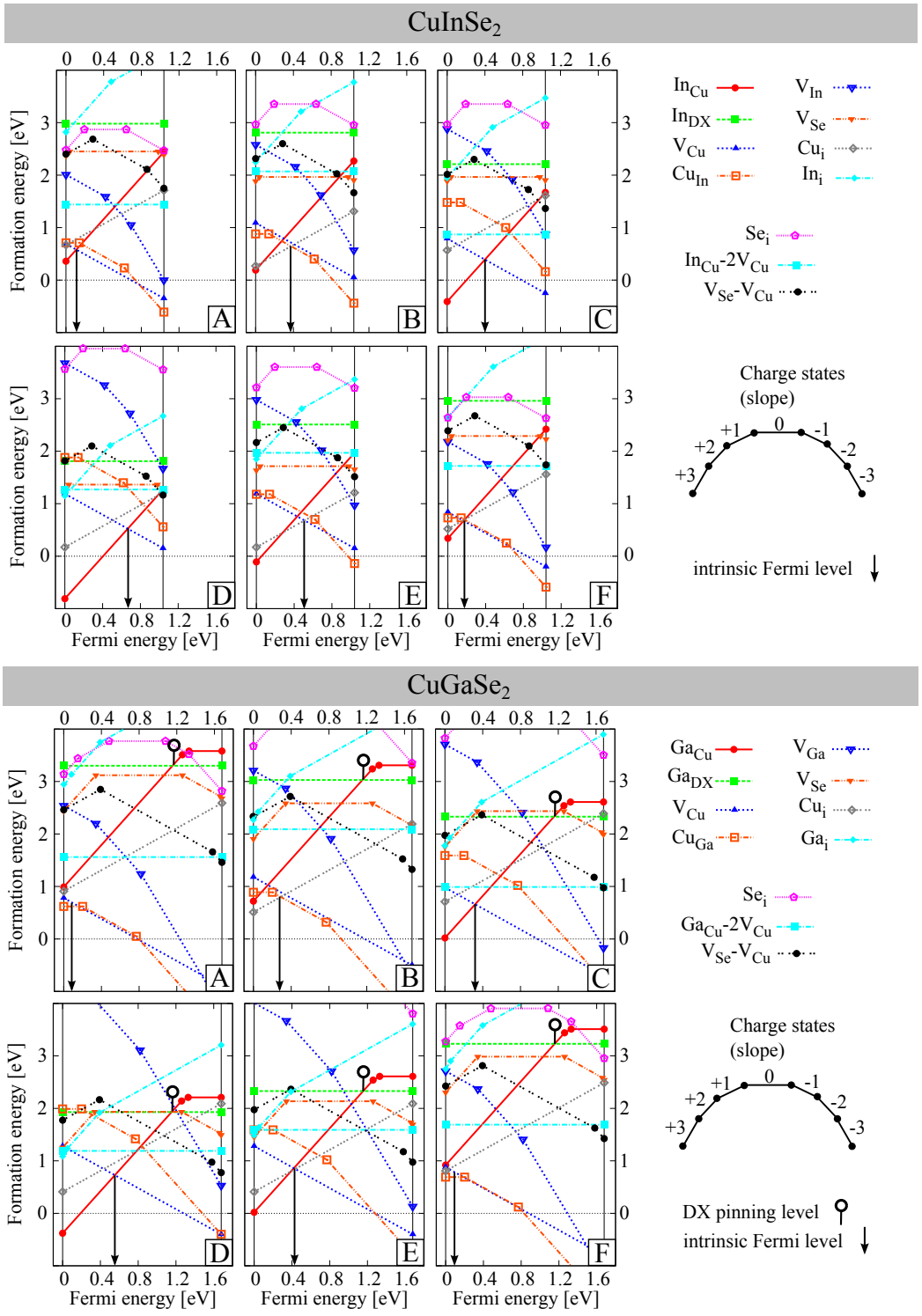

Figure 33: Defect formation energies in $CuInSe_2$ and $CuGaSe_2$ for various preparation conditions (chemical potentials) as displayed in the stability diagrams (Figure 32).

a theoretical point of view. Therefore, we analyze their properties in detail along with the already mentioned defects in Section 10.4.

$CuInSe_2$	+3	+2	+1	0	-1	-2	-3
In_{Cu}	-	-1.01	0.24	1.86	-	-	-
In_{Cu} Ref. [8]	-	1.85	2.55	3.34	-	-	-
In_{Cu} Ref. [34]	-	-0.73	0.01	0.9	-	-	-
Ga_{Cu}	-	-1.03	0.22	1.30	-	-	-
Cu_{In}		-	-	2.08	2.22	2.84	-
Cu_{In} Ref. [8]	-	-	-	1.54	1.83	2.41	-
V_{Cu}	-	-	-	-	1.19	-	-
V_{Cu} Ref. [8]	-	-	-	0.60	0.63	-	-
V_{Cu} Ref. [34]	-	-	-	0.83	0.9	-	-
V_{In}	-	-	-	3.85	3.88	4.3	4.99
V_{In} Ref. [8]	-	-	-	3.04	3.21	3.62	4.29
In_{DX}	-	-	-	1.61	-	-	-
Ga_{DX}	-	-	-	1.30	-	-	-
$In_{Cu} - V_{Cu}$	-	-	0.00	1.34	2.10	-	-
$In_{Cu} - 2V_{Cu}$	-	-	-	1.07	-	-	-
$In_{Cu} - 2V_{Cu}$ Ref. [8]	-	-	-	0.33	-	-	-
$In_{Cu} - 2V_{Cu}$ Ref. [32]	-	-	-	0.21	-	-	-
V_{Se}	-	2.37	-	2.45	3.43	4.78	5.66
V_{Se} Ref. [35]†	-	2.39	-	2.43	-	4.39	-
$V_{Se} - V_{Cu}$	-	-	2.9	-	3.47	4.33	5.66
$V_{Se} - V_{Cu}$ Ref. [36]*	-	-	2.63	-	3.01	3.99	5.24
Cu_i‡	-	-	0.17	1.68	-	-	-
Cu_i Ref. [8]	-	-	2.04	2.88	-	-	-
In_i	0.60§	0.95§	1.43‡	2.84‡	-	-	-
Se_i	-	2.48	2.67	2.87	3.51	4.87	-

Table 7: Defect formation energies in $CuInSe_2$

* as estimated from Figure 2 in Ref. [36] (1.8 eV) and translated to $\Delta\mu_{Se} = 0$
† as estimated from Figure 4 in Ref. [35] (1.6 eV) and translated to $\Delta\mu_{Se} = 0$
‡ tetrahedral site (with respect to neighbouring cations)
§ trigonal planar site (with respect to neighbouring cations), two nearest copper neighbours

$CuGaSe_2$	+3	+2	+1	0	-1	-2	-3
Ga_{Cu}	-	-0.68	0.58	1.91	-	-	-
Ga_{Cu} Ref. [31]	-	2.04	3.03	4.22	-	-	-
Ga_{Cu} Ref. [34]	-	0.05	1.07	2.43	-	-	-
In_{Cu}	-	-0.61	-	2.68	-	-	-
Cu_{Ga}		-	-	2.29	2.49	3.26	-
Cu_{Ga} Ref. [31]	-	-	-	1.41	1.70	2.33	-
V_{Cu}	-	-	-	-	1.28	-	-
V_{Cu} Ref. [31]	-	-	-	0.60	0.67	-	-
V_{Cu} Ref. [34]	-	-	-	0.83	0.71	-	-
V_{Ga}	-	-	-	4.7	4.71	5.05	5.87
V_{Ga} Ref. [31]	-	-	-	2.83	3.02	3.40	4.06
Ga_{DX}	-	-	-	1.63	-	-	-
In_{DX}	-	-	-	2.19	-	-	-
$Ga_{Cu} - V_{Cu}$	-	-	-0.05	1.41	3.14	-	-
$Ga_{Cu} - 2V_{Cu}$	-	-	-	0.89	-	-	-
$Ga_{Cu} - 2V_{Cu}$ Ref. [31]	-	-	-	0.7	-	-	-
V_{Se}	-	2.44	-	3.12	4.38	6.04	-
V_{Se} Ref. [36]*	-	2.86	-	3.14	4.01	5.12	-
$V_{Se} - V_{Cu}$	-	-	2.96	-	3.74	5.32	7.16
$V_{Se} - V_{Cu}$ Ref. [36]*	-	-	2.81	-	3.45	4.51	5.81
Cu_i†	-	-	0.41	2.26	-	-	-
Cu_i Ref. [31]	-	-	1.91	3.38	-	-	-
Ga_i	0.77‡	0.82‡	1.21†	3.01†	-	-	-
Se_i	-	3.14	3.29	3.77	4.85	6.18	-

Table 8: Defect formation energies in $CuGaSe_2$

10.3.3 *Charge transition levels*

The charge transition levels are visualized in the formation energy plots in Figure 33. In addition, the numerical values are also given in Table 9 as compared to literature values. Charge transition levels correspond to themal transitions, while optical transitions exclude the relaxation energies of the defects. However, if the relaxation energy can be neglected they should be approximately the same. Calculated optical transition energies are not reported within the present work.

* as estimated from Figure 2 in Ref. [36] and translated to $\Delta\mu_{Se} = 0$
† tetrahedral site (with respect to neighbouring cations)
‡ trigonal planar site (with respect to neighbouring cations), two nearest copper neighbours

$CuInSe_2$	ϵ (q_i/q_j)
V_{Cu}	shallow
In_{Cu}	shallow
In_{Cu} Refs. [8],[34]	0.7, 0.74 (+2/+1), 0.79, 0.89 (+1/0)
Ga_{Cu}	shallow
Cu_{In}	0.11 (0/-1), 0.67 (-1/-2)
Cu_{In} Ref. [8]	0.29 (0/-1), 0.61 (-1/-2)
$In_{DX,pin}$	none
$In_{DX,pin}$ Ref. [37]	0.92 (+2/0)
$Ga_{DX,pin}$	1.17 (+2/0)
V_{Se}	0.08 (+2/0), 0.98 (0/-1)
V_{Se} Ref. [36]	0.05 (+2/0), 0.85 (0/-1), 1.14 (-1/-2)
$V_{Se} - V_{Cu}$	0.29 (+1/-1), 0.86 (-1/-2)
$V_{Se} - V_{Cu}$ Ref. [36]	0.19 (+1/-1), 0.98 (-1/-2), 1.25 (-2/-3)
V_{In}	0.03 (0/-1), 0.42 (-1/-2), 0.69 (-2/-3)
V_{In} Ref. [31]	0.19 (0/-1) ,0.38 (-1/-2), 0.66 (-2/-3)
In_i	0.34 (+3/+2), 0.48 (+2/+1)
Se_i	0.19 (+2/+1), 0.20 (+1/0), 0.64 (0/-1)
$CuGaSe_2$	ϵ (q_i/q_j)
V_{Cu}	shallow
In_{Cu}	shallow
Ga_{Cu}	1.26 (+2/+1), 1.33 (+1/0)
Ga_{Cu} Refs. [31],[34]	0.99, 1.02 (+2/+1), 1.19, 1.36 (+1/0)
Cu_{Ga}	0.21 (0/-1), 0.74 (-1/-2)
Cu_{Ga} Ref. [31]	0.29 (0/-1), 0.58 (-1/-2)
$Ga_{DX,pin}$	1.17 (+2/0)
$Ga_{DX,pin}$ Ref. [37]	0.84 (+2/0)
$In_{DX,pin}$	1.40 (+2/0)
V_{Se}	0.34 (+2/0), 1.26 (0/-1), 1.66 (-1/-2)
V_{Se} Ref. [36]	0.14 (+2/0), 0.87 (0/-1), 1.14 (-1/-2)
$V_{Se} - V_{Cu}$	0.39 (+1/-1), 1.58 (-1/-2)
$V_{Se} - V_{Cu}$ Ref. [36]	0.32 (+1/-1), 1.06 (-1/-2), 1.30 (-2/-3)
V_{Ga}	0.01 (0/-1), 0.34 (-1/-2), 0.82 (-2/-3)
V_{Ga} Ref. [31]	0.17 (0/-1), 0.41 (-1/-2), 0.67 (-2/-3)
Ga_i	0.05 (+3/+2), 0.39 (+2/+1)
Se_i	0.15 (+2/+1), 0.48 (+1/0), 1.08 (0/-1), 1.32 (-1/-2)

Table 9: Charge transition levels of $CuInSe_2$ and $CuGaSe_2$ as compared to the literature in eV. Classification as "shallow" means that the charge transition levels lies closer to the band edge than the accuracy of the calculation ($\approx$<50 meV).

10.3.4 *Defect states*

All localized single-particle defect states of the investigated defects within the gap of $CuInSe_2$ and $CuGaSe_2$ are reported in Table 10. Even though they are not directly comparable to experiment, single-particle defect states provide useful additional information on the character of the defect, its degree of localization, and another possibility to check for consistency. It is an important advantage of the HSE06 functional employed here, that defect states can be observed over the entire band gap for all defects without shifts being necessary since the band gap is correctly described. Recombination via defects is only expected when a localized defect state occurs within the gap. It is interesting to note that most defect states align very well on an absolute scale. This is easy to see from Table 10, since the valence band offset between $CuInSe_2$ and $CuGaSe_2$ can be neglected.

$CuInSe_2$	ϵ (q)	**$CuGaSe_2$**	ϵ (q)
Cu_{In}	0.30[a] (0)	Cu_{Ga}	0.35[a] (0)
	-		0.63[b] (-1)
	0.25[a,c] (-2)		0.30[a,c] (-2)
In_{Cu}	shallow, 1.50[a] (0)	In_{Cu}	1.45[a] (0)
Ga_{Cu}	shallow, 1.05[a] (0)	Ga_{Cu}	1.17[a] (0)
Ga_{DX}	0.2 (0)	Ga_{DX}	0.5 (0)
-	-	Ga_{DX} Ref. [37]	0.5 (0)
In_{DX}	0.6 (0)	In_{DX}	0.55 (0)
In_{DX} Ref. [37]	0.6 (0)	-	-
$In_{Cu} - 2V_{Cu}$	no gap states	$Ga_{Cu} - 2V_{Cu}$	1.25[a] (-2)
V_{Se}	0.4-0.6 (-2)	V_{Se}	0.5-0.7 (-2)
$V_{Se} - V_{Cu}$	0.4-0.5 (-3)	$V_{Se} - V_{Cu}$	0.5-0.7 (-3)
V_{In}	0.3[a,c] (-3)	V_{Ga}	0.3[a,c] (-3)
		V_{Ga}	1.30[a,b] (-2)
		V_{Ga}	0.9[a] (-1)
In_i	0.3 (+1)	Ga_i	0.3 (+1)
Se_i	0.7 (-2)	Se_i	1.00 (-2)
	0.05 (0)		0.15 (0)

a results from supercells of 216 atoms
b empty state in the minority spin channel
c three closely-spaced defect states are present, centered at the given energy, see also Chapter 9 and Figure 30

Table 10: Single-particle defect states within the gap of $CuInSe_2$ and $CuGaSe_2$ for the given charge states q in eV. The single-particle energies obtained in this work are given to within 0.05 eV accuracy due to dispersion unless stated otherwise. Note that single-particle energies are not directly comparable to experimental data.

10.4 DISCUSSION OF INDIVIDUAL POINT DEFECTS

10.4.1 *Cation antisites*

The cation antisites In_{Cu} and Ga_{Cu} are the donors, which contribute most strongly to compensation in the material under most conditions (Figure 33). While In_{Cu} is very shallow in $CuInSe_2$, Ga_{Cu} is deep in $CuGaSe_2$ with a single-particle defect state at 1.17 eV and charge transition levels at 1.26 eV (+2/+1) and 1.33 eV (+1/0). Charging the Ga_{Cu} defect with two electrons into the neutral charge state Ga^0_{Cu} induces a relaxation of the Ga-Se bonds from 2.45 to 2.71 Å, while such a relaxation does not occur for In^0_{Cu} consistent with the fact that the excess charge does not localize on the defect. Ga_{Cu} may transform into the metastable Ga_{DX} configuration as discussed in Section 10.5, when the Fermi level is raised above the DX pinning level of 1.17 eV. Earlier work found transition levels for In_{Cu} clearly located within the gap [8]. These were assigned to defect states, which were believed to be removed from the gap by formation of a complex with vacancies. Since our results show that In_{Cu} is already shallow by itself and the binding energies of complexes with vacancies in $CuInSe_2$ as discussed in Section 10.6 are small, such interpretations should be abandoned.

In order to draw conclusions about antisites in the alloy $Cu(In,Ga)Se_2$, it is also instructive to examine In_{Cu} in a $CuGaSe_2$ host and vice versa Ga_{Cu} in a $CuInSe_2$ host. The respective results included in Tables 7, 8, 9 and 10. From the single-particle defect states as well as from the transition levels, it is seen that the defect state of In_{Cu} aligns on an absolute scale in both $CuInSe_2$ and $CuGaSe_2$ and the same holds true for Ga_{Cu}. The defect state of In_{Cu} is however located approximately 0.3 to 0.4 eV higher than the one of Ga_{Cu}. Therefore, the In_{Cu} defect state is located within the conduction band in $Cu(In,Ga)Se_2$ alloys unless for those with very high Ga content and is therefore not of any concern for device performance. However, the Ga_{Cu} charge transition levels are located at 1.26 and 1.33 eV (Table 9). This defect represents an important minority carrier trap when the defect state is located within the gap. It may thus lead to significant recombination if the Gallium content is raised to approx. 50 per cent or above.

Good agreement of the calculated optical transition energies of Ga_{Cu} antisites with low-temperature photoluminescence masurements in $CuGaSe_2$ thin-films was shown in Chapter 9. As was also shown, the Cu_{In} and Cu_{Ga} antisites are hole traps located at energies of about 0.2 eV above the valence band. Their low formation energies under reasonable growth conditions for thin-film solar cell absorber growth (e.g. at points A and B in Figure 33) and their calculated electronic properties suggest that they are the origin of the N2 signal.

All cation antisites may occur in large quantities in the material as their formation energies can be fairly low (see Figure 33). Note however, that In_{Cu} and Ga_{Cu} antisites are always abundant, while the preparation conditions determine whether Cu_{In} and Cu_{Ga} are contained in significant amounts.

10.4.2 *Cation vacancies*

The copper vacancy is characterized as a very shallow acceptor (<50 meV), as already done by many other studies before [8, 34]. The defect occurs abundantly under all preparation conditions and signifcantly contributes to self-doping and compensation.

The indium and gallium vacancies exhibit interesting properties from a theoretical point of view. Based on the charge transition levels as well as the single-particle defect states and the analysis of the charge densities we observe that V_{In} in $CuInSe_2$ as well as V_{Ga} represent deep hole traps. Localization of three closely spaced defect states in the fully occupied -3 charge state is achieved even at the GGA level with supercells of 512 atoms or larger. These states perfectly resemble the ones found for the Cu_{In} and Cu_{Ga} defects in their -2 charge state. However, in order to observe localization of holes in the -2 and -1 charge state, the screened-exchange hybrid functional turns out to be necessary. A single hole trapped on the defect in the -2 charge state is observed as an empty localized defect state in the minority spin channel (at 1.3 eV in case of V_{Ga}) and the defect carries a magnetic moment of one Bohr magneton. Again, the defect states are similar in character to the antisite defects Cu_{In} and Cu_{Ga}, which also constitute hole traps.

It has to be emphasized that V_{In} and V_{Ga} have fairly large formation energies under all possible preparation conditions (Figure 33), such that they are expected to occur only in minor concentrations and will most likely not be detectable in experiments. Note that the (-1/-2) and (-2/-3) transition levels for V_{In} and V_{Ga} found in Ref. [8] are not very different from our results (Table 9). However, the localization of holes on these defects needed to be shown in order to assign a physically meaningful hole trap level to these defects.

10.4.3 *Interstitials*

Copper interstitial defects in $CuInSe_2$ have been studied in Chapter 8. They were found to be shallow donors with low formation energies and migration barriers and are therefore important for fast copper ion migration. Here we additionally report data on the copper interstitial in $CuGaSe_2$, which exhibits very similar properties. In both materials the formation energies of the copper interstitial can be so low that copper interstitials contribute to self-compensation during deposition (see e.g. Figure 33, point B). However, when the temperature is lowered to room temperature most of the copper interstitials can be expected to recombine with copper vacancies because of their fast diffusion.

Both the indium and gallium interstitials in $CuInSe_2$ and $CuGaSe_2$ have rather high formation energies (between approximately 2 and 3 eV depending on the chemical potentials and the Fermi level, see Figure 33) and therefore should not

occur in significant quantities in thermodynamic equilibrium. At high temperatures during deposition they may however contribute to mass transport. Indium and gallium interstitials occupy the trigonal planar site with two nearest copper neighbours in its +3 and +2 charge state, while for the +1 charge state the tetrahedral site is more favourable. Furthermore, they exhibit a defect level around 0.3 eV above the valence band maximum in its +1 charge state. The defect state corresponds to the gallium 4*s* and indium 5*s* states and forms a lone pair. The fact that the interstitial may occur in various charge states may lead to complicated and possibly light-enhanced diffusion processes. Recent anomalous X-ray and neutron diffraction data suggests large concentrations of gallium interstitials in $CuGaSe_2$ [228]. Our data is not consistent with this finding, because of the high formation energies of the gallium interstitial under all possible preparation conditions (see Figure 33). Our data rather suggests that similar to $CuInSe_2$, V_{Cu} and Ga_{Cu} are the main compensating donors in $CuGaSe_2$, which can be expected to occur on the order of percentages. Contrasting findings of high formation enthalpies for Ga_{Cu} antisites (see Table 8) can be attributed to spurious correction schemes (Ref. [8]) or fundamental differences in the employed functionals (Ref. [34]) (see also Section 10.7).

The selenium interstitial exhibits relatively high formation energies and is therefore unlikely to affect the property of the material even at deposition conditions (Figure 33). Selenium interstitials are amphoteric defects located on the octahedral interstitial site (with respect to neighbouring anions). Two different single-particle defect states are observed within the gap, one very close to the valence band edge, and another one higher in the gap at 0.7 eV in $CuInSe_2$ and at 1.0 eV in $CuGaSe_2$. Selenium interstial diffusion is expected to be significant only at elevated temperatures.

10.4.4 *Metastable point defects*

The $V_{Se} - V_{Cu}$ complex and In and Ga DX centers have been studied in chapter 9. It was shown that $V_{Se} - V_{Cu}$ does indeed exhibit metastable properties. Indium DX centers do not exhibit a pinning level in the gap and the pinning level of gallium DX centers is located at 1.17 eV. Here, we additionally report the properties of the isolated V_{Se}.

The selenium vacancy shows metastable properties in the sense that it exhibits a charge transition level +2/0, which is associated with a large lattice relaxation of the indium and gallium atoms, respectively. These results are in line with findings by Lany *et al.* [35], with a charge transition level at 0.08 eV in our work versus 0.05 eV in their work in $CuInSe_2$, while in $CuGaSe_2$ we find a slightly higher transition level of 0.40 eV as compared to 0.14 eV. We therefore confirm that both the $V_{Se} - V_{Cu}$ and V_{Se} are metastable defects. The lower formation

energy of V_{Se} as compared to $V_{Se} - V_{Cu}$ implies that V_{Se} is much more abundant than the complex with the vacancy in equilibrium.

From the data in Table 9 we conclude that the Ga_{DX} pinning level is constant as a function of gallium concentration in Cu(In,Ga)Se_2 alloys at 1.17 eV. It is always lower than the In_{DX} pinning level. Therefore, metastabilities can only be expected from Ga_{Cu} antisites and only if a Fermi level as high as 1.17 eV is attained at the buffer-absorber interface.

10.5 IS METASTABILITY CAUSED BY POINT DEFECTS?

We believe that this question can ultimately not be answered by theory, but only new experimental results can finally yield a conclusive answer. In addition, we would like to emphasize that many different metastable phenomena may be involved, which may require separate explanations [48, 49].

Our results, while in principle confirming the metastable properties of V_{Se} and $V_{Se} - V_{Cu}$ defects and Ga_{DX} centers (but not In_{DX} centers), at the same time raise severe doubts about their relevance because:

- $V_{Se} - V_{Cu}$ can not occur in concentrations larger $10^{12}cm^{-3}$ in thermodynamic equilibrium (estimated from the minimum formation energy for all possible chemical potentials at 850 K deposition temperature). This is too small for the defect complex to account for significant metastabilities. If anything, the isolated selenium vacancy V_{Se} seems to be a better candidate.
- The lowest formation energy achievable for the isolated V_{Se} is about 1.3 eV at point B in Figure 33 in $CuInSe_2$. This could be sufficiently small for the defect to be contained in signifcant quantity. However, the conditions at point B are very far from realistic conditions for p-type solar cell absorber material as discussed in Section 10.3.1. The optimal conditions are rather supposed to be close to point A (Figure 33), for which the material achieves maximum p-type conductivity and the copper chemical potential is consistent with measurements [190, 225]. Therefore, under realistic preparation conditions the formation energy of the selenium vancancy is again as high as 2.4 eV and should not be contained in relevant quantities.
- A DX pinning level does not exist in $CuInSe_2$, which rules out metastabilities due to DX center in ternary $CuInSe_2$. For typical absorber Cu(In,Ga)Se_2 with a gallium content of 30 per cent the DX pinning level is calculated to lie at 1.17 eV very close to the conduction band. It is questionable whether such a high Fermi level is attained at the buffer-absorber interface.

Note that the formation energies obtained for V_{Se} and $V_{Se} - V_{Cu}$ within the present study are rather consistent with the formation energies formerly obtained in Refs. [35] and [36] (see Table 7 and 8).

A possibility for V_{Se} to be relevant, which can at present not be ruled out, is that the material contains a high amount of non-equilbrium selenium vacancies. This would however require a large non-equilibrium enhancement factor. While thin-film growth may be a far-from-equilibrium process, this does not apply to most single crystal growth methods. More detailed experimental single crystal studies on metastabilities are therefore necessary. In particular, it would be interesting to study metastabilities in the extreme cases of equilibrium-grown maximum p- versus n-type $CuInSe_2$ single crystals.

It should be kept in mind that other routes of explanations for metastabilities such as e.g. copper migration in the space-charge zone [205, 206], back-contact barriers [48] or even completely new explanations may finally contribute to definite answers. However, any proposed model has to match the experimental data. A necessary and useful requirement when a defect is to be assigned to a certain metastable phenomenon is that its intensity should correlate with the concentration of the defect. Therefore, chemical correlations which can be most accurately assessed in single crystals with well-defined stoichiometries may be key to separate metastabilities due to point defects from other possible mechanisms. Since the N2 defect signal and the photocapacitance signal around 0.8 eV shows metastable response to temperature [44, 55], it may be warranted to put greater focus on the $Cu_{In,Ga}$ defect. This defect was shown to trap holes, it can be paramagnetic since it carries a magnetic moment of one Bohr magneton in its -1 charge state and it is the only paramagnetic point defect, which is supposed to be signifcantly contained in the material under certain conditions based on the analysis of defect formation energies. In our opinion, the study of paramagnetic defects and their response to light and bias, e.g. by means of electron paramagnetic resonance (EPR), represents a promising avenue of research for $Cu(In,Ga)Se_2$ absorbers. In fact, a paramagnetic center has been reported to appear after illumination in the closely related compound $CuAlS_2$ [229].

10.6 COMPLEXES WITH COPPER VACANCIES

The formation of complexes of copper vacancies with other intrinsic defect such as In_{Cu} and Ga_{Cu} antisites [8, 31] and selenium vacancies V_{Se} [36] has been predicted to occur in $CuInSe_2$ and $CuGaSe_2$, and these theoretical findings have been invoked to explain certain properties of $CuInSe_2$ and $CuGaSe_2$ such as the stability of so-called ordered defect compounds (ODCs) and the favourable optoelectronic properties despite large off-stoichiometries [8]. In contrast, our results suggest that the binding energies for complexes with copper vacancies are in fact rather small (see Table 11). We find e.g. that the total binding energy of $(In_{Cu} - 2V_{Cu})^0$ is only -0.29 eV, whereas former studies have reported an *interaction energy* of -4.2 eV [8].

In order to avoid confusion, we give the definition of the binding energy ΔE_b of defect complexes, which is the difference of the formation energy of the complex $\Delta H_{f,complex}$ and the sum of the formation energies of its constituent point defects $\Delta H_{f,def(i)}$:

$$\Delta E_b^q(E_F) = \Delta H^q_{f,complex}(E_F) - \sum_i \Delta H^{q_i}_{f,def(i)}(E_F), \tag{10.3}$$

where the charge state q refers to the stable charge state given the Fermi energy E_F. Although it need not be generally the case, the charges of the constituent defects often add up to the charge of the complex over a large range of the Fermi energy. The binding energy within this range is then constant. This is for example the case for $(In_{Cu} - 2V_{Cu})^0$, for which the constituent point defects carry the charges In_{Cu}^{+2} and V_{Cu}^{-1} for almost any Fermi level E_F in the band gap and the data given in Table 11 should be understood in this sense.

	HSE06 this work	Refs. [8],[31]	Ref. [34]	Ref. [36]
$CuInSe_2$				
$(In_{Cu} - 2V_{Cu})^0$	-0.29	-2.72	-0.74	-
$(In_{Cu} - V_{Cu})^{+1}$	-0.18	-	-	-
$(V_{Se} - V_{Cu})^{-1}$	-0.17	-	-	$\approx$ -0.4
$CuGaSe_2$				
$(Ga_{Cu} - 2V_{Cu})^0$	-0.99	-2.68	-0.77	-
$(Ga_{Cu} - V_{Cu})^{+1}$	-0.65	-	-	-
$(V_{Se} - V_{Cu})^{-1}$	-0.66	-	-	$\approx$ -0.4

Table 11: Binding energies of complexes with copper vacancies ΔE_b in their dominant charge state in eV as compared to the literature. The numbers for Refs. [8], [31] and Ref. [34] are not directly given in the corresponding references (see text).

In the following, we explain that former findings of strongly interacting defect complexes resulted from an unphysical analysis as well as from inappropriate post-processing corrections. These former results, are subject to various sources of error: i) the *interaction energy* is reported with reference to neutral V_{Cu} and In_{Cu} defects. These neutral charge states do not occur in reality for shallow compensating defects. Binding energies should be reported with reference to the naturally occuring charge states V_{Cu}^{-} and In_{Cu}^{+2}. ii) a strong electrostatic interaction was reported to release -2.5 eV. This high value must result from spurious correction schemes. We find that there is hardly any electrostatic interaction between copper vacancies and In_{Cu} antisites, which is reasonable to expect because the shallow copper vacancy does not carry a localized point charge. iii) The local relaxation energy was reported to be -0.3 eV. This is very close to the total binding energy we find. We conclude that local relaxation is largely responsible

for the weak binding of copper vacancies to In_{Cu} antisites. The finding of weak binding of the $(In_{Cu} - 2V_{Cu})^0$ complex draws into doubt a lot of the theoretical explanations related to copper vacancy defect complexes in $CuInSe_2$. Pairing of In_{Cu} antisites with copper vacancies was formerly proposed to explain the very good tolerance to off-stoichiomtery of $CuInSe_2$ [8]. In contrast, in the picture that arises from our results the tolerance to off-stoichiometry simply results from the fact that copper vacancies as well as In_{Cu} defects are very shallow compensating defects. The binding energies are too small for the defects to exist predominantly as complexes in equilibrium. It should be emphasized that a large fraction of difference of the obtained binding energies in comparison to the *interaction energy* in Ref. [8] is a matter of the analysis and the applied corrections, not a matter of fundamental differences in the applied density functionals. However, the value for the binding energy obtained from the screened-exchange hybrid functional is still 0.45 eV bigger, i.e. less binding, than the value obtained within local density functional theory using the proper corrections.

Binding is also weak in case of the $(V_{Se} - V_{Cu})^{-1}$ complex in $CuInSe_2$, which was proposed to be responsible for metastabilities [36]. Here we find a binding energy of only -0.17 eV as compared to approximately -0.4 eV in Ref. [36].

The concentration of any defect - be it a complex or not - is given by its formation energy via

$$c_{def} = c_0 \cdot \exp\left(-\Delta H_{f,def}/k_B T\right). \tag{10.4}$$

The concentration of defect complexes can thus only be dominant when the formation energy of the complex is lower than the formation energy of the individual point defects. Based on our results, this is not the case for any of the defect complexes considered here (compare Table 11 and Figure 33).

We conclude that in contrast to the widely accepted view, defect complexes with copper vacancies do not exist in significant quantities in $CuInSe_2$ and $CuGaSe_2$ in equilibrium.

COMMENT TO THE COMPARISON WITH LITERATURE VALUES

It should be pointed out that the binding energies ΔE_b as displayed in Table 11 are not directly cited in Refs. [8], [31] and Ref. [34]. However, we calculated the binding energy for comparison via Equation 10.3 from the data in Ref. [8] using

$$\Delta H_f((In_{Cu} - 2V_{Cu})^0) = \Delta H_f(In^0_{Cu} - 2V^0_{Cu}) + \delta H_{int} = 0.33 \text{ eV}, \tag{10.5}$$

and from the data in Ref. [31] using

$$\Delta H_f((Ga_{Cu} - 2V_{Cu})^0) = \Delta H_f(Ga^0_{Cu} - 2V^0_{Cu}) + \delta H_{int} = 0.7 \text{ eV}, \tag{10.6}$$

with δH_{int} as defined in Ref. [8]. For the data in Table 11 of Ref. [34] the binding energies were calculated using $\Delta H_f((In_{Cu} - 2V_{Cu})^0)$ and $\Delta H_f((Ga_{Cu} - 2V_{Cu})^0)$

as obtained above from Ref. [8] and Ref. [31], but $\Delta H_f(In_{Cu}^{+2})$,$\Delta H_f(Ga_{Cu}^{+2})$ and $\Delta H_f(V_{Cu}^{-1})$ as given in Ref. [34] was used. This procedure is justified since no corrections are necessary for neutral defect complexes and thus the formation energies of neutral complexes are always reliable. In addition, we have carried out independent calulations using the generalized-gradient approximation (GGA) aaplying the valence band edge +U correction of Ref. [34] in order to check for consistency of the results and we obtained very similar results to the ones in Ref. [34].

10.7 COMPARISON TO THE LITERATURE: THEORY

This section provides a comparison of our obtained results to literature data. The numerical values of the obtained formation energies of point defects in comparison to literature values are given in Table 6 and the charge transition levels are quoted in Table 9.

Several trends can be recognized from the data. Generally, defect formation energy data published by Persson *et al.* in 2005 and later works [34–37], seem to agree with our results to within a deviation of generally not more than 0.5 eV, while earlier work sometimes shows significant deviations of more than 2.5 eV in some cases [8, 31]. As an example, we find a formation energy of -1.01 for the In_{Cu} defect, while Zhang *et al.* (in 1998) find +1.85 eV, but Persson *et al.* (in 2005) [34] find -0.73 eV in much better agreement with our result. Since in both cases a local density functional has been used the difference must lie in the correction schemes. This implies that point defect formation energy data published before 2005 has to be interpreted with great caution due to sometimes inappropriate correction schemes. Indeed the results of Zhang *et al.* show large deviations from our results in many cases (i.e. for In_{Cu}, Cu_i and V_{In}). The deviations of later works such as Refs. [34–37] are generally much less severe since similar correction schemes were applied, but the differences to our results in the range between 0.02 (for V_{Se}) to 0.56 eV (for V_{Cu} in $CuGaSe_2$) can still be important for the interpretation of the results and the understanding of the material. In particular, the differences may add up when charge transition levels are considered or when considering defect formation energies of complexes. The fact that the deviations of our results versus results based on the local density approximation seem to be larger for copper-related defects such as V_{Cu} and In_{Cu} in comparison to non-copper related defects such as V_{Se}, is most likely related to the improved description of the copper *d* electrons within screened-hybrid density functional theory. These differences add up in case of the defect complex of an indium antisite with two copper vacancies $In_{Cu} - 2V_{Cu}$ for which we find a formation energy as high as 1.07 eV as compared to 0.33 eV within LDA [8], a difference of 0.74 eV. This difference is also reflected in the binding energies of the complex, which is smaller in our approach than in previously published

works [8, 31]. This leads to the conclusion that copper vacancies hardly bind to In_{Cu} antisites in $CuInSe_2$. As discussed in the Section 10.6, complex formation is not needed in order to explain the favourable properties of $CuInSe_2$.

In conclusion, before comparing the results for point defect formation energies it has to be ensured that the corrections were properly carried out. Then, the comparison using different functionals may be ascribed to differences in the underlying approximation for the exchange and correlation energy. In the case of $CuInSe_2$ and $CuGaSe_2$ these physical differences lead to qualitatively different results in some cases, most notably in the position of the DX pinning levels, the high formation energy of the $In_{Cu} - 2V_{Cu}$ complex, which hardly binds the copper vacancies, and in the localization behaviour of holes on Cu_{In}, Cu_{Ga}, V_{In} and V_{Ga} deep hole traps.

10.8 COMPARISON TO THE LITERATURE: EXPERIMENT

In the picture that emerges from the obtained results In_{Cu} and Ga_{Cu} antisites are always abundant donors, In_{Cu} being shallow while Ga_{Cu} being deep, which are compensated mainly by shallow copper vacancy acceptors V_{Cu}. However, $Cu_{In,Ga}$ deep acceptors as well as Cu_i shallow donors may also be abundant and can contribute significantly to compensation depending on the preparation conditions. All other defects, including all complexes with copper vacancies, are only present in minor quantities and thus can not significantly affect the properties of the material. In the following we compare how this picture matches with the experimental situation. It should be kept in mind, that considering the necessary corrections associated with defect calculations, the given data can not be expected to give quantitative agreement to better than within 50 meV at most.

A recent review article gives a good overview on shallow defects in $CuInSe_2$, $Cu(In,Ga)Se_2$ and $CuGaSe_2$ as investigated by photoluminescence and Hall measurements [62]. For $CuInSe_2$, the situation is summarized as follows: A shallow donor is observed below 10 meV and one or two additional donors in the range between 60 and 90 meV. As far as shallow acceptors are concerned, there is one very shallow defect located around 30-40 meV, another one in the range 70 to 100 meV and maybe a third at 150 meV. Our data support the assignment of the very shallow donor to the In_{Cu} antisite. Another candidate for a shallow donor would be the copper interstitial, however one has to keep in mind that this defect is only expected to contribute to the doping in a narrow range of preparation conditions (e.g. Figure 33, points B, E and F). The shallowest acceptor should certainly be assigned to the copper vacancy. Furthermore, the Cu_{In} antisite can be assigned to one of the other two acceptor levels as the calculated charge 0/-1 transition level is located at 110 meV. Note that the same defect is also predicted to be associated with a much deeper transition at around 0.67 eV. Photoluminescence studies often show a shoulder associated with a free-to-bound transition or donor-acceptor

transition [230]. This could well be due to recombination of holes localized on Cu_{In} antisites with electrons from the conduction band. Such processes would be consistent with occurence of an additional peak in the photoluminescence spectra under copper-rich conditions [231–233], which minimize the formation energy of the Cu_{In} defect (see e.g. Figure 33, point B).

For $CuGaSe_2$, it is summarized in Ref. [62], that one shallow donor at 12 meV and three acceptors at 60, 100 and 135 meV are commonly observed. Again, based on the present results the shallowest acceptor should be assigned to the copper vacancy, while one of the deeper acceptors must correspond to the Cu_{Ga} antisite. Under most preparation conditions (Figure 33), compensation of the acceptors is solely due to the deep Ga_{Cu} donor defect. This finding is in line with the occurence of a deep photoluminescence signal in $CuGaSe_2$ as reported in Chapter 9. Cu_i could be present as a shallow compensating donor under certain conditions (eg. point B and E in Figure 33). However, the possibility of compensation solely due to deep Ga_{Cu} defects applies to a much broader range of preparation conditions. Note that $CuGaSe_2$ is predicted to be uncompensated p-type in a narrow range of preparation conditions (compare Figure 33, at points A and F). In this case only copper vacancies and Cu_{Ga} acceptors are abundantly present.

In the alloy $Cu(In,Ga)Se_2$, a similar occurrence of a shoulder in the photoluminescence spectra has been observed under copper-rich conditions, which is associate with a decrease of carrier lifetime [234, 235]. As in $CuInSe_2$, our data supports the occurence of relatively deep Cu_{In} and Cu_{Ga} acceptors under these conditions (between 110 and 210 meV, Table 9). Furthermore, we predict additional defect-related transitions to be present at Ga concentrations above approximately 50 per cent, when the conduction band is raised such that Ga_{Cu} becomes deep.

Furthermore, it should be mentioned that a deep defect around 0.8 eV of has been observed by photocapacitance measurements in $Cu(In,Ga)Se_2$ independent of gallium content [54, 55]. This defect signal could possibly be assigned to the deep -1/-2 transition level of $Cu_{In,Ga}$ hole traps as pointed out in Chapter 9.

In summary, the picture that arises from the present defect calculations seems to be in good agreement with many features of defect-related signals in photoluminescence and Hall measurements. In particular, it offers a natural explanation of the unfavourable properties of the material for solar cell applications under copper-rich conditions and when high gallium contents above approximately 50 per cent are employed.

10.9 IMPLICATIONS FOR DEVICE OPTIMIZATION

The intrinsic point defects, which are of concern for solar cell devices due to their trap properties as well as their low formation energies are only Cu_{In} in $CuInSe_2$,

and both Cu_{Ga} and Ga_{Cu} in $CuGaSe_2$. Thus, the optimal preparation conditions should minimize the concentrations of those defects, while the Fermi energy needs to be maintained at a favourable level. All other potentially detrimental defects are not contained in high quantities unless non-equilibrium concentrations are assumed.

In Section 10.3.1 we argued that reasonable growth conditons for high quality PV material are suspected to be close to point A in Figure 33. Looking at the formation energy plots in Figure 33, it is seen that the Cu_{In} defect has a rather low formation energy at this point. In order to raise its formation energy one can go to point C. This raises the formation energy of this defect to approximately 1.2 eV at the respective Fermi energy. However, it also raises the Fermi level to approximately 0.4 eV. This shows, that there is a tradeof between the position of the intrinsic Fermi level and the concentration of Cu_{In} antisites. The optimal conditions are supposed to be located between point A and point C. This location corresponds to copper-poor $CuInSe_2$ on the In_2Se_3-Cu_2Se pseudobinary cut in the pseudobinary phase diagram, which is consistent with the fact that the highest quality $Cu(In,Ga)Se_2$ absorbers are prepared copper-poor.

For $CuGaSe_2$, the concentration of Ga_{Cu} antisites should be minimized as an additional constraint. In fact, Ga_{Cu} is likely to be more harmful to the material that Cu_{Ga} since it represents a minority carrier trap in p-type absorber material. From Figure 33 it is seen, that Ga_{Cu} has rather low formation energies under all preparation conditions. However, the optimal conditions, at which the formation energy of Ga_{Cu} at the intrinsic Fermi level attains its maximum, are located at point B, corresponding to maximally copper-rich conditions on the pseudobinary line. Given that stoichiometry variations in $CuGaSe_2$ are mostly realized by Ga_{Cu}, Cu_{Ga} and V_{Cu}, the optimal conditions can also be understood as the requirement to be as close to perfect stoichiometry as possible, with p-type doping by copper vacancies on the order of only $10^{16}cm^{-3}$ approximately. Figure 33 implies that the conditions at point B will also entail a significant amount of detrimental Cu_{Ga} hole traps.

In summary, in order to prepare efficient $CuGaSe_2$ or high Gallium content $Cu(In,Ga)Se_2$ it seems important to understand that copper-rich conditions are optimal, in contrast to $CuInSe_2$, and low Gallium content $Cu(In,Ga)Se_2$ for which it has long been understood that copper-poor conditions are optimal. However, if it is possible at all to get close enough to stoichiometry in order to achieve efficient $CuGaSe_2$ remains uncertain. From a thermodynamic point of view, it might be possible using low temperature processes close to equilibrium.

10.10 CONNECTION TO DEFECTS IN OTHER MATERIALS: ZNO AND KESTERITES

The fact that Cu_{In}, Cu_{Ga}, V_{In} and V_{Ga} are characterized as hole traps based on our results using screened-exchange hybrid density functional theory can be linked

to defects in related materials which show similar behaviour. ZnO represents another well studied material with similar adamantine crystal structure containing full *d* shell cations and *p-d* character of the valence band in which cation vacancies or antisites trap holes [170, 236]. Similar to the present result that semilocal functionals do not correctly localize holes on Cu_{In}, Cu_{Ga}, V_{In} and V_{Ga}, it was found in a recent study using a generalized Koopmans approach, that the Zn vacancy and extrinsic dopants on the zinc site localize holes in ZnO [170]. Also in the case of Cu_2O screened-exchange hybrid density functional theory was recently found to give corectly localized holes for split copper vacancies [236]. Our results suggest that with respect to hole localization on defects the $CuInSe_2$ and $CuGaSe_2$ semiconductors behave similar to correlated oxides with full *d* shell elements. It is suggested that advanced methods are most likely also needed to observe localization of holes on cation antisites and vacancies in the closely related kesterites such as $Cu(Zn,Sn)Se_4$ and $Cu(Zn,Sn)S_2$ [237–240]. Furthermore, the fact that we rule out defect complex formation in $CuInSe_2$ and $CuGaSe_2$ deserves critical reevaluation of this issue in the related kesterites. Similar trends for the use of screened-exchange hybrid functionals as oberved for $CuInSe_2$ and $CuGaSe_2$ in the present study should be expected for kesterites, but confirmation by hybrid functional studies on these materials is desirable.

10.11 SUMMARY

In summary, we have presented a systematic and self-contained study of the intrinsic point defect physics based on screened-exchange hybrid density functional theory. The results were compared to literature data based on local density functional theory. Although many formerly obtained conclusions are found to be consistent with our results, there are a number of important differences. First, in addition to V_{Cu} and the antisites In_{Cu} and Ga_{Cu}, we also find Cu_{In} and Cu_{Ga} and Cu_i to be contained in high quantities in the material under certain preparation conditions, such that they can significantly alter the properties of the material and contribute to self-doping. Second, complex formation with copper vacancies is found not be relevant due to the low formation energies and binding energies of the complexes. Third, in contrast with the literature, In_{Cu} is found to be a very shallow donor, which explains the good tolerance of the material to off-stoichiometry rather than complex formation with vacancies. Fourth, localization of holes is observed not only on Cu_{In}, Cu_{Ga}, but also on V_{In} and V_{Ga} defects using the screened-exchange hybrid functional, while GGA fails to predict such behaviour. Similarly, the high - or even absent - DX pinning levels put a question mark to the relevance of DX centers for metastabilities, which suggests that further experimental studies on metastabilities are necessary. The results may serve as a guideline for optimization of the properties of $Cu(In,Ga)Se_2$ solar cell absorbers in terms of the point defect physics. It is suggested that the optimal

peparation conditions for $CuGaSe_2$ and $Cu(In,Ga)Se_2$ with high gallium content are located at the copper-rich side of the pseudobinary, in contrast to $CuInSe_2$ and low Gallium content alloys which are optimal when prepared copper-poor.

Part IV

TWIN BOUNDARY, STACKING FAULT AND VOID FORMATION IN MELT-GROWN SILICON

This part is concerned with the investigation of defect formation processes at the solid-liquid interface in silicon grown from the melt using molecular dynamics and lattice Monte Carlo techniques. First, in chapter 11, the formation process of twin boundaries in silicon growth from the melt is studied by molecular dynamics. Extended twin boundaries often occur in etch-defined film fed growth, but their nucleation mechanism has not been understood on an atomistic level. In Chapter 12, a new mechanism for void nucleation in silicon growth from the melt is presented. Faulted dislocation loops, which are grown in at the solid-liquid interface, are shown to rapidly dissolve into small vacancy clusters, which may act as the nucleation center for nanoscale voids in silicon crystals. Finally, in Chapter 13, a new lattice Monte Carlo model for silicon growth from the melt is presented. The model explicitly includes the possibility of stacking faults and twin boundaries. Based on this model, the consequences of low stacking fault formation energies for the growth kinetics of the solid-liquid interface are studied.

11

THE TWIN FORMATION MECHANISM IN MELT-GROWN SILICON

11.1 INTRODUCTION

In Section 3.4, the state of knowledge on twin boundaries in melt-grown silicon has been reviewed. An understanding of the exact formation mechanism of twin boundaries has been lacking until today. In this chapter, the issue of how and where low energy (111) twin boundaries may nucleate in silicon growth is clarified. By means of classical molecular dynamics simulations, the feasibility of twin formation at the (111) microfacets of a faceted interface is tested against the possibility of formation at a grain boundary. In addition, the question of why a very low twin boundary formation energy, which is in the range between 5 and 50 mJ/m^2 [241–246], does not necessarily imply a high twin density is addressed.

11.2 METHOD

For simulating the solidification of silicon we use an analytical-bond order potential (ABOP) that has been parametrized to model silicon and silicon carbide [140]. We use the first of the two given parameter sets for silicon (Si-I). This silicon potential of the Tersoff-Albe-type has been fitted to dimer binding energies as well as to formation energies of different crystal phases. It provides a reasonable description of the properties of silicon in the crystalline as well as in the liquid phase. The radial distribution function of the liquid phase, for example, agrees well with experiment and the angular distribution function compares as well to the one obtained by Car-Parrinello molecular dynamics [140]. We used the LAMMPS code [148] for all molecular dynamics simulations discussed here. The Nosé-Hoover thermostat is applied to control pressure and temperature. For setting up a periodic simulation box containing both crystal and liquid silicon we first perform silicon melting and equilibration to obtain a liquid at the melting point. The silicon crystal is separately heated up to the melting point. The crystal is then placed into the liquid in a way that two solid-liquid interfaces exist in the simulation box perpendicular to the z-direction and periodicity of the cell in all

directions is conserved. The setup is equilibrated and then some undercooling is applied to observe growth of the crystal. Pressure control is applied only in the growth direction, while the size of the box is fixed in lateral directions. Two geometries are considered in order to study the different mechanisms proposed for explaining twin formation, namely twin nucleation on a plain interface versus nucleation at a grain boundary. The first set of calculations consists of a (211) solid-liquid interface simulated with an undercooling of $\Delta T = 50$ K, 150 K and 250 K. In the second set of calculations we start with a crystal containing two grain boundaries. The grains are tilted by 45° relative to each other around the (110) axis, which is aligned with the y axis of the box. Initially, the grain boundaries are equilibrated at a temperature slightly lower (50 K) than the melting temperature in order to prevent them from melting. Again, the growth seed has a planar solid-liquid interface perpendicular to the z-direction (see Figure 35.a) and we use undercoolings of $\Delta T = 25$ K, 50 K and 150 K. In all simulations the simulation box contains roughly half a million atoms. Simulations lasted about 5 nanoseconds physical time with a time integration step of 2 femtoseconds. Such simulations take around 3-5 days of computing time on a state-of-the-art computer cluster using 100 processors. For analysis of the simulation snapshots we first applied a local energy minimization routine to facilitate analysis of the structure without thermal lattice vibrations. Then we performed a common neighbour analysis (CNA) routine [247] in order to identify the crystalline and the liquid phase, grain boundaries, stacking faults and twin boundaries. The CNA analysis as well as all snapshots shown in this chapter have been calculated with the Open Visualization Tool (OVITO) software package [248].

11.3 RESULTS

First, we study the growth of the (211) interface of a perfect crystal. At an undercooling of 50 K, we do not find formation of extended defects during growth. However, faceting of the (211) interface, i.e. formation of small (111) microfacets is observed (similar as in Figure 34.a for $\Delta T = 150$ *K*). At a higher undercooling of 150 K formation of loops consisting of coherency and anticoherency dislocations lying in the (111) crystal plane occurs. The observed loops are at least three atomic double-layers thick and lie in the (111) plane. They are roughly of hexagonal shape and some line segments of the hexagon correspond to a very small segment of an at least three layer high reconstructed symmetric $\Sigma 3$ (112) interface. An incoherent interface of this type, consisting of coherency and anti-coherency dislocations, has to exist between the matrix and the twin crystal perpendicular to the $\Sigma 3$ (111) twin boundary [249]. In the initial stage the interface forms (111) microfacets (see Figure 34.a). However, the faceting rapidly becomes more pronounced than for the lower undercooling of 50 K, which allows stacking fault islands to nucleate at the (111) facets (Figure 34.b). These stacking fault islands

are then grown into the perfect crystal resulting in the formation of a loop (Figure 34.c and Figure 34.d). Once the loops are grown in we observe them to shrink to smaller sizes. The density of the loops strongly depends on the undercooling. At a higher undercooling of 250 K significantly more loops are found. They can be regarded as being bound by stacking faults or twins. However, the boundaries do not extend in the growth direction of the crystal and as such they can not be identified with the twins one would expect to be present for facilitated growth of the crystal according to the Hamilton-Seidensticker growth mechanism [93].

In a second set of simulations, we study geometries with grain boundaries present in the initial crystal. In this case, we observe the formation of a characteristic growth front in the initial stage of growth (see Figure 35.a and Figure 35.b). After some time a (111) microfacet forms adjacent to the grain boundary-melt location. At this point where the grain boundary meets the melt multiple parallel twin boundaries form during growth (see Figure 35.c and Figure 35.d). Once the twin boundaries are formed, they continue stable growth until the end of the simulation (compare Figure 36.a). This twin formation process is largely independent of temperature. A very similar twin structure is formed for all three simulated undercoolings of $\Delta T = 25$ K, 50 K and 150 K (see Figure 36). The main difference here is the structure of the grain boundaries, which become more disordered at higher undercoolings.

A third set of simulations is run with a setup of two grains tilted by 45° relative to each other around the (100) crystal axis aligned with the y axis of the box, resulting in one grain with a (100) crystal-melt interface and the other with a (110) interface. For this setup twin formation at the grain boundary was not observed. The absence of twins in this case can be understood from the lack of faceting at the grain boundary, which in turn depends on the orientation of the grains as well as that of the crystal-melt interface.

It has to be mentioned at this point that the twin formation energy given by the potential we have used is zero. As the twin boundary energies are known to be very low (5-50 mJ/m^2) but different from zero, the twin density in our simulations can be expected to be somewhat larger than the real one. However, neither do we expect the different twin formation energies to change the qualitative nature of the twin nucleation process, nor to affect the conclusions drawn from the simulations presented here.

11.4 CONCLUSIONS

Our simulations show that parallel twins may form at grain boundaries in silicon growth from the melt. In contrast, we do not find evidence that twin boundaries may spontaneously form on the faceted interface of a perfect crystal. We therefore conclude that twin boundary formation may occur at grain boundaries in edge-defined film-fed growth (EFG), rapid solidification and in other crystal

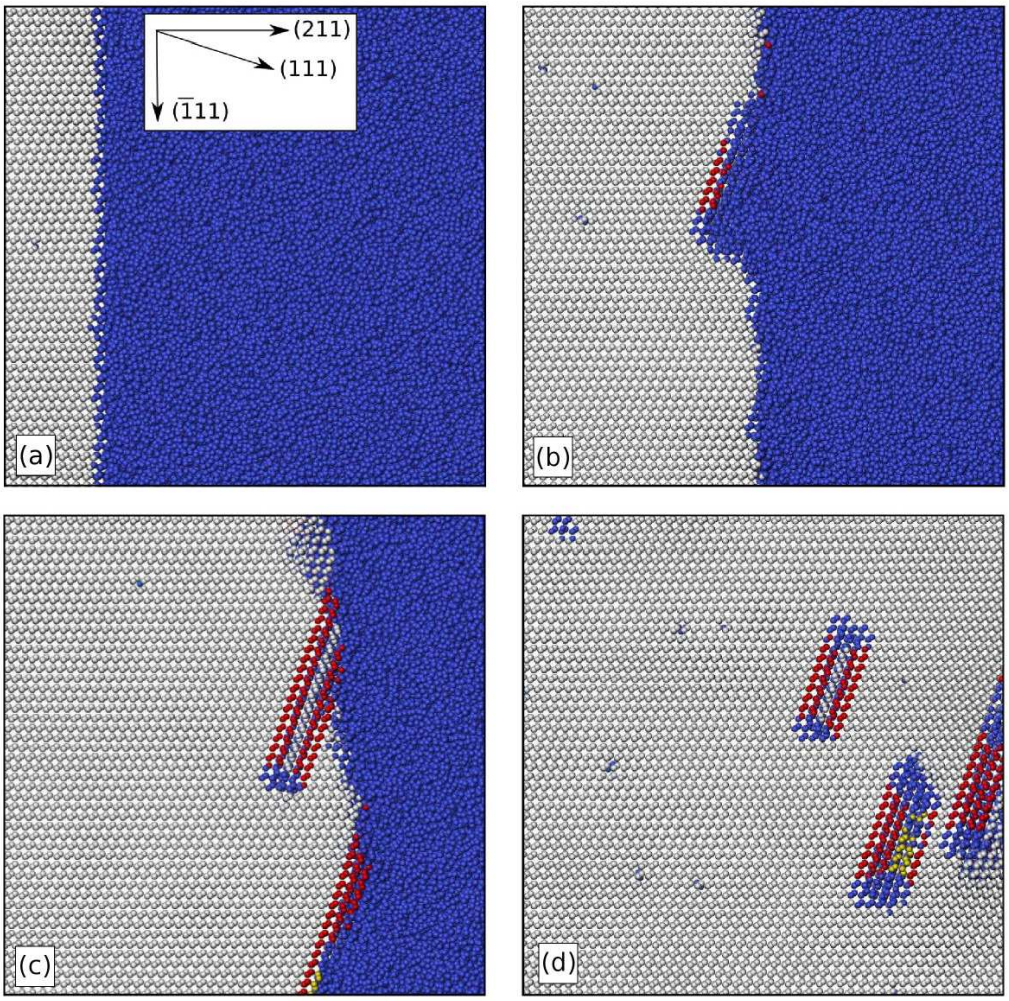

Figure 34: Si crystal growth at a solid-liquid interface in (211) orientation at 150 K undercooling: First, small (111) microfacets are occuring (a). Then stacking faults (marked in red) nucleate at these microfacets (b), resulting in a stacking fault island. These islands can be overgrown by the crystal (c) resulting in a loop (d) enclosed by two twin boundaries in the (111) plane and an array of coherency and anticoherency dislocations in all other directions. The plane of the picture cuts through the loops. Atoms next to dislocations are displayed in blue/dark grey as is the liquid phase. Colors: silicon crystal (white), amorphous/liquid/grain boundary (blue), single stacking fault or twin (red), double stacking fault or twin (yellow). All images: OVITO [201].

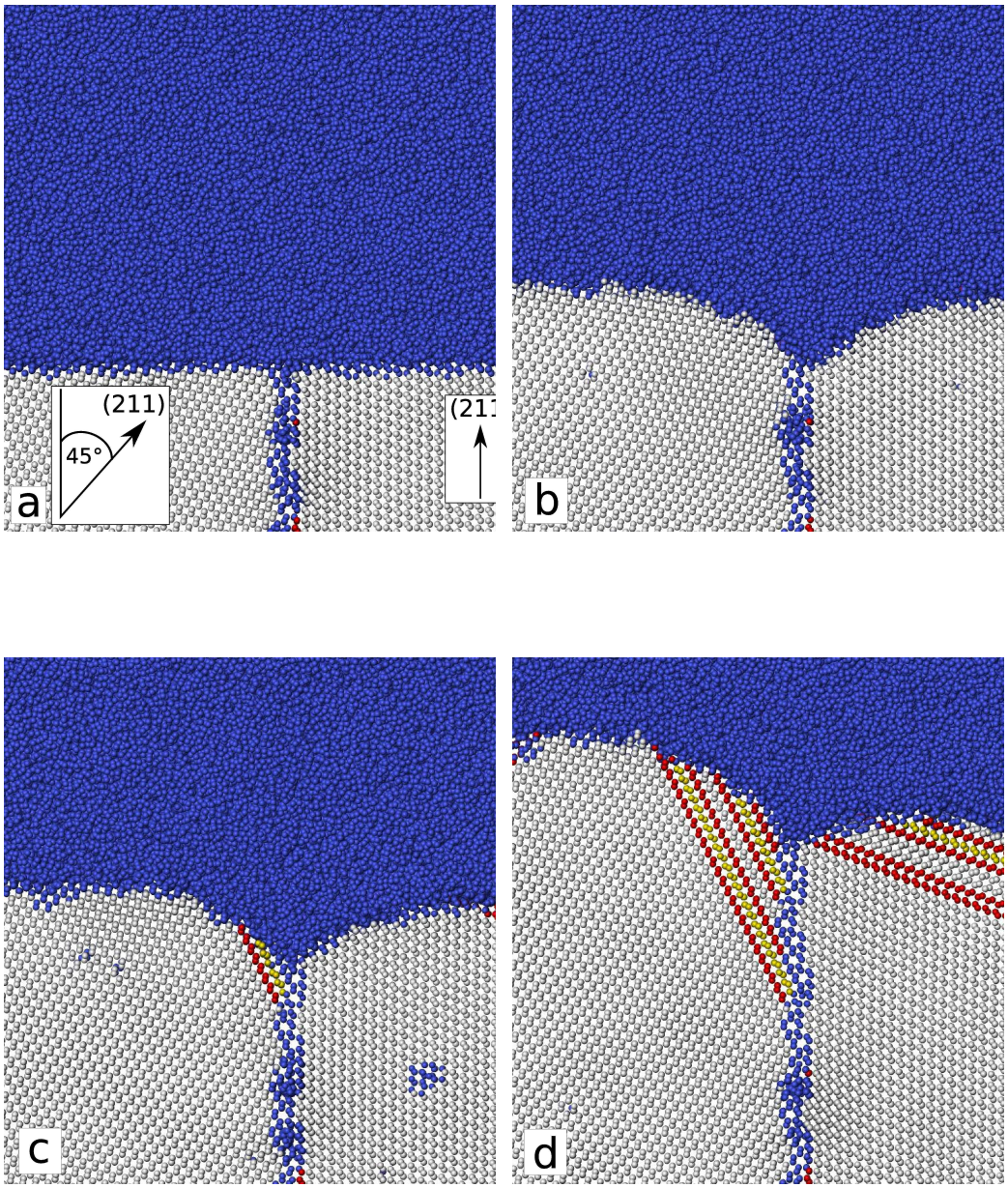

Figure 35: These pictures show formation of parallel (111) twins at a 45° tilt grain boundary at 25 K undercooling. Starting from the initial configuration with planar crystal melt interfaces (a), a characteristic growth shape with a groove between the two grains rapidly develops (b). Once a (111) microfacet has formed adjacent to the grain boundary, stacking faults start to nucleate (c), (marked in red/black). As additional layers are nucleated at the grain boundary a twin forms (c+d). Several parallel twins can form at the grain boundary due to this mechanism (d). The final configuration of this simulation containing multiple parallel twins is shown in Figure 36.a. Note that twin boundaries nucleate also at the second grain boundary contained in the simulation cell. These twins enter the picture from the right. Color coding as in Figure 34.

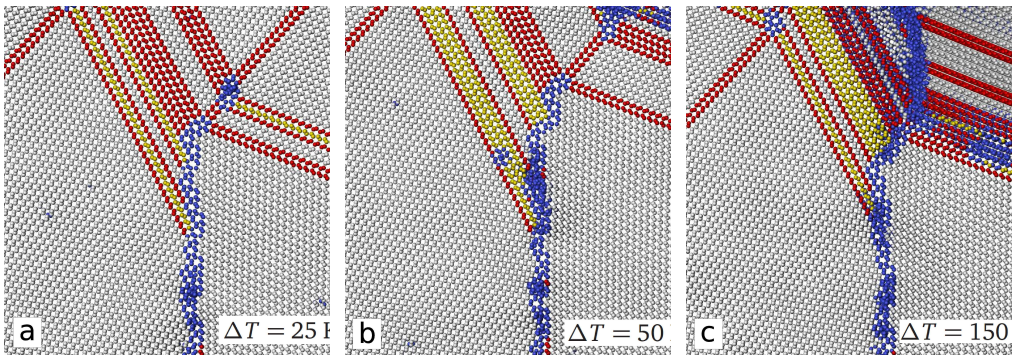

Figure 36: Comparison of twins grown from grain boundaries at 25 K (a), 50 K (b) and at 150 K undercooling (c). Different undercooling temperatures do not affect the twin formation mechanism. However, the grain boundary appears slightly more disordered at higher undercoolings. Color coding as in Figure 34.

growth methods, in which grain boundaries are present. Our findings contradict the results presented in Ref. [94] and Ref. [95], in which formation of twin boundaries at a faceted interface is proposed to be the relevant formation mechanism for experimentally observed twins even at low undercoolings. Formation of twin boundaries at a faceted interface seems highly unlikely not only because of the absence of the process in the simulation, but also from a thermodynamic point of view.

If a twin boundary layer was formed at a microfacet parallel to the growth direction as suggested in Ref. [94] and Ref. [95], then an incoherent interface between the perfect crystal and its mirror crystal is formed perpendicular to the $\Sigma 3$ (111) twin boundary, consisting of coherency and anti-coherency dislocations [249]. An interface of this type is the reconstructed $\Sigma 3$ (112) symmetric tilt boundary, for which several types of reconstructions have been suggested in the literature [250–254]. Theoretical values of the interface energies have been given to be between 340 and 1200 $\mathrm{mJ/m^2}$ [244, 255, 256]. Therefore, the high formation energy of the incoherent interface, not the formation energy of the twin boundary itself, is the limiting factor for coherent $\Sigma 3$ (111) twin boundaries. The high formation energy of the incoherent interface therefore prohibits the twin formation mechanism as suggested in Ref. [94] and Ref. [95], for which no direct experimental evidence has been given.

In contrast, if a twin nucleates adjacent to a grain boundary, no incoherent interface has to be formed, since the termination of the twin boundary can be accomodated in the grain boundary. Twin formation at a grain boundary therefore requires much less energy than in the perfect crystal. This explains twin formation at grain boundaries even at very low undercooling. It should be stressed,

however, that formation of a twin boundary still requires the (111) microfacet adjacent to the grain boundary at the crystal-melt interface. In the simulation we observed that a microfacet which is about five atoms wide but extends through the whole simulation cell parallel to the grain boundary is sufficient to form the twin boundary. This explains why for some grain orientations twin formation is not observed even in the presence of grain boundaries, as it may not be possible or favourable to form the (111) microfacet adjacent to the grain boundary for certain orientations. Therefore, the relative orientation of the grain also affects twin formation. As a consequence, control of the orientation of the grains and the grain boundary could provide a way to maximize the twin density in EFG silicon growth from the melt.

The argument that twin formation is limited by the formation energy of an incoherent interface also applies to twin formation in Czochralski growth. The fact that twinning in Czochralski growth occurs at a facet in the vicinity of the three-phase boundary between liquid, crystal and ambient [100–102] is consistent with this argument. No incoherent interface is needed when the twin boundary can form at a (111) facet adjacent to the ambient phase. In contrast, the twin boundaries can not spontaneously form at any arbitrary site of a faceted growth front in Czochralski growth, because the high formation energy of the incoherent interface would drive them out again. In conclusion, twinning is therefore possible at (111) facets adjacent to a three-phase boundary, independent of whether these phases are liquid, crystal and ambient as in Czochralski growth or liquid and two grains of different orientation as in EFG and in rapid solidification.

12

VOID FORMATION FROM GROWN-IN FAULTED DISLOCATION LOOPS

12.1 INTRODUCTION

As explained in Section 3.5, the origins of void formation in melt-grown silicon is commonly understood in terms of aggregation of excess vacancies. The respective models, however, rely on the assumption that vacancies and interstitials are incorporated into the growing crystal as isolated defects [106, 111–117]. On the other hand, it is well known that vacancy clusters of 6-32 atoms build very stable entities [112, 257–263]. Therefore, it is conceivable that vacancy clusters are already formed at the moving solid-liquid interface.

In this brief chapter, we report a mechanism derived from atomistic molecular dynamics simulations, which is responsible for the direct incorporation of vacancy clusters of 10 missing atoms and which occurs at the solid-liquid interface. This has important implications for void nucleation models, since it challenges our understanding of vacancy cluster nucleation and provides a possible hint on the origin of octahedral double-voids. The simulations presented in this chapter take the ones of the previous chapter a step further by asking: What happens after the dislocation loops as observed e.g. in Figure 34 have been grown into the crystal?

12.2 METHOD

For simulating the solidification of silicon, we used an analytical-bond order potential (ABOP) of the Tersoff-Albe-type with parameter sets for silicon (Si-I) [140]. We used the open source molecular dynamics code LAMMPS [148] and applied a Nosé-Hoover thermostat in order to control temperature and pressure perpendicular to the interface, while holding the lateral dimensions fixed. The initial setup consisted of a (211) solid-liquid interface in equilibrium at the melting point, which was rapidly cooled and constantly held at an undercooling of $\Delta T = 150$ K below the melting temperature of the model potential for Si. The simulation box contained about half a million atoms. Total simulation times were typically 9 ns with a time integration step of 2 fs. Moreover, we performed an energy mini-

mization and a common neighbor analysis (CNA) [247] in order to identify the crystalline and the liquid phases, stacking faults and twin boundaries.

12.3 RESULTS AND DISCUSSION

The originally planar (211) interface (Figure 34.a) rapidly forms (111) microfacets at an undercooling of 150 K. Then, the nucleation of two dimensional stacking fault islands on these (111) microfacets can be observed (Figure 34.b). When additional layers nucleate on top of the faulted areas, the stacking faults are overgrown by the crystal resulting in the formation of dislocation loops (Figure 34.c and 34.d). These loops are at least three atomic double-layers thick and lie in the (111) plane. They are roughly of hexagonal shape and some line segments of the hexagon correspond to very small segments of a $\Sigma 3$ (112) grain boundary. This grain boundary is incoherent and consists of coherency and anti-coherency dislocations, which naturally need to occur between the matrix and a twinned area of the crystal perpendicular to the $\Sigma 3$ (111) twin boundary [249, 264]. We have analyzed one specific dislocation loop in detail, which is shown in Figure 37, directly after it was grown into the crystal. The loop consists of three layers denominated as L1, L2 and L3 (see Figure 37). L1 and L3 are very similar in structure and consist of dislocations that occur predominantly in the form of eight- and five-membered rings (in contrast to the six–membered rings of the silicon crystal). Most of the atoms in these rings are perfectly coordinated, however, some over-(fivefold) and under (threefold)-coordinated atoms are observed. L2 is different in structure, the fit to the matrix is much better for this layer such that none of the eight and five-membered rings occur for this layer. The dislocation loop contains a total free volume equivalent to 11 vacancies.

In this simulation, it takes about 3 ns until the dislocation loop has grown. From here, the time evolution of the loop (only layer L3) is displayed in Figure 38. The loop shrinks by rapid rearrangements of bonds within the boundary of the loop. At about t = 3.8 ns (Figure 38) the loop is already much smaller as compared to Figure 37.d (L3). At t = 4.2 ns the loop has finally collapsed. It leaves two vacancy clusters behind, one consisting of 7 and one consisting of 4 vacancies. The larger cluster then rapidly emits one vacancy leaving a cluster with six vacancies. This situation corresponds to Figure 38 at t = 5.12 ns. Also the 4-vacancy cluster is not particularly stable. It dissociates within around one nanosecond and all of the four vacancies are absorbed into the larger six vacancy cluster leaving a stable 10 vacancy cluster behind (t = 6.36 ns). This cluster is very stable against dissociation. It does show bond rearrangements, but we do not observe any dissociation until the end of the simulation (within 3 nanoseconds after the 10-vacancy cluster has formed). The final configuration of the vacancy cluster is shown in Figure 39.

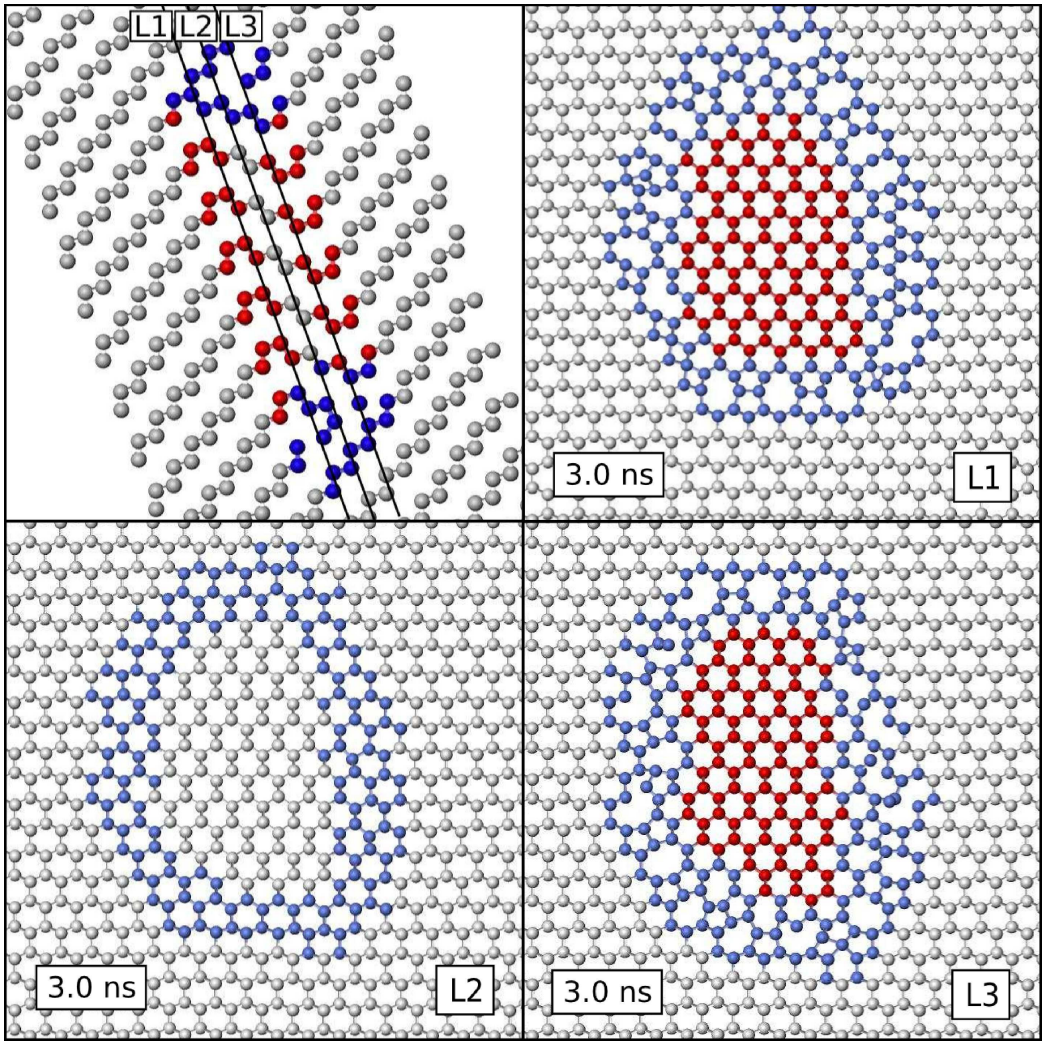

Figure 37: Structure of the small dislocation loop of Figure 34d. L1, L2, L3 correspond to the three layers in a (111) plane of the loop, marked by the black lines in the first figure. L1 and L3 have a similar structure in contrast to L2, where the inside of the loop (white) is classified as perfect diamond structure atoms.

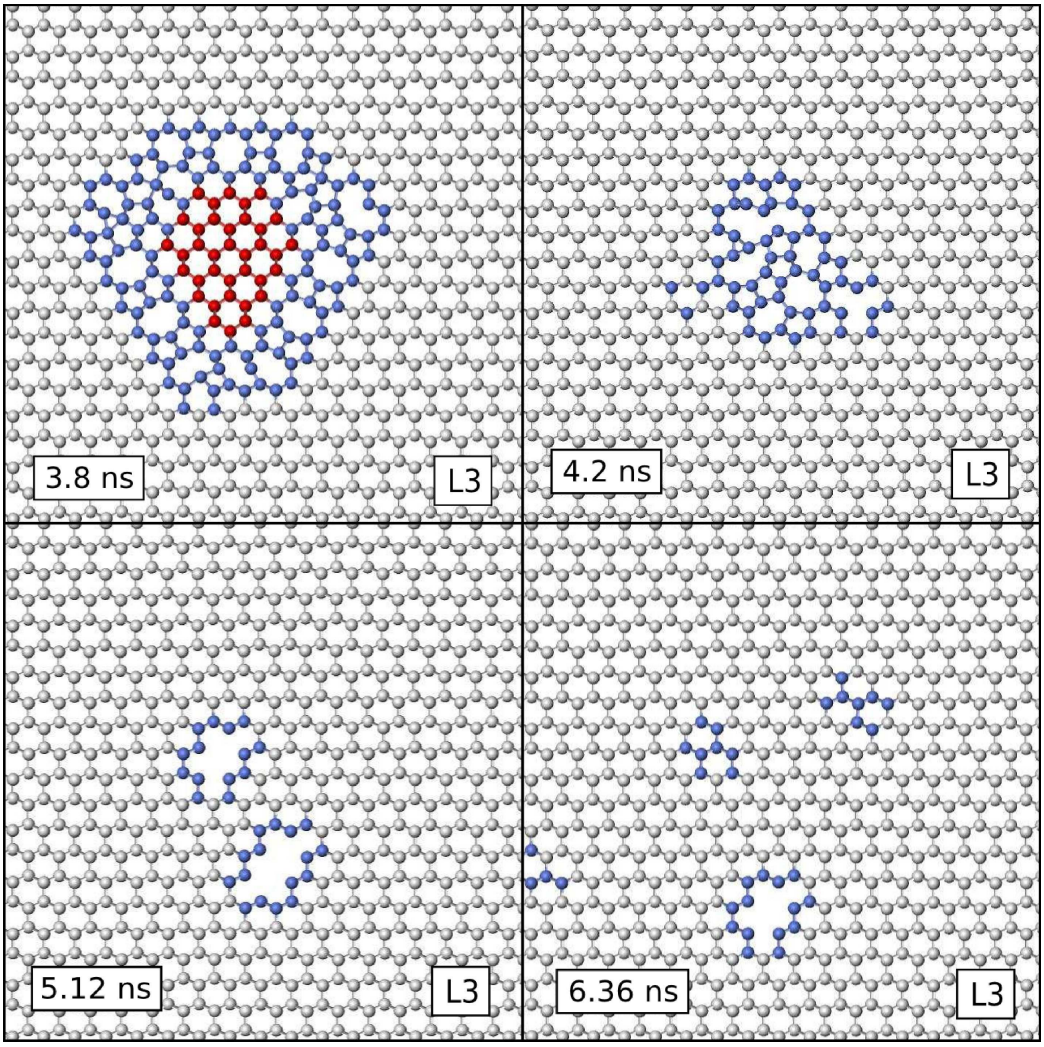

Figure 38: Time evolution of the grown-in faulted loop and the resulting vacancy clusters. Note that at t=5.12 ns the upper vacancy cluster consists of 6 vacancies and the lower one of 4 vacancies. The missing vacancies are located in an adjacent (111) plane.

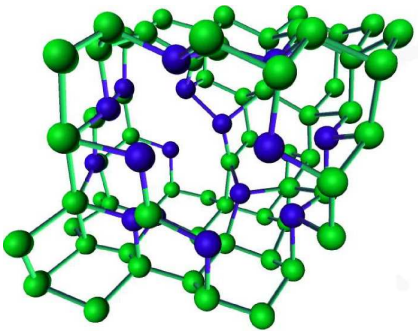

Figure 39: Structure of the final stable 10-vacancy cluster. Perfectly 4-fold coordinated atoms are displayed in green, 3-fold coordinated atoms in blue.

Electronic structure and other atomistic calculations indicate that clusters consisting of 10-vacancies are very stable against dissociation of a single vacancy [257, 260]. The empirical tight-binding (ETB) method gives a dissociation energy of $E_d = 4.7$ eV [257] and density functional tight-binding (DFTB) calculations predict 3.4 eV [260]. If we assume an additional kinetic energy barrier for dissociation of 0.6 eV and a typical prefactor of $\nu_0 = 10^{12} s^{-1}$, the frequency for the dissociation process $f = \nu_0 \exp\left(-E_d / k_B T\right)$ implies that the process should occur on the timescale of hours to seconds at the melting temperature of silicon. The time scale for complete dissociation may be even larger, considering that multiple dissociation events are necessary and single vacancies may also be absorbed or re-absorbed into the cluster. Therefore, we can conclude that the 10-vacancy cluster is stable on typical cooling timescales. The mechanism does not involve single vacancy aggregation for void formation, which involves a larger nucleation barrier. Easy stacking fault formation at the (111) interface is to be expected even at very low undercoolings considering first-principles stacking fault formation enthalpies as low as 8.4 $\mathrm{mJ/m^2}$ [242]. Thus, the nucleation rates of faulted and regular islands on the interface are almost equal. Faulted areas are competing with regular ones and may be removed from the interface in order to minimize the excess energy of coherency dislocations between faulted and regular areas at slow growth rates. When additional layers nucleate on faulted regions, the system gets kinetically trapped if the faulted region is large enough, such that dislocations are grown into the crystal even if the total coherency dislocation energy is high. As the amount of free volume is proportional to the circumference of the dislocation loop, considerably larger vacancy clusters can in principle also be formed by this mechanism. The fact that two stable vacancy clusters form in close vicinity to each other may offer an explanation to the origin of octahedral double void structures. The presented results exemplify that a very low stacking fault energy in a material can have unexpected results for void formation via complex interface kinetics effects involving a multi-stage process. Similar mech-

anisms may be expected to occur for all materials with diamond cubic crystal structure and low stacking fault energies (e.g. Germanium).

12.4 CONCLUSION

In summary, we have presented a mechanism by which vacancy clusters may be directly incorporated at a faceted solid-liquid growth interface in silicon. The mechanism involves four stages. First, formation of (111) microfacets. Second, the formation of a single layer stacking fault island occuring on a (111) microfacet. Third, as the island is overgrown by the crystal a dislocation loop of hexagonal shape is formed. Fourth, the loop shrinks and subsequently collapses into two vacancy clusters. Subsequently, depending on the size of the clusters, the vacancy clusters either dissociate or form one or two stable vacancy clusters that potentially act as seeds for the formation of larger voids.

13

A LATTICE MONTE CARLO MODEL FOR SILICON GROWTH INCLUDING TWIN BOUNDARIES

13.1 INTRODUCTION

In the two preceeding chapters, the twin formation mechanism in melt-grown silicon was clarified and it was shown that the incorporation of faulted dislocation loops at the growth interface may lead to the formation of voids in the crystal based on molecular dynamics. Both mechanisms arise from the very low stacking fault and twin boundary formation energies in silicon and the interplay with the structurally necessary coherency and anti-coherency dislocation, which have much higher energy. It is interesting to study the implications of these findings in larger systems and on longer time scales since the molecular dynamics method is limited to approximately hundreds of thousands of atoms on a nanosecond time scale. In addition, all available interatomic potentials for silicon exhibit zero twin boundary formation energy. This approximation is supposedly good enough considering that the true twin boundary formation energy is only of the order of around 20 meV, but results which take this small energy into account are desirable. This motivates the development of a Lattice Monte Carlo method, which allows for realistic twin boundary and stacking fault formation energies. This is the purpose of the present chapter.

The Lattice Monte Carlo methodology for crystal growth is briefly reviewed in the following section. Subsequently, we turn to the description of our model in Section 13.3. The reader, who is mostly interested in the results and their implications for silicon melt growth is referred to Section 13.4.

13.2 LATTICE MONTE CARLO MODELS FOR CRYSTAL GROWTH

Lattice Monte Carlo models have often been used and the findings for silicon crystal growth kinetics were reviewed in Section 3.3 of this thesis. These models describe the interactions of crystalline and liquid atoms with an Ising-like

Hamiltonian, which ,including only nearest neighbour interactions, has the familiar form:

$$H = J \sum_{i,j\ (1NN)} \sigma_i \sigma_j + h \sum_i \sigma_i. \tag{13.1}$$

Here, the two states $\sigma = +1$ and $\sigma = -1$ represent the crystalline (C) and liquid state (L) instead of the spins of a ferromagnet. Therefore, J determines the interactions at a solid-liquid interface. Any Ising-type Hamiltonian may also be written in terms of pair bond energies. In this case the total energy of the system is given by a sum over all bonds:

$$E = \sum_{i,j\ (1NN)} \epsilon_{1NN}^{ij}. \tag{13.2}$$

The pair bond energies for a crystal growth model take the following form dependent on J and h

$$\epsilon_{1NN}^{CC} = 0 \tag{13.3}$$
$$\epsilon_{1NN}^{LL} = -h \tag{13.4}$$
$$\epsilon_{1NN}^{CL} = \frac{1}{2}(J - h). \tag{13.5}$$

There are three different types of bonds and corresponding bond energies liquid-liquid ϵ_{LL}, crystal-liquid ϵ_{CL} and crystal-crystal ϵ_{CC}. In crystal growth modeling, the total energy E is interpreted as a free energy, which implies that the energies of the solid and the liquid phase have to be equal in absence of a thermodynamic driving force $\Delta\mu$, where $\Delta\mu = E_{solid} - E_{liquid} = \frac{1}{2} Z \epsilon_{1NN}^{CC} - \frac{1}{2} Z \epsilon_{1NN}^{CC} = \frac{Z}{2} h$, with Z being the number of nearest neighbours. This is achieved by casting the pair bond energies exactly in the way as stated above, dependent on the free parameters J and h. Models of this form abstract from the existence of a latent heat, i.e. in the absence of a driving force ($h = 0$) both the crystal and the liquid phase have zero energies. In other words, the Hamiltonian of such a model describes the free energy of the system rather than the internal energy.

13.3 THE MODEL

We first show how to construct a lattice that allows for twin boundaries and stacking faults. Second, based on the new lattice, a modified Hamiltonian is proposed. This Hamiltonian stabilizes the diamond phase as a ground state on the new lattice and allows for convenient parameterization of the stacking fault energy.

First, a unit cell that allows for twinning in one of the four equivalent (111) has to be constructed. We start from an orthorombic unit cell with the (111) direction as the z-axis of the cell so as to conserve the unit cell when performing the reflections (see Figure 40). The reflection planes have to be parallel to a boundary plane of the unit cell, so that the reflected unit cell can be put back into the original one. Starting from the diamond lattice A we first apply reflection b which gives the reflected lattice B. This lattice is then added to the original unit cell. In the same way reflections at the planes c and d are applied and the corresponding lattices C and D are added to the unit cell. The original and the final cell are displayed in Figure 41

In order to implement the appropiate Hamiltonian we have to consider the neighboorhood shells of the new lattice. The new unit cell gives rise to a different crystal lattice with three additional neighbourhoods indexed TN1, TN2 and TN3 (see Figure 42). The TN1 and TN2 neighbours are closer than the original nearest neighbours (1NN), while the TN3 neighbour are farther away than the second neighbours (2NN). For comparison of the number of neighbours in the new and in the original lattice see Table 12. The crystal atoms in the lattice can be regarded as interacting with a liquid reservoir when they have unoccupied neighbour sites.

The Hamiltonian in our model is a sum over pair bond energies corresponding to the five neighbourhood shells NN1, NN2, TN1, TN2 and TN3:

$$H = \sum_{i,j\ (1NN)} \epsilon^{ij}_{1NN} + \sum_{i,j\ (2NN)} \epsilon^{ij}_{2NN} \tag{13.6}$$

$$+ \sum_{i,j\ (1TN)} \epsilon^{ij}_{1TN} + \sum_{i,j\ (2TN)} \epsilon^{ij}_{2TN} + \sum_{i,j\ (3TN)} \epsilon^{ij}_{3TN}. \tag{13.7}$$

The set of pair bond energies for all neighborhood shells for bonds between crystal (C) and liquid states (L), which complete the model, are:

$$\begin{array}{lll}
\epsilon^{CC}_{1NN} = -\frac{3}{2}\epsilon^{CL}_{1NN} & \epsilon^{LL}_{1NN} = -\frac{4}{7}h & \epsilon^{CL}_{1NN} = \frac{4}{7}\frac{1}{2}(J_{1NN} - h) \\
\epsilon^{CC}_{2NN} = -\epsilon^{CL}_{2NN} & \epsilon^{LL}_{2NN} = 0 & \epsilon^{CL}_{2NN} = \frac{2}{3}\frac{1}{2}J_{2NN} \\
\epsilon^{CC}_{1TN} = \frac{1}{2}J_{1TN} & \epsilon^{LL}_{1TN} = 0 & \epsilon^{CL}_{1TN} = 0 \\
\epsilon^{CC}_{2TN} = \frac{1}{2}J_{2TN} & \epsilon^{LL}_{2TN} = 0 & \epsilon^{CL}_{2TN} = 0 \\
\epsilon^{CC}_{3TN} = \frac{1}{2}J_{3TN} & \epsilon^{LL}_{3TN} = 0 & \epsilon^{CL}_{3TN} = 0
\end{array}$$

These pair bond energies are parameterized by the six free parameters of the model: the interaction parameters J_{1NN}, J_{2NN}, J_{1TN}, J_{2TN} and J_{3TN} one for each neighborhood shell, and the parameter h, which is used to apply a thermodynamic driving force for growth. All of these parameters are supposed to be positive numbers.

The pair bond energies are chosen in order to satisfy four conditions:

- *Condition 1* The cubic diamond structure is the stable ground state of the lowest possible energy.
- *Condition 2* Parameterization of the stacking fault and twin boundary energy is achieved via one free parameter J_{TN3}.
- *Condition 3* In the absence of a thermodynamic driving force ($h = 0$) the cubic diamond phase can coexist with the liquid phase, i.e. their free energies have to be equal.
- *Condition 4* A thermodynamic force for growth $\Delta\mu$ may be applied via the parameter h, such that $\Delta\mu = 2h$ holds.

In order to stabilize the diamond structure as the ground state J_{TN1} and J_{TN2} should be set to very high positive values, so as to rule out that two lattice sites closer than the nearest neighbour distance of the original diamond lattice are allowed to be of type *crystalline*. This stabilizes the cubic diamond structure, but the ground state is still degenerate since hexagonal diamond has the same energy.

The degeneracy is lifted by letting J_{TN3} assume a non-zero positive value. J_{TN3} is also the parameter that gives the extrinsic stacking fault as well as the twin boundary energy, therefore including this parameter satisfies the second condition. J_{TN3} corresponds to the stacking fault energy because a stacking fault atom sees an occupied lattice neighbour $TN3$, while this is not the case for an atom in the perfect cubic diamond lattice.

The third condition, coexistence of the diamond and liquid phase in absence of a thermodynamic driving force is satisfied by choosing ϵ^{CC}_{1NN},ϵ^{CL}_{1NN},ϵ^{CC}_{2NN} and ϵ^{CL}_{2NN} as given above. It is easily verified by simple bond counting that the energy of the cubic diamond phase on the new lattice E_{dia} equals that of the liquid phase E_{liq}, which we have chosen to be zero.

$$E_{dia} = \frac{1}{2}(4 \cdot \epsilon^{CC}_{1NN} + 2 \cdot 3 \cdot \epsilon^{CL}_{1NN} + 12 \cdot \epsilon^{CC}_{2NN} + 2 \cdot 6 \cdot \epsilon^{CL}_{2NN}) = E_{liq} = 0 \qquad (13.8)$$

The factors of 2 occur here, because the ratio of occupied crystal atoms to non-occupied ones is $1 : 2$ on the new lattice. The other factors correspond to the number of neighbours on the diamond lattice and the number of non-occupied neighbour sites of diamond on the twin lattice (compare Table 12). The equation may be verified by plugging in the pair bond energies as given above.

In the presence of a thermodynamic driving force, however, it follows from the choice of the bond energies that $\Delta\mu = E_{dia} - E_{liq} = 2h$, which is the same as in the common diamond lattice Ising model. This completes the setup of the model and the proof that all necessary conditions above are fulfilled.

neighbours	nr. of sites cubic diamond lattice	nr. of sites twin lattice	nr. of empty sites diamond on twin lattice
1NN	4	7	3
2NN	12	18	6
1TN	-	1	1
2TN	-	6	6
3TN	-	1	1

Table 12: Number of neighbours on the cubic diamond, on the virtual twin lattice and number of empty sites when the virtual lattice is occupied with the cubic diamond structure. Naturally, the first and the third column sum up to the second column.

The parameters J_{NN1} and J_{NN2} are equivalent to the first and second nearest neighbours in a simple diamond lattice model with only first and second nearest neighbour interactions.

13.3.1 *Parameterization*

For parameterization of the model we follow along the lines of Beatty and Jackson [87]. We use available data for the free energies of solid-liquid interfaces for fitting, that has been determined by molecular dynamics simulations [265] (see Table 13). Using this solid-liquid interface free energy reference data for the (100), (110) and (111) interface and fitting J_{1NN} and J_{2NN} to it would result in an unphysically high second nearest neighbour interaction and a misplaced roughening transtion (Table 13). We found that the ratio of the nearest versus second nearest neighbour interaction has a large impact on the location of the roughening transition temperature of the (111) solid-liquid interface and its growth velocity as a function of undercooling. This is supposed to be due to the varying edge free energy. In order to improve the model, we fix the ratio J_{2NN}/J_{1NN} to a physically more meaningful value of 0.047, which still allows to describe the interface free energies quite reasonably. This assumption results in a realistic roughening transition temperature as shown in Figure 52. The fitting pocedure determines $J_{1NN} = 0.416$ eV and $J_{2NN} = 0.020$ eV. J_{TN1} and J_{TN2} are set to arbitrary large values in order to stabilize the diamond structure, leaving h and J_{TN3} to be defined.

The parameter h may be determined by using an estimate for the entropy difference between the solid and the liquid state, i.e. $\Delta S = L/T_m$, where L is the latent heat and T_m is the melting temperature. It then follows from

$$\Delta\mu = 2h = (T - T_m)\Delta S = (T - T_m)L/T_m, \tag{13.9}$$

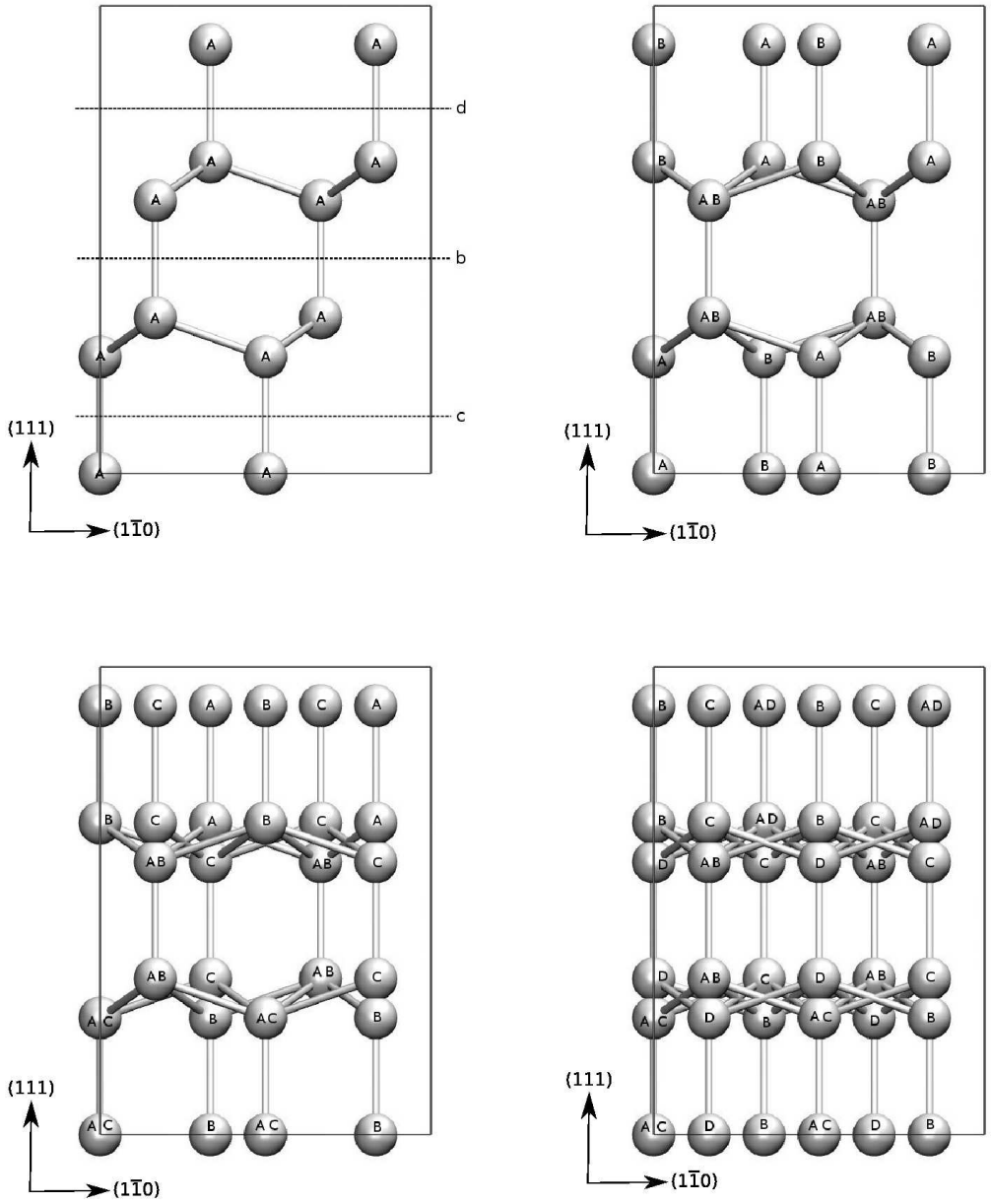

Figure 40: For constructing the lattice of our model, three reflection operations are applied at the planes b, c and d, corresponding to three different twin lattices B, C and D. These lattices are then added to the original lattice A. Note that this is only possible because the reflections have been applied in planes parallel to a unit cell boundary plane. All of the sites of the original lattice A overlap with sites of one of the twin lattices.

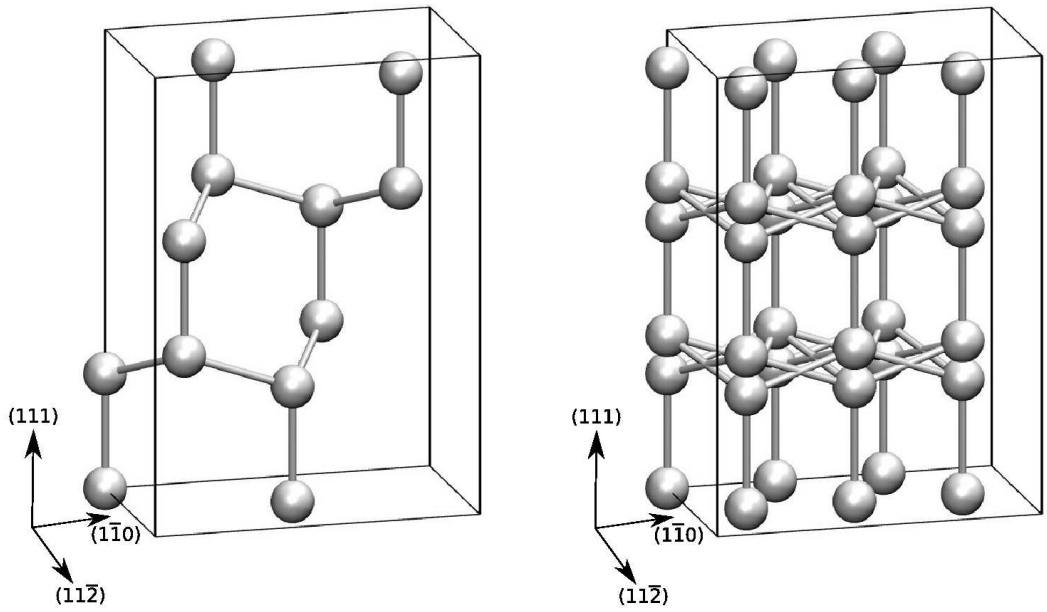

Figure 41: Left: An orthorombic unit cell of the cubic diamond crystal structure is used as the starting point for constructing the new lattice.
Right: The final twin lattice unit cell after construction as shown in Figure 40.

Interface	Interface energy	our model (eV/Atom)	our model (J/m^2)	Ref. [265] (J/m^2)
(111)	$\frac{2}{\sqrt{3}}(J_{1NN} + 6J_{2NN})/a^2$	0.268	0.340	0.34
(110)	$\sqrt{2}(J_{1NN} + 6J_{2NN})/a^2$	0.268	0.416	0.35
(100)	$(2J_{1NN} + 8J_{2NN})/a^2$	0.496	0.544	0.42

Table 13: Solid-liquid interface energies of silicon implied by the parameterization of the model in comparison to the reference energies from [265].

Figure 42: The different neighbourshells for the new twin lattice: 1NN and 2NN correpsond to the common nearest and second nearest neighbour distances in cubic diamond. 1TN, 2TN and 3TN are additional neighbour shells on the twin lattice. Note that 1TN and 2TN are closer than nearest neighbours (1NN). The 3TN shell is necessary to include in order to distinguish between the ideal diamond lattice and stacking faults and twin boundaries.

J_{1NN} (eV)	J_{2NN} (eV)	J_{TN1} (eV)	J_{TN2} (eV)	J_{TN3} (eV)	h (eV)
0.416	0.020	large	large	0.020	$(T - T_m) \cdot 1.56 \cdot 10^{-4}$eV/K

Table 14: Parameter set fitted to (111) interface energy of 0.34 J/m^2, and assuming a ratio of $J_{1NN}/J_{2NN} = 0.047$. J_{TN1} and J_{TN2} are set to large values (> 1000 eV) in order to stabilize the diamond structure as discussed in the text.

Authors	Ref.	Year	Method	ISF J/m^2	ESF	TSF	ISF meV/at	ESF	TSF
Ray/Cockayne	[266]	1971	Expt.	51	-	-	40	-	-
Alexander	[267]	1979	Expt.	58	-	-	46	-	-
Föll/Carter	[268]	1979	Expt.	69	60	-	54	47	-
Chen/Falicov	[269]	1974	PP	55	-	-	43	-	-
Weigel et al	[246]	1975	EHT	86	85.5	43	68	67	34
Mattheiss/Patel	[245]	1981	NTB U	110	85	38	87	67	30
Mattheiss/Patel	[245]	1981	NTB R	64	44	19	50	35	15
Sanchez-D. et al	[270]	1981	GWF	190	90	-	150	71	
Paxton/Sutton	[244]	1989	TB-SDM	115	-	56	91	-	44
Paxton/Sutton	[244]	1989	TB-IDM	56	-	29	44	-	23
Louie et al	[271]	1985	PW(U)	40	26	-	32	20	-
Chou et al	[272]	1985	PW(U)	33	26	-	26	20	-
Gross/Teichler	[243]	1991	LO-DFT	87.7	70.8	33.8	69	56	27
Käckell et al	[273]	1998	DFT-LDA	38	20	-	30	16	-
C. Raffy et al	[242]	2002	DFT-LDA	39.3	20.6	8.4	31	16	7
Iwata et al	[241]	2003	DFT-LDA	-	-	5.8	-	-	5

Table 15: Energies for the extrinsic (ESF), the intrinsic (ISF) and the twin stacking fault (TSF) from different sources.

and by using $L = 0.525$ eV/atom for the latent heat of silicon, that h is related to undercooling $T - T_m$ via

$$h = (T - T_m) \cdot 1.56 \cdot 10^{-4}\text{eV/K}. \tag{13.10}$$

The parameter J_{3TN} of the proposed model directly parameterizes the stacking fault and the twin boundary energy. Data for the formation energies of different stacking faults are available from the literature (see Table 15). We have concluded from this data that 20 meV/atom should be a reasonable value for the twin stacking fault energy $J_{3TN} = 2\epsilon^{CC}_{3TN} = 0.020$ eV. The final parameterization of our model is summarized in Table 14.

13.4 RESULTS AND DISCUSSION

13.4.1 *Qualitative assessment of the growth kinetics at the Si(111) solid-liquid interface*

Using the model as parameterized above we simulate growth of the silicon (111) solid-liquid interface with an undercooling of 25 K and 50 K, respectively. We use a simulation cell containing 11.4 million virtual lattice sites (of the twin lattice that allows stacking faults as decribed in Section 13.3). This allows for solidification of 3.8 million atoms. The size of the simulated patch of the (111) solid-liquid interface was 92.2 x 79.8 nm and periodic boundary conditions have been applied lateral to the surface. The simulations took only 6 hours to complete on a single processor standard desktop machine and corresponded to a physical time of 18 ns.

We find a pronounced difference in the growth modes and growth morphology at 25 K and at 50 K undercooling. At 25 K undercooling, growth proceeds layer-by-layer even though nucleation of two-dimensional nuclei occurs at various points of the same layer simultaneously (see Figure 43). At this undercooling stacking fault formation plays only a minor role, i.e. the formation of small faulted islands occurs only as a statistical fluctuation. We observe some faulted islands that grow larger (see the inset in Figure 43 and Figure 44), but subsequently disappear as neighbouring regular crystal steps are growing. All of the snaphots have been visualized using OVITO [274].

Growth of the (111) interface at an undercooling of 50 K is remarkably different and more complex then observed at 25 K. In this case, stacking fault islands are observed much more frequently (see Figure 45). Once faulted islands are formed, they are subsequently stabilized when regular atoms rapidly nucleate new layers on top of them (see arrows in Figure 45). During subsequent growth, faulted islands compete with the regular crystal (see Figure 46). At this stage smaller islands still disappear but larger ones are sustained until the end of the simulation (see Figure 47). As the boundary between faulted and regular islands perpendicular to the fault plane can not be coherent, coherency and anti-coherency dislocations may be expected to form at this boundary (see also the discussion in Chapters 12 and Chapter 11 of the present thesis). This process, however, can not be observed in the simulation due to the lattice approximation. When large faulted islands are entirely grown into the crystal, stacking fault tetrahedra can expected to be formed (compare e.g. the island in the lower right in Figure 47). Stacking fault tetrahedra are sometimes observed as defects in ion-implanted silicon [275], but have also been found in silicon rapidly solidified from the melt [276]. Our simulation suggests a possible mechanism for the formation of stacking-fault tetrahedra at a (111) solid-liquid interface or facet. To our knowledge, stacking-fault tetrahedra have so far not been considered to emerge from the kinetics of the growth interface.

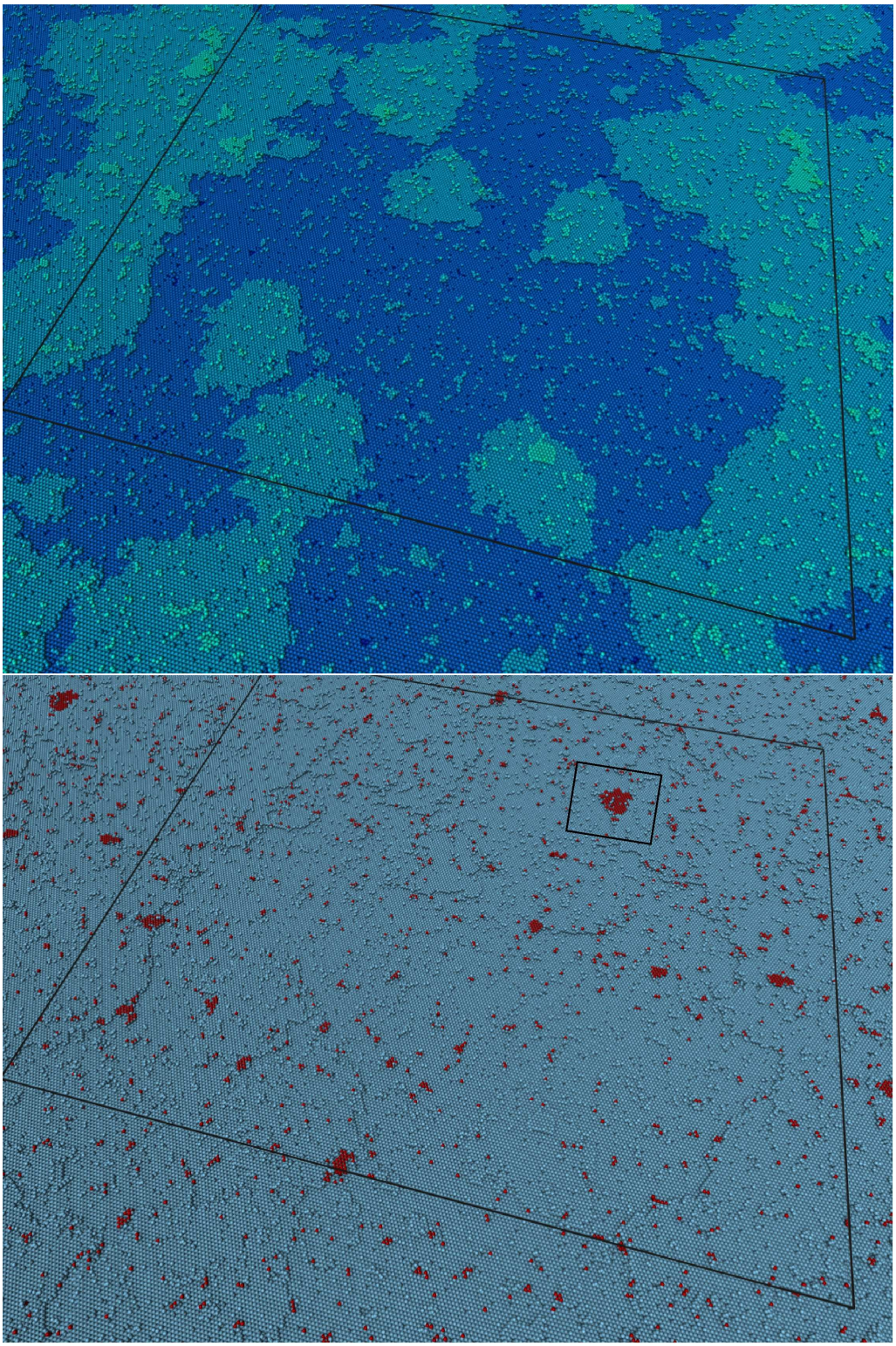

Figure 43: Top: At an undercooling of 25 K the (111) interface is grown layer by layer. Colour coding is z-direction. Bottom: Same snapshot with stacking fault atoms displayed in red.

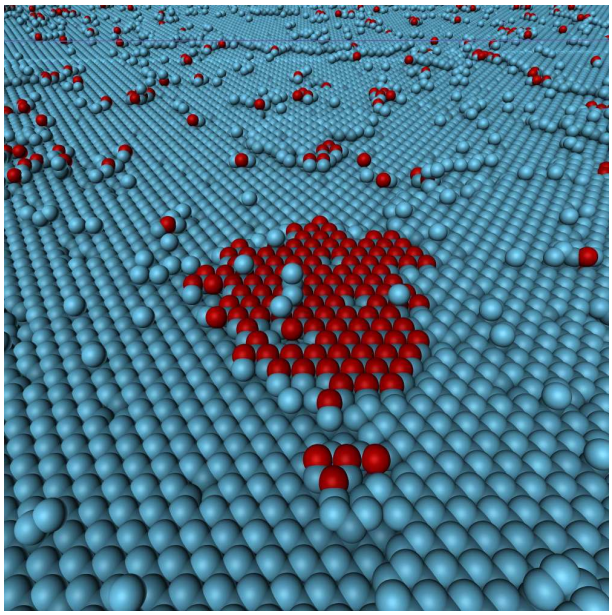

Figure 44: Zoom-in of a small faulted island adjacent to a regular crystal step at the interface, marked by the small rectangle in Figure 43. The faulted island will subsequently disappear, giving room to the regular crystal step.

13.4.2 *Interface growth velocities*

In order to access the velocity versus undercooling relation under Czochralski growth conditions, we adopt the procedure used by Beatty and Jackson [87]. The physical time corresponding to a simulation time step has been determined by fitting the growth velocity of the rough (100) interface to the relation measured in experiments

$$V_{(100)} = 0.12\Delta T \frac{\mathrm{m}}{\mathrm{sK}}. \tag{13.11}$$

Simulation of the growth of a (111) interface then yields a 2D nucleation rate. The 2D nuclei limit the growth rate on the smooth (111) interface, and thus the growth velocity in the simulations depends on the interface area. However, the 2D nucleation rate per interface area J can be determined. For the parameterization of our model as stated above we find

$$J = 3.64 \cdot 10^{26} \exp\left(\frac{-143.8\ \mathrm{K}}{\Delta \mathrm{T}}\right) \frac{1}{\mathrm{m^2 s}}. \tag{13.12}$$

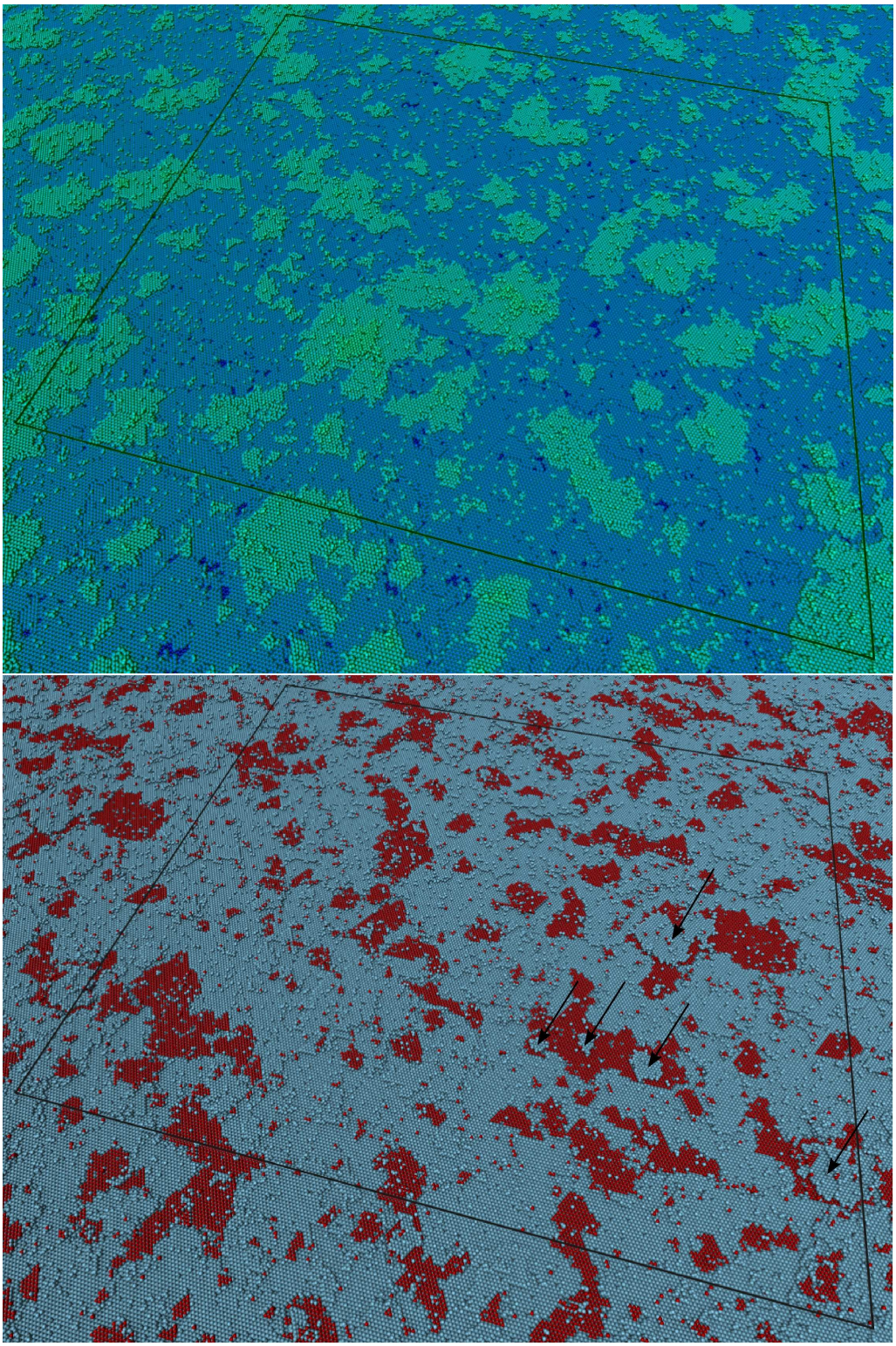

Figure 45: Si(111) solid-liquid interface at 50 K undercooling (snapshot 1 of 3). Top: Larger faulted islands may nucleate and regular atoms rapidly nucleate on top of them (arrows), which stabilizes the faulted nuclei. Bottom: Same with stacking faults in red.

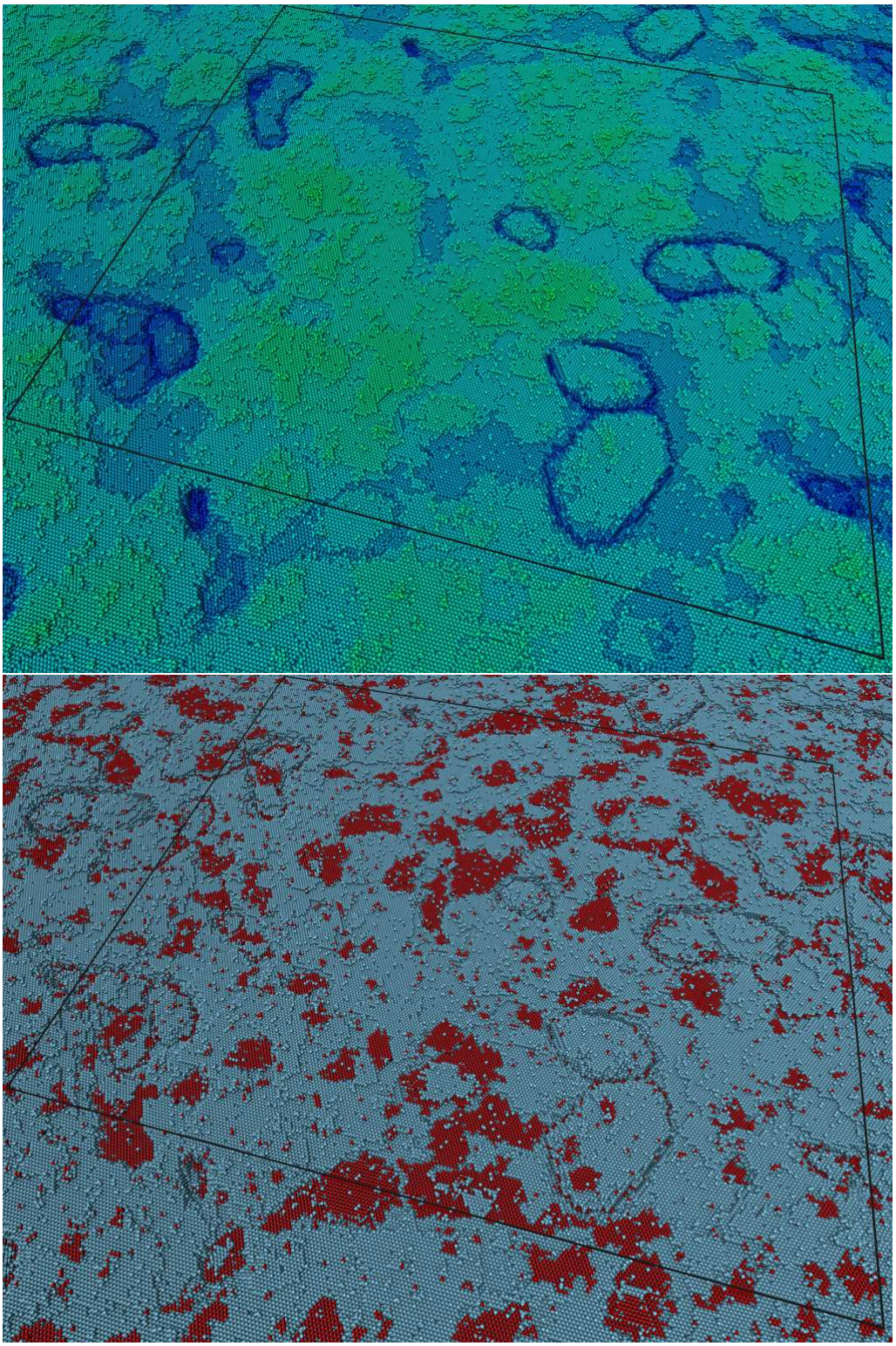

Figure 46: Si(111) solid-liquid interface at 50 K undercooling (snapshot 2 of 3). Top: Growth of additional layers on top of faulted islands and lateral growth leads to incoherent boundaries between faulted and regular islands. Bottom: Same with stacking faults in red.

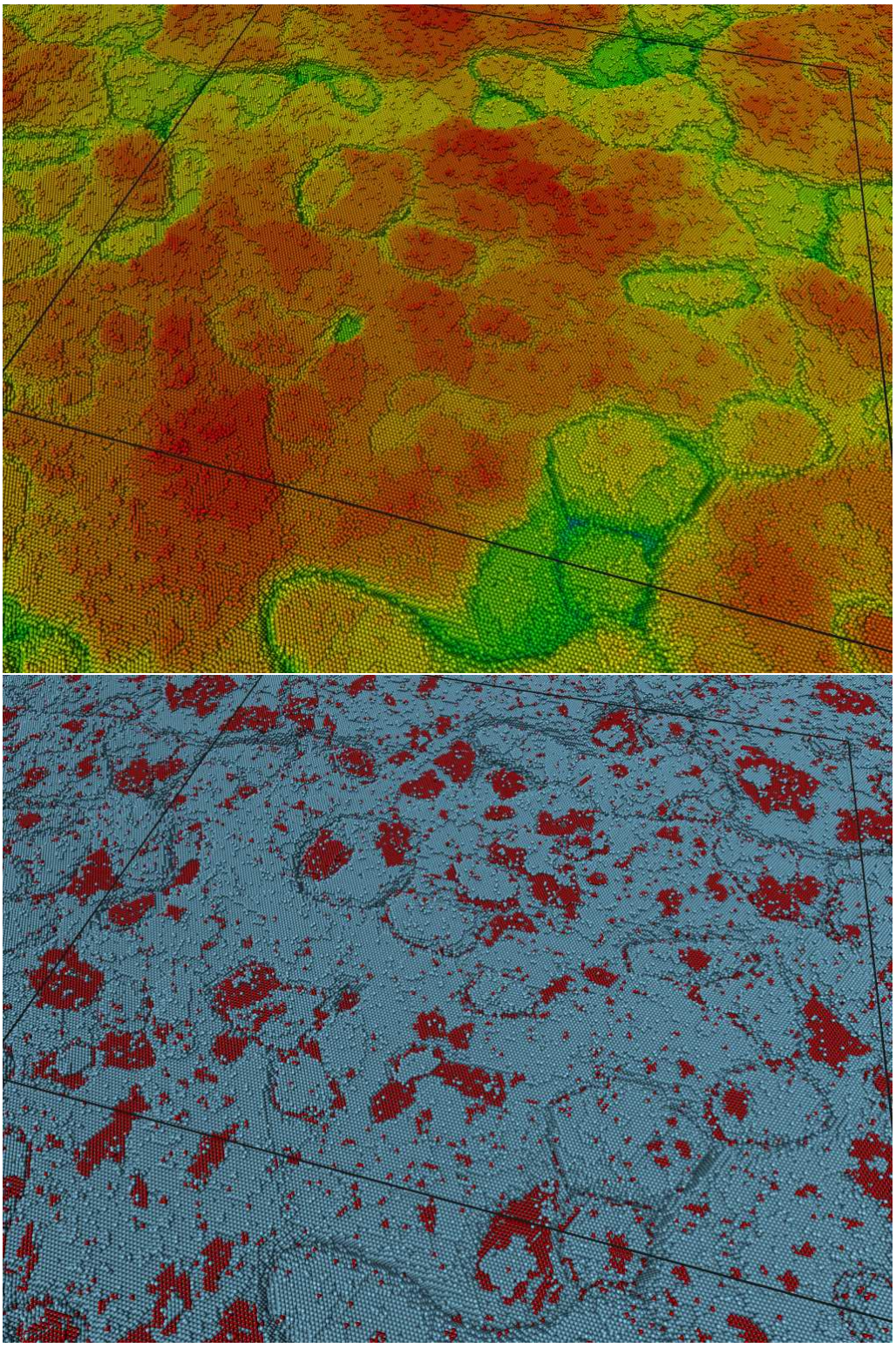

Figure 47: Si(111) solid-liquid interface at 50 K undercooling (snapshot 3 of 3). Top: Small faulted islands may grow out, butlarger faulted islands are sustained and continue to grow. Bottom: Same with stacking faults in red.

The expression for the steady-state growth velocity dependent on this nucleation rate J following Obretenov [277] is

$$V_{(111)} = \frac{hJS}{1 + (J/v)^{2/3} S/(\beta b^{1/3})}. \tag{13.13}$$

As in Ref. [87] we have used the following numbers: monolayer height $h = 3.13\text{A}^\circ$, geometric factor $b = 4$ and numerical factor $\beta = 0.97$, estimate of the interface corresponding to a facet under Czochralski conditions $S = 0.001\ \text{m}^2$. For the 2D spreading velocity of the nucleus we used $v = 0.3\frac{\text{m}}{\text{s}} \cdot \Delta\text{T}$. Eq. (13.13) is plotted in Figure 48. The nucleation of new layers occurs at an undercooling below approximately 3.5 K, somewhat lower than the estimate of Beatty and Jackson of 5 K [87]. The available values from experiments are 1.5 K by Edwards [89], 6 K by Ciszek [90] and 9 K by Abe [91].

The interface growth velocities of the rough (110) interface, and the rough (100) interface, which was used for calibration, are not limited by nucleation. Thus, their growth velocities do not depend on the interface area in the simulation cell and may directly be determined from the simulations. A linear dependence is expected and observed in this case (Figure 48).

Our model also allows to calculate the growth velocity in the presence of multiple (111) twin boundaries, when growing the crystal in the (211) direction parallel to the twin boundaries (see Figure 50). In this case we find a close to linear dependence above an undercooling of 2 K with growth velocities that are comparable in magnitude with the rough (100) and (110) interface (see Figure 49). The shape of the curve indicates that nucleation is much facilitated as compared to flat (111) interfaces, although it is not completely barrier free. This can be understood by the Hamilton-Seidensticker growth mechanism [93, 278], in which the twin boundary provides favourable site for nucleation of new layers. Although the nucleation barrier is largely reduced compared to the nucleation barrier of the perfect (111) interface, there is still a barrier present. Our simulations indicate that highly twinned silicon crystals may rapidly be grown from the melt with a very low density of extended defects being incorporated. The reason is that the (111) microfacets at the solid-liquid interface are too small for faulted islands to be sustained and growth proceeds in a controlled step-flow like manner after new layers are nucleated at the twin boundary, which would drive out faulted island as the step continues to grow.

13.4.3 *Roughening transition*

Considering the large number of publications concerned with the roughening transition of the (111) solid-liquid interface of silicon, it appears interesting to investigate the properties of the transition by our model when stacking faults are included. The roughening transition shows up as a peak in the interface

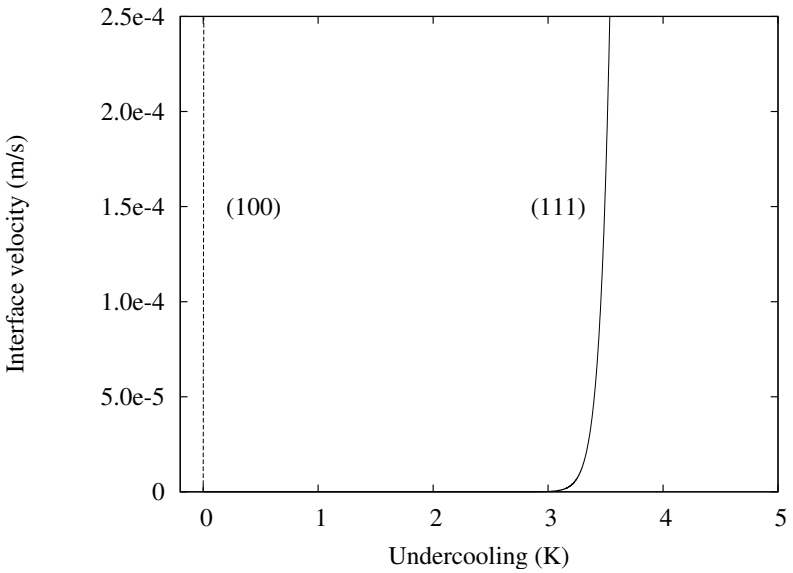

Figure 48: The (111) interface velocity (solid line) shows an onset for growth at about 3K, which compares to the onset at 5K in the work of Beatty and Jackson [87]. The (100) growth velocity (dashed line) is much faster so it shows as a vertical line on the scale of this plot.

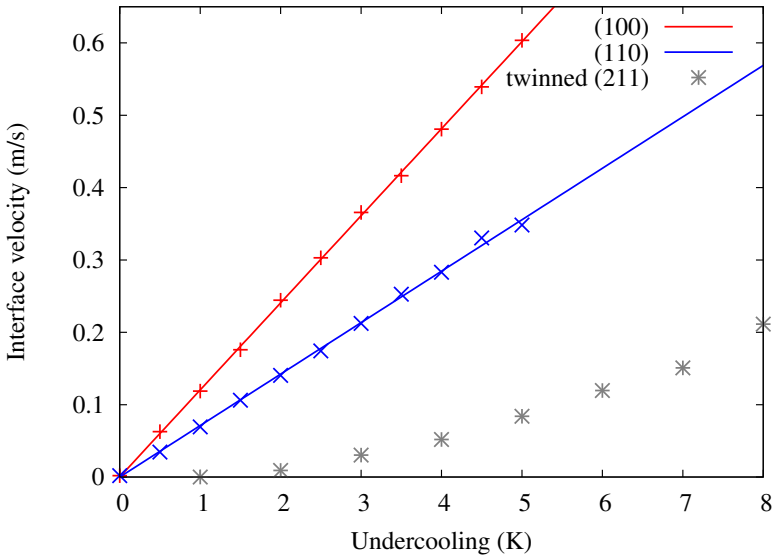

Figure 49: The velocity of the (100) and (110) interface as compared to the velocity of a growth front consisting of multiple twins parallel to the growth direction ((211) twinned). The twinned configuration is shown in Figure 50

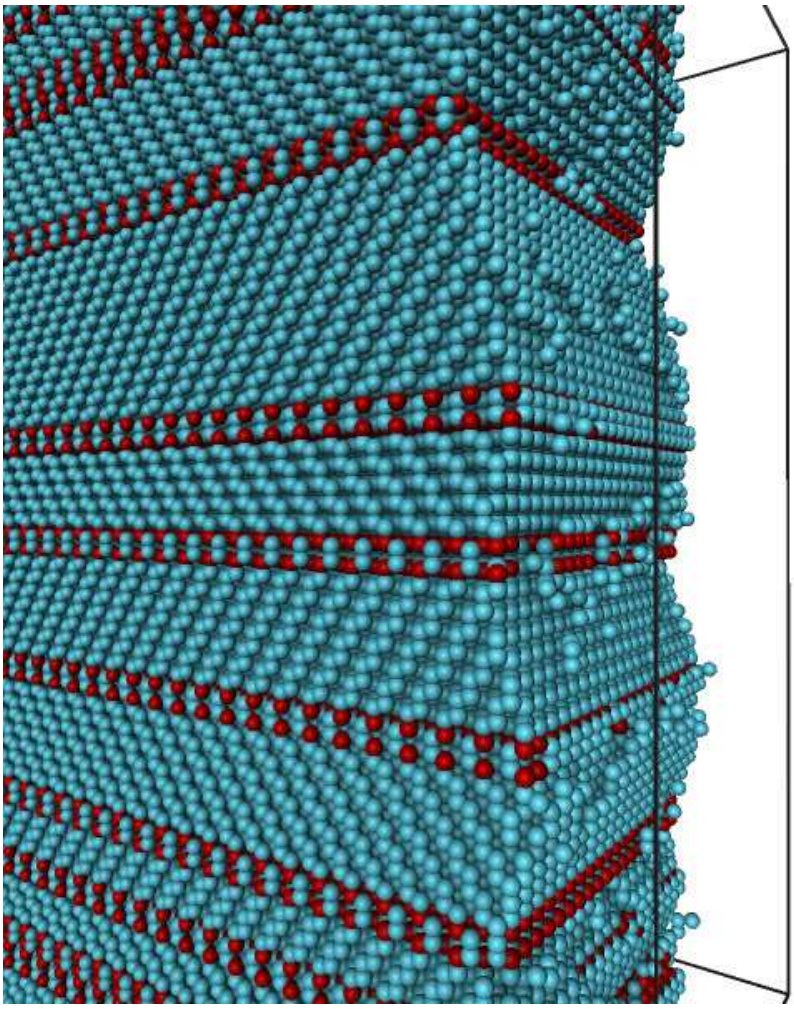

Figure 50: Growing a multiply twinned crystal with (111) facets in the (211) growth direction. The twin boundaries provide favourable nucleation sites for fast growth free of additional extended defects being incorporated through faulted islands.

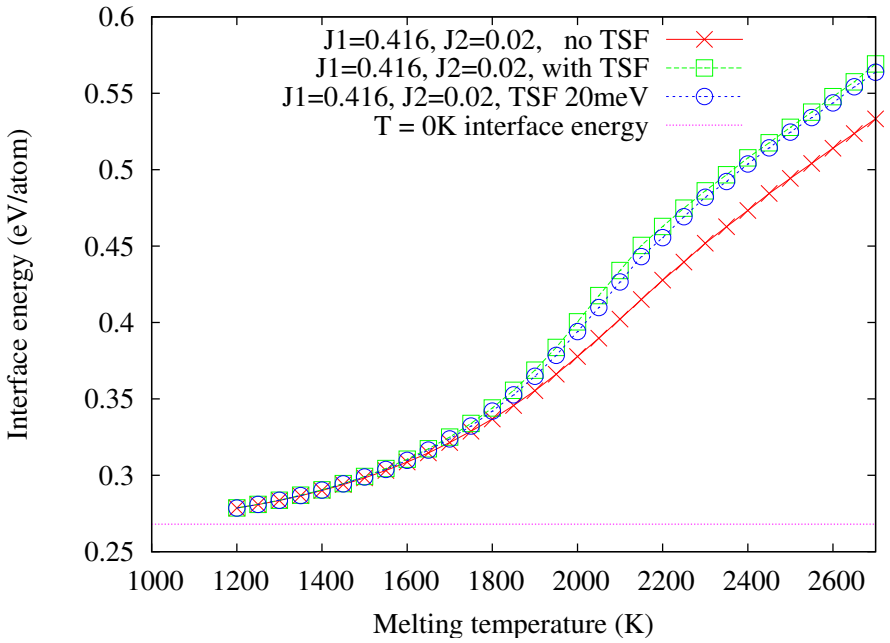

Figure 51: Interface free energy F^i as a function of the melting temperature for three different parameterizations of the stacking fault energy.

free energy as a function of the melting temperature. In this case, the melting temperature is treated as a free parameter and equilibrium simulations are carried out at these temperatures without undercooling. We compare three cases corresponding to three parameterizations of the stacking fault energy by adjusting J_{TN3}: First, we simulate the equilibrium curve with J_{TN3} set to a very high energy. This corresponds to the case of former models, that did not allow for the possibility of stacking fault formation. Second, we apply the model as in the sections above with a realistic stacking fault energy of 20 meV/atom. Third, we set the stacking fault energy to zero. We observe that stacking faults contribute to the interfacial free energy via configurational contributions (see Figure 51). In the two cases where stacking faults are possible we observe a more pronounced peak in the interface heat capacity curve (Figure 52). Furthermore, the roughening transition occurs at an approx. 100 K lower temperature , when stacking faults are possible (compare Figure 52).

13.5 CONCLUSIONS

We have presented a Lattice Monte Carlo for silicon growth from the melt that explicitly includes the possibility of stacking faults and twin boundaries. For this purpose a new crystal lattice has been constructed and a new model Hamiltonian

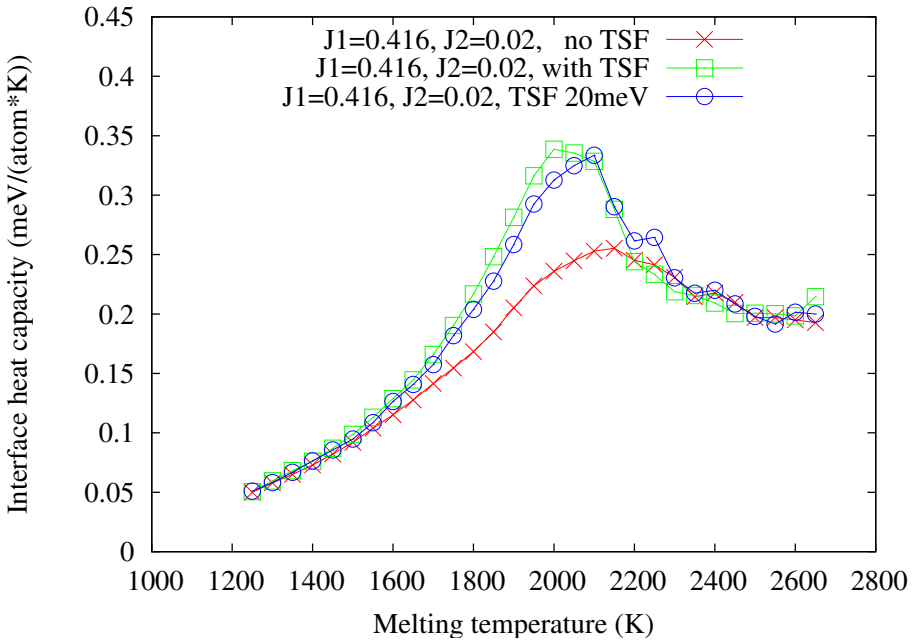

Figure 52: The interface heat capacity $c_V^i = \frac{\partial F^i}{\partial T_m}$ as a function of the melting temperature. Note the somewhat lower peak, when stacking faults are included.

has been devised. The model includes nearest and second nearest neighbour interactions and the interaction with stacking fault and twin boundary sites. It allows for easy paramterization of the stacking fault energy via a single parameter. The model provides a convenient tool to study phenomena that are related to twin boundary and stacking fault formation in silicon growth. We have shown that stacking fault formation significantly affects the growth kinetics and morphology of the silicon (111) solid-liquid growth interface. Two distinct growth modes of the interface have been identified: At an undercooling of 25 K growth of the interface proceeds layer-by-layer. Faulted islands may temporarily form but normally decay on short time scales. At an undercooling of 50 K faulted islands may be sustained and faulted areas compete with areas of the regular crystal. As faulted islands are laterally not commensurate with the regular crystal, formation of extended defects may be expected. We conclude that large islands do not decay on the relevant timescales and may lead to the kinetically determined formation of stacking-fault tetrahedra. Furthermore, we calculated the growth velocity of a multiply twinned silicon crystal parallel to the twins. We find that growth is fast as compared to the (111) solid-liquid interface. An exact linear relationship between growth velocity and undercooling, as expected for nucleation barrier-free growth, however, does not hold. The twins provide favourable sites for nucleation as described by the Hamilton-Seidensticker growth mecha-

nism. As this mechanism is reentrant and faulted islands may not be sustained on (111) microfacets, this implies that multiply twinned silicon crystals may most likely be rapidly grown from the melt with very low densities of extended defects. As twin boundaries have almost no influence on the electronic properties of a silicon crystal, growth of such highly-twinned crystals may be an interesting alternative for electronic applications of silicon crystals. Finally, we have shown that the inclusion of stacking faults results in a significant correction to the roughening transition temperature and affects the height of the peak in the interface heat capacity.

SUMMARY

In the present work the intrinsic point defect physics of $CuInSe_2$ and $CuGaSe_2$ has been rigorously studied by use of the HSE06 screened-exchange hybrid functional. Additionally, the formation processes of twin boundaries, stacking faults and voids in silicon growth form the melt were studied by molecular dynamics and by a new lattice Monte Carlo model. The key findings are summarized below.

INTRINSIC POINT DEFECT PHYSICS IN CU(IN,GA)SE_2

- It was shown that the Heyd-Scuseria-Ernzerhof functional provides an accurate description of the band gaps of all investigated chalcopyrite compounds $CuInSe_2$, $CuGaSe_2$, $CuInS_2$ and $CuGaS_2$, when a single value of the exchange screening parameter of 0.13 $Å^{-1}$ is used. At the same time the structural parameters and bulk moduli improve towards the experimental values. This established that the functional can be expected to yield more accurate defect formation energies than local density functionals.

- With respect to the copper vacancy, it was found that the defect formation energy obtained from screened-exchange hybrid density functional theory is about 0.4 to 0.6 eV higher than the values obtained from LDA in former studies [8, 34]. The formation energies under copper-rich conditions are around 0.5 eV higher for the sulfides than for the selenides. In contrast, substituting indium with gallium has a negligible effect on the formation energies.

- The Fermi pinning level due to spontaneous copper vacancy formation at the buffer-absorber interface depends on the copper chemical potential. Experimentally observed pinning in $CuInSe_2$ and $CuGaSe_2$ is consistent with the theoretical pinning levels under copper-rich conditions. Given the same copper chemical potential, the sulfides $CuInS_2$ and $CuGaS_2$ may sustain up to 0.5 eV higher Fermi levels before pinning occurs.

- The migration barriers of the copper vacancy were found to be very similar, i.e. 1.26 eV for $CuInSe_2$ and of comparable magnitude for the other chalcopyrites. The estimated diffusion coefficent for $CuInSe_2$ is consistent with some measurements on single crystals when direct experimental methods are used such that internal electric fields and the influence of grain boundaries can be ruled out.

- Copper interstitials may relax into a stable or metastable configuration on four symmetrically inequivalent sites with formation energies as low as 0.17-0.38 eV (referenced to $\Delta\mu_{Cu} = 0, E_F = 0$), which are much lower than previously reported values based on local approximations.
- A direct interstitial and indirect interstitialcy diffusion mechanism with migration barriers as low as 0.22 and 0.34 eV have been identified. These results provide evidence that the fast interstitial diffusion of copper is important for understanding metastabilities, Fermi level pinning at interfaces, electric-field induced creation of p-n junctions and widely varying experimentally measured diffusion coefficients in CIS devices.
- Characterization of the cation antisites revealed that $Cu_{In,Ga}$ antisites are hole traps in $CuInSe_2$ and $CuGaSe_2$. The interactions of the full copper d shell of the defect atom with the anion p electrons and contributions from the d shells of the nearest copper neighbours lead to two deep levels in the gap, which can be attributed to defect transitions commonly observed in admittance and photocapacitance spectroscopy. Low-temperature photoluminescence measurements in $CuGaSe_2$ thin-film solar cells show a free-to-bound transition in very good agreement with the calculated optical transition of an electron trap arising from the Ga_{Cu} antisite. Cu_{In} and Cu_{Ga} can be contained in high quantities under certain conditions and may contribute to self-compensation in addition to $(In, Ga)_{Cu}$ antisites and copper vacancies.
- With repect to the previously proposed lattice-relaxed DX configuration of $(In, Ga)_{Cu}$, no pinning level was found within the band gap of $CuInSe_2$ in contrast to $CuGaSe_2$, thus excluding metastable DX behaviour for $CuInSe_2$.
- As additional formerly proposed candidates for metastable point defects, the $V_{Se} - V_{Cu}$ complex and the single selenium vacancy V_{Se} were found to exhibit similar metastable charge transition levels as was found based on former local density functional theory studies. However, the high formation energies of these defects imply that its concentration in thermal equilibrium is not sufficiently high to explain experimentally observed metastabilities.
- V_{In} and V_{Ga} show similar hole localization properties as $Cu_{In,Ga}$, but are contained only in minor quantities in the material.
- In order to observe localization of holes on Cu_{In}, Cu_{Ga} antisites as well as on V_{In} and V_{Ga} vacancies use of the screened-exchange hybrid functional in conjunction with supercells of 216 atoms turned out to be essential.
- The complete picture of the intrinsic defect physics allowed to draw conclusions about the optimal preparation conditions of $Cu(In,Ga)Se_2$ absorber

material in terms of the chemical potentials. It was found that the optimal conditions as far as the point defect physics is concerned are located towards the selenium-rich side. However, the conditions should not be pushed to the maximally selenium-rich end (equivalent to maximally copper-poor *and* indium-rich conditions) in order to avoid the formation of detrimental $Cu_{In,Ga}$ antisites hole traps.

- Finally, it should be emphasized, that Figure 33 on page 106 represents a *guide map* to the complete intrinsic point defect physics in $CuInSe_2$ and $CuGaSe_2$ and can be viewed as a convenient representation of the most central results.

TWIN BOUNDARY, STACKING FAULT AND VOID FORMATION IN SILICON GROWTH FROM THE MELT

- By using molecular dynamics, the twin boundary formation mechanism in melt-grown silicon has been revealed.
- In contrast to formerly proposed models, we find that twins do not nucleate on (111) microfacets in the perfect crystal, but exclusively occur in the vicinity of grain boundaries. The excess energy of the interfacial area between matrix and twinned crystal prevents spontaneous twin formation at the growth interface of a perfect crystal.
- At an undercooling of 150 K, the formation of metastable twin bounded loops with incoherent interfaces to the matrix consisting of coherency and anticoherency dislocations has been observed.
- These dislocation loops disband within nanoseconds into vacancy clusters of 10 or more vacancies. Subsequently, they can act as nucleation seeds for the experimentally observed octahedral single and double voids.
- A Lattice Monte Carlo growth model was presented that extends the model commonly used for silicon and other cubic diamond materials, for the possibility to include (111) stacking faults and twin boundaries. This model has been applied to study the growth kinetics at the (111) and densely twinned (211) solid-liquid interface.
- Simulations show that the inclusion of stacking faults naturally leads to the emergence of two distinct growth modes of the (111) solid-liquid interface. By accurate modelling of the stacking fault energy, Monte Carlo simulations show that faulted islands can be sustained at the (111) growth interface at an undercooling higher than approximately 25 to 50 K.

- The interface growth velocities as a function of undercooling were calculated and it was shown that multiply twinned silicon crystals may rapidly be grown parallel to the direction of the twin boundaries. Such a crystal growth process is expected to result in crystals with a very low density of extended defects.
- The inclusion of stacking faults into the model adds a correction to the location of the (111) interface roughening transition.

CONTRIBUTIONS

I declare that Chapter 9 contains results of photoluminescence measurements on $CuGaSe_2$ thin-film devices, which do not represent orginal work of the author of the present dissertation. I would particularly like to thank Thomas Unold for the permission to reprint these results here and for many useful discussions. Furthermore, I would like to thank Stefan Kretschmar for the photoluminescence measurements and Raquel Caballero for sample preparation. The experimental work was carried out by the aforementioned persons at the Helmholtz Center for Materials and Energy in Berlin.

ERKLÄRUNG – DISCLAIMER

Die vorliegende Arbeit wurde im Zeitraum von Oktober 2008 bis November 2012 im Fachgebiet Materialmodellierung am Institut für Materialwissenschaft der Technischen Universität Darmstadt bei Herrn Prof. Dr. rer. nat. Karsten Albe angefertigt.

Hiermit versichere ich an Eides statt, dass ich die vorliegende Arbeit selbstständig und nur unter Verwendung der angegebenen Hilfsmittel angefertigt habe. Von mir wurde weder an der Technischen Universität Darmstadt noch an einer anderen Hochschule ein Promotionsversuch unternommen.

Darmstadt, den 19. November 2012

Johan Pohl

DANKSAGUNG – ACKNOWLEDGMENTS

Sehr herzlich bedanken möchte ich mich bei einigen Personen, die durch ihre Hilfe und Unterstützung diese Arbeit erst möglich gemacht haben, und auch bei denen, die die letzten 4 Jahre zu einer angenehmen und bereichernden Erfahrung gemacht haben.

Zuerst möchte ich sehr herzlich meinen lieben Eltern Lana und Günther und meinem Großvater für 32 Jahre Unterstützung danken, auf die man sich jederzeit verlassen konnte. Ganz besonders danke ich auch Marjan, die mich besonders gegen Ende der Arbeit sehr liebevoll unterstützt hat.

Nun möchte ich zunächst ganz besonders Prof. Karsten Albe für die hervorragende Betreuung und das entgegengebrachte Vertrauen bei der selbständigen Bearbeitung vieler Teilprojekte meinen Dank aussprechen. Ich denke, ich habe in den vergangenen vier Jahren sowohl wissenschaftlich als auch persönlich sehr viel im Fachgebiet Materialmodellierung lernen können. Dies wäre sicherlich ohne einen guten Chef, der die richtigen Rahmenbedingungen schafft, nicht möglich gewesen.

Desweiteren danke ich Herrn Prof. Hans-Werner Schock für die Erstellung des Zweitgutachtens. Ich freue mich sehr darüber, die mit Sicherheit erfahrungsreichste Person auf dem Gebiet der Forschung zu Cu(In,Ga)Se_2 für diese Aufgabe gewonnen zu haben.

Dr. Thomas Unold (HZB) danke ich für viele Stunden gemeinsamer Diskussion über Photolumineszenzmessungen und Defekte in Cu(In,Ga)Se_2. Auch die zigste Iteration über die Formulierungen im Paper hat noch Spaß gemacht und war es wert.

Prof. Andreas Klein möchte ich ebenfalls für eine gelungene Zusammenarbeit und viele erleuchtende Diskussionen danken.

Ich danke allen Mitarbeitern des Fachgebiets Materialmodellierung für eine schöne Zeit und eine sehr gute Arbeitsatmosphäre. Renate Hernichel danke ich für Unterstützung in organisatorischen Dingen und ihre angehme Art. Besonderer Dank geht an Peter Agoston für manchmal endlose, aber immer erhellende Diskussionen und das gewisse Maß an “Durchdrehen”.

Ohne jeden einzelnen zu nennen, möchte ich allen Personen innerhalb des GRACIS-Projektes danken. Es war nicht nur thematisch ein spannendes Projekt, sondern besonders die stete Bereitschaft zu Diskussion und Austausch von allen Teilnehmern fand ich persönlich sehr positiv und bereichernd. Es waren durchweg sehr positive Begegnungen, die ich während der vielen Projekttreffen und Konferenzen gemacht habe.

Desweiteren danke ich Dr. Michael Müller für die produktive Kooperation im Bereich der Modellierung des Siliziumwachstums, die während der ersten Phase dieser Arbeit zusammen mit der Firma Wacker Schott Solar GmbH realisiert wurde.

Prof. Anton van der Ven danke ich für einen interessanten Forschungsaufenthalt an der University of Michigan in Ann Arbor im Jahr 2011 und für die Möglichkeit, die Clusterexpansionsmethode zu erlernen.

Curiculum Vitae

Personal data

Name	Johan Pohl
Address	Waidmannstr. 35 60596 Frankfurt am Main
Email	pohl@mm.tu-darmstadt.de
Date of birth	7. August 1980 Friedberg, Germany

University Education

12/2012	Expected Defense of PhD-Thesis (Degree: *Dr.-Ing.*, PhD in Materials Science and Engineering)
since 10/2008	**PhD Thesis:** *Structure and properties of defects in photovoltaic absorber materials: Atomic scale computer simulations of Si and Cu(In,Ga)Se_2* Materials Modeling Division (Prof. K. Albe), Technische Universität Darmstadt, Germany
10/2007–10/2008	**PhD studies:** PhD program in Economics Goethe Universität Frankfurt, Germany
9/2004–8/2005	**Studies:** Physics Ecole Polytechnique Federale de Lausanne (EPFL), Switzerland
10/2001–08/2007	**Studies:** Physics and Computer Science Degree: *Physik-Diplom* Technische Universität Darmstadt, Germany

Research Experience

10/2008–Present	**Research Associate** (Wissenschaftlicher Mitarbeiter) Materials Modeling Division (Prof. K. Albe), Technische Universität Darmstadt, Germany
02/2011–08/2011	**Visiting Scientist**, Department of Materials Science and Engineering Materials Modeling Group (Prof. Anton van der Ven),

University of Michigan, Ann Arbor, USA

12/2006 **Research Intern**,
Division of Materials Physics (Prof. Kai Nordlund),
University of Helsinki, Helsinki, Finland

11/2004–8/2005 **Research Intern**,
Physics Department (Prof. Harald Brune),
Ecole Polytechnique Federale de Lausanne (EPFL), Lausanne, Switzerland

School Education

1998–2000 **Secondary School:** Goetheschule Wetzlar, *gymnasiale Oberstufe*, Germany

06/2000 Graduation from secondary school (*Abitur*)

Book chapter

B1 K. Albe, P. Agoston, J. Pohl, *Ab-initio Modeling of Defects in Semiconductors*, in: Advanced Characterization Techniques for Thin Film Solar Cells, Wiley-VCH, Weinheim (2011).

Publications based on the present dissertation

A1 J. Pohl, T. Unold, K. Albe, *Antisite traps and metastable defects in Cu(In,Ga)Se_2 thin-film solar cells studied by screened-exchange hybrid density functional theory*, submitted to Phys. Rev. B (2012), arXiv:1205.2556.

A2 J. Pohl, A. Klein, K. Albe, *Role of copper interstitials in $CuInSe_2$: First-principles calculations* Phys. Rev. B **81**, 121201 (2011).

A3 J. Pohl, K. Albe, *Void formation in melt-grown silicon studied by molecular dynamics simulations: From grown-in faulted dislocation loops to vacancy clusters*, Appl. Phys. Lett. **99**, 081910 (2011).

A4 J. Pohl, K. Albe, *Thermodynamics and kinetics of the copper vacancy in $CuInSe_2$, $CuGaSe_2$, $CuInS_2$ and $CuGaS_2$ (vol 108, 023509, 2010)* J. Appl. Phys. **110**, 109905 (2011).

A5 J. Pohl, K. Albe, *Thermodynamics and kinetics of the copper vacancy in $CuInSe_2$, $CuGaSe_2$, $CuInS_2$ and $CuGaS_2$*, J. Appl. Phys. **108**, 023509 (2010).

A6 J. Pohl, K. Albe, *Formation of parallel (111) twin boundaries in silicon growth from the melt*, J. Cryst. Growth **312**, 1411 (2010).

A7 J. Pohl, K. Albe, *Intrinsic point defects in CuInSe2 and CuGaSe2: A comprehensive study based on calculations within screened-exchange hybrid density functional theory*, in preparation.

A8 J. Pohl, K. Albe, *A Lattice Monte Carlo growth model for silicon including (111) stacking faults and twin boundaries*, in preparation.

Conference proceeding based on the present thesis

A9 W. Witte, M. Powalla, D. Hariskos, A. Eicke, M. Botros, H.-W. Schock, D. Abou-Ras, R. Mainz, H. Rodriguez-Alvarez, T. Unold, G. H. Bauer, R. Brğgemann, S. J. Heise, O. Neumann, M. Meessen, J. Christen, F. Bertram, M. Müller, A. Klein, T. Adler, K. Albe, J. Pohl, M. Martin, R. A. De Souza, L. Nagarajan, T. Beckers, C. Boit, J. Dietrich, M. Hetterich, Z. Zhang, R. Scheer, H. Kempa, T. Orgis, *Chemical gradients in Cu(In,Ga)(Se,S)$_2$ thin-film solar cells: Results of the GRACIS project*, 27th European Photovoltaic Solar Energy Conference (EU-PVSEC) proceedings, p. 2166-2173 (2012).

Other publications

A10 J. Pohl, C. Stahl, K. Albe, *Size-dependent phase diagrams of metallic alloys: A Monte Carlo simulation study on order-disorder transitions in Pt-Rh nanoparticles*, Beilstein Journal of Nanotechnology **3**, 1 (2012).

A11 J. Pohl, K. Albe, *Phase equilibria and ordering in solid Pt-Rh calculated by means of a refined bond-order simulation mixing model*, Acta Mater. **57**, 4140 (2009).

Darmstadt, November 2012

BIBLIOGRAPHY

[1] W. Shockley and H. J. Queisser, J. Appl. Phys. **32**, 510 (1961).

[2] M. Green, K. Emery, Y. Hishikawa, W. Warta, and E. Dunlop, Prog. Photovoltaics **20**, 606 (2012).

[3] D. Azulay, O. Millo, I. Balberg, H. Schock, I. Visoly-Fisher, and D. Cahen, Sol. Energ. Mat. Sol. C. **91**, 85 (2007).

[4] L. Shay and J. Wernick, *Ternary Chalcopyrite Semiconductors* (Pergamon Press, Oxford, 1975).

[5] B. J. Stanbery, Critical Reviews In Solid State and Materials Sciences **27**, 73 (2002).

[6] H.-W. Schock and U. Rau, Physica B **308-310**, 1081 (2001).

[7] P. Jackson, D. Hariskos, E. Lotter, S. Paetel, R. Wuerz, R. Menner, W. Wischmann, and M. Powalla, Prog. Photovoltaics **19**, 894 (2011).

[8] S. Zhang, S.-H. Wei, A. Zunger, and H. Katayama-Yoshida, Phys. Rev. B **57**, 9642 (1998).

[9] P. Würfel, *Physics of Solar Cells*, 2nd edition ed. (Wiley-VCH, Weinheim, 2009).

[10] S. J. Fonash, *Solar cell device physics*, 2nd edition ed. (Academic Press / Elsevier, Amsterdam, 2010).

[11] R. Scheer and H.-W. Schock, *Chalcogenide Photovoltaics: Physics, Technologies, and Thin Film Devices* (Wiley-VCH, Weinheim, 2011).

[12] *Advanced Characterization Techniques for Thin Film Solar Cells*, edited by D. Abou-Ras, T. Kirchartz, and U. Rau (Wiley-VCH, Weinheim, 2011).

[13] M. Green, *Third generation photovoltaics - advanced solar energy conversion*, *Springer Series in Photonics 12* (Springer Verlag, Berlin, 2003).

[14] C.-S. Jiang, F. Hasoon, H. Moutinho, H. Al-Thani, M. Romero, and M. Al-Jassim, Appl. Phys. Lett. **82**, 127 (2003).

[15] S. Sze and K. K. Ng, *Physics of Semiconductor Devices*, *3rd edition* (John Wiley & Sons, New York, 2006).

[16] S. Li and Y. Fu, *3D TCAD Simulation for Semiconductor Processes, Devices and Optoelectronics* (Springer, New York, 2012).

[17] S. Degrave, M. Burgelman, and P. Nollet, IEEE Proceedings of 3rd World Conference on Photovoltaic Energy Conversion **3**, 487 (2003).

[18] H. Zhu, A. K. Kalkan, J. Hou, and S. J. Fonash, AIP Conference Proceedings **462**, 309 (1999).

[19] H.-W. Schock and R. Noufi, Prog. Photovoltaics **8**, 151 (2000).

[20] D. Abou-Ras, G. Kostorz, D. Bremaud, M. Kälin, F. Kurdesau, A. Tiwari, and M. Döbeli, Thin Solid Films **480 - 481**, 433 (2005).

[21] K. Ramanathan *et al.*, Prog. Photovoltaics **11**, 225 (2003).

[22] A. Chirila *et al.*, Nature Mater. **10**, 857 (2011).

[23] U. Rau, A. Jasenek, H. W. Schock, F. Engelhardt, and T. Meyer, Thin Solid Films **361**, 298 (2000).

[24] U. Rau and J. H. Werner, Appl. Phys. Lett. **84**, 3735 (2004).

[25] J. H. Werner, J. Mattheis, and U. Rau, Thin Solid Films **480**, 399 (2005).

[26] S. Siebentritt, Sol. Energ. Mat. Sol. C. **95**, 1471 (2011).

[27] S. Siebentritt, N. Papathanaslou, and M. C. Lux-Steiner, Physica B **376**, 831 (2006).

[28] J. Zhao and A. Wang, IEEE Conference Record of the 4th World Conference on Photovoltaic Energy Conversion **1**, 996 (2006).

[29] C. Kaufmann, A. Neisser, R. Klenk, and R. Scheer, Thin Solid Films **480 - 481**, 515 (2005).

[30] S. Zhang, S. Wei, and A. Zunger, Phys. Rev. Lett. **78**, 4059 (1997).

[31] S.-H. Wei, S. Zhang, and A. Zunger, Appl. Phys. Lett. **72**, 3199 (1998).

[32] C. Domain, S. Laribi, S. Taunier, and J. Guillemoles, J. Phys. Chem. Solids **64**, 1657 (2003).

[33] Y. Zhao, C. Persson, S. Lany, and A. Zunger, Appl. Phys. Lett. **85**, 5860 (2004).

[34] C. Persson, Y.-J. Zhao, S. Lany, and A. Zunger, Phys. Rev. B **72**, 035211 (2005).

[35] S. Lany and A. Zunger, Phys. Rev. B **72**, 035215 (2005).

[36] S. Lany and A. Zunger, J. Appl. Phys. **100**, 113725 (2006).

[37] S. Lany and A. Zunger, Phys. Rev. Lett. **100**, 016401 (2008).

[38] J. Pohl and K. Albe, J. Appl. Phys. **108**, 023509 (2010).

[39] J. Pohl and K. Albe, J. Appl. Phys. **110**, 109905 (2011).

[40] J. Pohl, A. Klein, and K. Albe, Phys. Rev. B **84**, 121201 (2011).

[41] L. E. Oikkonen, M. G. Ganchenkova, A. P. Seitsonen, and R. M. Nieminen, J. Phys. Cond. Matter **23**, 422202 (2011).

[42] T. Meyer, F. Engelhardt, J. Parisi, and U. Rau, J. Appl. Phys. **91**, 5093 (2002).

[43] M. Ruberto and A. Rothwarf, J. Appl. Phys. **61**, 4662 (1987).

[44] M. Igalson and H. W. Schock, J. Appl. Phys. **80**, 5765 (1996).

[45] R. Herberholz, U. Rau, H. Schock, T. Haalboom, T. Godecke, F. Ernst, C. Beilharz, K. Benz, and D. Cahen, Eur. Phys. J.: Appl. Phys. **6**, 131 (1999).

[46] M. Igalson, M. Bodegard, L. Stolt, and A. Jasenek, Thin Solid Films **431**, 153 (2003).

[47] F. Engelhardt, M. Schmidt, T. Meyer, O. Seifert, J. Parisi, and U. Rau, Phys. Lett. A **245**, 489 (1998).

[48] T. Eisenbarth, R. Caballero, M. Nichterwitz, C. Kaufmann, H. Schock, and T. Unold, J. Appl. Phys. **110**, 094506 (2011).

[49] J. Pohl, T. Unold, and K. Albe, submitted, arXiv: 1205.2556v1 (2012).

[50] M. Igalson, M. Bodegard, and L. Stolt, Sol. Energ. Mat. Sol. Cells **80**, 195 (2003).

[51] T. Walter, R. Herberholz, C. Muller, and H. W. Schock, J. Appl. Phys. **80**, 4411 (1996).

[52] G. Hanna, A. Jasenek, U. Rau, and H. W. Schock, Phys. Status Solidi A **179**, R7 (2000).

[53] V. Mertens, J. Parisi, and R. Reineke-Koch, J. Appl. Phys. **101**, 104507 (2007).

[54] J. T. Heath, J. D. Cohen, W. N. Shafarman, D. X. Liao, and A. A. Rockett, Appl. Phys. Lett. **80**, 4540 (2002).

[55] T. Sakurai, H. Uehigashi, M. Islam, and *et al.* , Thin Solid Films **517**, 2403 (2009).

[56] J. T. Heath, J. D. Cohen, and W. N. Shafarman, J. Appl. Phys. **95**, 1000 (2004).

[57] S. Siebentritt and T. Rissom, Appl. Phys. Lett. **92**, 062107 (2008).

[58] R. Herberholz, M. Igalson, and H. W. Schock, J. Appl. Phys. **83**, 318 (1998).

[59] D. J. Schroeder, J. L. Hernandez, G. D. Berry, and A. A. Rockett, J. Appl. Phys. **83**, 1519 (1998).

[60] A. Jasenek, U. Rau, V. Nadenau, and H. W. Schock, J. Appl. Phys. **87**, 594 (2000).

[61] A. Krysztopa, M. Igalson, P. Zabierowski, J. Larsen, Y. Aida, S. Siebentritt, and L. Guetay, Thin Solid Films **519**, 7308 (2011).

[62] S. Siebentritt, *Wide-Gap Chalcopyrites, Chapter 7* (Springer Series in Materials Science, Springer, Berlin, 2006), pp. 113–156.

[63] T. Haalboom, T. Godecke, F. Ernst, M. Ruhle, R. Herberholz, H. W. Schock, C. Beilharz, and K. W. Benz, Inst. Phys. Conf. Ser. **152**, 249 (1998).

[64] T. Gödecke, T. Haalboom, and F. Ernst, Zeitschrift f. Metallkd. **91**, 622 (2000).

[65] S. Lehmann *et al.*, J. Appl. Phys. **109**, (2011).

[66] W. Paszkowicz, R. Lewandowska, and R. Bacewicz, Journal of Alloys and Compounds **362**, 241 (2004).

[67] J. M. Merino, M. Di Michiel, and M. Leon, J. Phys. Chem. Solids **64**, 1649 (2003).

[68] I. Lyubomirsky, M. Rabinal, and D. Cahen, J. Appl. Phys. **81**, 6684 (1997).

[69] K. Gartsmann, L. Chernyak, V. Lyahovitskaya, D. Cahen, V. Didik, V. Kozlovsky, R. Malkovich, and E. S. abd V. Usacheva, J. Appl. Phys. **82**, 4282 (1997).

[70] M. Kleinfeld and H.-D. Wiemhöfer, Solid State Ionics **28-30, Part 2**, 1111 (1988).

[71] G. Dagan, T. Ciszek, and D. Cahen, J. Phys. Chem. **96**, 11009 (1992).

[72] I. Lubomirsky, K. Gartsman, and D. Cahen, J. Appl. Phys. **83**, 4678 (1998).

[73] D. Cahen, J. Gile, C. Schmitz, L. Chernyak, K. Gartsman, and A. Jakubowicz, Science **258**, 271 (1992).

[74] L. Chernyak, D. Cahen, S. Zhao, and D. Haneman, Appl. Phys. Lett. **65**, 427 (1994).

[75] L. Chernyak, K. Gartsman, D. Cahen, and O. Stafsudd, J. Phys. Chem. Solids **56**, 1165 (1995).

[76] D. Cahen and L. Chernyak, Adv. Materials **9**, 861 (1997).

[77] K. Gartsman, D. Cahen, and R. Scheer, Appl. Phys. Lett. **79**, 2919 (2001).

[78] W. von Ammon, in *Springer Handbook of Electronic and Photonic Materials* (Springer Verlag, Berlin, 2006), pp. 101 – 117.

[79] P. M. Fahey, P. B. Griffin, and J. D. Plummer, Rev. Mod. Phys. **61**, 289 (1989).

[80] K. Jackson, *Kinetic Processes Crystal Growth, Diffusion, and Phase Transitions in Materials* (Wiley-VCH, Weinheim, 2004).

[81] K. Jackson, Interface Science **10**, 159 (2002).

[82] W. Van Enckevort and J. Van Der Eerden, J. Cryst Growth **47**, 501 (1979).

[83] D. Woodraska and J. Jaszczak, Phys. Rev. Lett. **374**, 319 (1997).

[84] D. Woodraska and J. Jaszczak, Surf. Sci. **374**, 319 (1997).

[85] P. van Beurden, E. van Veenendaal, W. van Enckefort, and H. Knops, Surf. Sci. **424**, 109 (1999).

[86] D. Gao and J. JA, Phys. Rev. B **67**, 155420 (2003).

[87] K. Beatty and K. Jackson, J. Cryst. Growth **211**, 13 (2000).

[88] A. Tan, C. Ong, and H. Tan, Semicond. Sci. Technol. **3**, 1 (1988).

[89] W. Edwards, Can. J. Phys. **38**, 439 (1960).

[90] T. Ciszek, in *Semiconductor Silicon*, edited by R. Haberecht and E. Kern (The Electrochemical Society, Pennington, New Jersey, 1969), p. p. 156.

[91] T. Abe, J. Cryst. Growth **24/25**, 463 (1974).

[92] M. Müller, B. Birkmann, F. Mosel, I. Westram, and A. Seidl, J. Cryst. Growth **312**, 1397 (2010).

[93] D. Hamilton and R. Seidensticker, J. Appl. Phys. **31**, 1165 (1960).

[94] K. Fujiwara, K. Maeda, N. Usami, G. Sazaki, Y. Nose, and K. Nakajima, Scr. Mater. **57**, 81 (2007).

[95] K. Fujiwara, K. Maed, N. Usami, G. Sazaki, Y. Nose, A. Nomura, T. Shishido, and K. Nakajima, Acta Mater **56**, 2663 (2008).

[96] K. Kitamura, N. Usami, T. Sugawara, K. Kutsukake, K. Fujiwara, Y. Nose, T. Shishido, and K. Nakajima, J. Cryst. Growth **280**, 419 (2005).

[97] R. Wang, W. Lu, and L. Hohan, Metall. Mater. Trans. **28A**, 1233 (1997).

[98] R. Cahn, Adv. Phys. **3**, 363 (1954).

[99] H. MÃűller, Solid State Phen. **95-96**, 181 (2004).

[100] E. Billig, J. Inst. Met. **83**, 1565 (1954).

[101] D. Hurle, J. Crystal Growth **147**, 239 (1995).

[102] V. Voronkov, Sov. Phys. Crystallogr. **19**, 573 (1975).

[103] M. Itsumi, H. Akiya, T. Ueki, M. Tomita, and M. Yamawaki, J. Appl. Phys. **78**, 5984 (1995).

[104] T. Ueki, M. Itsumi, and T. Takeda, Appl. Phys. Lett. **70**, 1248 (1997).

[105] T. Sinno, J. Dai, and S. Kapur, Mat. Sci. Eng. B **159-160**, 128 (2009).

[106] P. Plekhanov, U. Gösele, and T. Tan, J. Appl. Phys. **84**, 718 (1998).

[107] T. Ebe, J. Cryst. Growth **203**, 387 (1999).

[108] V. Voronkov and R. Falster, J. Appl. Phys. **86**, 5975 (1999).

[109] V. Voronkov and R. Falster, J. Appl. Phys. **87**, 4126 (2000).

[110] R. Falster, V. Voronkov, and F. Quast, Phys. Status Solidi B **222**, 219 (2000).

[111] A. La Magna, S. Coffa, and L. Colombo, Phys. Rev. Lett. **82**, 1720 (1999).

[112] L. Colombo, Physica B **273-274**, 458 (1999).

[113] M. Prasad and T. Sinno, Phys. Rev. B **68**, 045206 (2003).

[114] A. La Magna, V. Privitera, G. Fortunato, M. CuscunÃă, B. Svensson, E. Monakhov, K. Kuitunen, J. Slotte, and F. Tuomisto, Phys. Rev. B **75**, 235201 (2007).

[115] S. H. Lee, J. W. Kang, Y. H. Hong, H. J. Oh, and D. H. Kim, J. Cryst. Growth **311**, 3592 (2009).

[116] M. Prasad and T. Sinno, Appl. Phys. Lett. **80**, 1951 (2002).

[117] T. Frewen, S. Kapur, W. Haeckl, W. von Ammon, and T. Sinno, J. Cryst. Growth **279**, 258 (2005).

[118] E. Jaynes, Am. J. Phys. **33**, 391 (1965).

[119] C. Cohen-Tannoudji, B. Diu, and F. Laloë, *Quantenmechanik, Teil 1 und 2* (Walter de Gruyter publishers, Berlin, 1999).

[120] P. Hohenberg and W. Kohn, Phys. Rev. **136**, B864 (1964).

[121] W. Kohn and L. J. Sham, Phys. Rev. **140**, A1133 (1965).

[122] R. Martin, *Electronic Structure : Basic Theory and Practical Methods* (Cambridge University Press, Cambridge, 2004).

[123] *Planewaves, Pseudopotentials, and the LAPW Method*, edited by D. Singh and L. Nordstrom (Springer Verlag, Berlin, 2006).

[124] D. Ceperley and B. Alder, Phys. Rev. Lett. **45**, 566 (1980).

[125] J. Perdew, K. Burke, and M. Ernzerhof, Phys. Rev. Lett. **77**, 3865 (1996).

[126] J. Hubbard, Proc. Roy. Soc. A **276**, 238 (1963).

[127] V. Anisimov, J. Zaanen, and O. Andersen, Phys. Rev. B **44**, 943 (1991).

[128] V. Anisimov, F. Aryasetiawan, and A. Lichtenstein, J. Phys.: Cond. Mat. **9**, 767 (1997).

[129] A. Becke, J. Chem. Phys. **98**, 5648 (1993).

[130] C. Adamo and V. Barone, J. Chem. Phys. **110**, 6158 (1999).

[131] J. Heyd, G. Scuseria, and M. Ernzerhof, J. Chem. Phys. **118**, 8207 (2003).

[132] J. Heyd, G. Scuseria, and M. Ernzerhof, J. Chem. Phys. **124**, 219906 (2006).

[133] M. Marsman, J. Paier, A. Stroppa, and G. Kresse, J. Phys.: Cond. Matter **20**, 064201 (2008).

[134] S. Kümmel and L. Kronik, Rev. Mod. Phys. **80**, 3 (2008).

[135] H. Henderson, J. Paier, and G. Scuseria, in *Advanced Calculations for Defects in Materials* (Wiley-VCH, Weinheim, 2011), pp. 97–110.

[136] M. Payne, M. Teter, D. Allen, T. Arias, and J. Joannopoulos, Rev. Mod. Phys. **64**, 1045 (1992).

[137] W. Foulkes, L. Mitas, R. Needs, and G. Rajagopal, Rev. Mod. Phys. **73**, 33 (2001).

[138] F. Stillinger and T. Weber, Phys. Rev. B **31**, 5262 (1985).

[139] J. Tersoff, Phys. Rev. B **37**, 6991 (1988).

[140] P. Erhart and K. Albe, Phys. Rev. B **71**, 035211 (2005).

[141] E. Ising, Z. Physik **31**, 253 (1925).

[142] S. Brush, Rev. Mod. Phys. **39**, 883 (1967).

[143] R. Peierls, Proc. Cambridge Phil. Soc. **32**, 477 (1936).

[144] J. Sanchez, F. Ducastelle, and D. Gratias, Physica **128A**, 334 (1984).

[145] A. Gonis, X. Zhang, A. Freeman, P. Turchi, G. Stocks, and D. Nicholson, Phys. Rev. B **36**, 4630 (1987).

[146] J. M. Sanchez, Phys. Rev. B **81**, 224202 (2010).

[147] R. Car and M. Parrinello, Phys. Rev. Lett. **55**, 2471 (1985).

[148] S. Plimpton, J. Comp. Phys. **117**, 1 (1995), uRL: http://lammps.sandia.gov.

[149] N. Metropolis, A. Rosenbluth, M. Rosenbluth, A. Teller, and E. Teller, J. Chem. Phys. **21**, (1953).

[150] A. Voter, Radiation Effects in Solids, edited by K.E. Sickafus and E.A. Kotomin, Springer, NATO publishing unit, Dordrecht, Netherlands (2005).

[151] K. Fichthorn and W. Weinberg, J. Chem. Phys. **95**, 1090 (1991).

[152] G. Henkelman, G. Jóhannesson, and H. Jónsson, in *Theoretical methods in Condensed Phase Chemistry*, Vol. 5 of *Progress in Theoretical Chemistry and Physics*, edited by S. Schwartz (Springer, Berlin, 2001), Chap. Methods for finding saddle points and minimum energy paths, p. 269.

[153] G. Henkelman and H. Jonsson, Journal of Chemical Physics **113**, 9978 (2000).

[154] G. Henkelman, B. P. Uberuaga, and H. Jonsson, Journal of Chemical Physics **113**, 9901 (2000).

[155] J. Heyd, G. Scuseria, and M. Ernzerhof, J. Chem. Phys. **118**, 8207 (2003).

[156] J. Heyd, G. Scuseria, and M. Ernzerhof, J. Chem. Phys. **124**, 219906 (2006).

[157] T. Morgan, Phys. Rev. B **34**, 2664 (1986).

[158] D. Chadi and D. Chang, Phys. Rev. B **39**, 10063 (1989).

[159] D. J. Chadi, Phys. Rev. Lett. **59**, 15181 (1999).

[160] S.-H. Wei and S. B. Zhang, Phys. Rev. B **66**, 155211 (2002).

[161] S. Lany and A. Zunger, Phys. Rev. B **72**, 035215 (2005).

[162] P. Erhart, K. Albe, and A. Klein, Phys. Rev. B **73**, 205203 (2006).

[163] P. Erhart and K. Albe, J. Appl. Phys. **104**, (2008).

[164] C. Van de Walle and P. E. Blöchl, Phys. Rev. B **47**, 4244 (1993).

[165] M. J. Puska and R. M. Nieminen, Rev. Mod. Phys. **66**, 841 (1994).

[166] Y. C. Ma, M. Rohlfing, and A. Gali, Phys. Rev. B **81**, 041204 (2010).

[167] S. Zhang and J. Northrup, Phys. Rev. Lett. **67**, 2339 (1991).

[168] G. Makov and M. C. Payne, Phys. Rev. B **51**, 4014 (1995).

[169] S. Lany and A. Zunger, Phys. Rev. B **78**, 235104 (2008).

[170] S. Lany and A. Zunger, Model. Simul. Mater. Sci. Eng. **17**, 084002 (2009).

[171] H.-P. Komsa, T. T. Rantala, and A. Pasquarello, Phys. Rev. B **86**, 045112 (2012).

[172] A. Alkauskas, P. Broqvist, and A. Pasquarello, Phys. Rev. Lett. **101**, 046405 (2008).

[173] A. Alkauskas and A. Pasquarello, Phys. Rev. B **84**, 125206 (2011).

[174] G. Kresse and J. Furthmüller, Phys. Rev. B **54**, 11169 (1996).

[175] K. Takarabe, K. Kawai, K. Kawamura, S. Minomura, and N. Yamamoto, J. Cryst. Growth **766**, (1990).

[176] H. Neumann, phys. stat. sol. a **96**, K121 (1986).

[177] T. Tinoco, A. Polian, D. Gómez, and J. Itié, phys. stat. sol. B **198**, 433 (1996).

[178] H. Spiess, U. Haeberlein, G. Brandt, A. Räuber, and J. Schneider, phys. stat. sol. b **62**, (1974).

[179] A. Kraft, G. Kühn, and W. Möller, Z. anorg. allg, Chem. **504**, 155 (1983).

[180] S. Abrahams and J. Bernstein, J. Chem. Phys. **59**, 5415 (1973).

[181] M. Bettini and W. Holzapfel, Solid State Commun. **16**, 27 (1975).

[182] A. Werner, H. Hocheimer, and A. Jayaraman, Phys. Rev. B **23**, 3836 (1981).

[183] R. Philip and B. Pradeep, Semicond. Sci. Technol. **18**, 768 (2003).

[184] U. Rau and H. Schock, Appl. Phys. A **69**, 131 (1999).

[185] A. Klein and W. Jaegermann, Appl. Phys. Lett. **74**, 2283 (1999).

[186] A. Klein, J. Fritsche, W. Jaegermann, J. Schön, C. Kloc, and E. Bucher, Appl. Surf. Sci. **166**, 508 (2000).

[187] D. Schmid, M. Ruckh, F. Grunwald, and H. W. Schock, J. Appl. Phys. **73**, 2902 (1993).

[188] S. Fiechter, Y. Tomm, K. Diesner, and T. Weiss, Jpn. J. Appl. Phys. **39 (Suppl. 39-1)**, 123 (2000).

[189] R. Scheer and H. Lewerenz, J. Vac. Sci. Technol. A **12**, 51 (1994).

[190] M. Jean, S. Peulon, J. Guillemoles, and J. Vedel, Ionics **3**, 149 (1997).

[191] K. Becker and S. Wagner, Phys. Rev. B **27**, 5240 (1983).

[192] S. Wagner, Electrochem. Soc. Proc. **83**, 410 (1984).

[193] P. Stallworth, J.-F. Guillemoles, J. Flowers, J. Vedel, and S. Greenbaum, Solid State Comm. **113**, 527 (2000).

[194] J. Parkes, R. Tomlinson, and M. Hampshire, J. Cryst. Growth **20**, 315 (1973).

[195] P. Yu, S. Faile, and Y. Park, Appl. Phys. Lett. **26**, 384 (1975).

[196] B. Tell and P. Bridenbaugh, J. Appl. Phys. **48**, 2477 (1977).

[197] D. Soltz, G. Dagan, and D. Cahen, Solid State Ionics **28-30**, 1105 (1988).

[198] B. Tell, S. Wagner, and P. Bridenbaugh, Appl. Phys. Lett. **28**, 454 (1976).

[199] U. Böhnke and G. Kühn, J. Mat. Sci. **22**, 1635 (1987).

[200] C. Freysoldt, J. Neugebauer, and C. G. Van de Walle, Phys. Rev. Lett. **102**, 016402 (2009).

[201] A. Stukowski, Modelling Simul. Mater. Sci. Eng. **18**, 015012 (2010).

[202] M. Cwil, M. Igalson, P. Zabierowski, and S. Siebentritt, J. Appl. Phys. **103**, 063701 (2008).

[203] A. Urbaniak and M. Igalson, J. Appl. Phys. **106**, 063720 (2009).

[204] S. Siebentritt, M. Igalson, C. Persson, and S. Lany, Prog. Photovoltaics **18**, 390 (2010).

[205] M. Burgelman *et al.*, Prog. Photovoltaics **5**, 121 (1997).

[206] J.-F. Guillemoles, L. Kronik, D. Cahen, U. Rau, A. Jasenek, and H.-W. Schock, J. Phys. Chem. B **104**, 4849 (2000).

[207] I. Eisgruber, J. Granata, J. Sites, J. Hou, and J. Kessler, Sol. Energ. Mat. Sol. C. **53**, 367 (1998).

[208] A. Niemegeers, M. Burgelman, R. Herberholz, U. Rau, D. Hariskos, and H. W. Schock, Prog. Photovoltaics **6**, 407 (1998).

[209] G. Hanna, J. Mattheis, V. Laptev, Y. Yamamoto, U. Rau, and H. Schock, Thin Solid Films **431-432**, 31 (2003).

[210] C. Stephan, S. Schorr, M. Tovar, and H. W. Schock, Appl. Phys. Lett. **98**, 091906 (2011).

[211] R. Caballero, C. A. Kaufmann, M. Cwil, C. Kelch, D. Schweigert, T. Unold, M. Rusu, H. W. Schock, and S. Siebentritt, J. Phys. Cond. Matter **19**, 356222 (2007).

[212] J. Krustok, J. Raudoja, M. Yakushev, R. Pilkington, and H. Collan, phys. stat. sol. a **173**, 483 (1999).

[213] D. Cahen and R. Noufi, J. Phys. Chem. Solids **53**, 991 (1992).

[214] N. Meyer, Ph.D. thesis, Freie Universität Berlin, 2000.

[215] V. Milman, Acta Crystallogr. Sect. B **B58**, 437 (2002).

[216] V. Glazov, A. Pashinkin, and V. Fedorov, Inorg. Mater. **36**, 641 (2000).

[217] N. Morimoto and K. Koto, Science **152**, 345 (1966).

[218] G. Gattow and A. Schneider, Z. Anorg. Allg. Chem. **286**, 296 (1956).

[219] J. Rigoult, A. Rimsky, and A. Kuhn, Acta Crystallogr. Sect. B **36**, 916 (1980).

[220] K. Osamura, Y. Murakami, and Y. Tomije, J. Phys. Soc. Japan **21**, 1848 (1966).

[221] U. Schwarz, H. Hillebrecht, H. J. Deiseroth, and R. Walther, Z. Kristallogr. **210**, 342 (1995).

[222] J. Li, M. Record, and J. Tedenac, Z. Metallkd. **94**, 381 (2003).

[223] A. Kuhn, A. Chevy, and R. Chevalier, phys. stat. sol. a **31**, 469 (1975).

[224] D. Lübbers and V. Leute, J. Solid State Chem. **43**, 339 (1982).

[225] J.-F. Guillemoles, Thin Solid Films **361**, 338 (2000).

[226] H. Neumann and R. D. Tomlinson, Solar Cells **28**, 301 (1990).

[227] S. Lany, Phys. Rev. B **78**, 245207 (2008).

[228] C. Stephan, T. Scherb, C. A. Kaufmann, S. Schorr, and H. W. Schock, Appl. Phys. Lett. **101**, 101907 (2012).

[229] K. Sato, Mat. Sci. Semicon. Proc. **6**, 335 (2003).

[230] P. Lange, H. Neff, M. Fearheiley, and K. J. Bachmann, Phys. Rev. B **31**, 4074 (1985).

[231] P. Migliorato, J. L. Shay, H. M. Kasper, and S. Wagner, J. Appl. Phys. **46**, 1777 (1975).

[232] G. Dagan, F. Abou-Elfotouh, D. Dunlavy, R. Matson, and D. Cahen, Chem. Mater. **2**, 286 (1990).

[233] M. Wagner, I. Dirnstorfer, D. M. Hofmann, M. D. Lampert, F. Karg, and B. K. Meyer, phys. stat. sol. A **167**, 131 (1998).

[234] B. Keyes, P. Dippo, W. Metzger, J. Abushama, and R. Noufi, Conference record of the 29th IEEE PV specialists conference p. 511 (2002).

[235] T. Unold, T. Enzenhofer, C. A. Kaufmann, R. KIenk, A. Neisser, K. Sakurai, and H. W. Schock, Conference Record of the 2006 IEEE 4th World Conference on Photovoltaic Energy Conversion p. 356 (2006).

[236] D. O. Scanlon, B. J. Morgan, G. W. Watson, and A. Walsh, Phys. Rev. Lett. **103**, 096405 (2009).

[237] A. Nagoya, R. Asahi, R. Wahl, and G. Kresse, Phys. Rev. B **81**, 113202 (2010).

[238] S. Chen, X. G. Gong, A. Walsh, and S.-H. Wei, Appl. Phys. Lett. **96**, 021902 (2010).

[239] S. Chen, J.-H. Yang, X. G. Gong, A. Walsh, and S.-H. Wei, Phys. Rev. B **81**, 245204 (2010).

[240] A. Walsh, S. Chen, S.-H. Wei, and X.-G. Gong, Advanced Energy Materials **2**, 400 (2012).

[241] H. Iwata, U. Lindefelt, S. Öberg, and P. Briddon, Phys. Rev. B **68**, 113202 (2003).

[242] C. Raffy, J. Furthmüller, and F. Bechsted, Phys. Rev. B **66**, 075201 (2002).

[243] A. Gross and H. Teichler, Phil. Mag. B **64**, 413 (1991).

[244] A. Paxton and A. Sutton, Acta metall. **37**, 1693 (1989).

[245] L. Mattheiss and J. Patel, Phys. Rev. B **23**, 5384 (1981).

[246] C. Weigel, H. Alexander, and J. Corbett, Phys. Status Solidi B **71**, 701 (1975).

[247] D. Faken and H. Jónsson, Comp. Mat. Sci. **2**, 279 (1994).

[248] OVITO is developed by A. Stukowski, URL: http://ovito.sourceforge.net .

[249] A. Sutton and R. Balluffi, *Interfaces in Crystalline Materials* (Oxford Science Publications, Oxford, 1995, p. 84 and Fig. 2.11).

[250] R. Pond, J. Physique **43**, C1 (1982).

[251] R. Pond and D. Vlachavas, Proc. R. Soc. A **386**, 95 (1983).

[252] R. Pond, D. Bacon, and A. Bastaweesy, Inst. Phys. Conf. Ser. **76**, 253 (1985).

[253] A. Papon and M. Petit, Scripta metall. **19**, 391 (1985).

[254] A. Bourret and J. Bacmann, Surf. Sci. **162**, 495 (1985).

[255] M. Kohyama, Y. R, and M. Doyama, Phys. Status Solidi **137**, 11 (1986).

[256] M. Kohyama, Y. R, and M. Doyama, Phys. Status Solidi **138**, 387 (1986).

[257] D. Chadi and K. Chang, Phys. Rev. B **38**, 1523 (1988).

[258] J. Hastings, S. Estreicher, and P. Fedders, Phys. Rev. B **56**, 10215 (1997).

[259] A. Bongiorno, L. Colombo, and T. Diaz de la Rubia, Europhys. Lett. **43**, 695 (1998).

[260] T. Staab, A. Sieck, M. Haugk, M. Puska, T. Frauenheim, and H. Leipner, Phys. Rev. B **65**, 115210 (2002).

[261] R. Wixom and A. Wright, Phys. Rev. B **74**, 205208 (2006).

[262] S. Lee and G. S. Hwang, Phys. Rev. B **78**, 125310 (2008).

[263] S. Lee, R. Bondi, and G. Hwang, Phys. Rev. B **80**, 245209 (2009).

[264] J. Pohl, M. M"uller, A. Seidl, and K. Albe, J. Cryst. Growth **312**, 1411 (2010).

[265] P. Apte and X. Zeng, Appl. Phys. Lett. **92**, 221903 (2008).

[266] I. Ray and D. Cockayne, Proc. R. Soc. A **325**, 543 (1971).

[267] H. Alexander, J. Phys. (Paris) Suppl. **6**, 7 (1979).

[268] H. Föll and C. Carter, Phil. Mag. A **40**, 497 (1979).

[269] L. Chen and L. Falicov, Phil. Mag. **29**, 1 (1974).

[270] J. Sanchez-Dehesa, J. Verges, and C. Tejedor, Phys. Rev. B **23**, 5384 (1981).

[271] S. Louie, J. Physique **46**, C4 (1985).

[272] M. Chou, M. Cohen, and S. Louie, Phys. Rev. B **32**, 7979 (1985).

[273] P. Käckell, J. Furthmüller, and F. Bechstedt, Phys. Rev. B **58**, 1326 (1998).

[274] A. Stukowski, Modelling Simul. Mater. Sci. Eng. **18**, 015012 (2010).

[275] W. Coene, H. Bender, and S. Amelinckx, Phil. Mag. A **52**, 369 (1985).

[276] R. Oshima, F. Hori, M. Komatsu, and H. Mori, Jpn. J. Appl. Phys. **37**, L1430 (1998).

[277] W. Obretenov, D. Kashchiev, and V. Bostanov, J. Cryst. Growth **96**, 843 (1989).

[278] D. Hamilton and R. Seidensticker, J. Appl. Phys. 1450 (1963).